



The University of Manchester

DOCTORAL THESIS

---

# Modelling of the relativistic Sunyaev-Zeldovich effect and related Compton scattering processes

---

*Author:*  
Elizabeth G. LEE

*Supervisor:*  
Jens CHLUBA

*A thesis submitted to the University of Manchester  
for the degree of Doctor of Philosophy*

*in the*

Faculty of Science and Engineering

Jodrell Bank Centre for Astrophysics

Department of Physics and Astronomy in the School of Natural Sciences

2023

# Contents

<b>Contents</b>	<b>2</b>
<b>List of Figures</b>	<b>7</b>
<b>List of Tables</b>	<b>9</b>
<b>Abbreviations</b>	<b>10</b>
<b>Physical Constants</b>	<b>11</b>
<b>Abstract</b>	<b>12</b>
<b>Declaration of Authorship</b>	<b>13</b>
<b>Copyright Statement</b>	<b>14</b>
<b>Acknowledgements</b>	<b>15</b>
<b>Dedication</b>	<b>16</b>
<b>The Author</b>	<b>17</b>
<b>Supporting Publications</b>	<b>18</b>
<b>1 Introduction</b>	<b>19</b>
1.1 A brief history of the CMB and SZ observations . . . . .	20
1.2 Compton Scattering . . . . .	22
1.2.1 The Kompaneets equation . . . . .	24
1.3 The SZ Effect . . . . .	25
1.3.1 Thermal SZ Effect . . . . .	26
1.3.2 Kinematic SZ Effect . . . . .	28
1.3.3 Relativistic SZ Corrections . . . . .	30
1.3.4 Multiple Scatterings . . . . .	31
1.3.5 Polarised SZ Effect . . . . .	31
1.4 Variations to the SZ effect . . . . .	32
1.4.1 Alternate backgrounds . . . . .	32
1.4.2 Non-thermal contributions . . . . .	33

1.5	Simulations and predicting temperatures in clusters	34
1.5.1	SZ Temperatures	35
1.5.2	X-ray Temperatures	37
1.5.3	Halo definition and redshift dependence	38
1.6	Thesis Overview	39
<b>2</b>	<b>Bahamas+Macsis SZ temperature scalings</b>	<b>41</b>
2.1	Introduction	41
2.2	Simulations	43
2.2.1	BAHAMAS Simulation	44
2.2.2	MACSIS Simulation	44
2.2.3	Combined Sample	45
2.2.4	Core-Excised Averages	45
2.2.5	Hot and Relaxed Sub-samples	46
2.3	Cluster Temperature Scalings	48
2.3.1	Causes for differences in temperature measures	48
2.3.2	The effect of averaging over volumes of radii $R_{500c}$ or $R_{200c}$	48
2.3.3	Temperature-mass scaling relations	50
2.3.4	Covariance of Fits	54
2.3.5	Mass dependence of the quality of the fits	56
2.3.6	Temperature-temperature scaling relations	56
2.3.7	Volume-averaged $Y$ relations	59
2.3.8	Hot and Relaxed Samples	60
2.3.9	$y$ -weighted Temperature Dispersion	62
2.4	Cluster temperature profiles	62
2.4.1	Radial Profiles	63
2.4.2	Cylindrical Profiles	66
2.4.3	Profiles of $y$ -weighted Temperature Moments	68
2.5	Implications for Cosmology	68
2.5.1	Effect on $Y_{SZ}$ -Mass relation	70
	Comparison to other temperature-mass scaling relations	72
	Corrections from temperature dispersion	73
2.5.2	Applications to the determination of $H_0$	74
2.6	Conclusions	76
<b>3</b>	<b>Multi-Simulation SZ temperature scalings</b>	<b>79</b>
3.1	Introduction	79
3.2	Simulations	80
3.2.1	Bahamas and Macsis	82
3.2.2	The Three Hundred Project	83
3.2.3	Magneticum Pathfinder	83
3.2.4	IllustrisTNG	84
3.3	Temperature Scaling Relations	84

3.3.1	Redshift evolution . . . . .	86
3.3.2	Radial dependence . . . . .	89
3.3.3	Temperature–Y scalings . . . . .	91
3.3.4	DT-temperature scalings . . . . .	93
3.4	Resilience of results . . . . .	94
3.4.1	Resolution . . . . .	94
3.4.2	Gas fraction . . . . .	96
3.4.3	Feedback . . . . .	98
3.4.4	Relaxation . . . . .	100
3.4.5	Core-Excision . . . . .	100
3.4.6	Particle temperature cut . . . . .	103
3.5	Cross-simulation averaged results . . . . .	103
3.5.1	Comparison to X-ray observations . . . . .	109
3.6	Discussion . . . . .	110
3.6.1	$\gamma$ -weighted temperature – Y self-calibration . . . . .	110
3.6.2	Applications to current and future SZ analyses . . . . .	111
3.7	Conclusions . . . . .	113
<b>4</b>	<b>Radio SZ modelling</b>	<b>116</b>
4.1	Introduction . . . . .	116
4.2	The radio SZ signal . . . . .	117
4.2.1	A summary of the SZ formalism . . . . .	117
4.2.2	The asymptotic expansion . . . . .	118
	Final signal in the CMB rest frame . . . . .	119
4.2.3	The radio SZ signal . . . . .	121
	Expression inside cluster frame . . . . .	122
	Expression inside CMB frame . . . . .	123
4.2.4	Anisotropies in the radio background . . . . .	124
4.2.5	Effect of the observer motion . . . . .	125
4.2.6	Additional small effects . . . . .	126
4.3	Results . . . . .	127
4.3.1	Main dependence of total signal and degeneracies . . . . .	127
4.3.2	Relativistic and kinematic corrections . . . . .	129
4.3.3	Corrections to the null . . . . .	131
4.3.4	Radio background variations . . . . .	134
4.3.5	Anisotropy in the radio background . . . . .	137
4.4	Discussion . . . . .	139
4.5	Conclusion . . . . .	140
<b>5</b>	<b>High energy non-thermal and anisotropic SZ</b>	<b>143</b>
5.1	Introduction . . . . .	143
5.2	The analytic anisotropic SZ scattering kernel . . . . .	144
5.2.1	Anisotropy in the photon population . . . . .	146



5.2.2	Anisotropy in the electron population	151
5.2.3	Discussion	152
5.3	Thermal and Non-thermal models of electron distributions	155
5.3.1	Toy models	156
5.3.2	Illustrations	157
5.3.3	Discussions	158
5.4	Conclusions	160
<b>6</b>	<b>Compton Scattering Kernel</b>	<b>161</b>
6.1	Introduction	161
6.2	Isotropic Compton Scattering Kernel	162
6.2.1	Anatomy of the Compton Kernel	163
6.2.2	Simplified exact Kernel	164
6.2.3	A brief exploration of the isotropic kernel	165
	Extreme cases	166
6.3	Anisotropic Compton Scattering Kernels	168
6.3.1	Analytics	168
	$l=0$	169
	$l=1$	170
	$l=2$	170
	$l=3$	170
6.3.2	Exploration	172
	Extreme cases	173
6.4	Conclusion	174
<b>7</b>	<b>Summary and Future Work</b>	<b>176</b>
<b>A</b>	<b>Scaling fits for Bahamas+Macsis</b>	<b>191</b>
A.1	Volume Averages over R500c	191
A.2	Volume Averages over R200c	191
A.3	Volume Averaged Y Fits	191
A.4	Profile Fits	196
<b>B</b>	<b>Scaling fits for multi-Simulation SZ temperature scalings</b>	<b>212</b>

# List of Figures

1.1	<i>Planck</i> tSZ map (Planck Collaboration et al., 2016b)	21
1.2	MACS J1423.8+2404 (Adam et al., 2016)	21
1.3	Compton Scattering Schematic	22
1.4	The relativistic SZ effect	27
1.5	The kinematic SZ effect	29
2.1	Projected temperature measure comparisons in select haloes	47
2.2	The temperature-mass effects of different radii	49
2.3	The redshift effects on the temperature-mass relationship	51
2.4	A cluster by cluster comparison of the temperature measures	52
2.5	The covariance in the fits of the temperature measures	55
2.6	The spread of data around the Temperature-Mass fits	57
2.7	The redshift evolution of the temperature dispersion	61
2.8	The radial profiles of the temperature measures	64
2.9	The redshift evolution of the radial profiles	65
2.10	The cylindrical profiles of the temperature measures	67
2.11	The radial profiles of the $y$ -weighted temperature and temperature dispersion	69
2.12	The relativistic SZ effect compared to the <i>Planck</i> bands	71
2.13	An indicative plot of the potential fractional corrections to $H_0$	75
3.1	The three temperature mass relations in each simulation at $z = 0$	85
3.2	The redshift evolution of the SZ temperatures in each simulation	87
3.3	A depiction of the radial dependence of each simulation	89
3.4	The temperature-mass relation within three different radii	90
3.5	The temperature-Compton- $Y$ relation	92
3.6	The relative variation in temperature measures against temperature	93
3.7	The effects of resolution in TNG	95
3.8	The gas fraction in each simulation at $z = 0$ and 1	97
3.9	A comparison of different feedback mechanisms in THE300	99
3.10	The effects of relaxation criteria on the observed temperatures	101
3.11	The effects of core excision in the MAGNETICUM sample	102
3.12	The effects of particle temperature cut-off in MAGNETICUM	104

3.13 The cross simulation-averaged temperature scaling relations compared to observational results . . . . .	108
4.1 The CMB SZ signal, radio SZ signal, and combined signal . . . . .	128
4.2 The effects of kinematic and relativistic SZ contributions . . . . .	130
4.3 The relativistic corrections to the radio null . . . . .	132
4.4 The kinematic corrections to the radio null . . . . .	134
4.5 The effects of modifying the radio background distribution . . . . .	136
4.6 A comparison of the effects of a radio dipole, and kinematic corrections . . . . .	138
5.1 Repeat of Compton Scattering Schematic . . . . .	145
5.2 The anisotropic photon scattering kernel . . . . .	149
5.3 The anisotropic electron scattering kernel . . . . .	152
5.4 Anisotropic SZ signals . . . . .	153
5.5 Toy models for electron distributions . . . . .	156
5.6 Spectral distortion from fixedd momenta electrons . . . . .	158
5.7 Spectral distortion from different electron distributions . . . . .	159
6.1 Compton scattering zones . . . . .	164
6.2 Compton scattering kernel . . . . .	166
6.3 Extreme Compton scattering kernels . . . . .	167
6.4 Anisotropic Compton scattering kernel . . . . .	172
6.5 Extreme Compton scattering kernels . . . . .	173

# List of Tables

2.1	Cosmological Parameters for BAHAMAS and MACSIS . . . . .	43
2.2	Halo counts for BAHAMAS and MACSIS . . . . .	45
2.3	Halo counts for the Hot and Relaxed subsamples . . . . .	46
2.4	Temperature-Mass fit parameters . . . . .	54
2.5	Temperature-Temperature fit parameters . . . . .	58
2.6	Temperature-Y fit parameters . . . . .	59
2.7	Temperature-Mass fit parameters for the Hot and Relaxed samples .	60
3.1	Simulation characteristics for each sample . . . . .	81
3.2	Halo counts in each simulation . . . . .	81
3.3	Cosmological parameters used in each of the simulations. . . . .	82
3.4	Approximations for a mass independent redshift correction . . . . .	88
3.5	Temperature-Mass fit parameters for the cross-simulation sample . .	105
3.6	The median redshift correction for the cross-simulation sample . . .	106
3.7	The average variations in radius, mass, $T_m$ and $T_y$ within each radius for the cross-simulation sample . . . . .	107
3.8	Temperature-Y fit parameters for the cross-simulation sample . . . .	111
4.1	The null of the radio+CMB SZ signal under relativistic corrections . .	131
A.1	Complete temperature-mass fits within $R_{500c}$ . . . . .	192
A.2	Complete temperature- $T_{500c}$ fits within $R_{500c}$ . . . . .	193
A.3	Complete temperature- $T_m$ fits within $R_{500c}$ . . . . .	194
A.4	Complete temperature-mass fits for the Hot and Relaxed samples within $R_{500c}$ . . . . .	195
A.5	Complete $\sigma(T_y)$ -mass fits within $R_{500c}$ . . . . .	196
A.6	Complete temperature-mass fits within $R_{200c}$ . . . . .	197
A.7	Complete temperature- $T_{200c}$ fit parameters within $R_{200c}$ . . . . .	198
A.8	Complete temperature- $T_m$ fits within $R_{200c}$ . . . . .	199
A.9	Complete temperature-mass fits for the Hot and Relaxed samples within $R_{200c}$ . . . . .	200
A.10	Complete $\sigma(T_y)$ -mass fits within $R_{200c}$ . . . . .	201
A.11	Temperature-Y fits within $R_{500c}$ . . . . .	201
A.12	Temperature-Y fits within $R_{200c}$ . . . . .	202

A.13 $Y$ -mass fits within $R_{500c}$ . . . . .	202
A.14 $Y$ -mass fits within $R_{200c}$ . . . . .	203
A.15 The radial temperature profiles of $T/T_{500}$ at $z = 0$ . . . . .	204
A.16 The radial temperature profiles of $T/T_{500}$ at $z = 0.5$ . . . . .	205
A.17 The radial temperature profiles of $T/T_{500}$ at $z = 1$ . . . . .	206
A.18 The radial temperature profiles of $\sigma(T_y)/T_{500}$ at each redshift . . . . .	207
A.19 The cylindrical temperature profiles of $T/T_{500}$ at $z = 0$ . . . . .	208
A.20 The cylindrical temperature profiles of $T/T_{500}$ at $z = 0.5$ . . . . .	209
A.21 The cylindrical temperature profiles of $T/T_{500}$ at $z = 1$ . . . . .	210
A.22 The cylindrical temperature profiles of $\sigma(T_y)/T_{500}$ at each redshift . . . . .	211
B.1 Complete 2-parameter temperature-mass fits for the cross-simulation sample at $z = 0$ within $R_{200c}$ . . . . .	213
B.2 Complete 3-parameter temperature-mass fits for the cross-simulation sample at $z = 0$ within $R_{200c}$ . . . . .	213
B.3 Complete temperature-mass fits for each sample at $z = 0$ within $R_{200c}$ . . . . .	214
B.4 2-parameter temperature-mass fits for the cross-simulation sample at higher redshifts within $R_{200c}$ . . . . .	215
B.5 The average variations in radius, mass, $T_m$ and $T_y$ within each radius for each sample . . . . .	216
B.6 Complete 2-parameter temperature-mass fits for the cross-simulation sample at $z = 0$ within $R_{500c}$ . . . . .	217
B.7 Complete 3-parameter temperature-mass fits for the cross-simulation sample at $z = 0$ within $R_{500c}$ . . . . .	217
B.8 Complete temperature- $Y$ fits for the cross-simulation sample at $z = 0$ within $R_{200c}$ . . . . .	218
B.9 2-parameter $T_y$ - $Y$ fits for each sample at $z = 0$ within $R_{200c}$ . . . . .	218
B.10 Complete 2-parameter $T_y$ - $Y$ fits for the 'hot' cross-simulation sample within $R_{200c}$ at each redshift . . . . .	219

## List of Abbreviations

<b>SZ</b>	<b>S</b> unyaev <b>Z</b> eldovich
<b>tSZ</b>	<b>t</b> hermal <b>SZ</b>
<b>kSZ</b>	<b>k</b> inematic <b>SZ</b>
<b>rSZ</b>	<b>r</b> elativistic <b>SZ</b>
<b>pSZ</b>	<b>p</b> olarised <b>SZ</b>
<b>CMB</b>	<b>C</b> osmic <b>M</b> icrowave <b>B</b> ackground
<b>ICM</b>	<b>I</b> ntra- <b>C</b> luster <b>M</b> edium
<b>AGN</b>	<b>A</b> ctive <b>G</b> alactic <b>N</b> uclei
<b>SPT</b>	<b>S</b> outh <b>P</b> ole <b>T</b> elescope
<b>ACT</b>	<b>A</b> tacama <b>C</b> osmology <b>T</b> elescope

# Physical Constants

Speed of Light	$c = 2.997\,924\,58 \times 10^8 \text{ m s}^{-1}$ (exact)
Boltzmann constant	$k_B = 1.380\,649 \times 10^{-23} \text{ J K}^{-1}$ (exact)
Planck constant	$h = 6.626\,070\,15 \times 10^{-34} \text{ J Hz}^{-1}$ (exact)
Electron charge	$e = 1.602\,176\,634 \times 10^{-19} \text{ C}$ (exact)
Electron rest mass	$m_e = 9.109\,384 \times 10^{-31} \text{ kg}$
	$m_e c^2 = 510.998\,950 \text{ keV}$
Thomson cross section	$\sigma_T = 6.652\,459 \times 10^{-29} \text{ m}^2$
Gravitational constant	$G = 6.674 \times 10^{-11} \text{ m}^3 \text{ kg}^{-1} \text{ s}^{-2}$
Proton rest mass	$m_p = 1.6726 \times 10^{-27} \text{ kg}$
CMB temperature	$T_{\text{CMB}} = 2.7255 \text{ K}$
Intensity normalisation constant	$I_0 = 270.33 (T_{\text{CMB}}/2.7255)^3 \text{ MJy/sr}$

# Abstract

## Modelling of the relativistic Sunyaev-Zeldovich effect and related Compton scattering processes

by Elizabeth G. LEE

Doctor of Philosophy

November 2022

The Sunyaev-Zeldovich (SZ) effect is caused by Compton scattering where the electron population has far higher energies than the incident photons – i.e., in the Doppler-dominated regime. As such, the SZ effect is a unique probe of galaxy clusters and groups, some of the largest structures in our Universe, where the electron populations lead to a distinctive signal in the scattering of the cosmic microwave background (CMB). This thesis contains an exploration of corrections to the SZ effect, alongside a discussion of analytic approaches to Compton scattering.

In particular, in Chapter 2, using the BAHAMAS and MACSIS simulations, I examine the appropriate temperature measures to derive the cluster-averaged relativistic SZ effect. This allows a comparison with other commonly used temperature measures, and the generation of temperature-mass scaling relations to allow for forward modelling of future cluster SZ observations. Chapter 3 extends this work to also compare to the ILLUSTRISTNG, MAGNETICUM and THE THREE HUNDRED PROJECT simulations. We find consistency in the SZ temperature despite the wide range of simulation parameters and investigate the impact of these simulation parameters, such as feedback prescriptions and resolution. The agreement between simulations indicates an exciting avenue for observational and theoretical exploration, determining the extent of relativistic SZ corrections.

In Chapter 4, a detailed examination of the radio SZ effect is carried out. This signal would be caused by a cosmological radio background scattering alongside the CMB in clusters. This chapter focuses on detailed modelling of kinematic and relativistic corrections to this signal, and the impact of anisotropies and variation in the radio background on the observed radio SZ signal.

Chapter 5 examines the effects high-energy non-thermal electron distributions alongside anisotropic electron or photon distributions. Here an analytic form of the anisotropic scattering kernels for photons or electrons has been derived and investigated. An exploration of various toy-models of non-thermal distributions is carried out.

Finally, in Chapter 6, a numerically stable form of the isotropic general Compton scattering kernel is presented and explored. Further extensions to analytic kernels for the low-multipole anisotropic Compton scattering problem are also derived and discussed. These allow for the rapid and accurate computation of scattering processes throughout the history of the Universe.



## Declaration of Authorship

I, Elizabeth G. LEE, declare that this thesis titled, “Modelling of the relativistic Sunyaev-Zeldovich effect and related Compton scattering processes” and the work presented in it are my own. I confirm that:

- This work was done wholly while in candidature for a research degree at this University.
- No part of this thesis has previously been submitted for a degree or any other qualification at this University or any other institution.
- Where I have consulted the published work of others, this is always clearly attributed.
- Where I have quoted from the work of others, the source is always given. With the exception of such quotations, this thesis is entirely my own work.
- Where the thesis is based on work done by myself jointly with others, I have made clear exactly what was done by others and what I have contributed myself.
- I have acknowledged all main sources of help.
- SZpack has been extended from code originally developed by Jens Chluba, with assistance by Eric Switzer.
- The more computational aspects of this thesis used either the SIRIUS computer network funded by the ERC grant of Jens Chluba or the DiRAC@Durham facility managed by the Institute for Computational Cosmology on behalf of the STFC DiRAC HPC Facility.

## Copyright Statement

- (i) The author of this thesis (including any appendices and/or schedules to this thesis) owns certain copyright or related rights in it (the “Copyright”) and they have given The University of Manchester certain rights to use such Copyright, including for administrative purposes.
- (ii) Copies of this thesis, either in full or in extracts and whether in hard or electronic copy, may be made **only** in accordance with the Copyright, Designs and Patents Act 1988 (as amended) and regulations issued under it or, where appropriate, in accordance with licensing agreements which the University has from time to time. This page must form part of any such copies made.
- (iii) The ownership of certain Copyright, patents, designs, trademarks and other intellectual property (the “Intellectual Property”) and any reproductions of copyright works in the thesis, for example graphs and tables (“Reproductions”), which may be described in this thesis, may not be owned by the author and may be owned by third parties. Such Intellectual Property and Reproductions cannot and must not be made available for use without the prior written permission of the owner(s) of the relevant Intellectual Property and/or Reproductions.
- (iv) Further information on the conditions under which disclosure, publication and commercialisation of this thesis, the Copyright and any Intellectual Property and/or Reproductions described in it may take place is available in the University IP Policy (see [documents.manchester.ac.uk/DocuInfo.aspx?DocID=24420](https://documents.manchester.ac.uk/DocuInfo.aspx?DocID=24420)), in any relevant Thesis restriction declarations deposited in the University Library, The University Library’s regulations (see [www.library.manchester.ac.uk/about/regulations/](https://www.library.manchester.ac.uk/about/regulations/)) and in The University’s policy on Presentation of Theses

## *Acknowledgements*

First of all, I want to thank Jens for his excellent direction and guidance in this endeavour. His enthusiasm and joy in astrophysics and cosmology has only increased my own. I also want to thank him for his empathy and support; it has truly been invaluable, and I would not have got so far without it.

I am also grateful to Scott Kay, who has been a wonderful co-supervisor. His patience and kindness have been invaluable throughout my degree. Thank you to Andrew Markwick and Christopher Conselice for their pastoral advice throughout this process. I would also like to thank the many members of our research group: Luke, Tom, Charis, Boris, Abir, Mathieu, Inigo, Andrea, Aditya, Sandeep, Bryce and Jiten. I am also deeply grateful to my collaborators, in particular Dhayaa Anbajagane, Priyanka Singh, Daisuke Nagai and David Barnes.

I must thank the wonderful people in JBCA; Laura, not least for the use of this thesis template; Fiona, Josh, Shankar, Robin, Mike, Emma, Jamie, Chessi, Imogen, Kammy, Jonathan, Mey and many others. You have all been wonderfully distracting and wonderfully supportive. Thanks also to my friends, Hugo, Alex, Lizzie, Ellie, Hannah and Claudia who have often kept me from being overwhelmed. You are all brilliant, thank you.

To my parents, who instilled us with a love of learning and never doubted what we could achieve, thank you for letting me talk at you for hours on end, and pulling me away to do other things when I need it. And finally thanks to my siblings, to Andrew, Samuel and Ella, Joanna and Eli. I could never have done this without all of you.

*To Joanna  
for being the best sister*

## The Author

Elizabeth Lee graduated MSci (Hons 1st class) in Astrophysics from the University of Cambridge in 2018. In the final year of her degree, she worked on the  $H_0$  tension supervised by Prof. George Efstathiou, working alongside Dr. Steven Gratton and Dr. Pablo Lemos. This project focused on using a cosmic inverse distance ladder to create a model independent  $H(z)$  reconstruction. This led to a published article on which EL was second author.

The work presented in this thesis is a result of the Royal Society funded studentship (grant No. RGF/EA/180053) with Prof. Jens Chluba.

Supervisor: Prof. Jens Chluba

Cosupervisor: Prof. Scott Kay

Advisors: Dr. Andrew Markwick & Prof. Christopher Conselice

## Supporting Publications

### **Relativistic SZ temperature scaling relations of groups and clusters derived from the BAHAMAS and MACSIS simulations**

*Elizabeth Lee; Jens Chluba; Scott T. Kay; David J. Barnes*

*2020 MNRAS, 493, p.3274-3292*

Chapter 2 is based on this article.

### **A multi-simulation study of relativistic SZ temperature scalings in galaxy clusters and groups**

*Elizabeth Lee; Dhayaa Anbajagane; Priyanka Singh; Jens Chluba; Daisuke Nagai; Scott T. Kay; Weiguang Cui; Klaus Dolag; Gustavo Yepes*

*2022 MNRAS, 517, p.5303-5324*

Chapter 3 is based on this article.

### **Refined modelling of the radio SZ signal: kinematic terms, relativistic temperature corrections, and anisotropies in the radio background**

*Elizabeth Lee; Jens Chluba; Gilbert P. Holder*

*2022 MNRAS, 512, p.5153-5164*

Chapter 4 is based on this article.

### **Dissecting the Compton scattering kernel I: Isotropic media**

*Abir Sarkar; Jens Chluba; Elizabeth Lee*

*2019 MNRAS, 490, p.3705-3726*

The first half of chapter 6 is based on this article. EL contributed to this paper mainly in the review process and with associated analytics.

# Chapter 1

## Introduction

Just over 50 years ago, it was shown that free electrons in hot ionized plasmas scatter photons from the cosmic microwave background (CMB) (Zeldovich & Sunyaev, 1969; Sunyaev & Zeldovich, 1970). Generally speaking, the Sunyaev-Zeldovich (SZ) effect is the observed unique spectral signature corresponding to this scattering – and is particularly evident for plasmas with temperatures  $T_e \geq 10^7$  K (i.e.,  $k_B T_e \gtrsim 1$  keV). The most dominant of these scatterings is the thermal SZ effect (Sunyaev & Zeldovich, 1972), which comes from the upscattering of CMB photons by the hot intracluster medium (ICM). The effect was proposed as a test to see if the then newly-discovered CMB (Penzias & Wilson, 1965) was truly cosmic in origin.

The pockets of hot ionized plasma that can be probed in this way form in the largest overdensities of large-scale structure. In particular, these occur in galaxy clusters, groups and intergalactic filaments, which comprise of giant dark matter structures, where the baryonic plasma is located. While some of this gas cools to form galaxies, the majority remains as ionised plasma (Briel et al., 1992), also known as the intracluster medium. These objects are excellent probes for cosmology, sensitive to fundamental cosmological parameters such as the matter density and power spectrum (e.g., Voit, 2005; Allen et al., 2011; Kravtsov & Borgani, 2012; Weinberg et al., 2013). The ICM also induces X-ray emission through both bremsstrahlung and line-emission processes (see, e.g., Sarazin, 1986, for a review). A recent, in-depth review of the SZ effect can be found in Mroczkowski et al. (2019) (see also Carlstrom et al., 2002) which covers much of the information presented in this chapter.

In this chapter, I will review the theoretical background for the SZ effect and details of the underlying cosmology and astrophysical behaviour of Galaxy clusters, crucial for understanding later points in this thesis. This starts with a review of the observational history of the CMB and SZ effect in section 1.1. In section 1.2, I will review the Compton scattering process and the derivation of the Kompaneets equation. In section 1.3, I discuss the SZ effect and its various forms. Section 1.4 explores causes behind non-traditional SZ effects. Finally, in section 1.5,

the use of simulations to model SZ physics is explored and a discussion of temperature determination in clusters is provided, relevant for chapters 2 and 3.

## 1.1 A brief history of the CMB and SZ observations

The CMB is an ambient, broadly uniform microwave signal that reaches us from the earliest stages of cosmic history. According to the Big Bang model, photons decoupled from the ambient plasma at a redshift  $z \approx 1100$  (around 380,000 years after the Big Bang) at what is known as the surface of last scattering – that is, when the elastic scattering rate between photons and charged particles fell below the universal expansion rate. As such the CMB is an almost perfect blackbody which, at the time of last scattering, had an effective temperature of around 3000 K. However, due the expansion of space, this temperature has been redshifted such that the CMB now has an ambient temperature of  $T_{\text{CMB}} \approx 2.7$  K. The largest deviation from a blackbody, comes from a dipole correction around 0.1% of the amplitude of the blackbody itself. This dipole is almost entirely caused by the peculiar motion of the Earth/Sun against the CMB background itself – that is, it is a Doppler term from e.g., the Sun’s Galactic rotation and the Galactic motion within the Local Group, alongside the Earth’s rotation around the Sun.

In the 1990s, the first large CMB space-mission, *COBE* (Cosmic Background Explorer) launched. This measured the primary anisotropies of the CMB at the largest scales (Smoot et al., 1994), alongside the energy spectrum, giving the well-known temperature measurement of  $T_{\text{CMB}} = 2.7377 \pm 0.0038$  K (Mather et al., 1994; Fixsen et al., 1996; Bennett et al., 1996). However the revealed variations (hot and cold spots) in the CMB prompted two further CMB missions by NASA and ESA respectively, *WMAP* (2001) and *Planck* (2009). We have seen tremendous advances in CMB observations both through these space-based missions, and ground-based observatories (i.e., SPT and ACT) leading to a more and more detailed understanding of both the foregrounds in the CMB (in particular the Galactic foregrounds, see, e.g., Ichiki, 2014) and the variations in the CMB temperature itself (Komatsu et al., 2011; Planck Collaboration et al., 2020a).

Attempts to measure the SZ effect began in the 1970s, with reliable detections of the effect obtained by the Owens Valley Radio observatory by the mid-1980s (Birkinshaw et al., 1984). Interferometric observations followed within a few years by the Very Large Array (Moffet & Birkinshaw, 1989) and the Ryle telescope (Jones et al., 1993; Grainge et al., 1993). The field of SZ observations has greatly increased over the following decades. The modern field of SZ observation is split following improvements in angular resolution and frequency coverage, allowing for the SZ effect within nearby clusters to be examined in close detail alongside an increased understanding of higher-order effects on the ‘classical’ SZ effect originally theorised.



**FIGURE 1.1:** Reconstructed *Planck* all-sky Compton- $y$  parameter maps in orthographic projections. The grey region indicates the masked region due to Galactic foregrounds. Figure reproduced from [Planck Collaboration et al. \(2016b\)](#).

**FIGURE 1.2:** A composite image of MACS J1423.8+2404. In blue, the derived tSZ map obtained from NIKA at 150 GHz. In red, the X-ray signal from the *Chandra* photon counts (Obs-ID 04195). In green, the Hubble Space Telescope image using the F814W filter obtained by the CLASH program ([Postman et al., 2012](#)) showing predominantly the galaxies. The white contours are the mass-distribution model obtained from lensing ([Zitrin et al., 2011, 2015](#)). Figure reproduced from [Adam et al. \(2016\)](#).

In particular, the recent observational capacity of telescopes such as SPT and ACT have allowed for the detection of previously unknown clusters through the thermal SZ (tSZ) effect ([Staniszewski et al., 2009](#); [Menanteau et al., 2010](#)) and the *Planck* satellite observed in nine separate photometric bands allowing for the detection of over a thousand clusters through the SZ effect ([Planck Collaboration et al., 2016d](#)). *Planck* also provided a whole-sky tSZ map (see Fig. 1.1 [Planck Collaboration et al., 2016b](#)).

The first high-significance deviation from the classical tSZ effect was a kinematic effect found in a high-velocity sub-cluster of MACS J0717.5+3745 ([Sayers et al., 2013](#); [Adam et al., 2017](#)) using *Herschel*-Spire and NIKA data, respectively, in combination with X-ray observations. Relativistic effects, on which a large portion of this thesis focuses, remain hard to constrain. Many attempts in single-cluster measurements have been made (e.g., [Hansen et al., 2002](#); [Hansen, 2004](#); [Zemcov et al., 2012](#); [Prokhorov & Colafrancesco, 2012](#); [Chluba et al., 2013](#); [Butler et al., 2022](#)) alongside stacking analyses (e.g., [Hurier, 2016](#); [Erler et al., 2018](#)), but the detection significance remains low.

However, the future of SZ measurements remains bright with the continuing observational advances in angular resolution and sensitivities and, in particular, upcoming experiments such as CCAT-prime ([Stacey et al., 2018](#)), NIKA2 ([Adam et al., 2018](#)), ToITEC ([Austermann et al., 2018](#)) and The Simons Observatory ([Ade et al., 2019](#)), which promise to measure, for instance, the ICM temperature using the relativistic SZ effect for even high-redshift objects ([Morandi et al., 2013](#); [Remazeilles & Chluba, 2020](#)) independent of X-ray measurements.

The history of the SZ measurements is intertwined with X-ray observations of those same clusters. Much SZ science still depends on observations by, in particular, *Chandra* and *XXM-Newton*, which have transformed our understanding of galaxy clusters and ICM physics. From a galaxy cluster perspective, SZ observations and X-ray measurements will continue to go hand in hand, each providing complementary information to the other. For instance, X-ray measurements tend to be more sensitive to central emission, while the SZ effect can probe further out. Figure 1.2 shows complementary information about the cluster MACS J1423.8+2404 obtained through the SZ effect, X-ray observations, strong lensing

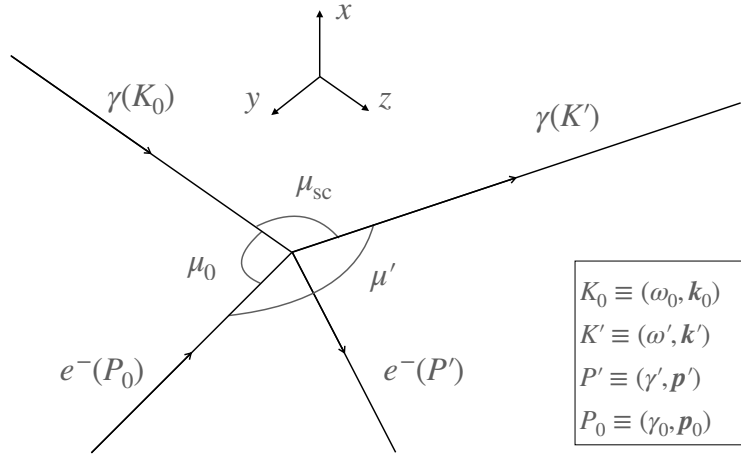


**FIGURE 1.3:** A schematic of the Compton scattering problem. Here  $K_0$  and  $K'$  are the four-vectors for the incoming and outgoing photons, with dimensionless frequencies  $\omega_0$  and  $\omega'$  and dimensionless momenta  $\mathbf{k}_0$  and  $\mathbf{k}'$ .  $P_0$  and  $P'$  are the 4-vectors for the incoming and outgoing electrons, with dimensionless energies  $\gamma_0$  and  $\gamma'$  and momenta  $\mathbf{p}_0$  and  $\mathbf{p}'$ .  $\mu_0$ ,  $\mu'$  and  $\mu_{sc}$  are the cosines of the marked angles. Note that since the scattering is three-dimensional the relationship between these angles is complex. The axes are to emphasise the dimensionality of the scattering, with  $z$  aligned with the direction of the incoming photon.

and the galaxies themselves.

## 1.2 Compton Scattering

At its core, the SZ effect can be understood as a special case of Compton scattering – wherein the incoming photons (the CMB) have considerably less energy than the scattering electrons (the hot ICM). Generally speaking, Compton scattering is one of the most important processes in astrophysical plasmas (e.g., [Blumenthal & Gould, 1970](#); [Rybicki & Lightman, 1979](#)).

Compton scattering is the process of an incoming photon and electron, exchanging energy and momentum. The reaction takes the form  $\gamma(K_0) + e^-(P_0) \leftrightarrow \gamma(K') + e^-(P')$  where here,  $K_0$ ,  $P_0$ ,  $K'$  and  $P'$  are the associated 4-vectors of the involved particles. A schematic of this process can be seen in Figure 1.3. Assuming the electrons are non-degenerate (that is, Fermi blocking can be neglected), the kinetic equation is then given by (e.g., [Pomraning, 1972](#); [Buchler & Yueh, 1976](#); [Nagirner & Poutanen, 1994](#))

$$\frac{1}{c} \frac{dn(\omega_0)}{dt} = \frac{(2\pi)^4}{2\omega_0} \int \frac{d^3\mathbf{p}_0}{(2\pi)^3\gamma_0} \frac{d^3\mathbf{p}'}{(2\pi)^3\gamma'} \frac{d^3\mathbf{k}'}{(2\pi)^3\omega'} \delta^{(4)}(P' + K' - P_0 - K_0) |\mathcal{M}|^2 \times [f'n'(1+n_0) - f_0n_0(1+n')]. \quad (1.1)$$

Here  $n(\omega_0)$  is the photon occupation number at dimensionless frequency  $\omega_0 = h\nu_0/m_e c^2$ ;  $\mathbf{p}_0$ ,  $\mathbf{p}'$ ,  $\mathbf{k}_0$  and  $\mathbf{k}'$  are the three-vectors associated with  $P_0$ ,  $P'$ ,  $K_0$  and

$K'$  respectively. We are using energies and momenta in units of  $m_e c^2$  and  $m_e c$ , respectively, such that  $\omega_0$  and  $\omega'$ , the dimensionless frequencies, denote also the photon energies;  $\gamma_0$  and  $\gamma'$  are the electron energies and also the Lorentz factors, i.e.,  $\gamma_0 = E/m_e c^2 = \sqrt{1+p_0^2} = 1/\sqrt{1-\beta_0^2}$ , where  $p_0$  is the dimensionless momentum, and  $\beta_0 = v/c = p_0/\gamma_0$  the dimensionless speed.

The electron distribution functions are denoted by  $f_0 = f(\gamma_0)$  and  $f' = f(\gamma')$ , and the photon distribution functions by  $n_0 = n(\omega_0)$  and  $n' = n(\omega')$ .  $|\mathcal{M}|^2$  is the squared matrix element for the Compton process and given by

$$|\mathcal{M}|^2 = e^4 X = 2e^4 \bar{X}; \quad \bar{X} = \frac{\kappa'}{\kappa} + \frac{\kappa}{\kappa'} + 2 \left( \frac{1}{\kappa} - \frac{1}{\kappa'} \right) + \left( \frac{1}{\kappa} - \frac{1}{\kappa'} \right)^2. \quad (1.2)$$

$\bar{X}$  is averaged over polarization states and  $\kappa$  and  $\kappa'$  are invariants given by

$$\kappa = -P_0 \cdot K_0 = -P' \cdot K' = -\gamma_0 \omega_0 (1 - \beta_0 \mu_0) \quad (1.3a)$$

$$\kappa' = -P_0 \cdot K' = -P' \cdot K_0 = -\gamma_0 \omega' (1 - \beta_0 \mu') \quad (1.3b)$$

$$\kappa' - \kappa = K_0 \cdot K' = \omega_0 \omega' (1 - \mu_{sc}). \quad (1.3c)$$

The  $\mu$ s refer to the cosines of the angles between each vector (as can be seen in Figure 1.3) and we can write that  $\mu_0 = \mu' \mu_{sc} + \cos(\phi' - \phi_{sc}) \sqrt{(1 - \mu_{sc}^2)(1 - \mu'^2)}$ , where the  $\phi$  are the associated azimuthal angles.

Carrying out the  $d^3 \mathbf{p}'$  integral in Eq. (1.1), we can use the 4-dimensional Dirac- $\delta$  function to simply set  $\mathbf{p}' = \mathbf{p}_0 + \mathbf{k}_0 - \mathbf{k}'$  and ensure that  $\gamma' = \gamma_0 + \omega_0 - \omega'$  everywhere. The kinetic equation then becomes

$$\begin{aligned} \frac{1}{c} \frac{dn(\omega_0)}{dt} &= \frac{e^4}{2^3 (2\pi)^2} \int \frac{d^3 \mathbf{p}_0}{(2\pi)^3} d^3 \mathbf{k}' \delta(\gamma' + \omega' - \gamma_0 - \omega_0) \frac{\bar{X}}{\gamma_0 \gamma' \omega_0 \omega'} \\ &\times \left[ f' n' (1 + n_0) - f_0 n_0 (1 + n') \right]. \end{aligned} \quad (1.4)$$

Then we can express  $e$ , the electron charge, in terms of the Thomson cross-section,  $\sigma_T$ , and redefine the electron distribution to remove the factor of the electron number density,  $N_e = \int \frac{d^3 \mathbf{p}_0}{(2\pi)^3} f(\mathbf{p}_0)$ . That is we define  $\bar{f}(\gamma_0) = f(\gamma_0)/(2\pi^2 N_e)$ , so that the integral over  $\bar{f}$  is normalised to unity, and then relabel  $\bar{f} \rightarrow f$ . The  $z$ -axis is aligned with the incoming photon<sup>1</sup>.

To evaluate the remaining Dirac- $\delta$  function, the customary approach is to note that  $d(\gamma' + \omega') = \frac{\gamma_0 \omega_0}{\gamma' \omega'} (1 + \beta_0 \mu_0) d\omega'$ . Defining the Thomson optical depth  $\tau = \int c N_e \sigma_T dt$  we can write the kinetic equation as

$$\frac{dn(\omega_0)}{d\tau} = \int p_0^2 dp_0 \frac{d\mu_0 d\phi_0 d\mu_{sc} d\phi_{sc}}{4\pi} \frac{d\sigma}{d\Omega} \left[ f' n' (1 + n_0) - f_0 n_0 (1 + n') \right]. \quad (1.5)$$

<sup>1</sup>Due to the symmetry in  $\bar{X}$ , absent of any angular dependence in  $n$ , the alignment of  $\frac{dn(\omega_0)}{d\tau}$  with the incoming photon versus  $\frac{dn(\omega')}{d\tau}$  with the outgoing photon, is simply equivalent to the replacement of the integral  $\omega_0^2 d\omega_0$  to  $\omega'^2 d\omega'$ . An alignment with the outgoing photon and expression in terms of  $\frac{dn(\omega')}{d\tau}$  will be used in Chapters 5 and 6.

Here we have also introduced the differential Compton scattering cross section, (including and cancelling the factor of  $(1 - \beta_0\mu_0)$  from the Møller speed)

$$\frac{d\sigma}{d\Omega} = \frac{3}{16\pi} \left[ \frac{\omega'}{\omega_0} \right]^2 \frac{\bar{X}}{\gamma_0^2(1 - \beta_0\mu_0)}, \quad (1.6)$$

$$\bar{X} = \frac{\kappa'}{\kappa} + \frac{\kappa}{\kappa'} - \frac{2(1 - \mu_{sc})}{\gamma_0^2(1 - \beta_0\mu_0)(1 - \beta_0\mu')} + \frac{(1 - \mu_{sc})^2}{\gamma_0^4(1 - \beta_0\mu_0)^2(1 - \beta_0\mu')^2}.$$

Finally we can note that the ratio of ingoing and outgoing photon frequencies can be found to be

$$\frac{\omega'}{\omega_0} = \frac{1 - \beta_0\mu_0}{1 - \beta_0\mu' + \frac{\omega_0}{\gamma_0}(1 - \mu_{sc})}. \quad (1.7)$$

### 1.2.1 The Kompaneets equation

The SZ effect was originally derived under a number of assumptions that allow for the simplification of the Compton Scattering problem. In particular, to quickly obtain the classical thermal SZ effect it is first useful to understand the derivation of the Kompaneets equation (Kompaneets, 1956) – a detailed review can be found in Katz (1987).

Firstly, in the **non-relativistic limit**, the 4-vector conservation can be written as energy and momentum conservation equations as

$$\omega_0 + \frac{p_0^2}{2} = \omega' + \frac{p'^2}{2} \quad (1.8)$$

$$\mathbf{k}_0 + \mathbf{p}_0 = \mathbf{k}' + \mathbf{p}'.$$

Now, the Kompaneets equation relies on an expansion in terms of  $\Delta = \omega' - \omega_0$ . Eliminating  $p'$  from the conservation equations and rearranging, it is possible to find, assuming  $\Delta \ll 1$  (i.e., to first order in  $\Delta$ ),

$$\Delta = -\frac{\omega_0^2(1 - \hat{\mathbf{k}}_0 \cdot \hat{\mathbf{k}}') + \omega_0 \mathbf{p}_0 \cdot (\hat{\mathbf{k}}_0 - \hat{\mathbf{k}}')}{1 + \omega_0(1 - \hat{\mathbf{k}}_0 \cdot \hat{\mathbf{k}}') - \mathbf{p}_0 \cdot \hat{\mathbf{k}}'}. \quad (1.9)$$

Here, we have introduced  $\hat{\mathbf{k}}_0$  and  $\hat{\mathbf{k}}'$  as the unit vectors in the directions of  $\mathbf{k}_0$  and  $\mathbf{k}'$ . In the case of the SZ effect, the CMB provides a ‘cold’ source of photons compared to the hot electrons in clusters, so it is reasonable to assume that  $\omega_0 \ll p_0$  and that, since cluster electrons are non-relativistic,  $p_0 \ll 1$ . As such, in the denominator, the second and third terms are considered small, and the denominator can be approximated  $\simeq 1$ . In the numerator, the first term is small compared to the second, and as such,

$$\Delta \simeq -\omega_0 \mathbf{p}_0 \cdot (\hat{\mathbf{k}}_0 - \hat{\mathbf{k}}') = -\omega_0 p_0 (\mu_0 - \mu'). \quad (1.10)$$

Now one assumes the electrons are an isotropic, isothermal medium following a Maxwell-Boltzmann distribution. That is,  $f(\mathbf{p}_0) \propto e^{-p_0^2/2\theta_e}$  where we have introduced the dimensionless electron temperature  $\theta_e = k_B T_e / m_e c^2$ . Then, due to the conservation of energy, it is evident that  $f' = e^{\Delta/\theta_e} f$ . Introducing  $x_e = \omega_0/\theta_e$ , an expansion of Eq. (1.5) can be written as

$$\begin{aligned} \frac{dn(\omega_0)}{d\tau} &= \int d^3\mathbf{p}_0 d^2\Omega_{sc} \frac{d\sigma}{d\Omega} [f'n'(1+n_0) - f_0 n_0(1+n')] \\ &= - \left[ \frac{dn}{dx_e} + n(1+n) \right] \int d^3\mathbf{p}_0 d^2\Omega_{sc} \frac{d\sigma}{d\Omega} f \frac{\Delta}{\theta_e} \\ &\quad - \frac{1}{2} \left[ \frac{d^2n}{dx_e^2} + 2(1+n) \frac{dn}{dx_e} + n(1+n) \right] \int d^3\mathbf{p}_0 d^2\Omega_{sc} \frac{d\sigma}{d\Omega} f \frac{\Delta^2}{\theta_e^2} + O\left(\frac{\Delta^3}{\theta_e^3}\right). \end{aligned} \quad (1.11)$$

Since the scattering conserves photons, and the photon distribution is assumed to be isotropic, the change in photon occupation number must have a functional form,

$$\frac{dn(\omega_0)}{d\tau} = - \frac{1}{x_e^2} \frac{d(x_e^2 j(n, x_e))}{dx_e}, \quad (1.12)$$

where we have dropped the explicit dependence on  $\theta_e$ . Here, directly by observation, one can write that the photon current density,  $j$ , is of the form

$$j(n, x_e) = g(x_e) \left( \frac{dn}{dx_e} + h(n, x_e) \right). \quad (1.13)$$

As this must equal zero at equilibrium when  $n = 1/(e^{x_e} - 1)$ , one can assert that  $h(n, x_e) = n(1+n)$ . Then,  $g(x_e)$  depends on solving one of the integrals within Eq. (1.11). In the non-relativistic limit, the differential scattering cross-section can be reduced to the Thomson cross-section i.e.,  $\frac{d\sigma}{d\Omega} = \frac{3}{16\pi} (1 + \mu_{sc}^2)$ , and we can write

$$\begin{aligned} g(x_e) &= \frac{1}{2} \int d^3\mathbf{p}_0 d^2\Omega_{sc} \frac{d\sigma}{d\Omega} f \frac{\Delta^2}{\theta_e^2} \\ &= - \frac{3}{4\pi} \frac{\omega_0^2}{\theta_e^2} \int dp_0 4\pi p_0^4 f \int \frac{d^2\Omega_0}{4\pi} \frac{d^2\Omega_{sc}}{4\pi} (1 + \mu_{sc}^2) (\mu_0 - \mu')^2 \\ &= - \frac{3}{4\pi} x_e^2 \left( \frac{3\theta_e}{2} \right) \left( \frac{8\pi}{9} \right) = -x_e^2 \theta_e. \end{aligned} \quad (1.14)$$

Accordingly the Kompaneets equation, which will be discussed more shortly, is

$$\frac{dn(\omega_0)}{d\tau} = \frac{\theta_e}{x_e^2} \frac{d}{dx_e} \left[ x_e^4 \left( \frac{dn}{dx_e} + n + n^2 \right) \right]. \quad (1.15)$$

### 1.3 The SZ Effect

In a general sense, to consider the SZ effect, it is worth making a few observations. Firstly, no effect is produced by electrons at rest with respect to the CMB, since the number of photons scattered in and out of the line of sight cancel out

(in the Thomson limit). Hence, an effect is only seen when electrons are moving, and can transfer their kinetic energy to the photon field.

Secondly, when the energy of the photons is a lot less than that for the electrons (i.e., in a Doppler-dominated regime) and  $\omega_0 < 1/2$ ,<sup>2</sup> the ratio of incoming and outgoing photons can be approximated (cf. Eq (1.7))

$$\frac{\omega'}{\omega_0} \simeq \frac{1 - \beta_0 \mu_0}{1 - \beta_0 \mu'}. \quad (1.16)$$

In this regime, the outgoing photon frequency is bounded, since  $-1 \leq \mu_0, \mu' \leq 1$ ,

$$\frac{1 - \beta_0}{1 + \beta_0} \leq \frac{\omega'}{\omega_0} \leq \frac{1 + \beta_0}{1 - \beta_0}. \quad (1.17)$$

This is equivalent to assuming the recoil of the electrons due to their collisions with the CMB photons can be omitted. These two bounds correspond to the scattering coming from an electron heading either directly towards or away from the incoming photon. However, we also see that *upscattering* happens only when  $\mu' > \mu_0$  – that is, when the photon is deflected along the direction of the incoming electron. It should be reiterated however, that these considerations only hold in the Doppler-dominated regime and will not be true for the general Compton scattering effect (see, e.g., [Sarkar et al., 2019](#), or Chapter 6).

Klein-Nishina corrections to the cross section,  $O(\omega_0^2)$ , are also omitted. In these limits we can also simplify the differential cross section to find

$$\frac{d\sigma}{d\Omega} = \frac{3}{8\pi} \left[ \frac{\omega'}{\omega_0} \right]^2 \frac{1}{\gamma_0^2 (1 - \beta_0 \mu_0)} \left[ 1 - \frac{\omega'}{\omega_0} \frac{(1 - \mu_{sc})}{\gamma_0^2 (1 - \beta_0 \mu_0)^2} + \frac{1}{2} \left( \frac{\omega'}{\omega_0} \frac{(1 - \mu_{sc})}{\gamma_0^2 (1 - \beta_0 \mu_0)^2} \right)^2 \right]. \quad (1.18)$$

The main forms of the SZ effect occur due to different motions of the electrons — as the different velocity distributions lead to different angular and frequency dependencies, and thus a different distortion signal. The thermal SZ effect (tSZ), mentioned before, is caused by ‘thermal’ electrons, i.e., those that obey an isotropic, Maxwell-Boltzmann distribution. The kinematic SZ effect (kSZ) is caused by the bulk motion of the electrons, while any relativistic corrections if the characteristic velocity of the electrons is high are included in the relativistic SZ corrections (rSZ) to both the tSZ and kSZ signals. Any non-thermal electron distributions give rise to non-thermal SZ effects (ntSZ, discussed in the next section). There are then further effects from polarization and multiple scattering events, which I will discuss briefly here for completeness.

### 1.3.1 Thermal SZ Effect

As described in Section 1.2.1, the thermal SZ (tSZ) effect can be simply derived under a number of assumptions. In particular, we assume the hot thermal gas

<sup>2</sup>This will be discussed more in Chapter 6.

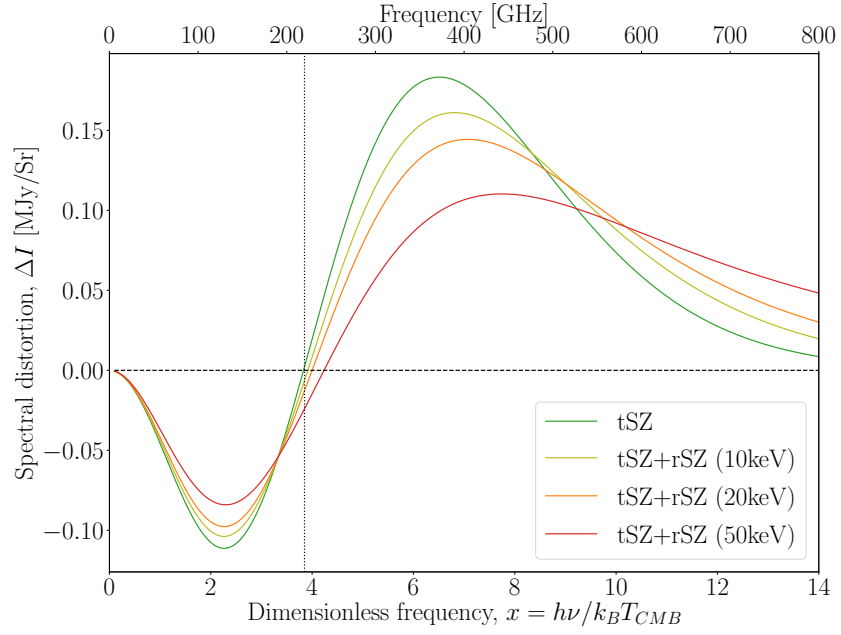


**FIGURE 1.4:** The spectral distortion from the thermal SZ effect - that is the Compton-y distortion. We have included the relativistic corrections for various temperatures. For this figure we have taken  $y = 10^{-4}$ . We can see that the relativistic corrections lead to a broadening of the upscattering and a shift in the distortion node to increasing frequencies with temperature.

obeys an isotropic electron velocity distribution in the CMB rest frame and that only single scattering effects occur. As such to first order there is no net effect, but an effect arises to second order in  $\beta_0$ .

The original approach by [Zeldovich & Sunyaev \(1969\)](#) was to compute this effect using the Kompaneets equation. Eq. (1.15) is rewritten in terms of  $x = h\nu_0/k_B T_{\text{CMB}}$  (instead of  $x_e$ ), and uses the photon distribution  $n = 1/(e^x - 1)$ . Now the  $n(1+n)$  part is multiplied by a factor of  $T_{\text{CMB}}/T_e \ll 1$ , compared to the derivative term, and thus can be neglected. That is we assume

$$\frac{dn(\omega_0)}{d\tau} = \frac{\theta_e}{x^2} \frac{d}{dx} \left[ x^4 \left( \frac{dn}{dx} \right) \right]. \quad (1.19)$$

Now,  $n$  can be substituted in directly to find that, in terms of the CMB intensity,

$$\Delta I_\nu \approx I_0 y \frac{x^4 e^x}{(e^x - 1)^2} \left( x \frac{e^x + 1}{e^x - 1} - 4 \right) \equiv I_0 y g(x). \quad (1.20)$$

Here,  $y = \theta_e \tau$  is the Compton-y parameter, the spectral function  $g(x)$  for the tSZ effect is defined here implicitly, and the intensity normalisation constant is

$$I_0 = \frac{2(k_B T_{\text{CMB}})^3}{(hc)^2} = 270.33 \left[ \frac{T_{\text{CMB}}}{2.7255\text{K}} \right]^3 \text{ MJy/sr}. \quad (1.21)$$

In Figure 1.4, we have plotted the tSZ effect alongside a number of relativistic

corrections, using SZpack<sup>3</sup>. If we assume that this distortion is small, that is  $|\Delta I_\nu| \ll I_\nu$ , the derivative with respect to the temperature can be used to express the signal as:

$$\frac{\Delta T_{\text{CMB}}}{T_{\text{CMB}}} \approx y \left( x \frac{e^x + 1}{e^x - 1} - 4 \right) = y f(x). \quad (1.22)$$

Here,  $f(x)$  is the tSZ spectrum in terms of  $\Delta T_{\text{CMB}}$ . Again the change is explicitly proportional to the Compton- $y$  parameter, which depends on the temperature of the hot electron gas,  $T_e$ , and the Thomson scattering optical depth,  $\tau_e$ :

$$y \equiv \int \theta_e d\tau = \int \frac{k_B T_e}{m_e c^2} N_e \sigma_T dl = \frac{\sigma_T}{m_e c^2} \int P_e dl. \quad (1.23)$$

Here, we have used  $N_e$ , the number density of electrons;  $\sigma_T$ , the Thomson cross section;  $dl$  the line element for the proper distance over the line of sight; and  $P_e = N_e k_B T_e$ , the pressure due to the electrons. Hence, the magnitude of the tSZ signal is a measure of the integrated pressure along the line of sight.

Now, the central optical depth of clusters can be  $\tau \simeq 10^{-2}$  and typical clusters have electron temperatures of  $k_B T_e \simeq 5$  keV, so for massive clusters,  $y \simeq 10^{-4}$ . The signal itself has a distinctive ‘shadow-source’ signature. That is, it appears as a dip in number of photons (and thus intensity) below  $\nu \approx 217$  GHz, and a peak above – since total photon number is conserved, for photons to be scattered to higher frequencies, they are also scattered out of lower frequencies (Figure 1.4).

A further important property of the tSZ effect is its redshift independence. This has two aspects, firstly, the intensity change is defined fractionally to the incident intensity of the CMB, and as such it is not dimmed by time, relative to the dimming of the CMB itself. Secondly, the frequency dependence of the distortion comes in only through  $x$  which is itself redshift independent. This makes it a unique probe of the large-scale structure of the Universe at high redshifts.

### 1.3.2 Kinematic SZ Effect

When free electrons move with a bulk motion relative to the CMB rest frame, they will scatter the CMB photons in an anisotropic manner (Sunyaev & Zel-dovich, 1980). The electron velocity distribution has an underlying directionality, so that upon averaging over all angles of the incoming photons, a linear order Doppler term  $\propto \beta_c$ , the peculiar velocity, remains.

This shift can be written, for a cluster moving with velocity  $\beta_c$ , relative to the line-of-sight direction  $\hat{n}$ , in terms of effective shift in CMB temperature as

$$\frac{\Delta T_{\text{CMB}}}{T_{\text{CMB}}} \approx - \int \sigma_T N_e \hat{n} \cdot \beta_c dl = - \int \hat{n} \cdot \beta_c d\tau \equiv -y_{\text{kSZ}} \quad (1.24)$$

<sup>3</sup>SZpack is a computational package used for the fast and accurate computation of the SZ effect from hot, moving clusters.



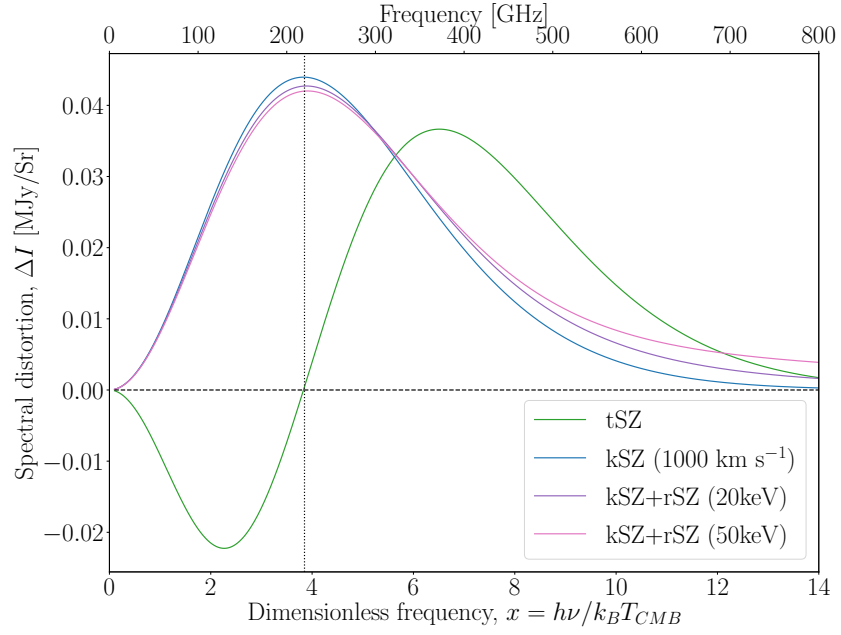


**FIGURE 1.5:** The spectral distortion from the kinematic SZ effect, including the relativistic corrections for various temperatures. We have taken  $\tau = 0.01$  and also included a scaled tSZ distortion ( $y = 0.2 \times 10^{-4}$ ) for reference. We can see that the kSZ effect appears as temperature perturbations (like the hot and cold spots in the CMB), and is around an order of magnitude smaller than the tSZ signal. Again, we see the relativistic corrections lead to a broadening of the signal.

or, in terms of CMB intensity shift, (with  $I_0$  as in Eq. (1.21))

$$\Delta I_\nu \approx -I_0 \frac{x^4 e^x}{(e^x - 1)^2} y_{\text{kSZ}} \quad (1.25)$$

Here, the parameter  $y_{\text{kSZ}}$  (see Figure. 1.5) has been defined as an analogue to the Compton- $y$  parameter found in tSZ (see, e.g., [Ruan et al., 2013](#)). This shift is indistinguishable from hot and cold spots in the CMB unless other information is used, such as scale dependence or correlations with other observations. At leading order, only the line of sight component of the peculiar motion of the cluster is relevant (i.e.,  $\beta_{c,\parallel} = \hat{\mathbf{n}} \cdot \boldsymbol{\beta}_c = \mu_c \beta_c$ ). It is also worth noting that, as a Doppler shift, the temperature shift is negative if the cluster is receding and positive if it is approaching.

From standard cosmological models, typical peculiar motions of clusters are speeds  $O(100) \text{ km s}^{-1}$ , or  $\beta_c = O(10^{-3})$ , so that  $y_{\text{kSZ}} = O(10^{-5})$  at its peak. This is around an order of magnitude smaller than the average tSZ  $y$  parameter.

The kinematic corrections can also be considered as a Lorentz transformation of the tSZ effect in the cluster frame (with an anisotropic CMB photon field) to the CMB frame. Then the optical depth can be interpreted directly as the cluster frame optical depth (see [Chluba et al., 2014](#)). Higher-order corrections in  $\beta_c$  can be added through a multipole-dependent Kompaneets equation, or anisotropic scattering kernels. These corrections are expected to be small.

A further kinematic correction can be found due to the motion of the observer. As with the dipole in the CMB, this can be accounted for through a Lorentz transformation of the SZ signal from the CMB rest frame to the observer's frame (Chluba et al., 2005; Nozawa et al., 2005).

### 1.3.3 Relativistic SZ Corrections

In discussions of the SZ effect so far, we have assumed that the speeds of the electrons were always non-relativistic. For kSZ electrons, where the bulk motions are relatively slow, this seems like a good approximation. However, for thermal electron distributions, there will always be some proportion of the electrons moving relativistically. In our cases, even for a thermal gas at  $k_B T_e \simeq 5$  keV, we have typical speeds of  $\beta_0 \simeq \sqrt{3\theta_e} \simeq 0.1 - 0.2$ . Here, the non-relativistic approximation of only taking terms to second order in  $\beta_0$  is no longer appropriate, and relativistic corrections are relevant. These change both the tSZ and kSZ spectral shapes with respect to the non-relativistic form. The exact mathematical formalism for this effect is discussed in detail in Chapter 4.

There are multiple approaches to calculating these corrections – using varied methods of determining the Compton collision term. Insights into the physics can be obtained by expanding in various orders of  $x$ ,  $\theta_e$  and  $\beta_e$ , using Taylor series approximations. These approaches have been explored in great detail by e.g., Sazonov & Sunyaev (1998); Challinor & Lasenby (1998); Itoh et al. (1998); Nozawa et al. (2006). However, these approaches tend to become inaccurate as  $x$  increases (in particular for  $x \gtrsim 10$ ) and inefficient for the higher temperatures common in clusters, where they converge slowly due to the scattering kernel widening quickly with increasing temperature. Direct numerical integrations with levels of analytic reductions (i.e., Enßlin & Kaiser, 2000; Nozawa & Kohyama, 2009) generally lead to the most precise results, but can be time consuming. If a fixed temperature range is specified, these can be computed more quickly, by relying on precomputed values, leading to methods using precomputed basis functions (Chluba et al., 2012b, as is applied in SZpack) or fits to numerical results (Nozawa et al., 2000; Itoh & Nozawa, 2004). Variations in temperature and peculiar velocity within clusters can be accounted for using moments of the scattering parameters (as is also implemented in SZpack).

In the relativistic case, the average energy shift and broadening per scattering increase more with temperature – that is, say, in Figure 1.4 the peak of the distribution shifts to higher energies, and the entire signal broadens. This extra dependence theoretically allows for the signal to be used to directly measure the temperature of clusters individually (e.g., Wright, 1979; Rephaeli, 1995; Pointecouteau et al., 1998). In the kSZ effect, the relativistic corrections (seen in Figure 1.5) become particularly relevant when evaluating the moments of the distortions. The bulk motion leads to anisotropy in the CMB blackbody field

at second order, inducing a correction to the monopole  $\propto \beta_c^2$  and quadrupole  $\propto \beta_c^2(3\mu_c^2 - 1)/2$  in the clusters rest frame (e.g., [Chluba et al., 2012b](#)).

### 1.3.4 Multiple Scatterings

Inside dense clusters, it is necessary to consider the effects of photons scattering multiple times i.e., colliding with more than one electron in their transit of the electron gas (e.g., [Sunyaev & Zeldovich, 1980](#)). Normally, this correction is derived by assuming that the radiation field remains locally isotropic, the so called, *isotropic scattering approximation*. In this limit, the contribution is suppressed relative to the single-scattering tSZ signal, and becomes a  $\approx 0.1\%$  correction ([Itoh et al., 2001](#)). Furthermore, in this limit, no correction  $\propto \tau$  arises, and thus no up-scattering.

However, when including the anisotropy induced by the previous scattering, the corrections become slightly larger ([Chluba et al., 2014](#); [Chluba & Dai, 2014](#)). This effect is noticeable even in a constant density sphere, due to the variations of the photon's path in different directions. The arising contribution is  $\propto \tau/20$  compared to the tSZ effect. The final signal depends explicitly on the line of sight considered and details of the medium, although measurements are yet to differentiate between these possibilities.

### 1.3.5 Polarised SZ Effect

These signals are all difficult to observe, due to their intrinsic faintness, instrumental challenges in measuring polarization, contamination from other astrophysical polarization sources and beam depolarization effects. However, generally speaking the polarised SZ (pSZ) effects will be generated by any quadrupolar dependence which arises in the SZ effect.

Thomson scattering of CMB photons by free electrons inside clusters leads to a small polarization effect through physics similar to the way primordial CMB E-mode polarization pattern are created (e.g., [Sunyaev & Zeldovich, 1980](#)). These generally rely on the presence of a quadrupole anisotropy in the incoming photon field.

The largest effect comes from the local primordial CMB quadrupole, which leads to a polarization amplitude  $\approx 0.1\tau Q$  in units of  $T_{\text{CMB}}$  ([Kamionkowski & Loeb, 1997](#); [Sazonov & Sunyaev, 1999](#)). Here  $Q$  is the CMB quadrupole moment at the location of the cluster. Accordingly, this signal can reach  $\approx 10^{-3}$  of the primary CMB temperature for rich clusters, and could allow for another way to measure the CMB quadrupole at different locations in the Universe. However, to first order, the frequency-dependence of this signal is the same as that of the primordial CMB polarization anisotropies, and thus knowledge of the cluster location and redshift are also required.

The next largest effect arises from multiple scatterings occurring within the cluster. In particular, the second scattering corrections of the tSZ and kSZ signals (Sazonov & Sunyaev, 1999). For both, to first order, the spectral dependence follows that of the rescattered distributions. For tSZ, the signal can be of similar order of magnitude as the one caused by the primordial CMB quadrupole, but could vanish along the centre of the cluster, as it requires a scattering-induced quadrupole anisotropy. For second-scattering kSZ-induced pSZ, only tangential components of the cluster motion are relevant.

At second order in  $\beta_c$ , the higher-multipole kinematic effects can cause a form of pSZ. This was the pSZ effect originally highlighted in Sunyaev & Zeldovich (1980). This again only relies on tangential components of the cluster's velocity,  $\beta_{c,\perp}$ , and leads to a signal  $\simeq 0.1\tau\beta_{c,\perp}^2$ . Similarly, complex polarization patterns can be formed from internal gas motions (e.g., Chluba & Mannheim, 2002; Diego et al., 2003).

Another source of polarization in the CMB could come from the anisotropic distribution of electrons (Khabibullin et al., 2018). In the ICM, magnetic moments of particles are conserved between collisions, and so the evolving magnetic fields, or heat fluxes could create pressure anisotropies. This could lead to different characteristic thermal velocities of electrons in different directions relative to the field, inducing further polarization patterns. This would have the same spectral dependence as kSZ induced polarization, but would be distinguishable by its pattern. A general discussion of these features occurs in Chapter 5.

## 1.4 Variations to the SZ effect

There are, however, a number of modifications to the standard formulation of the SZ effect that will lead to variations in the observed SZ signal. In particular, in this section I first discuss alternate photon backgrounds besides the CMB. I will also discuss how the variation in clusters themselves lead to modified SZ effects.

### 1.4.1 Alternate backgrounds

In general, any cosmic source of photons – that is, a photon distribution that has passed through a cluster to reach the observer – will have a distortion from passing through the cluster.

In the last two years, this has been discussed for the low-frequency radio background (Fixsen et al., 2011; Seiffert et al., 2011; Singal et al., 2018; Dowell & Taylor, 2018), a signal which may or may not be cosmic. The radio SZ signal (Holder & Chluba, 2021; Lee et al., 2022a), if detected, would be a signal at  $\nu \lesssim 3$  GHz, and could be used to help determine the origins of this signal. This is discussed in significantly more detail in Chapter 4.

One can also discuss the SZ signal formed by the cosmic infrared background (CIB) (Sabyr et al., 2022; Acharya & Chluba, 2022). This creates a complex signal as the CIB itself is generated by galaxies in clusters and, as such, has a complicated redshift dependence. The signal is further complicated as there would be contributions to the CIB scattering from the signal generated within clusters themselves. In this case, the signal peaks around 1000 GHz with contributions in the region of the classical SZ effect but two orders of magnitude smaller than the rSZ corrections at these frequencies.

In both situations, it is not sufficient to consider the background radiation (radio background or CIB) alone, but the combined background of both the CMB and the radio background/CIB must be considered. This methodology may be extended to other cosmic backgrounds, e.g., the 21cm line or X-rays emitted by clusters themselves (e.g., Cooray, 2006; Grebenev & Sunyaev, 2020). However, these signals will all be significantly smaller than the background itself and as such future measurements may not be simple.

### 1.4.2 Non-thermal contributions

In general, clusters are largely thermalised, both locally and more broadly – they sit in massive gravitationally-bound haloes that are the primary cause of the high cluster temperatures. However, firstly, there is a temperature distribution over clusters, with them (generally speaking) being hotter closer to the core and cooler towards the edges. Secondly, local non-thermal disruption can be caused by a number of processes – e.g., jets, feedback, shocks, turbulence and cosmic rays. These must be considered in a variety of ways.

In general, when there is temperature variance within clusters, it must be determined whether the electron distribution is always locally thermalised, in which case the SZ effect can be calculated by superposing the contribution from each component within clusters. However, this is rarely possible. As such, approaches to manage this temperature variance must be accounted for – and in general expansions about the mean temperature can account for much of this variance (cf., Section 1.5 and Chapters 2 and 3). On the other hand, when the departures lead to local non-thermal electron distributions, the inherent local SZ distortion will necessarily change shape.

A further distinction must also be made about the source of non-thermality. While, for instance, turbulence and ‘non-thermal’ pressure exist in clusters leading to low-energy modifications to the SZ distortion – the effects on the observed cluster tSZ effect and relativistic corrections will be small (although the effects may be relevant in consideration of the resolved kSZ effect). However, in this thesis, I will focus on high-energy non-thermal contributions sourced by, for instance, jets and shocks. These could have significant effects on the observed

signal, especially into the high-energy tail of the SZ signal. These same high-energy phenomena may also cause over-heated regions outside of the extent of the clusters themselves, that could be observed with high-precision, well resolved measurements (Malu et al., 2017; Acharya et al., 2021).

In SZ calculations, clusters are also generally imagined to be isotropic spheres. However, as they are located at the intersections of the cosmic web, it is unsurprising that this is a poor approximation. Once again, on the cluster scale, anisotropy generally is caused by local flows of electrons due to the internal structure of the halo itself. These are best represented by localised kSZ corrections to the overall cluster SZ signal.

However, it is also possible, particularly in the cases of jets and outflows, that the SZ effect is caused by locally *anisotropic* electron distributions. In these cases the Kompaneets equation (or its generalisations) no longer encapsulates the scattering event, and complex scattering occurs between different anisotropies – as the scattering generally tends towards creating isotropy within the medium. These effects are all discussed in more detail in Chapter 5.

## 1.5 Simulations and predicting temperatures in clusters

In Chapters 2 and 3, I will expand on the notion mentioned in the previous section of using an averaged temperature (with corrections) to account for the intrinsic variation of temperatures within clusters. In both these chapters, a similar formalism is used which is worth expanding upon here.

It has been long established (Pointecouteau et al., 1998; Hansen, 2004; Kay et al., 2008) that X-ray and SZ measurements do give rise to different temperatures once realistic cluster atmospheres are being considered. In this thesis, I consider three different average temperatures relevant in clusters – the X-ray temperature, specifically here we will use the spectroscopic-like temperature; the mass-weighted temperature, associated with the Compton- $y$  parameter; and the  $y$ -weighted temperature that is relevant for calculating the rSZ corrections. In this section, I will explain each temperature measure, the higher-order  $y$ -weighted temperature corrections, and then mention a number of specifics relevant to calculating temperatures consistently within simulations.

Generally, a consideration of groups and clusters must first define the extent of clusters. Observationally, when these objects are not resolved, this is obtained through taking some boundary according to a certain intensity decrease compared to the ‘brightest’ point in the observed cluster. This leads to a ‘cylindrical’ slice through the cluster (along each line of sight). However, in simulations it is conventional to calculate the signal from a sphere colocated with the dark matter halo, with a certain radius,  $R_\Delta$ . These radii are defined as the radii containing a certain averaged density, and thus mass  $M_\Delta$ , as will be explored further in Section 1.5.3. For an isothermal, fully gravitationally heated sphere of gas, the

virial temperature can then be defined as

$$k_B T_\Delta = \frac{GM_\Delta \mu m_p}{2R_\Delta}, \quad (1.26)$$

which can be used as a reference temperature. Here,  $\mu$  is the mean molecular weight of the plasma<sup>4</sup>.

However, any observed cluster temperature will be an averaged quantity, due to the inherent variation of temperature and density within haloes. These averages are always defined by the weighting procedure, which depends on the observable at hand, and can be generically written as

$$\langle T \rangle \equiv \frac{\int w T dV}{\int w dV}, \quad (1.27)$$

where  $w$  represents the weighting. As discussed later in this section, for the mass-weighted,  $y$ -weighted and spectroscopic-like temperatures one respectively has  $w = n$ ,  $w = nT$  and  $w = n^2 T^{-\alpha}$  with  $\alpha \simeq 0.75$  and  $n$  and  $T$  are the electron density and temperature, respectively.

### 1.5.1 SZ Temperatures

*Compton- $y$  parameter:* As previously described, the classical thermal SZ (tSZ) signal has an amplitude proportional to the Compton- $y$  parameter. This Compton- $y$  parameter is proportional to the integrated electron pressure,  $P_e$ ,

$$y \equiv \int \frac{k_B T}{m_e c^2} d\tau = \frac{\sigma_T}{m_e c^2} \int P_e dl = \frac{\sigma_T k_B}{m_e c^2} \int n T dl. \quad (1.28)$$

*Mass-weighted temperature:* Eqs. (1.28) and (1.20) directly motivate the use of a mass-weighted or  $\tau$ -weighted temperature:

$$T_m \equiv \frac{\int T_e dm}{\int dm} = \frac{\int n T_e dV}{\int n dV}, \quad (1.29)$$

with  $m$  the mass of the electron gas. Hence, the volume-integrated Compton- $y$  parameter,  $Y$ , is

$$Y = \frac{\sigma_T k_B}{m_e c^2} \int n T dV \propto M_{\text{gas}} T_m \quad (1.30)$$

where  $M_{\text{gas}}$  is the total gas mass within the halo. From observations, this temperature measure can be estimated by combining tSZ and X-ray measurements, where the latter is used to obtain a mass/ $\tau$  estimate. However, since the X-ray temperature does not have the same weighting (see below) and because non-thermal pressure contributions can affect the inference, this may lead to a mass

<sup>4</sup>In Chapter 2, where this temperature is used, the mean molecular mass is set to  $\mu = 0.59$ .



bias (e.g., [Arnaud et al., 2005](#); [Nagai et al., 2007a](#); [Battaglia et al., 2012b](#); [Nelson et al., 2012](#); [Shi et al., 2016a,b](#)). It is also worth noting that a similar method can be used by combining measurements from the kinematic SZ and tSZ effect which would minimise this bias (e.g., [Lim et al., 2020](#)).

*y-weighted temperature:* The relativistic corrections to the SZ effect lead to a temperature-dependent modification to the spectral function,  $\Delta I_\nu = I_0 y f(x, T_e)$ . However, since the temperature varies within each cluster, one can write an expansion about an arbitrary temperature pivot  $\bar{T}$  ([Chluba et al., 2013](#); [Remazeilles et al., 2019](#)). To second order in  $\Delta T = T_e - \bar{T}$ , this yields

$$\frac{\Delta I}{I_0} \simeq y f(x, \bar{T}) + y^{(1)}(\bar{T}) f^{(1)}(x, \bar{T}) + \frac{1}{2} y^{(2)}(\bar{T}) f^{(2)}(x, \bar{T}), \quad (1.31)$$

where  $f^{(k)} = \partial_T^k f(x, T)$  and  $y^{(k)} = \langle (T - \bar{T})^k y \rangle$ , and the  $y$  within the brackets, and below, is a ‘local’  $y \propto nT$ . Here,  $\langle X \rangle$  is indicating the cluster-averaged value. This motivates a relativistic temperature, which removes the first-order correction (i.e.,  $y^{(1)}(\bar{T}) = 0$ ) and we call the  $y$ -weighted temperature

$$T_y \equiv \frac{\int y T dV}{\int y dV} = \frac{\int n T^2 dV}{\int n T dV}. \quad (1.32)$$

This  $y$ -weighted temperature is found to be systematically higher than the mass-weighted and X-ray temperatures ([Lee et al., 2020](#); [Lee et al., 2022b](#), also Chapters 2 and 3), indicating that, especially for the largest clusters in the Universe, the relativistic corrections will be relevant and may bias cosmological inferences if not modelled.

In [Planck Collaboration et al. \(2016b\)](#), the assumption that  $f(\nu, \bar{T}_e) \simeq f(\nu, 0)$ , or equivalently that the observed signals are well-modeled by the classical tSZ distortion, was used. However, in [Remazeilles et al. \(2019\)](#), it was shown that due to rSZ effect this can be insufficient. Relativistic corrections will lead to a lower amplitude of the SZ signal at fixed  $y$ -parameter as well as broadening of the SZ signal, which causes a miscalibration and underestimation of the true Compton- $y$  values for each cluster.

*Higher order temperature moments:* While using the  $y$ -weighted temperature removes the first-order correction to the SZ signal, higher order terms proportional to  $y^{(k)}$  remain. We thus define the volumetric  $y$ -weighted temperature moments<sup>5</sup> as

$$T_y^{(k)} = \frac{\int \Delta T_e^k y dV}{\int y dV} = \frac{\int y (T - T_y)^k dV}{\int y dV}. \quad (1.33)$$

<sup>5</sup>In the work [Chluba et al. \(2013\)](#), a different definition for the SZ temperature moments is used. Firstly, they take the mass-weighted temperature moments  $T_m^{(k)}$ , so that their moments are weighted by  $n dV$  rather than  $y dV$ . Furthermore, they use dimensionless moments  $\omega^{(k)} = T_m^{(k+1)} / (T_m)^{k+1}$ . In the limit of many moments, the definitions in terms of  $T_m$  and  $T_y$  are equivalent and yield the same result.



It follows that  $T_y^{(0)} = 1$  and  $T_y^{(1)} = 0$ . While we could theoretically expand to arbitrarily many orders of  $\Delta T$ , we will consider only the lowest-order correction, i.e.,  $T_y^{(2)}$ . We can see that this is closely related to the intrinsic variance of the electron temperature within the cluster gas. To match the dimensionality of the  $y$ -weighted temperature, we will later discuss  $\sigma(T_y) = (T_y^{(2)})^{1/2}$  instead, which provides a proxy for the standard deviation of temperature variation within clusters.

The higher order temperature moments further change the detailed shape of the SZ signal, and thus may cause additional biases to SZ measurements if omitted (Chluba et al., 2013). In Chapter 2, this standard deviation is shown to be around  $\simeq 40\%$  of the cluster temperature; however, overall this is likely to only lead to a  $\lesssim 0.5\%$  correction in  $Y$ .

*Applications to the Compton- $\gamma$  power spectra:* In Remazeilles & Chluba (2020), it is shown that to correctly calculate the tSZ power spectrum, the  $y$ -weighted temperature profiles are necessary. They show that for the tSZ power spectrum one requires a  $y^2$ -weighted or  $C_\ell^{yy}$ -weighted temperature as a pivot. This demands that for each multipole  $\ell$ ,  $\langle y_\ell^* y_\ell^{(1)} \rangle = 0$ , for an isotropic homogeneous, spherical cluster. For an isothermal temperature profile for each cluster, this yields the definition

$$k\bar{T}_{e,\ell}^{yy} = \frac{\langle kT_e(M, z) |y_\ell|^2 \rangle}{\langle |y_\ell|^2 \rangle} = \frac{C_\ell^{T_e, yy}}{C_\ell^{yy}}. \quad (1.34)$$

This choice assures only second-order terms in  $\Delta T_e$  remain in the theoretical tSZ power spectrum,  $C_\ell^{tSZ}(\nu) \propto |y_{\ell m}|^2$ . The outputs from Chapter 2 could be used to improve the calculation by using explicit temperature profiles and their Fourier transforms for the computation of the relativistic temperature power spectra.

### 1.5.2 X-ray Temperatures

X-ray emission, from hot clusters ( $k_B T_e \gtrsim 3$  keV),<sup>6</sup> is dominated by bremsstrahlung radiation within the ICM, and as such has classically been modeled by the emission-weighted temperature. This can be motivated from a simple consideration of the X-ray surface brightness,

$$S_x = \frac{1}{4\pi(1+z)^3} \int n^2 \Lambda_{ee}(T, Z) dl. \quad (1.35)$$

Here,  $\Lambda_{ee}(T, Z)$  is the X-ray emissivity measured by the instrument within the energy band used for the observation;  $z$  is the cluster's redshift and  $Z$  is the metallicity of the ICM.

It has been shown that, due to the non-isothermality of the gas, it is more appropriate to use a modified weighting determined by fitting the X-ray spectrum with a thermal emission model (Mazzotta et al., 2004; Vikhlinin, 2006). This has

<sup>6</sup>This cut off is in large part due to the dominance of emission lines rather than bremsstrahlung in the observed X-ray spectra below these temperatures.

led to the *spectroscopic-like temperature*,

$$T_{\text{sl}} \equiv \frac{\int n^2 T^{1-\alpha} dV}{\int n^2 T^{-\alpha} dV}, \quad (1.36)$$

with  $\alpha = 0.75$  for high temperatures ( $k_B T_e > 3.5$  keV). This matches well with observations from both *Chandra* and *XMM-Newton*. X-ray temperatures have also been calibrated within simulations, determining the differences between different X-ray temperatures and confirming the  $T_{\text{sl}}$  weighting (e.g., [Rasia et al., 2014](#)).

### 1.5.3 Halo definition and redshift dependence

*Radius definitions:* As previously mentioned, to define the extent of groups and clusters within our simulations, we consider spheres of a given radius, co-located with the halo, i.e., centred on the minimum of potential. Then a halo of radius  $R_\Delta$ , is defined so that it contains the mass  $M_\Delta$ .

In this thesis, I use five different radii, in particular,  $R_{500c}$ ,  $R_{200c}$ ,  $R_{500m}$ ,  $R_{200m}$  and  $R_{\text{vir}}$ . For  $R_{\Delta c}$ , these are defined in terms of an overdensity of  $\Delta$  times the critical density of the Universe,  $\rho_{\text{crit}}$ , i.e.,

$$M_{\Delta c} = \frac{4\pi}{3} R_{\Delta c}^3 \rho_{\text{crit}}(z) \Delta, \quad (1.37)$$

while the  $R_{\Delta m}$  are defined in terms of overdensities of  $\rho_{\text{mean}}$ , the mean density of the Universe. The critical density and mean density are defined as,

$$\begin{aligned} \rho_{\text{crit}} &\equiv \frac{3H_0^2}{8\pi G} [\Omega_m (1+z)^3 + \Omega_\Lambda] = \frac{3H_0^2}{8\pi G} E^2(z) \\ \rho_{\text{mean}} &\equiv \frac{3H_0^2}{8\pi G} [\Omega_m (1+z)^3] \end{aligned} \quad (1.38)$$

for a flat  $\Lambda$ CDM universe. This also implicitly defines  $E(z)$ , which describes the redshift evolution of the Hubble parameter. The virial radius  $R_{\text{vir}}$  is defined by  $\rho_{\text{crit}}$  and  $\Delta_{\text{vir}}$  calculated using the approximation in [Bryan & Norman \(1998\)](#), that is,  $\Delta_{\text{vir}} \approx 102$  at  $z = 0$ .

In Chapter 2, clusters are mainly defined as being within the radius  $R_{500c}$  the radius used in most X-ray observations. In Chapter 3, instead they are defined as being within  $R_{200c}$ , a common proxy for the observational radii used in many SZ calculations. It is also worth noting that in this thesis, the *true* (simulation) mass is always used, rather than any proxy for the observed mass (i.e., the hydrostatic mass), which could introduce observational biases (e.g., [Nagai et al., 2007a](#); [Lau et al., 2009, 2013](#); [Nelson et al., 2014](#); [Shi et al., 2016b](#); [Biffi et al., 2016](#); [Barnes et al., 2017a](#)). As such, for direct comparison with any observational quantities,

the associated mass bias must be considered; however, a detailed mass calibration based on mocks for specific observations is beyond the scope of this thesis.

*Redshift dependence:* As the critical density has a redshift dependence, one can accordingly expect an evolution of the cluster properties. A simple geometric consideration and assumption of isothermality within the virialized sphere would lead to a temperature dependence akin to

$$T_{\Delta} \propto M_{\Delta}/R_{\Delta}. \quad (1.39)$$

Then, by using the  $\rho_{\text{crit}}$  redshift dependence, self-similar evolution is expressed as

$$\begin{aligned} M_{\Delta} &\propto E^2(z) R_{\Delta}^3, \\ T_{\Delta} &\propto E^{2/3}(z) M_{\Delta}^{2/3}, \\ T_{\Delta} &\propto E^{2/5}(z) Y_{\Delta}^{2/5}. \end{aligned} \quad (1.40)$$

As such, any deviation from this evolution can be considered as being inherent evolution of the temperatures, due to non-gravitational processes in the clusters themselves. I highlight some of these trends in Chapters 2 and 3.

## 1.6 Thesis Overview

Chapter 2 examines the differences in  $T_y$ ,  $T_m$  and  $T_{\text{sl}}$  in the BAHAMAS and MACSIS simulations. I computed the volume-averaged quantities to obtain Temperature-mass, temperature-temperature and temperature- $Y$  scaling relations and to examine the  $y$ -weighted temperature dispersion term. I consider the effects of redshift and also examine the profiles of these temperature measures. Finally, I briefly discuss the impact of these determinations on observational measurements of  $Y$ , and cluster determinations for  $H_0$ .

In Chapter 3, I extend the work of Chapter 2 to compare between simulations, using the MAGNETICUM PATHFINDER, ILLUSTRISTNG and THE THREE HUNDRED PROJECT simulations, alongside the BAHAMAS and MACSIS simulations. I restrict my focus to volume-averaged temperatures, but using five different radial extents for each halo. The redshift effects are again considered, and the variations in resolution and feedback mechanisms between simulations are discussed in relation to differences in the observed temperatures. Cross-simulation temperature scaling relations are derived, and are compared to X-ray measurements of cluster temperatures, as well as a discussion on the impact of these scaling relations on future SZ measurements.

Chapter 4 focuses on the radio SZ signal, examining in detail the kinematic terms and relativistic temperature corrections. Using the framework of an asymptotic expansion, I discuss how the radio SZ effect may be quickly and accurately

calculated, and how variations within the radio background itself may lead to differences in the observed radio SZ effect. The next steps required to carry out observations of the radio SZ effect are also discussed.

Chapter 5 examines the potential effects of anisotropic photon and electron distributions and high-energy non-thermal electron populations on the observed SZ signal. New analytic forms for anisotropic SZ scattering are presented and explored for arbitrary multipoles in a spherical harmonic decomposition. I then carry out a brief exploration of toy models for high-energy non-thermal electron populations and their impacts on the SZ signal.

In Chapter 6, I move the discussion to general Compton scattering (instead of the Doppler-dominated regime used for SZ calculations). A summary of the isotropic Compton-scattering kernel is provided, and its behaviour in extreme regimes is explored. New Compton-scattering kernels for anisotropic photon populations are presented for low multipoles and their behaviour is discussed.

Finally, Chapter 7 concludes this thesis, and discusses future work to be carried out on these subjects.

## Chapter 2

# Relativistic SZ temperature scaling relations of groups and clusters derived from the BAHAMAS and MACSIS simulations

This chapter is based on the published work, [Lee et al. \(2020\)](#). The code used was modified from code written by David Barnes, but otherwise the work was carried out by EL. The BAHAMAS simulations were used with the kind permission of Ian McCarthy.

### 2.1 Introduction

The ICM is often modeled as an isothermal sphere of electrons, allowing for simple mass-temperature relations to be derived. However, both direct measurements and hydrodynamical simulations indicate that clusters are neither isothermal nor spherical (e.g., [Nagai et al., 2003](#); [Vikhlinin et al., 2009b](#)). As such, instead of directly obtaining the thermodynamic temperature, we obtain volume-averaged temperatures, weighted according to the physical process they derive from (as described in Section 1.5).

The SZ distortion in groups and clusters is dominated by the thermal SZ (tSZ) signal ([Zeldovich & Sunyaev, 1969](#)), which gives a redshift- and temperature-independent spectrum. However, relativistic corrections at typical cluster temperatures lead to both a broadening and drop in magnitude of this signal at fixed  $y$ -parameter. The rSZ effect can be efficiently modeled with SZpack ([Chluba et al., 2012b, 2013](#)); for this, accurate estimates for the  $y$ -weighted temperature are required. The  $y$ -weighted temperature is also relevant to precise computations of the SZ power spectra and the interpretation of SZ data from *Planck*, as

rSZ can cause biases in cosmological parameters such as  $\sigma_8$  (Remazeilles et al., 2019).

In this chapter, the BAHAMAS and MACSIS simulations are used to examine the differences between three temperature measures; a proxy for the observed X-ray temperature  $T_{\text{sl}}$  (the spectroscopic-like temperature; Mazzotta et al., 2004); a proxy for the Compton- $y$  parameter,  $T_{\text{m}}$  (i.e., the mass-weighted temperature); and finally a measure that accounts for the relativistic temperature correction to the tSZ distortion (rSZ),  $T_y$  (the  $y$ -weighted temperature; Hansen, 2004; Remazeilles et al., 2019). The latter in particular, so far, has not been studied systematically; as previously discussed, current observational measurements have only attained low-significance measurements of the rSZ effect. However, due to the growing sensitivity of planned and ongoing CMB experiments, rSZ is now coming into reach, and future observations with the Simons Observatory and CCAT-prime ought to be able to extract this signal more accurately.

Furthermore, precise SZ power spectrum calculations depend directly on the clusters' average pressure and  $y$ -weighted temperature profiles. Cluster pressure profiles have been extensively studied using simulations (e.g., Nagai et al., 2003; Battaglia et al., 2010, 2012a) and also have been calibrated against X-ray observations (Arnaud et al., 2010; Planck Collaboration et al., 2013). The  $y$ -weighted temperature profiles again have not been studied directly but will affect the precise shape of the relativistic temperature power spectrum (Remazeilles et al., 2019), which could become a novel cluster observable (Remazeilles & Chluba, 2020; Basu et al., 2019) for future CMB missions similar to CORE (Melin et al., 2018) and PICO (Hanany et al., 2019). This chapter carries out a comparative study of various temperature profiles with a particular focus on obtaining a new prescription of the  $y$ -weighted temperature profiles.

The study is based on BAHAMAS (McCarthy et al., 2017, 2018) and MACSIS (Barnes et al., 2017a), two giant hydrodynamical simulations generating over 14,000 haloes of masses between  $\approx 10^{13} M_{\odot}/h$  to  $4 \times 10^{15} M_{\odot}/h$  with outputs at redshifts of  $z = 0, 0.5$  and  $1$ . With these, temperature-mass relations for each temperature measure can be generated, alongside a detailed analysis of the temperature profiles. To match with the work of Barnes et al. (2017a), the effects of restricting our analysis to only the hot and relaxed subsets of clusters within our samples are also considered.

Moreover, since clusters are not isothermal, further corrections to the observed SZ signal must arise from averaging processes. This comes from the understanding that the distortions are caused by electrons of varying temperature along the line of sight, and thus will not be completely modeled by a single temperature. The first corrections to the signal can be found through a temperature moment expansion (Chluba et al., 2012b, 2013) and is related to the dispersion of  $y$ -weighted temperatures within clusters, which is systematically studied

**TABLE 2.1:** Cosmological parameters used in the BAHAMAS and MACSIS simulations.

Simulation	$\Omega_\Lambda$	$\Omega_m$	$\Omega_b$	$\sigma_8$	$n_s$	$h^\dagger$
BAHAMAS	0.6825	0.3175	0.0490	0.8340	0.9624	0.6711
MACSIS	0.6930	0.3070	0.0482	0.8288	0.9611	0.6777

$^\dagger$  where  $h \equiv H_0/(100 \text{ km s}^{-1} \text{ Mpc}^{-1})$

here. The results suggest that this dispersion scales at around  $\simeq 40\%$  of the cluster temperature, but overall leads to negligible corrections to the rSZ signal (see Section 2.5.1).

The mathematical background behind this chapter has already been described in Section 1.5. Later in this chapter (Section 2.5.2), I will also briefly discuss the relevance of rSZ to determinations of  $H_0$  through SZ measurements (Cavaliere et al., 1979; Birkinshaw et al., 1991; Hughes & Birkinshaw, 1998; Reese et al., 2002), showing that it could lead to a systematic shift in the derived  $H_0$  values if rSZ effects are neglected.

## 2.2 Simulations

This chapter uses a combined sample of clusters from the BAHAMAS and MACSIS simulations. Over 14,000 haloes with masses  $M_{500c} \geq 10^{13} M_\odot h^{-1}$  were obtained from the BAHAMAS project (McCarthy et al., 2017). However, this provides a limited number of high-mass clusters, and so are supplemented by the compatible MACSIS project (Barnes et al., 2017a), which generated 390 clusters with  $M \gtrsim 10^{15} M_\odot$ . These two projects were designed to match hydrodynamical properties and use compatible cosmologies, as shown in Table 2.1.

While there is a small redshift discrepancy between the BAHAMAS sample at  $z = 0.5$  and the MACSIS sample at  $z = 0.46$ , these are combined without correction as the redshift dependence of our quantities are slight. There is also a mismatch in cosmological parameters, however, these are left unadjusted as we believed the correction would be small.

It is also worth noting that to calculate the temperature measure in simulations, the process must be discretised. That is, all of the weighted volume integrals become weighted sums, recalling that  $\mu m_p n dV = dm$ . Furthermore, all particles with a temperature lower than  $10^{5.2} \text{ K}$  are ignored as they make a negligible contribution to the total X-ray or SZ emission (cf., Barnes et al., 2017a), but their inclusion can bias the measured temperature through weighting approximations. This will be discussed briefly in Chapter 3.

This section highlights the key properties of these two simulations and discusses the method involved in combining the samples. Two subsamples are also used within this chapter – designed to examine the hot and relaxed clusters as defined in Barnes et al. (2017a).



### 2.2.1 BAHAMAS Simulation

The BAHAMAS simulation (McCarthy et al., 2017, 2018) is a calibrated version of the model used in the cosmo-OWLS simulations (Le Brun et al., 2014). It consists of a 400 Mpc/ $h$  periodic box and, for the simulations used in this thesis, uses cosmological parameters consistent with those from *Planck* 2015 (Planck Collaboration et al., 2016c).

The full BAHAMAS run has  $2 \times 10^{24}$  particles, yielding a dark matter mass of  $m_{\text{DM}} = 4.5 \times 10^9 M_{\odot}/h$  and initial baryon particle mass of  $m_{\text{gas}} = 8.1 \times 10^8 M_{\odot}/h$ . The Plummer equivalent gravitational softening length was fixed to 4 kpc/ $h$  in comoving units for  $z > 3$  and in physical coordinates thereafter. The simulations were run with a version of the smoothed particle hydrodynamics code `P-GADGET3`, which was last publicly discussed in Springel (2005) but has since been greatly modified to include new subgrid physics as part of the OWLS project (Schaye et al., 2010). The feedback calibration was set to match the observed gas mass fraction of groups and clusters and galaxy stellar mass function at  $z = 0$  (see McCarthy et al., 2017, for details).

### 2.2.2 MACSIS Simulation

The MACSIS project (described in detail in Barnes et al., 2017a) was developed to extend the BAHAMAS simulations to higher-mass haloes. The sample was generated using a zoomed simulation technique from a large-volume Dark-Matter-only simulation (a periodic cube with side length 3.2 Gpc). The cosmological parameters match those from the *Planck* 2013 results combined with baryonic acoustic oscillations, *WMAP* polarization and high multipole moments experiments (Planck Collaboration et al., 2014a).

The MACSIS sample was then selected by finding all haloes with a Friends-of-Friends (FoF) mass,  $M_{\text{FoF}} > 10^{15} M_{\odot}$ , and grouping them into logarithmically spaced bins of width  $\Delta \log_{10}(M_{\text{FoF}}) = 0.2$ . The bins with masses above  $10^{15.6} M_{\odot}$  had less than 100 haloes each and all were selected. The other bins were further subdivided, each into 10 logarithmic bins, from each of which 10 haloes were randomly selected, obtaining a total of 390 haloes – this ensured the sample is not biased to low masses by the steep slope of the mass function.

These selected clusters were then re-simulated using the zoomed simulation technique (Katz & White, 1993; Tormen et al., 1997) to recreate the chosen sample at an increased resolution compared to the parent simulation. Both a Dark-Matter-only and full-gas-physics resimulation was then carried out. The latter, used in this work, had a dark matter mass of  $m_{\text{DM}} = 4.4 \times 10^9 M_{\odot}/h$  and gas particle initial mass of  $m_{\text{gas}} = 8.0 \times 10^8 M_{\odot}/h$ . The softening length was fixed as in the BAHAMAS simulation. The simulations were again run with the same version of the smoothed particle hydrodynamics code `P-GADGET3`. The resolution and softening of the zoom re-simulations were deliberately chosen to match the values of



**TABLE 2.2:** Selected halo counts with  $M_{500c} > 10^{13} M_{\odot}/h$ , and with a mass cut between the BAHAMAS and MACSIS samples at the given values.

Redshift	BAHAMAS	MACSIS	$M_{500c, \text{cut}}/M_{\odot}$
0	14333	295	$6.03 \times 10^{14}$
0.5/0.46 <sup>a</sup>	10791	263	$3.55 \times 10^{14}$
1	6344	186	$2.00 \times 10^{14}$

<sup>a</sup> that is, 0.5 for BAHAMAS and 0.46 for MACSIS.

the periodic box simulations of the BAHAMAS project. [Barnes et al. \(2017a\)](#) further shows that the MACSIS clusters reproduce the observed mass dependence of the hot gas mass, X-ray luminosity and SZ signal at redshift  $z = 0$  and  $z = 1$ .

### 2.2.3 Combined Sample

We combine these simulations to allow for clear comparison with the work in [Barnes et al. \(2017a\)](#), taking only haloes with  $M_{500c} > 10^{13} M_{\odot}/h$ . Further we take a mass cut at each redshift, as detailed in Table 2.2, above which we take only MACSIS haloes and below which we take only BAHAMAS haloes. The final halo counts at each redshift are detailed there. Haloes are identified in both simulations through the friends-of-friends method described in [McCarthy et al. \(2017\)](#). The centre of these haloes is taken to be the minimum of the local gravitational potential, and any sub-haloes lying outside a given characteristic radius,  $R_{\Delta}$ , are ignored.

### 2.2.4 Core-Excised Averages

It is a common technique in X-ray observations to exclude the central regions of clusters to reduce the scatter in X-ray properties. These core-excised quantities are generally considered to be better mass proxies ([Pratt et al., 2009](#)). Within simulations, this can have an added effect of reducing the potential impact of the central (more uncertain) physics inside the cores. In the work of [Barnes et al. \(2017a\)](#), the excluded region is that of  $r < 0.15 R_{500c}$ .

In simulations, it would be possible to core-excise all of the volume averaged quantities, not just the X-ray temperatures. However, in the BAHAMAS and MACSIS samples,  $T_{\text{sl}}$  has a large correction under core-excision – raising the temperatures increasingly at higher masses, but undergoing a more complex increase across the entire mass range – but both  $T_y$  and  $T_m$  undergo very minimal modifications (the mean corrections are  $(T_{\text{CE}} - T_{\text{full}})/T_{\text{CE}} = -0.011 \pm 0.065$  and  $-0.003 \pm 0.015$  for each measure, respectively<sup>1</sup>).

<sup>1</sup>These are the values for the volume average over  $R_{500c}$ ; when averaged over  $R_{200c}$  instead, arguably a more applicable volume for SZ measurements, these corrections reduce to  $-0.010 \pm 0.048$  and  $-0.004 \pm 0.009$  respectively.

**TABLE 2.3:** Selected Halo counts with  $M_{500c} > 10^{13} M_{\odot}/h$ , and with a Mass cut between the BAHAMAS and MACSIS samples at the given values for the Hot and Relaxed samples.

Redshift	BAHAMAS	MACSIS	$M_{500c,cut}/M_{\odot}$	$M_{500c,min}/M_{\odot}$
Hot Sample				
0	271	295	$6.03 \times 10^{14}$	$2.29 \times 10^{14}$
0.5/0.46 <sup>a</sup>	87	263	$3.55 \times 10^{14}$	$2.09 \times 10^{14}$
1	4	186	$2.00 \times 10^{14}$	$1.91 \times 10^{14}$
Relaxed Sample				
0	165	188	$6.03 \times 10^{14}$	$2.29 \times 10^{14}$
0.5/0.46 <sup>a</sup>	50	178	$3.55 \times 10^{14}$	$2.09 \times 10^{14}$
1	3	126	$2.00 \times 10^{14}$	$1.91 \times 10^{14}$

<sup>a</sup> that is, 0.5 for BAHAMAS and 0.46 for MACSIS.

As many SZ measurements are flux and resolution limited, taking core excised values would be difficult in practice. Accordingly, in this chapter, the full volume averages are used for  $T_m$  and  $T_y$ , but the core-excised values for  $T_{sl}$ .

## 2.2.5 Hot and Relaxed Sub-samples

As previously noted, the models for the X-ray temperatures, all rely on continuum emission, while at low cluster temperatures the effects of spectral lines begin to seriously affect the observed X-ray spectra. Accordingly, following the analysis of [Mazzotta et al. \(2004\)](#), we note that the spectroscopic-like temperature is validated only for higher temperatures. This motivates the use of a Hot Sample, where  $T_{sl}$  is a more reliable proxy for the X-ray emission. To avoid biases, we introduce a mass cut by finding the minimal mass that fulfills  $T_{sl}(M) \geq 3.5$  keV – this ensures that the maximal temperature at a given mass is  $T_{sl}(M) \gtrsim 3.5$  keV.<sup>2</sup> The resulting mass cuts and halo counts are summarized in Table 2.3.

The final sample is a relaxed subsample of these Hot clusters. Although there are many ways to define a relaxed halo (see, e.g., [Neto et al., 2007](#); [Duffy et al., 2008](#); [Klypin et al., 2011](#); [Dutton & Macciò, 2014](#); [Klypin et al., 2016](#); [Barnes et al., 2017b](#)), in this thesis we follow the criteria used in [Henson et al. \(2017\)](#), that is

$$X_{\text{off}} < 0.07; f_{\text{sub}} < 0.1 \text{ and } \lambda < 0.07,$$

with  $X_{\text{off}}$  the distance offset between the point of minimum gravitational potential in a cluster and its centre of mass, divided by  $R_{\text{vir}}$ ;  $f_{\text{sub}}$  the mass fraction within  $R_{\text{vir}}$  that is bound to substructures and  $\lambda$  the spin parameter<sup>3</sup> for all particles within  $R_{200c}$ . It should be noted that, as in [Barnes et al. \(2017a\)](#), this is not a small sample of the most relaxed objects, but instead a simple metric to remove those that are significantly disturbed.

<sup>2</sup>In the work of [Barnes et al. \(2017a\)](#), they take the smaller sample of all clusters with  $T_{sl} > 5$  keV.

<sup>3</sup>Using the alternative expression for the spin parameter from [Bullock et al. \(2001\)](#).

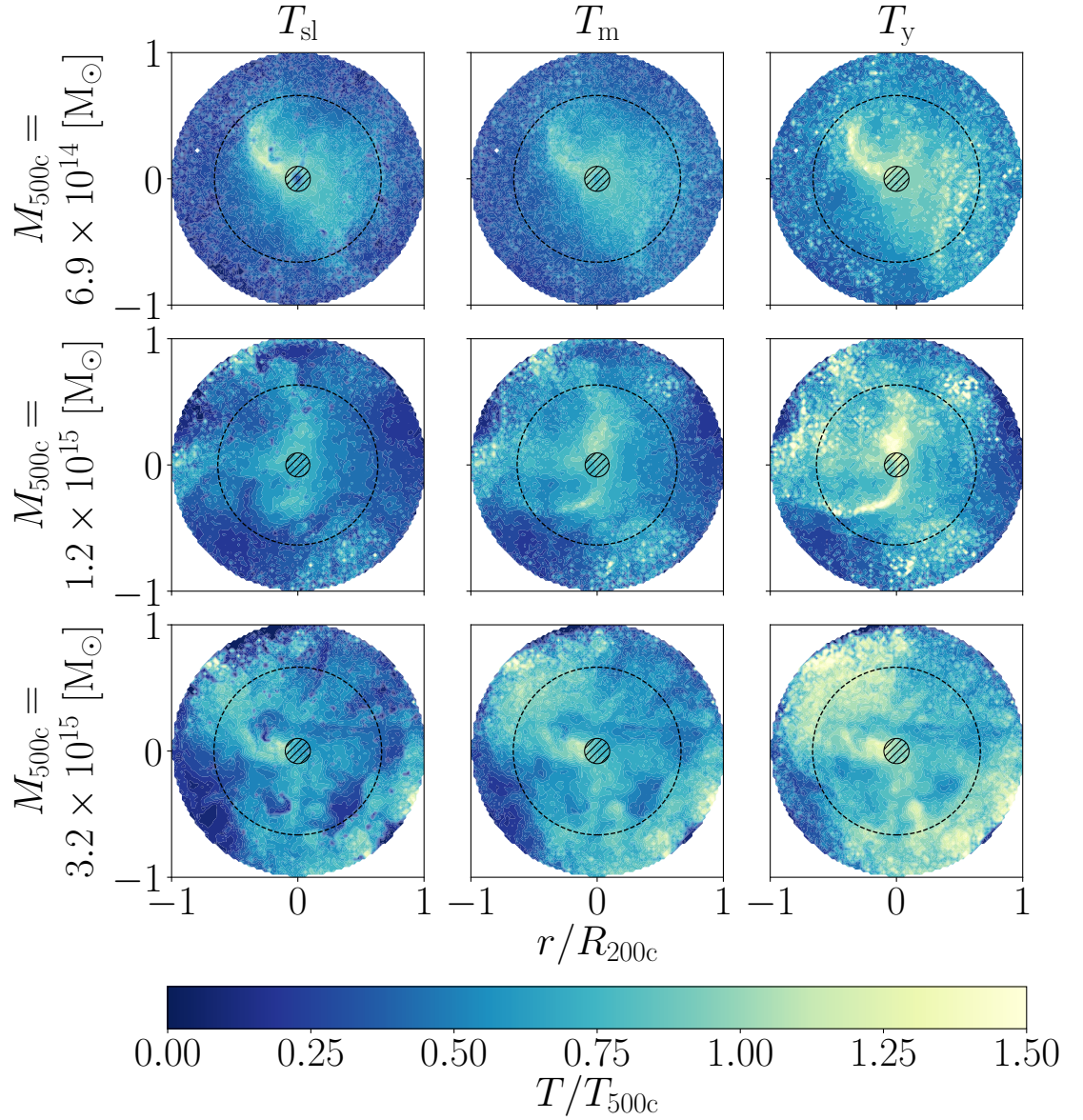


**FIGURE 2.1:** A comparison of the cylindrically-projected temperatures through a range of clusters at  $z = 0$ , relative to  $T_{500c}$  for that cluster. These projections are taken within spheres of radius  $R_{200c}$  about the cluster centre of potential. From left to right we see  $T_{sl}$ ,  $T_m$  and  $T_y$ , and from top to bottom clusters of various masses. Since these are just the projections for single clusters, they are subject to variations from the median expected behaviours. To guide the eye, on each plot a dashed line at  $R_{500c}$  has been drawn, alongside a hatched region at  $0.15 \times R_{500c}$ , which would be the core-excised region. These clusters have been chosen with  $T_{sl,500} > 3.5$  keV so that it is an appropriate proxy for the X-ray temperature.

## 2.3 Cluster Temperature Scalings

To understand the cluster-wide, i.e., volume-averaged temperatures, it is instructive to first consider the contributions to each temperature measure, given by each part of the cluster. These lead to variations between the temperature measures calculated over spheres of radius  $R_{500c}$  (as typical for X-ray measurements) and  $R_{200c}$  (a proxy for the viral radius and arguably more applicable for SZ measurements). In this chapter, all the figures are presented with respect to the  $R_{500c}$  sphere, but Appendix A contains the fits tabulated within both regions.

### 2.3.1 Causes for differences in temperature measures

From an illustrative point of view, the differences between the volume-averaged temperature measures can be examined from the projected temperatures through a selection of clusters. These, as can be seen in Figure 2.1, give an indicative understanding of various features (e.g., shocks, outflows, sub-haloes and filamentary behaviours that might exist within haloes).

Generally, it appears that  $T_y > T_m > T_{sl}$  – an aspect clearest in the features, but also evident in the slightly brighter overall colours of the halo from left to right across the figure. It is also the case that at larger radii,  $T_y$  is very susceptible to the structures within the haloes. This can be understood fairly simply:  $T_{sl}$  depends on the square of the local density, so in regions of high density – i.e., the core of the cluster or in dramatic substructures – high temperature regions will be clearly visible; however, where the density falls – i.e., warm diffuse gas – the temperature is greatly suppressed.  $T_y$  on the other hand, is weighted by the local pressure (it depends on both the local temperature and density) so highlights shocks and outflows. This exacerbates the difference in observed temperatures in the outer regions of haloes, e.g.,  $R_{500c} \rightarrow R_{200c}$  which are minimally probed by the X-ray temperatures (as reflected in  $T_{sl}$ ).  $T_m$  in general, lies somewhere between the other two measures.

### 2.3.2 The effect of averaging over volumes of radii $R_{500c}$ or $R_{200c}$

It is important to determine the difference between averaging over spheres of radii  $R_{200c}$  and  $R_{500c}$ . X-ray measurements, in particular, are almost always taken over  $R_{500c}$ , and as such  $R_{500c}$  values are those commonly used in the literature. However, it can be argued that  $R_{200c}$  should also be widely considered. Since  $R_{500c}$  generates a smaller region, it encapsulates only the hotter core with less of the cooler outskirts of the cluster. As such, regardless of the temperature measure, it returns a higher temperature than that obtained within  $R_{200c}$ .

This can be seen graphically in Figure 2.2. Here, the fractional variation between  $R_{500c}$  and  $R_{200c}$  values has been plotted. These appear to be predominantly redshift independent; while there are variations between each redshift,

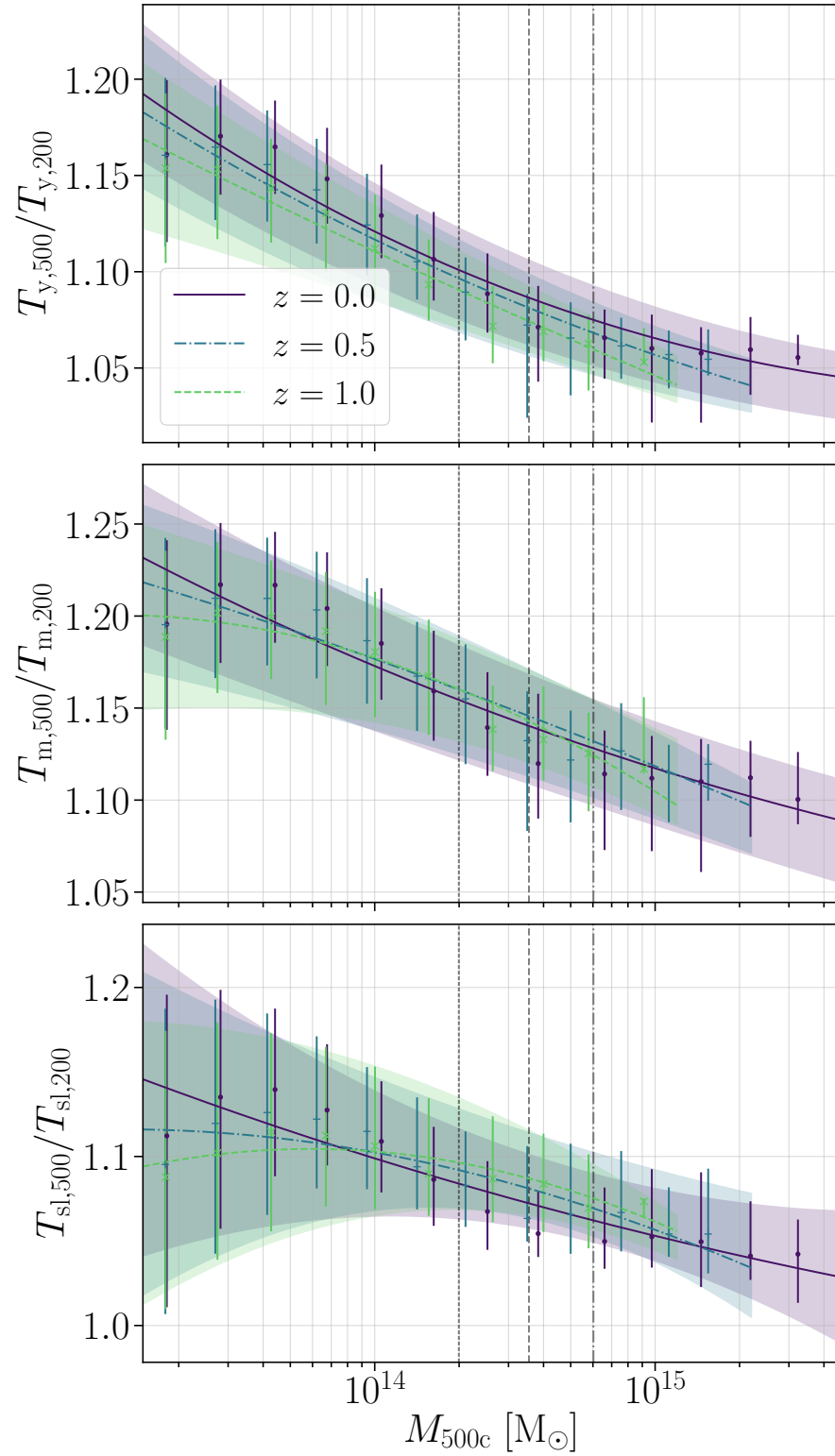


**FIGURE 2.2:** A comparison of the temperature measures depending on whether they are calculated over a sphere of radius  $R_{200c}$  or  $R_{500c}$  against  $M_{500c}$ . The redshift dependence is also displayed. The vertical dot-dashed, dashed and dotted lines here depict the mass cut offs between the BAHAMAS and MACSIS samples at  $z = 0$ , 0.5 and 1, respectively. The datapoints and errors show the median, 84 and 16 percentile regions for the various mass bins, while the solid line and shaded regions demonstrate the best fits (discussed in Section 2.3.3) for the same.

they are all within the intrinsic scatter. Secondly, for all measures the differences between the two measures become smaller at higher masses. This may in fact be an averaging effect due to the distribution of temperatures in clusters (see, Section 2.4), and the mass-dependent changes to the profiles and thus the fall-off of temperatures nearer the outskirts of clusters. These will lead to the averaged effects that can be seen here.

In general, the changes to  $T_m$  are the most acute, followed by  $T_{sl}$ , with  $T_y$  undergoing the smallest corrections. However, this is still a sizeable effect:  $\approx 10\%$  at  $M_{200c} = 10^{14} M_\odot$  ( $\approx 20\%$  for  $T_m$ ). Indicating that when clusters are unresolved, this effect should be considered for SZ measurements as the extent of the observed cluster may be closer to  $R_{200c}$  than  $R_{500c}$  and as such, using the temperatures within  $R_{500c}$  will lead to misestimations of the ‘observed’ cluster temperature.

For the rest of this chapter,  $R_{500c}$  is used to reproduce the results commonly cited in cluster papers – the analysis has also been carried out across a radii of  $R_{200c}$  with few qualitative variations. The full tabulated numerical results can be found in Appendix A.

### 2.3.3 Temperature-mass scaling relations

In Figures 2.3 and 2.4, the temperature mass scaling relationships for the three temperature measures at each redshift are displayed. Figure 2.3 shows the redshift dependence of each temperature measure individually, relative to self-similar scaling – i.e., scaling out  $E(z)^{2/3}$ ; while Figure 2.4 shows the results divided through by  $T_m$ , the mass weighted temperature, so that the variations between the three measures are more visible. It can be seen immediately that the spread in the data is far larger for  $T_{sl}$  than for  $T_y$  or  $T_m$ . This furthers the common observation that the SZ signal,  $Y_{SZ}$ , provides a tighter mass proxy than the X-ray signal.<sup>4</sup>

In Figure 2.3, the redshift variation of each temperature measure is similar to the self-similar relation – i.e.,  $T \propto E(z)^{2/3}$ . In particular, while with increasing redshift  $T_y$  falls a little at low masses and has a slightly steeper mass dependence, overall the  $y$ -weighted temperature is consistent within the intercluster variation with self-similar evolution. The mass-weighted temperature shows more departures from self-similarity, and  $T_{sl}$  shows the greatest departure from this  $E(z)^{2/3}$  scaling. The spectroscopic-like temperature both falls in magnitude and has increasing curvature, indicating that at the highest masses, the differences under redshift evolution are magnified.

From a physical point of view, this can be understood since at higher redshifts, the haloes have had a shorter cooling time, leading to denser cooler gas, and thus a lower  $T_{sl}$ . However, the pressure of the gas is largely fixed to match

<sup>4</sup>It should be noted however, that this has many factors, and generally relies on the accurate calibration of the SZ mass relation.



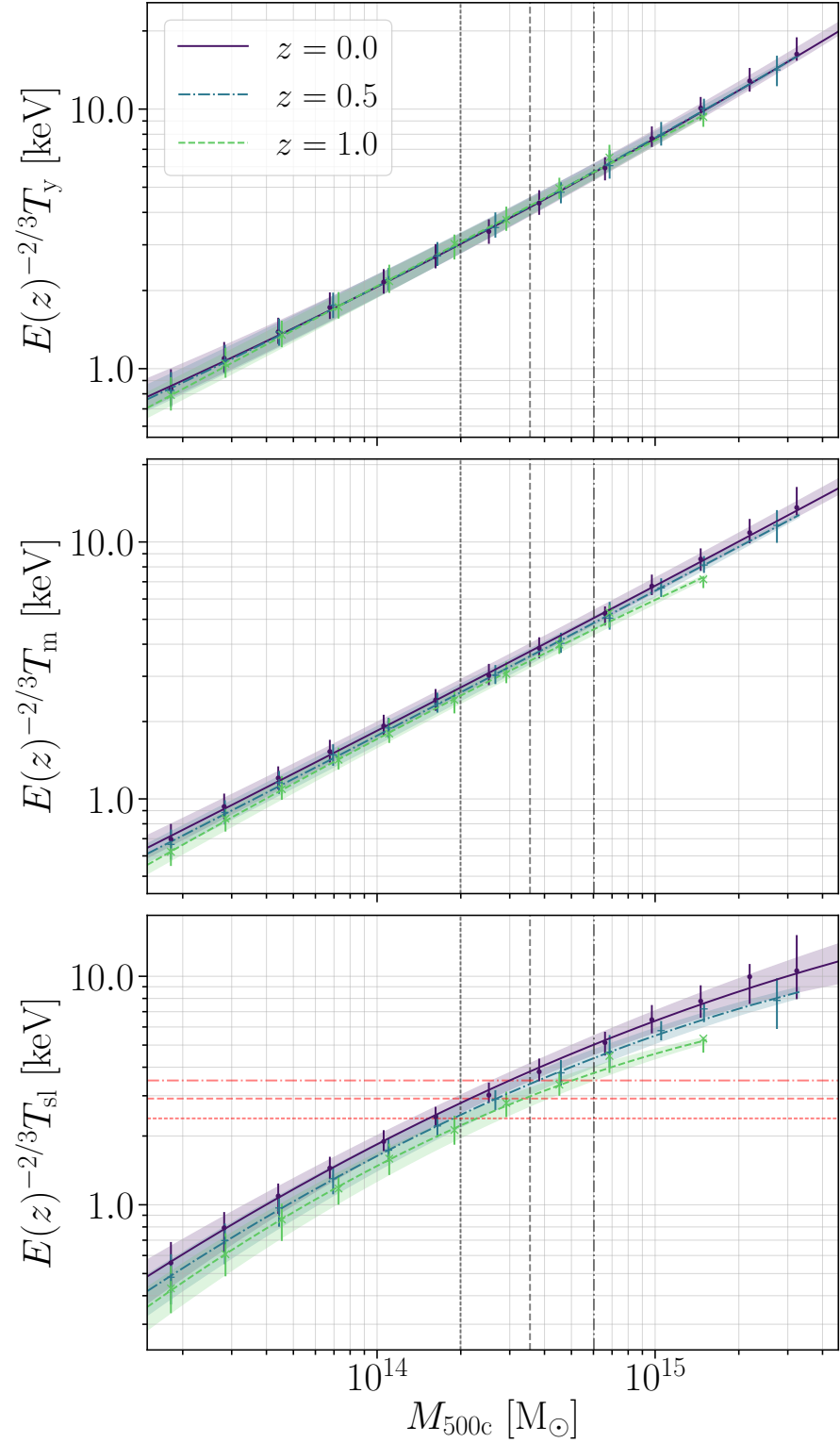


**FIGURE 2.3:** A comparison of the three temperature measures at three different redshifts. The plotted points show the medians of the binned data, with the error bars demonstrating their 16 and 84 percentile regions. The solid lines show the fits to the data, with the shaded regions showing the 68% confidence region. The horizontal lines in the bottom panel show the 3.5 keV cutoff for the reliability of  $T_{\text{sl}}$  as a proxy for the X-ray temperature.

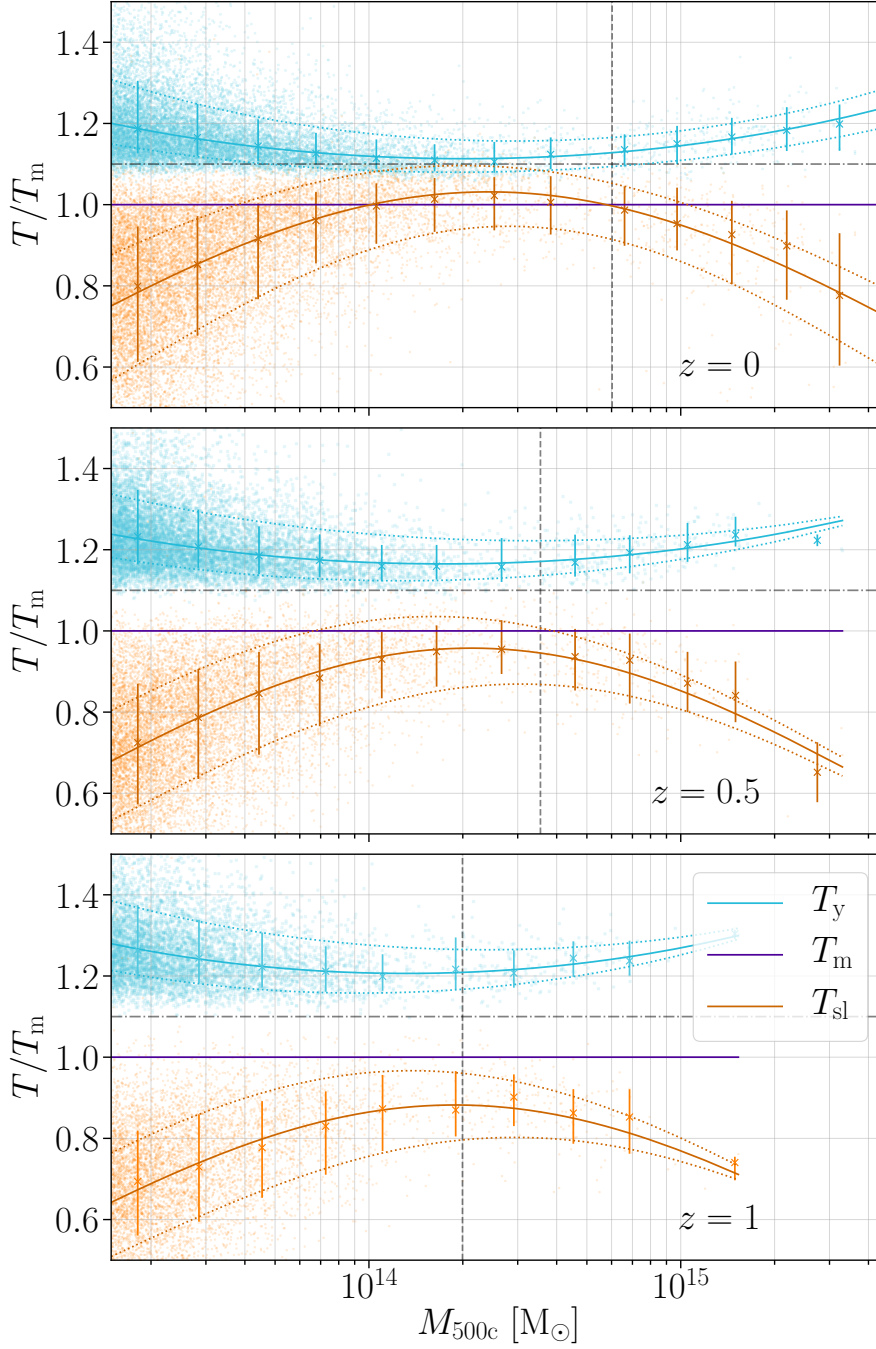


**FIGURE 2.4:** A comparison of the three temperature measures on a cluster by cluster basis. Here we consider the temperature measures with respect to  $T_m$ . The solid lines indicate the line of best fit of the data sets, while the dotted lines show the 16 and 84 percentiles. The horizontal dot-dashed line lies at  $T/T_m = 1.1$  to guide the eye. In the case against  $T_y$  we can see that the minimum values of the means lie at 1.11, 1.16 and 1.21 for  $z = 0, 0.5$  and  $1$ , respectively.



the potential wells of the haloes themselves (as they are roughly in hydrostatic equilibrium) and reduces the redshift dependence of  $T_y$ , which is less affected by the evolution of the clusters themselves.

In Figure 2.4,  $T_y$  has a larger magnitude than  $T_m$  and  $T_{sl}$ , while the latter two are at points consistent, with  $T_m$  higher at both higher and lower masses. This may be a consequence of the calibration scheme used in defining the spectroscopic-like temperature, which is focused on clusters at low redshifts with masses  $M_{500c} \simeq 10^{14} M_\odot$ , but more work would have to be done to fully analyse this effect. Furthermore, there are hints of a strong cluster by cluster correlation in the values of  $T_y$  and  $T_m$ , from the  $\gtrsim 10 - 20\%$  shift between these two values. With respect to  $T_{sl}$  there is a correction for  $T_y$  of  $\gtrsim 10\%$  (or  $\gtrsim 40\%$ ) at  $z = 0$  ( $z = 1$ ), increasing greatly to both higher and lower masses with equality around  $2.3 \times 10^{14} M_\odot$  ( $1.8 \times 10^{14} M_\odot$ ). It can also be seen that the differences between these three temperature measures increases strongly with redshift. At  $z = 0$ , for instance,  $T_m$  and  $T_{sl}$  lie within each other's intrinsic scatters, while by  $z = 1$  they are clearly separated. This means that accounting for these corrections will become even more important when considering distant clusters, which are typically those probed more easily through the SZ signal.

We found in general that our data is well modelled by a three-parameter fit, which corresponds to a quadratic equation in log-log space. In this chapter, this fit is expressed as

$$E(z)^{-2/3} T = A \left( \frac{M}{M_{\text{fid}}} \right)^{B+C \log(M/M_{\text{fid}})} \text{ keV}, \quad (2.1)$$

where  $M_{\text{fid}} = 3 \times 10^{14} h^{-1} M_\odot$ . Hence, a self similar fit around  $M \simeq M_{\text{fid}}$ , would be given by  $B = 2/3$  and  $C = 0$ . By simply examining these fit values,<sup>5</sup> as tabulated in Table 2.4, the differences between the three temperature measures are immediately visible. Here, is also tabulated the scatter about the best fit relation by calculating the root-mean-squared dispersion across the haloes according to

$$\sigma_{\log_{10} T} = \sqrt{\frac{1}{N} \sum_{i=1}^N \left[ \log_{10} \left( \frac{T_i}{T_{\text{fit}}} \right) \right]^2}, \quad (2.2)$$

where  $i$  indexes all the haloes at a given redshift and  $T_{\text{fit}}$  is the value given by the best fit at the mass,  $M_i$ , associated with the halo.

In particular, as previously observed in Figures 2.3 and 2.4,  $T_y$  appears to be systematically higher than  $T_m$ , which itself lies above  $T_{sl}$ . The gradients of these three temperature measures seem to match this same pattern. Finally we note that  $T_y$  always has a positive curvature, while  $T_{sl}$  has a strong negative curvature and  $T_m$  seems to develop mild curvature at higher redshifts. Further, none of

<sup>5</sup>These fits are for the median of the distributions, in Appendix A the fits to the 84 and 16 percentiles of the data set can be found to clarify the cluster-to-cluster spread in temperatures.

**TABLE 2.4:** Best fit values for the medians of each temperature measure at each redshift. The errors are determined through bootstrap methods. The fit parameters correspond to those described in Eq. (2.1).

$M_{500c}$	$A$	$B$	$C$	$\langle \sigma_{\log_{10} T} \rangle$
$z = 0.0$				
$T_y$	$4.763^{+0.015}_{-0.015}$	$0.581^{+0.003}_{-0.002}$	$0.013^{+0.001}_{-0.001}$	$0.2707 \pm 0.0014$
$T_m$	$4.248^{+0.013}_{-0.012}$	$0.565^{+0.003}_{-0.002}$	$0.002^{+0.001}_{-0.001}$	$0.2861 \pm 0.0012$
$T_{sl}$	$4.295^{+0.023}_{-0.025}$	$0.514^{+0.012}_{-0.013}$	$-0.039^{+0.005}_{-0.005}$	$0.323 \pm 0.005$
$z = 0.5$				
$T_y$	$4.353^{+0.019}_{-0.020}$	$0.571^{+0.006}_{-0.006}$	$0.008^{+0.002}_{-0.002}$	$0.2521 \pm 0.0016$
$T_m$	$3.702^{+0.013}_{-0.013}$	$0.546^{+0.005}_{-0.004}$	$-0.006^{+0.002}_{-0.001}$	$0.2523 \pm 0.0019$
$T_{sl}$	$3.474^{+0.027}_{-0.025}$	$0.483^{+0.023}_{-0.028}$	$-0.051^{+0.008}_{-0.010}$	$0.350 \pm 0.007$
$z = 1.0$				
$T_y$	$3.997^{+0.021}_{-0.020}$	$0.593^{+0.004}_{-0.004}$	$0.009^{+0.001}_{-0.001}$	$0.2438 \pm 0.0016$
$T_m$	$3.237^{+0.015}_{-0.017}$	$0.558^{+0.004}_{-0.005}$	$-0.005^{+0.001}_{-0.001}$	$0.2142 \pm 0.0018$
$T_{sl}$	$2.754^{+0.036}_{-0.035}$	$0.478^{+0.015}_{-0.014}$	$-0.053^{+0.004}_{-0.004}$	$0.401 \pm 0.004$

these are consistent with hydrostatic equilibrium scalings, which would have  $B = 2/3$  and  $C = 0$ . While  $T_y$  has the closest gradients to this value for hydrostatic equilibrium, even at the highest cluster masses the curvature is not sufficient for  $T_y$  to match this scaling.

### 2.3.4 Covariance of Fits

It is now instructive to understand the spread of cluster temperatures about the best fits of the temperature measures as displayed in the previous section. Figure 2.5 shows the covariances at  $z = 0$  of the quantity  $\log_{10}(T_{\text{data}}(M)/T_{\text{fit}}(M))$  for each of the three temperature measures. Here  $T_{\text{fit}}(M)$  is the tabulated best-fit value, while  $T_{\text{data}}(M)$  refers to the calculated temperature measure for each cluster. We find that this behaviour is replicated well for  $z = 0.5$  and  $1.0$ .

From the diagonal part, one can immediately see that, while  $T_m$  is almost normally distributed in the log-log space (that is, log-normally), the other two temperature measures have visible skews. This is most apparent for  $T_{sl}$ , which skews to higher temperatures with a long tail to lower temperatures, while the  $y$ -weighted temperature measure seems only gently skewed to lower temperatures – thus being almost log-normally distributed in the log-log space.

Furthermore, from the lower triangle we can see the correlations between the temperature measures within each cluster – in particular the strong interdependency between  $T_y$  and  $T_m$ . This indicates that on a cluster by cluster basis the difference between the  $y$ -weighted and mass-weighted temperatures are maintained. However, the spectroscopic-like temperature seems to be distributed independently of the other two measures.

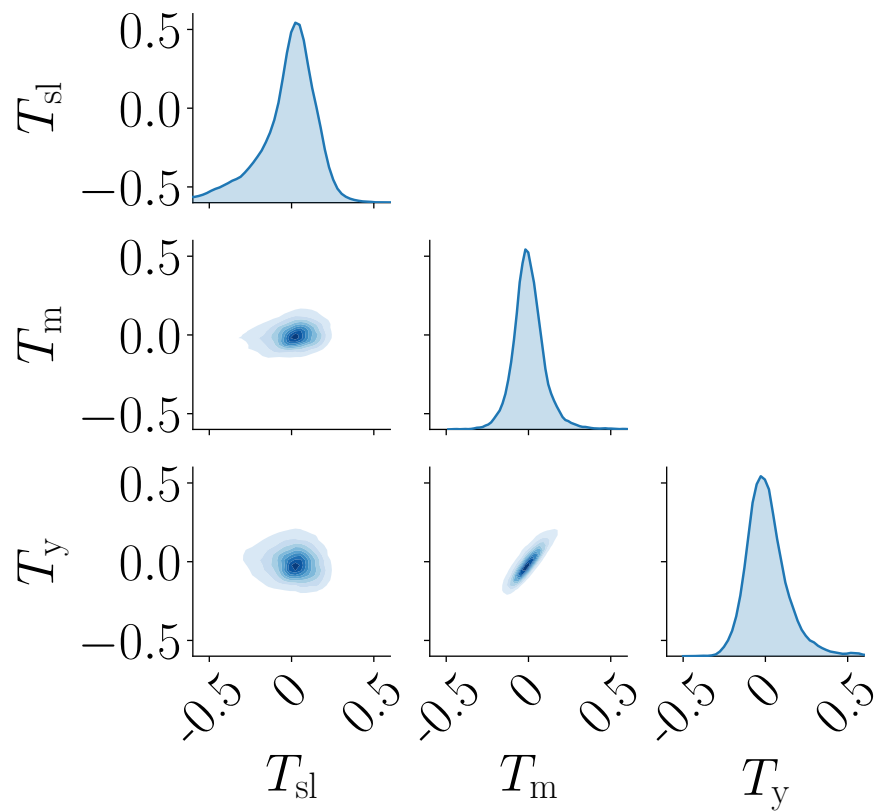


**FIGURE 2.5:** A representation of the covariance of  $\log(T_{\text{data}}(M)/T_{\text{fit}}(M))$  for the three temperature measures at  $z = 0$ . That is, a comparison of the overall distributions around the line of best fit for each temperature measure. The diagonal parts show the overall distributions for each measure, while the lower triangle shows the contours of these covariances.

This strong correlation in the values of  $T_m$  and  $T_y$  motivates the exploration of temperature-temperature scaling relations – and moreover, since these two temperatures define the complete SZ signal, they motivate a volume averaged  $Y-T_y$  scaling relation. This allows for a self calibration of the relativistic corrections to the SZ signal, from measurements of the SZ signal itself.

### 2.3.5 Mass dependence of the quality of the fits

Although Figure 2.5 displays the skewness of the quality of fits as a whole, across all the data, it is instructive to consider how the quality of the fit varies over the mass range of the samples. This can be seen graphically in Figure 2.6, where the contours are plotted for the percentiles associated with what would be the 0.5, 1, 2 and 3 $\sigma$  confidence regions were the data normally distributed against its line-of-best-fit.

The first thing to note is that there is a change over in dataset at  $M_{500c} \simeq 10^{15} M_\odot$ , on the left is the BAHAMAS data and on the right the MACSIS. This is of note simply because the data in the MACSIS set is less dense than that in the BAHAMAS set, and this will contribute to the increased errors we see to the right of the graph – the errors are driven by lack of data as much as by the intrinsic scatter.

Secondly, especially in  $T_y$ , there are some anomalous results at low masses, skewing the 2 and 3 $\sigma$  contours dramatically. In  $T_m$ , the data is in fact roughly normally distributed across the entire mass range, with roughly constant errors – this skew at low masses appears to be the only changing factor. In fact, the 3 $\sigma$  region outside of this skew is, if anything, underrepresented compared to a normal distribution – that is, indicating smaller tails in the distribution than would be expected. This may, however, be simply a limitation in the number of clusters in each mass bin to be considered.

In  $T_y$ , however, this low mass skew is continued strongly in the 2 $\sigma$  region but is still present to an extent across the entire range. This corroborates the long tail seen in the distribution of  $T_y$  in Figure 2.5 – however, it is worth noting that the skew appears to decrease to higher masses. A similar, but opposite, phenomena is seen in the  $T_{sl}$  contours, where we see a persistent and strong skew in the data to lower temperatures. This indicates that although the fits model the median well and, even the 1 $\sigma$  variations, it would be inappropriate to consider this data as normally distributed.

### 2.3.6 Temperature-temperature scaling relations

An alternative to temperature-mass relations are temperature-temperature scaling relations. These lead to a predominantly mass independent conversion between temperature measures. We see that a similar fitting formula (to that in

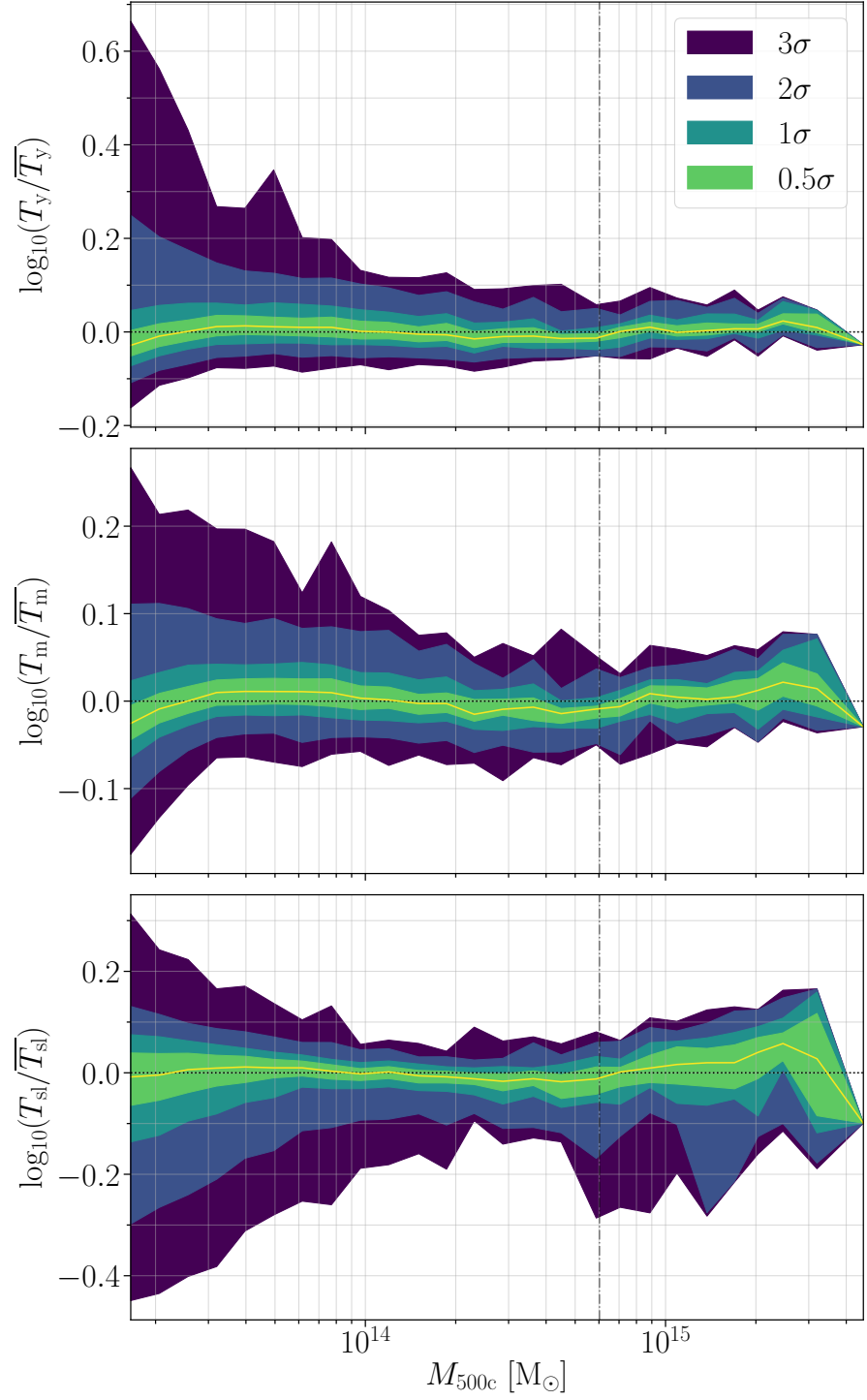


**FIGURE 2.6:** A graphical depiction of the spread of data around the  $T$ - $M_{500c}$  fits at  $z = 0$ . The shaded regions here are the percentile regions associated with the  $\sigma$  values, if the data were spread normally about the mean, that is at the 0.2-99.8, 2.5-97.5, 16-84 and 31-69 percentiles for the 3, 2, 1 and  $0.5\sigma$  regions labelled. The medians of the data are plotted in yellow. The dot-dashed line indicates the cross over from BAHAMAS to MACSIS data.

**TABLE 2.5:** Best-fit values for the medians of each temperature measure against  $T_{500c}$  at each redshift. The errors are determined through bootstrap methods. The fit parameters correspond to those described in Eq. (2.3).

$T_{\text{rel}} = T_{500c}$	$A$	$B$	$C$
$z = 0.0$			
$T_y$	$4.812^{+0.014}_{-0.013}$	$0.889^{+0.003}_{-0.003}$	$0.041^{+0.002}_{-0.002}$
$T_m$	$4.289^{+0.011}_{-0.011}$	$0.873^{+0.004}_{-0.004}$	$0.021^{+0.002}_{-0.002}$
$T_{\text{sl}}$	$4.293^{+0.023}_{-0.022}$	$0.825^{+0.018}_{-0.018}$	$-0.049^{+0.010}_{-0.011}$
$z = 0.5$			
$T_y$	$4.964^{+0.021}_{-0.019}$	$0.868^{+0.006}_{-0.005}$	$0.026^{+0.004}_{-0.003}$
$T_m$	$4.247^{+0.013}_{-0.013}$	$0.835^{+0.005}_{-0.004}$	$-0.006^{+0.003}_{-0.002}$
$T_{\text{sl}}$	$4.039^{+0.021}_{-0.022}$	$0.804^{+0.010}_{-0.011}$	$-0.093^{+0.005}_{-0.006}$
$z = 1.0$			
$T_y$	$5.108^{+0.024}_{-0.024}$	$0.875^{+0.005}_{-0.005}$	$0.020^{+0.003}_{-0.003}$
$T_m$	$4.196^{+0.017}_{-0.016}$	$0.846^{+0.004}_{-0.006}$	$-0.010^{+0.003}_{-0.003}$
$T_{\text{sl}}$	$3.681^{+0.029}_{-0.029}$	$0.807^{+0.015}_{-0.015}$	$-0.118^{+0.009}_{-0.009}$

Eq. (2.1)) can be used, replacing  $M_{\text{fid}}$  with  $T_{\text{fid}} = 5 \text{ keV}$ ,

$$T = A \left( \frac{T_{\text{rel}}}{T_{\text{fid}}} \right)^{B+C \log(T_{\text{rel}}/T_{\text{fid}})} \text{ keV}. \quad (2.3)$$

Since the cluster temperature is often a good mass proxy I will not discuss these fits in much detail here as they take a very similar form to those against the mass, although the full tables fitting the temperature relations with respect to  $T_{\text{rel}} = T_m$  and  $T_\Delta$  can be found in Appendix A. While it is true that, due to the covariance of  $T_y$  and  $T_m$ , the spread in the fits of  $T_y$  against  $T_m$  are smaller than those against  $M_{500c}$ , this effect is minimal.

A shortened selection of the fits against  $T_{500c}$  can be found in Table 2.5. First, it is clear that  $T_y$  is always the closest temperature measure to  $T_{500c}$ , the temperature assuming the cluster is an isothermal sphere (agreeing with Kay et al., 2008). However, there is significant curvature in all of these fits alongside the gradient of the temperature measures being significantly lower than that for  $T_{500c}$ , indicating further that the assumption of isothermality often used in SZ cluster calculations is inaccurate. In fact, while  $T_{500c}$  appears to be an overestimate of  $T_y$  for the most massive clusters, it becomes an underestimate for lower-mass, cooler clusters, particularly at higher redshifts. This is likely due to the increased AGN feedback effects driving gas from these lower-mass systems. This would lead to a decreased  $T_{500c}$  (which is mass dependent) compared to the  $y$ -weighted temperature.

**TABLE 2.6:** Best-fit values for the medians, 84 and 16 percentiles of  $T_y$  to  $Y_{500c}$  at each redshift. The errors are determined through bootstrap methods. The fit parameters correspond to those described in Eq. (2.4).

$T^Y - Y_{500c}$	$A$	$B$	$C$
$z = 0.0$			
median	$4.784^{+0.022}_{-0.019}$	$0.3363^{+0.0026}_{-0.0031}$	$0.0118^{+0.0005}_{-0.0006}$
84	$5.203^{+0.026}_{-0.024}$	$0.3276^{+0.0017}_{-0.0020}$	$0.0120^{+0.0005}_{-0.0005}$
16	$4.415^{+0.047}_{-0.024}$	$0.3438^{+0.0026}_{-0.0030}$	$0.0120^{+0.0007}_{-0.0015}$
$z = 0.5$			
median	$5.370^{+0.020}_{-0.020}$	$0.3358^{+0.0017}_{-0.0010}$	$0.0106^{+0.0003}_{-0.0002}$
84	$5.860^{+0.027}_{-0.028}$	$0.3218^{+0.0015}_{-0.0016}$	$0.0090^{+0.0003}_{-0.0003}$
16	$4.954^{+0.016}_{-0.016}$	$0.3508^{+0.0009}_{-0.0008}$	$0.0128^{+0.0002}_{-0.0002}$
$z = 1.0$			
median	$6.250^{+0.042}_{-0.038}$	$0.3429^{+0.0044}_{-0.0037}$	$0.0090^{+0.0009}_{-0.0007}$
84	$6.656^{+0.053}_{-0.062}$	$0.3329^{+0.0071}_{-0.0058}$	$0.0096^{+0.0015}_{-0.0011}$
16	$5.784^{+0.042}_{-0.040}$	$0.3579^{+0.0051}_{-0.0048}$	$0.0107^{+0.0009}_{-0.0008}$

### 2.3.7 Volume-averaged $Y$ relations

As already noted,  $T_m$  forms a strong proxy for the volume-averaged  $y$ -parameter,  $Y$ . Since this relates to the amplitude of the SZ signal, while the shape is dependent on  $T_y$ , it is instructive to consider the scaling of  $T_y$  with respect to  $Y$ . This gives us a self-calibrated scaling relationship to determine the rSZ signal. We use a fit similar to equations (2.1) and (2.3),

$$T_y = A \left( \frac{Y}{Y_{\text{fid}}} \right)^{B+C \log(Y/Y_{\text{fid}})} \text{ keV}, \quad (2.4)$$

choosing  $Y_{\text{fid}} = 0.00003 \text{ Mpc}^2$ . These results are shown in Table 2.6 – we also tabulate the  $Y$ - $M$  relationship in Appendix A. It is interesting to observe that while these are 3-parameter fits, there is significantly less curvature in all of these fits than is seen in the mass-temperature and temperature-temperature relations. Further, from Eq. (1.40), we recall self similarity,  $T \propto (Y)^{2/5}$ , and in Table 2.6, we note that  $B$  lies close to the expected value  $B = 2/5$ .

While there is no explicit redshift dependence in these fits, there is distinct redshift evolution in the fit parameters; in particular in the normalisation factor,  $A$ , which seems to almost scale  $\propto E(z)^{1/2}$  (similar to, but above, the self-similar prediction), increases dramatically towards higher redshifts. There is a similar but smaller decrease in the gradient to higher redshifts. However, overall this dependence shows that at higher redshifts it becomes increasingly important to consider the relativistic corrections to the SZ signal.

**TABLE 2.7:** Best-fit values for the medians of each temperature measure for the Hot and Relaxed Samples against  $M_{500c}$  at each redshift. The errors are determined through bootstrap methods. The fit parameters correspond to those described in Eq. (2.1), taking  $C = 0$ .

$M_{500c}$	Hot Sample		Relaxed Sample	
	$A$	$B$	$A$	$B$
$z = 0.0$				
$T_y$	$4.693^{+0.028}_{-0.028}$	$0.633^{+0.009}_{-0.010}$	$4.635^{+0.035}_{-0.036}$	$0.626^{+0.010}_{-0.010}$
$T_m$	$4.174^{+0.023}_{-0.025}$	$0.598^{+0.019}_{-0.010}$	$4.147^{+0.033}_{-0.034}$	$0.593^{+0.019}_{-0.013}$
$T_{sl}$	$4.117^{+0.064}_{-0.053}$	$0.531^{+0.043}_{-0.055}$	$4.206^{+0.049}_{-0.051}$	$0.531^{+0.051}_{-0.014}$
$z = 0.5$				
$T_y$	$4.335^{+0.030}_{-0.027}$	$0.597^{+0.017}_{-0.016}$	$4.329^{+0.040}_{-0.034}$	$0.598^{+0.018}_{-0.016}$
$T_m$	$3.677^{+0.018}_{-0.021}$	$0.561^{+0.011}_{-0.011}$	$3.681^{+0.021}_{-0.024}$	$0.561^{+0.011}_{-0.011}$
$T_{sl}$	$3.433^{+0.034}_{-0.033}$	$0.457^{+0.023}_{-0.099}$	$3.445^{+0.036}_{-0.037}$	$0.455^{+0.025}_{-0.098}$
$z = 1.0$				
$T_y$	$3.984^{+0.029}_{-0.030}$	$0.611^{+0.016}_{-0.016}$	$3.974^{+0.035}_{-0.035}$	$0.610^{+0.020}_{-0.018}$
$T_m$	$3.235^{+0.019}_{-0.023}$	$0.586^{+0.008}_{-0.011}$	$3.228^{+0.023}_{-0.024}$	$0.581^{+0.012}_{-0.013}$
$T_{sl}$	$2.745^{+0.036}_{-0.049}$	$0.469^{+0.017}_{-0.037}$	$2.767^{+0.036}_{-0.043}$	$0.473^{+0.017}_{-0.027}$

### 2.3.8 Hot and Relaxed Samples

Finally, it is useful to consider the behaviors of the Hot and Relaxed samples, as defined in Section 2.2.5, for which the median fits of the  $T - M$  relation are found in Table 2.7. There are fits for both the hot and relaxed samples with a simple two-parameter model,<sup>6</sup> or equivalently, we have taken Eq. (2.1), setting  $C = 0$ .

While there are variations in the medians between the Hot and Relaxed samples, we also find that the 16 and 84 percentiles are wider for the Relaxed sample, so that these two samples give fits that lie within each others cluster-to-cluster variance. Further, they agree well with the three-parameter combined-sample fits for both  $T_m$  and  $T_y$ , though the fit can be found to be less appropriate for the spectroscopic-like temperature due to the strong curvature in the  $T_{sl}$  combined-sample fits.

It is also interesting to note that while the larger 68% error region in the Relaxed sample for  $T_y$  and  $T_m$  seems to be well centred over the errors predicted by the complete sample fits, for  $T_{sl}$  these extend to higher temperatures, indicating that Relaxed clusters are more likely to have higher spectroscopic-like temperatures. This can be understood as  $T_{sl}$  is largely driven by the denser central region, and since more spherical (i.e., more relaxed) clusters are more likely to have a larger region for the same given mass, they are likely to lead to higher observed values for  $T_{sl}$ .

<sup>6</sup>Since we ultimately find little difference between these values and those for the whole combined sample, these two-parameter fits allow for comparison with other fits found in previous studies.



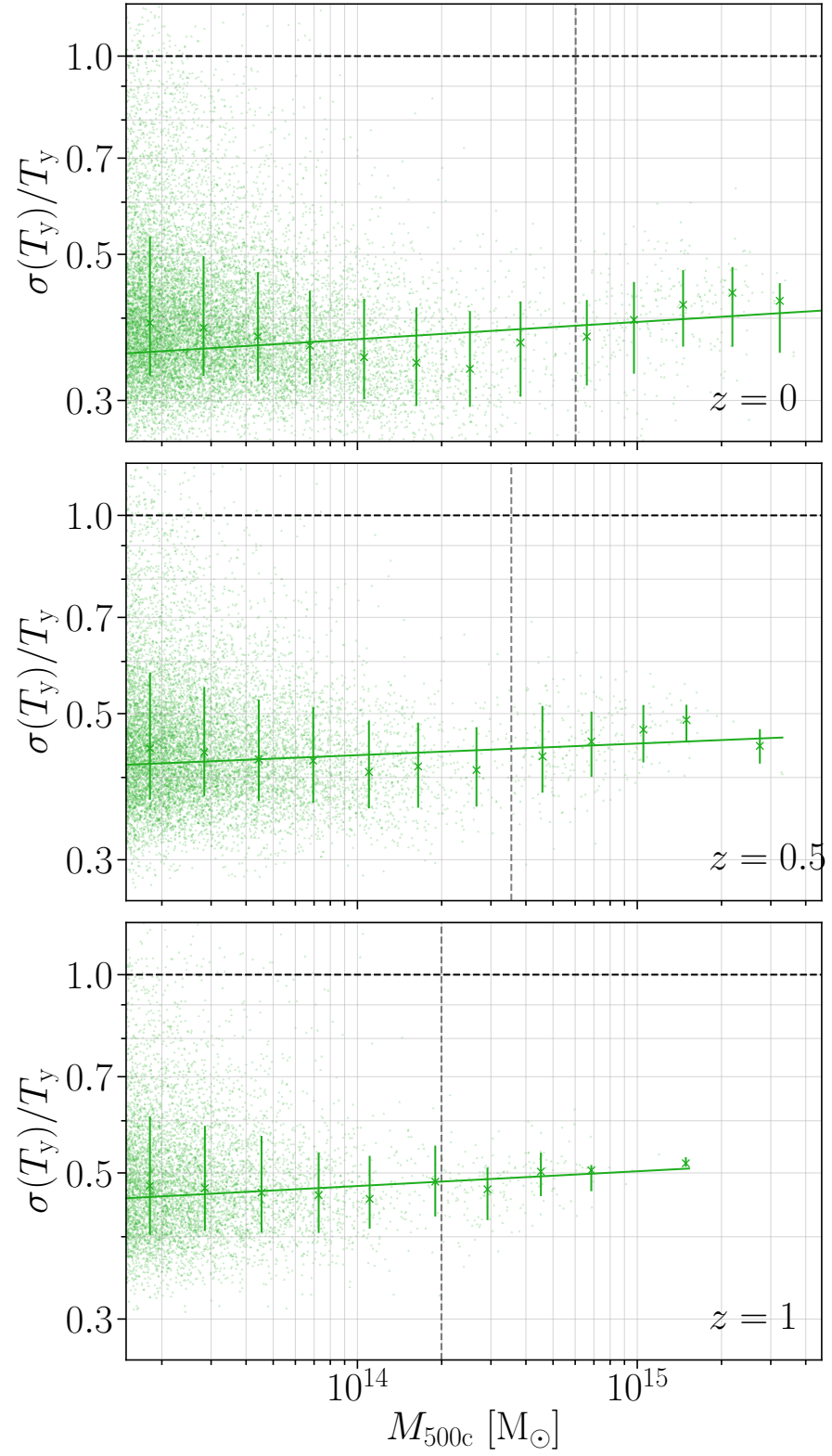


**FIGURE 2.7:** The redshift evolution of  $\sigma(T_y) = \sqrt{T_y^{(2)}}$  with respect to  $T_y$ , as a function of  $M_{500c}$ . The scattered points show the whole dataset, the error bars show the same data binned and the straight line shows the 2 parameter best fit of the data.

### 2.3.9 $y$ -weighted Temperature Dispersion

As noted in Section 1.5, the second moment of the  $y$ -weighted temperature,  $T_y^{(2)}$ , is a measure of the variance of the temperature distribution within the cluster.<sup>7</sup> Here, we discuss  $\sigma(T_y)$ , the standard deviation and its comparison to  $T_y$ . Under a temperature moment expansion about  $T_y$ , the leading-order correction is proportional to  $[\sigma(T_y)]^2 = T_y^{(2)}$ .

Figure 2.7 shows  $\sigma(T_y)/T_y$  and it is evident that, while there is a small variation of the values across the mass range, they are well approximated by a power law (i.e., straight lines in the log-log space) – which are tabulated in Appendix A. Generally, at higher redshifts,  $\sigma(T_y)/T_y$  increases and, at all redshifts, it increases slightly with increased mass, approximately scaling as  $\sigma(T_y)/T_y \simeq 0.39 (1+z)^{0.34} [M_{500c}/M_{\text{fid}}]^{0.022}$ . Since this redshift evolution closely matches the evolution of  $T_y$  with respect to  $T_{500c}$ , it may be that  $\sigma(T_y)$  is mainly dependent on  $T_{500c}$  or equivalently the potential well of the cluster rather than the specifics of the substructure. That is, the variation in  $\sigma(T_y)/T_y$  with redshift with respect to mass, is dominated by the near self-similar redshift evolution of  $T_y$ . It is also possible that there is an effect of clusters thermalising over time, since this would explain the increase in variance for larger clusters and clusters at higher redshifts. However, since there are no clear differences between the dispersion of the relaxed sample and the combined sample there is little evidence either way. In Section 2.4.3, the radial profiles of these values will show that these clusters see almost constant values across the whole width of the clusters, so that the overall dispersion is indicative of the dispersion at each point in the cluster.

Generally the data spread is small, with around  $\simeq 68\%$  of the values for  $\sigma(T_y)$  lying at around 40% of the overall temperature. However, we do see a characteristic small dip in the values of  $\sigma(T_y)$  in the middle of our mass range ( $\simeq 2 - 3 \times 10^{14} M_\odot$  at  $z = 0$ ). One possibility is that as the masses increase from  $\simeq 10^{13} - 10^{14} M_\odot$ , the systems become more resilient to AGN feedback due to the increased potential well. As the masses increase further, the temperature variance is likely to increase again, due to the clusters still thermalising (i.e., they are still forming). The exact details however are not explored in this thesis.

## 2.4 Cluster temperature profiles

This section discusses various cluster temperature profiles. To find analytic averages of the temperature profiles (to discern between each in a quantitative

<sup>7</sup>This is different from the distribution between clusters at each temperature, and as such is a measure of the intrinsic temperature variation within clusters rather than the variation between different clusters.

manner), I use the fits suggested by [Vikhlinin et al. \(2006\)](#)

$$\begin{aligned}
 T_{\text{tot}}(r) &= T_0 t_{\text{cool}}(r) t(r) \\
 t_{\text{cool}}(r) &= \frac{x_{\text{cool}} + T_{\text{min}}/T_0}{x_{\text{cool}} + 1} \\
 t(r) &= \frac{x_t^{-a}}{[1 + x_t^b]^{c/b}}.
 \end{aligned} \tag{2.5}$$

This model has eight fit parameters  $\{T_0, r_{\text{cool}}, a_{\text{cool}}, T_{\text{min}}, r_t, a, b, c\}$ , and requires fitting data within the ‘core-excised region’ to allow the fit to access the central cooler region. It is also necessary to define  $x_t = r/r_t$  and  $x_{\text{cool}} = (r/r_{\text{cool}})^{a_{\text{cool}}}$ .  $t_{\text{cool}}(r)$  accounts for the temperature decline of the central region of most clusters, while  $t(r)$  acts as a broken power law with a transition region, to model the area outside this central region.

There are two methods, I will explore, of generating profiles from the simulations, each intuitive in different respects. From a simulation perspective, it is natural to consider a full radial profile, where the particles are binned in spherical shells from the centre of the cluster, and volume average the particles within each bin. However, from an observational standpoint, it is perhaps more relevant to consider the line-of-sight profiles, which I will here refer to as cylindrical profiles. In the next section, we will discuss these radial profiles, as they are those normally discussed of the literature, first and then briefly examine the cylindrical profiles.

In most observational work, the observed line of sight profiles are deprojected to generate radial profiles, and radial profiles are compared in the literature. However, an examination of the cylindrical profiles shows that care must be taken in this deprojection process, as the different weighting in each temperature measure, lead to complicated variations in the behaviour of the radial and cylindrical profiles.

### 2.4.1 Radial Profiles

To account for any potential mass dependence of the profiles, the clusters are first sorted into 5 mass bins. Three of these are graphically displayed in Figure 2.8. The 5<sup>th</sup> bin (lowest panel of figure) corresponds to the selection of clusters from the MACSIS sample, hence the uneven bin width. A corresponding figure to show the redshift evolution of each temperature profile is found in Figure 2.9. This displays the clusters with  $13.5 \leq \log_{10}(M_{500c}/M_{\odot}) \leq 14$ , but is indicative of the variation of all mass bins. The median fits of all of these quantities can be found in Appendix A.

Firstly, it is evident in Figure 2.8 that  $T_y$  is once again systematically larger than  $T_m$  which is in turn larger than  $T_{s1}$ . Further, this increase appears systematically

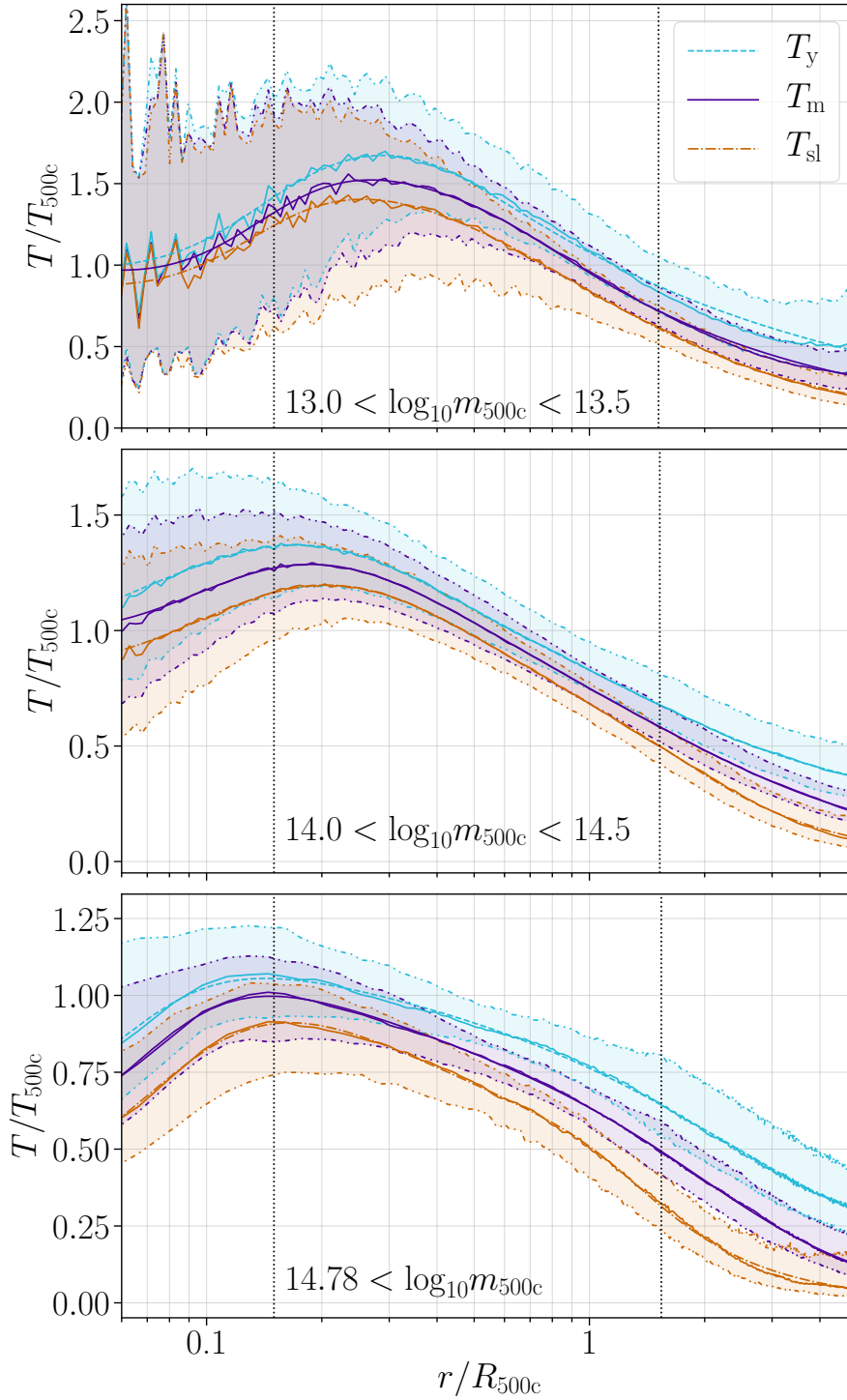


**FIGURE 2.8:** The radial profiles of the three different temperatures across 3 different mass bins – note here  $m_{500} = M_{500c}/M_{\odot}$ . As is standard, the temperatures have all been scaled by  $T_{500c}$  for the same cluster, and the radii have been scaled by  $R_{500c}$ . The vertical dotted lines indicate the core region ( $0.15 R_{500c}$ ) and  $R_{200c}$  respectively. The solid lines show the median values at each radial bin across the clusters and the shaded region the 68% confidence region. The dotted lines show the fits using the Vikhlinin model.

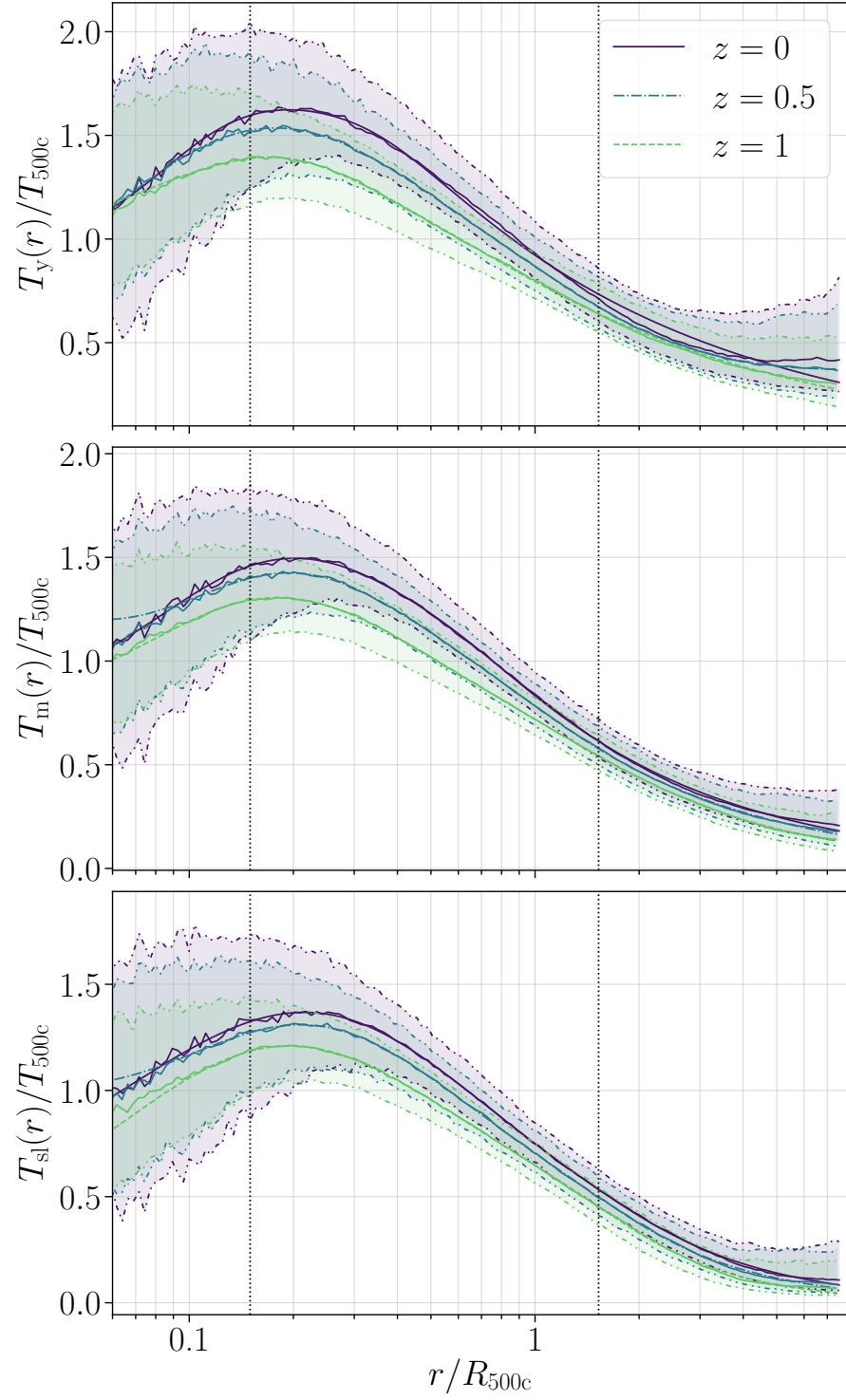


**FIGURE 2.9:** The radial profile evolution across  $z$  for the clusters of masses  $M_{500c} = 13.5 - 14 \times 10^{14} M_{\odot}$  clusters. This is indicative of the evolution of all of the clusters, although the profile fits for the others can be found in Appendix A. This figure is otherwise arranged as in Figure 2.8. Recall also that  $T_{500c}$  is defined to be redshift dependent, so is removing the  $E^{2/3}(z)$  dependence. Note, that these are the same clusters traced over the redshift evolution, so they would appear to have lower masses at higher redshifts.

larger at larger radii. This is in agreement with our previous observations that the  $y$ -weighted temperature is more attuned to the affects of larger radii.

These differences also appear enhanced at higher masses (see also, [Henson et al., 2017](#); [Pearce et al., 2020](#)). For instance, at higher masses  $T_{sl}$  develops a defined downwards turn between  $R_{500c}$  and  $R_{200c}$  where the density falls and thus the contribution to the temperature drops markedly. As the masses increase, the initial peak in the temperature tends to shift to smaller radii; that is that the cooled central region of clusters (which generates the cooling flow) becomes proportionally smaller for higher-mass clusters. This indicates that the highly variable inner regions of the clusters will have a smaller effect on the overall temperatures in higher-mass clusters than smaller.

Considering the redshift evolution as seen in Figure 2.9, all of the temperature measures appear to evolve self-similarly in the outskirts of clusters ( $r \gtrsim R_{500c}$ ) while the interior appears to heat up comparatively from high to low redshift. This indicates that there is some true increase in temperature in the center of clusters not explained by self-similar evolution, as redshift decreases. The differences between the three temperature measures are very small, largely dominated by the overall scaling of the three volume-averaged temperature measures.

### 2.4.2 Cylindrical Profiles

To create these cylindrical profiles, for each cluster the central sphere of radius  $R_{200c}$  was first extracted from the simulation,<sup>8</sup> and then cylindrical shells were sliced from this sphere along six maximally spaced lines of sight through the core of the cluster. These six lines-of-sight cylindrical profiles were then averaged, to reduce the influence of inhomogeneity between the viewing angles in each cluster. One would in general expect the cylindrical profiles to have similar qualities to the radial profiles, albeit smoothed.

This behaviour can be seen in Figure 2.10. Here, once again  $T_y$  lies at systematically higher temperatures than the other temperature measures. Curiously, however, (especially at lower masses)  $T_m$  and  $T_{sl}$  become somewhat indistinguishable. However, at larger radii,  $T_m$  does always rise above  $T_{sl}$  which could lead to the trends in the observed volume averages. This is a result of the associated weightings in each temperature measure.  $T_{sl}$  has a  $n_c^2$  dependence, which in line-of-sight averages will substantially upweight the central hotter regions of the cluster making the overall line of sight appear far greater relative to  $T_m$  than one would naively assume from the radial profiles. It is also interesting to note that core-excision removes a dramatic turn down observed in the  $T_{sl}$  profile for higher-mass clusters, which is not seen as clearly in the other two temperature measures.

---

<sup>8</sup>This causes some lack of precision very close to these edges as the number of particles in each bin becomes small.

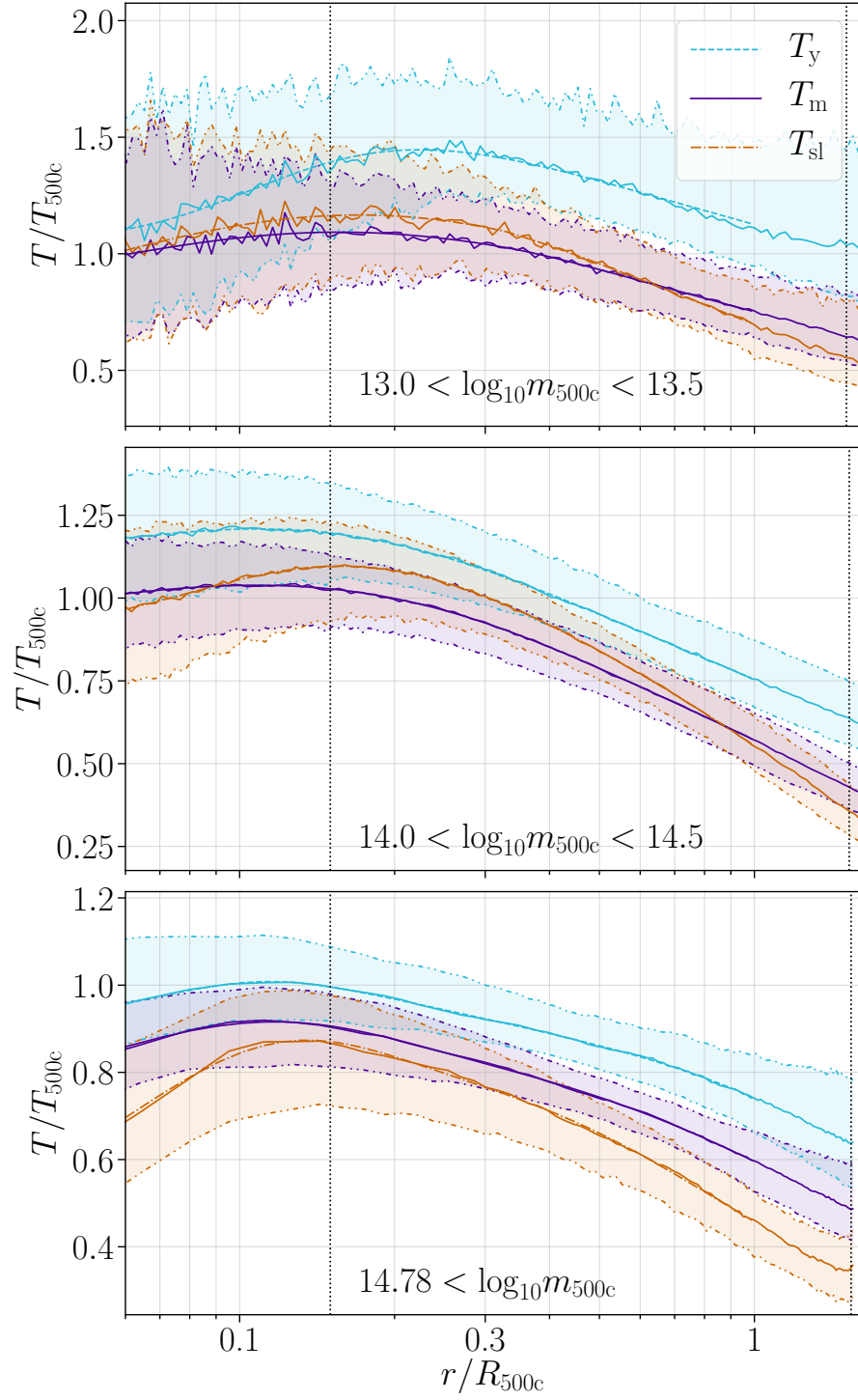


**FIGURE 2.10:** The cylindrical profiles of the three different temperatures across three different mass bins. This figure is arranged as in Figure 2.8.



Under redshift variation, these cylindrical profiles follow almost identical variation to that seen in the radial profiles, so while tabulated in Appendix A, these are not discussed further here. By definition, in these cylindrical profiles we do not have the outer regions of the clusters so it is difficult to compare their behaviours as in the previous section for the radial profiles.

### 2.4.3 Profiles of $y$ -weighted Temperature Moments

We find that the radial and cylindrical profiles for  $\sigma(T_y)$  behave very similarly across all masses and redshifts, in that they are approximately constant with respect to  $T_{500c}$ . This can be seen in Figure 2.11. Here, these are defined, identically to the temperature weightings, as the averaged values over each spherical shell. This approximate mass independence matches what is observed in Figure 2.7 where  $\sigma(T_y)$  is a roughly constant fraction of  $T_y$ . Furthermore, we see that under redshift evolution  $\sigma(T_y)(r)/T_{500c}$  remains roughly constant, suggesting that the variation in  $\sigma(T_y)$  seen in Section 2.3.9 is due to the variation of  $T_y$  against  $T_{500c}$  rather than reflective of an increase in temperature dispersions within clusters at higher redshifts.

However, the values are not entirely constant; at higher masses  $\sigma(T_y)$  rises at higher radii, implying that as the temperatures fall the variation in the temperature increase. This makes sense if we suppose the outskirts of clusters to contain clumpy substructure, leading to cool and hot regions at the same radii – this could also be related to the cluster asphericities causing similar hot and cool effects in the spherically averaged shells. Similarly the variation falls off in the central regions of the clusters, implying that the central region (as modelled in the simulations) are approximately isothermal and thus display little variation.

## 2.5 Implications for Cosmology

In this section, I will discuss the effects these different temperature measures have on determining  $Y_{SZ}$ , and the further effects of the higher-order moments on the determination of the  $y$ -weighted temperature from examining the spectral shape. Finally, I will discuss the effect of these corrections and related ‘corrections’ to the radial profiles and their impacts on the common method to determine  $H_0$  through the SZ effect – this will give an indicative view of the magnitude of the necessary corrections.



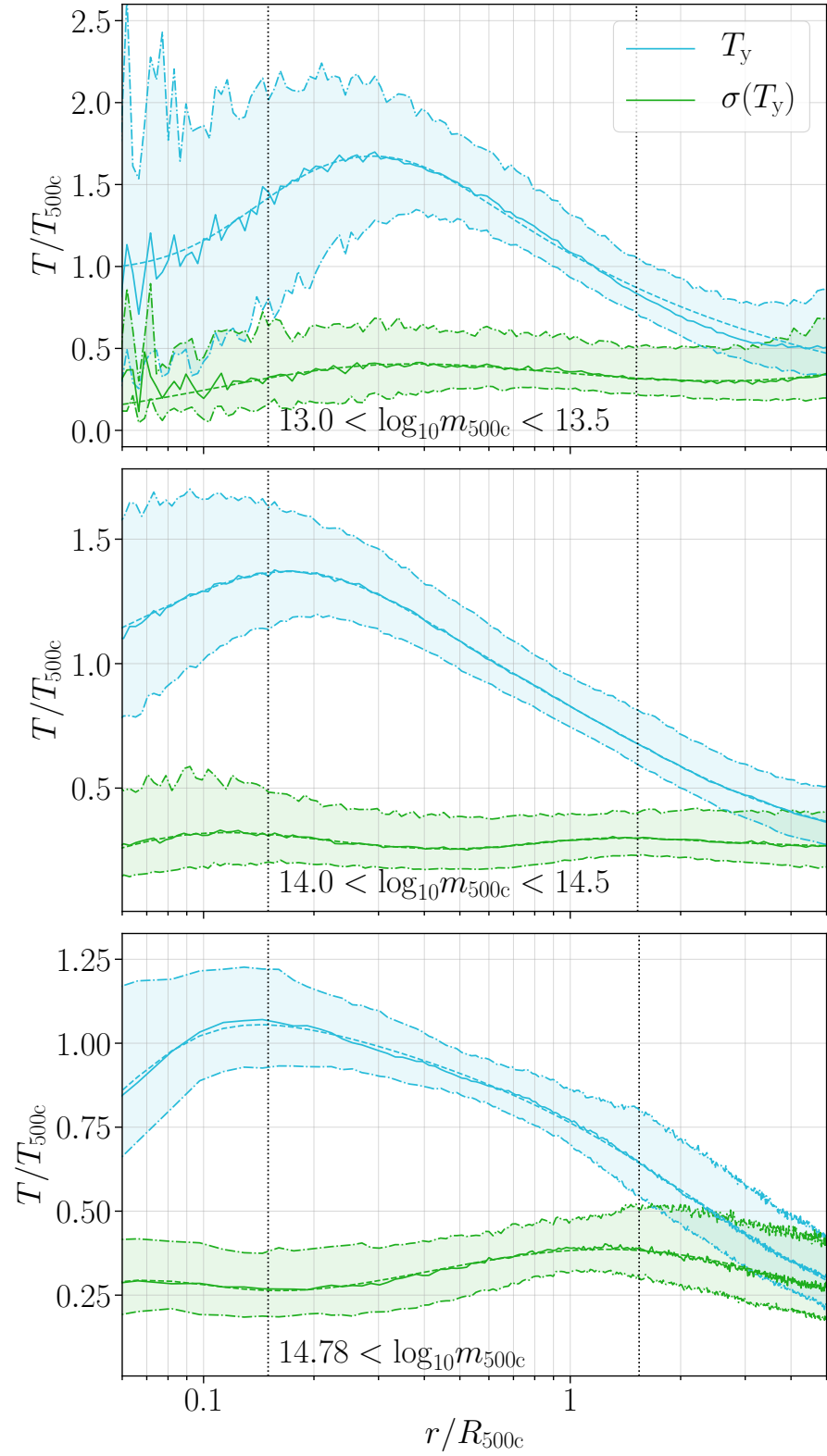


**FIGURE 2.11:** The radial profiles of  $T_y$  and the first moment,  $\sigma(T_y) = \sqrt{T_y^{(2)}}$ . This figure is arranged as in Figure 2.8.

### 2.5.1 Effect on $Y_{\text{SZ}} - M$ relation

First recall that, as mentioned in Section 1.5, to second order in  $\Delta T$  the SZ signal can be expressed as

$$S(\nu) = y f(\nu, T_e) + y^{(1)} f^{(1)}(\nu, T_e) + \frac{1}{2} y^{(2)} f^{(2)}(\nu, T_e). \quad (2.6)$$

By setting the pivot temperature  $T_e = T_y$ , when taking the volume averages one finds that

$$\Delta I \propto Y f(\nu, T_y) + \frac{1}{2} Y^{(2)} f^{(2)}(\nu, T_y). \quad (2.7)$$

Here,  $Y$  is the volume-integrated  $y$ -parameter and  $Y_{T_y}^{(2)} = Y T_y^{(2)} = Y [\sigma(T_y)]^2$  relates to the temperature dispersion. In Remazeilles et al. (2019), it is explained that in the analysis of Planck Collaboration et al. (2016b) it is implicitly assumed that  $f(\nu, T_e) \simeq f(\nu, 0)$ , i.e., a non-relativistic signal. This leads, as already mentioned, to an underestimation of the deduced  $y$ -parameter and also biases the tSZ power spectrum amplitude. Remazeilles et al. (2019) characterise the correction to  $C^{yy}$  (which is  $\propto S^2$ ) showing that for Planck it scales as  $C_\ell^{yy}(T_e)/C_\ell^{yy}(0) \simeq 1 + 0.15[k_B T_e/5 \text{ keV}]$ , where the electron temperature should be the  $y$ -weighted temperature. Hence, the correction to the SZ signal around the maximum at  $\nu \simeq 353 \text{ GHz}$  can be approximated as

$$\frac{f(353 \text{ GHz}, T_e)}{f(353 \text{ GHz}, 0)} \simeq 1 - 0.08 \left[ \frac{k_B T_y}{5 \text{ keV}} \right], \quad (2.8)$$

which can also be seen in Figure 2.12,<sup>9</sup> which shows the observed distortions, expected from our scaling relations given  $T_e = T_y = 0, 5$  and  $10 \text{ keV}$ . In the presence of foregrounds, this was found to give a reasonable estimate for the effect of rSZ on the Planck  $y$ -analysis (Remazeilles et al., 2019).

When folded into the analysis of  $Y_{\text{SZ}}$ , for Planck this leads to a systematic mismatch between the observed relativistic temperature distortions and the magnitude of the integrated pressure from  $Y_{\text{SZ}}$ . This leads to the calculation that:

$$\frac{Y(T_y)}{Y(T_y = 0)} \simeq 1 + 0.08 \left[ \frac{k_B T_y}{5 \text{ keV}} \right]. \quad (2.9)$$

The temperatures here refer to those assumed in the analysis of the spectral shape. This chapter has already established that, for a given mass, the spectroscopic-like temperature underestimates the  $y$ -weighted temperature in a mass-dependent way by  $\gtrsim 9 - 38\%$ . As such, these relativistic corrections lead to even larger errors in the calculations of  $Y_{\text{SZ}}$  than X-ray measurements alone would suggest, especially for hotter clusters or clusters at higher redshifts.

In Remazeilles et al. (2019), a standard X-ray temperature-mass relation was used, indicating  $T_e \simeq 5 - 7 \text{ keV}$  to be a typical cluster temperature relevant to tSZ

<sup>9</sup>A similar figure to Figure 1.4, but included for ease of reference.

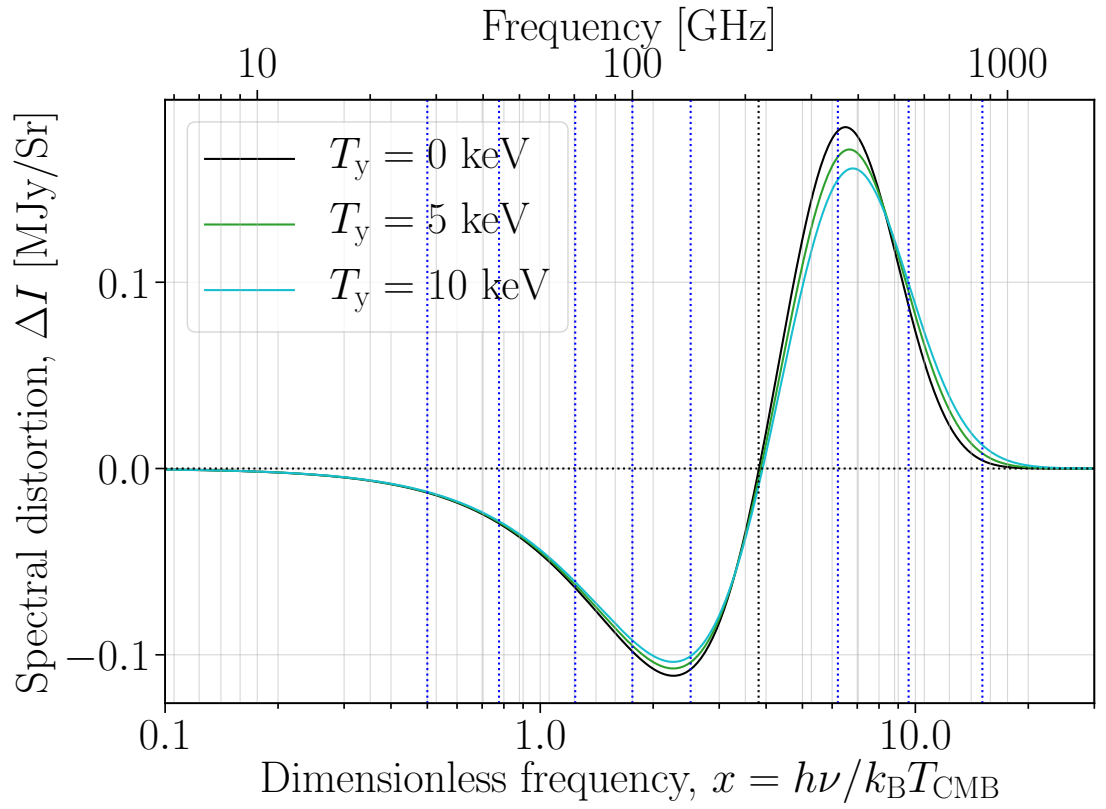


**FIGURE 2.12:** A comparison of the different spectral shapes determined by  $T_e = T_y$  given  $T_y = 0, 5$  or  $10$  keV. The blue vertical lines mark the *Planck* bands, with the black line at  $217$  GHz to show the expected mean of the distribution. These plots were made with SZpack, taking  $y = 10^{-4}$ .

power spectrum measurements. Using the  $T_y - M$  relations, this typical temperature would increase to  $\simeq 6 - 9$  keV, which could further help reduce apparent differences in the deduced hydrostatic mass bias seen in various SZ observables (Remazeilles et al., 2019). For refined estimates our new  $T_y - M_{500c}$  (i.e., the true mass) relations should thus be very useful.

As previously discussed, the  $T_y - Y$  scaling relations can also be considered to fully calibrate the SZ signal within SZ measurements. That is, one could consider the SZ signal explicitly as a function of  $Y$ , by defining  $f(\nu, Y) = f(\nu, T_y(Y))$ , such that  $\Delta I \propto Y f(\nu, Y)$ . This form of self-calibrated scaling allows for an X-ray independent calculation of the relativistically-corrected SZ signal, which could theoretically be confirmed by direct checks of the shape of the signal.

### Comparison to other temperature-mass scaling relations

In Remazeilles et al. (2019), they use a temperature-mass scaling relationship derived from Arnaud et al. (2005) of

$$k_B T_X \simeq 5 \text{ keV} \left( \frac{E(z) M_{500c}}{3 \times 10^{14} h^{-1} M_\odot} \right)^{2/3}. \quad (2.10)$$

Arnaud et al. (2005) used observations of 10 nearby relaxed galaxy clusters with masses ranging between  $(0.8 - 8) \times 10^{14} M_\odot$ . This is a form consistent with the results seen in Barnes et al. (2017a), although the latter extends this work to higher masses, which fit the simulated hydrostatic mass to the simulated observed spectroscopic X-ray temperature using the BAHAMAS and MACSIS simulations. Eq. (2.10) can now be replaced with our  $T_y - M_{500c}$  relation from simulations to avoid conversion issues.

It is commonly known that there is a hydrostatic mass bias between X-ray derived masses and the true total mass of clusters (e.g., Rasia et al., 2006, 2012; Nagai et al., 2007b; Meneghetti et al., 2010; Nelson et al., 2014; Shi et al., 2015; Biffi et al., 2016; Barnes et al., 2017b; Ansarifard et al., 2020) – which can in particular be seen in comparisons of the X-ray and weak lensing derived masses of clusters. Weak Lensing, as a probe of the depth of the gravitational well, gives a closer result to the true mass of clusters than X-ray observations. This underestimate of the hydrostatic model is due to the limitations of the assumption of hydrostatic equilibrium within clusters. In particular, the mass biases calculated to occur from the MACSIS and BAHAMAS simulations have been discussed in e.g., Henson et al. (2017). Generally, this mass bias is considered to be that the observed spectroscopic mass,  $M_{\text{spec}} \simeq (1 - b) M_{\text{total}}$  with  $b \simeq 0.2$ , although in fact, this bias is both mass and redshift dependent (e.g., Henson et al., 2017; Pearce et al., 2020; but see also Ansarifard et al., 2020).

However, the temperature-temperature scalings discussed in Section 2.3.6 will hold entirely independently of the mass measured of a given cluster. As such,

any of these scaling relationships measured to obtain the X-ray temperatures (at high temperatures where  $T_{\text{sl}}$  is an appropriate proxy for the spectroscopic X-ray temperature) can be adjusted by the  $\gtrsim 10 - 40\%$  conversion discussed before between  $T_{\text{sl}}$  and  $T_y$ .

Furthermore, for  $T_y(M)$  we currently can only rely on numerical simulations, as no accurate direct measurements of this variable exist. In computation of the rSZ effect, the scaling relations given in Table 2.4 and 2.6 should thus be most useful and directly applicable in computations of the SZ power spectra, e.g., using C1ass-SZ (Bolliet et al., 2018).

### Corrections from temperature dispersion

While so far the discussion has focused on the leading order rSZ correction, the 2<sup>nd</sup> order correction due to the temperature dispersion is also worth discussing. As previously noted, the volume averaged dispersion is significant, scaling with the cluster temperatures, i.e.,  $\sigma(T_y) \simeq 0.4 T_y$ . However, as I will argue now, at the current level of precision this rSZ correction remains negligible.

Using the asymptotic expansions (e.g., Sazonov & Sunyaev, 1998; Chluba et al., 2012b), the fully relativistic SZ signal at low temperatures can be expressed as:

$$f(\nu, \theta) \simeq \left( Y_0(\nu) + \theta Y_1(\nu) + \theta^2 Y_2(\nu) + \theta^3 Y_3(\nu) + \dots \right), \quad (2.11)$$

where these  $\theta$  are again the dimensionless temperature.<sup>10</sup> This allows us to directly calculate an approximation for the signal associated with the second order corrections,  $f^{(2)}(\nu, \theta) \simeq (2 Y_2(\nu) + 6 \theta Y_3(\nu) + \dots)$ . As such the full signal can be expressed, with second order corrections as,

$$S(\nu) \simeq y \left( Y_0(\nu) + \theta Y_1(\nu) + \theta^2 \left( 1 + \left[ \frac{\sigma(T_y)}{T_y} \right]^2 \right) Y_2(\nu) + \dots \right). \quad (2.12)$$

Now,  $Y_2(\nu)$  has an effect on broadening the SZ signal and pushing it to slightly higher frequencies – a full explanation of the functions can be found in Chluba et al. (2012b). In particular, at 343 GHz (the frequency most applicable for determining the SZ signal magnitude in *Planck*),  $Y_2(343 \text{ GHz})/Y_0(343 \text{ GHz}) \simeq 70$ . Assuming a cluster temperature of 5 keV, one has  $\theta \simeq 0.01$  and with  $\sigma(T_y)/T_y \equiv 0.4$  we find a  $\simeq 70 \times (0.01)^2 \times (0.4)^2 \simeq 0.1\%$  correction to the overall SZ signal stemming from the average intracluster temperature-dispersion.

It is worth noting that since the radial  $\sigma(T_y)$  is constant even as the temperature changes (see Figure 2.11), this correction accordingly will be larger proportionally near the outskirts of clusters. However, these outskirts also correspond to lower temperatures – which would both make the signal itself harder to detect, but also damp further the corrections from the temperature dispersion.

<sup>10</sup>In the range of interest, i.e., temperatures 1 keV – 10 keV,  $\theta$  assumes values  $\simeq 2 \times 10^{-3} - 2 \times 10^{-2}$ .

More work must be done to see how different feedback models affect these values of  $\sigma(T_y)$  – and thus to see if there is any possibility of them giving detectable results. The intercluster temperature variations, relating to the shape of the mass-function, should also be carefully considered.

### 2.5.2 Applications to the determination of $H_0$

It has long been established that  $H_0$  can be determined through a combination of X-ray and SZ measurements (e.g., Birkinshaw, 1979; Jones et al., 2005; Reese, 2004; Bonamente et al., 2006; Kozmany et al., 2019). While these are generally less precise than those calculations from the CMB (e.g., Planck Collaboration et al., 2020b) or direct measurements (e.g., Riess et al., 2019), as the systematics in the approach are being accounted for, they are becoming both increasingly competitive and complementary.

The general approach for this is as follows (see also Bourdin et al., 2017; Kozmany et al., 2019). From the X-ray data, the density and temperature profiles can be constrained (i.e.,  $n_e(r)$  and  $T_{sl}(r)$ ), and from the SZ data the pressure profile,  $P_e(r)$  can be constrained through the measurements of  $y$  assuming the distortion is wholly non-relativistic. This allows for a second temperature profile to be calculated,  $T_m(r) = \eta_T P_e(r) / n_e(r)$ . By assuming these two temperature profiles are equal, i.e.,  $T_m(r) \equiv T_{sl}(r)$ , this allows for a measurement of  $\eta_T$ , which can be found to depend on (among other variables) the angular diameter distance,  $d_A$ . As such,  $\eta_T \propto d_A^{-1/2} \propto H_0^{1/2}$ , which provides a way to obtain  $H_0$  estimates.

Now, in this consideration, there are already two relevant issues, the first is the estimation of the  $P_e$  which, as discussed before, will be underestimated due to the omission of relativistic effects (exactly as in Eq. (2.9)). The second is the concordance of  $T_{sl}(r)$  and  $T_m(r)$ , which, as can be seen in Figure 2.8, is not an accurate assumption. If  $T_m(r) > T_{sl}(r)$ , this method leads to an underestimation of the temperature. As such, these two corrections counteract one another, and it must be determined which one is dominant. The two temperature profiles furthermore have slightly different shapes, which will additionally bias the derived value for the  $H_0$  parameter. However, I do not go into more detail here. Overall, the correction due to rSZ can be expressed as,

$$\frac{H_{0, \text{corr}}}{H_0} \simeq \left[ \frac{P_0}{P_{\text{corr}}} \right] \left[ \frac{T_m}{T_{sl}} \right], \quad (2.13)$$

where  $P_0$  is the pressure calculated assuming there are no relativistic corrections. For instance, to estimate the effect, at  $T_y = 5$  keV, we have already determined that  $P_{\text{corr}} \simeq 1.08 P_0$ . The previous temperature fits can be used to estimate the mismatch in the  $T_m(r)$  and  $T_{sl}(r)$  profiles. Since  $T_y = 5$  keV corresponds to a mass  $M_{500c} \simeq 5.0 \times 10^{14} M_\odot$ , here this temperature correction is  $T_{sl}(r) \simeq 0.92 T_m(r)$ .

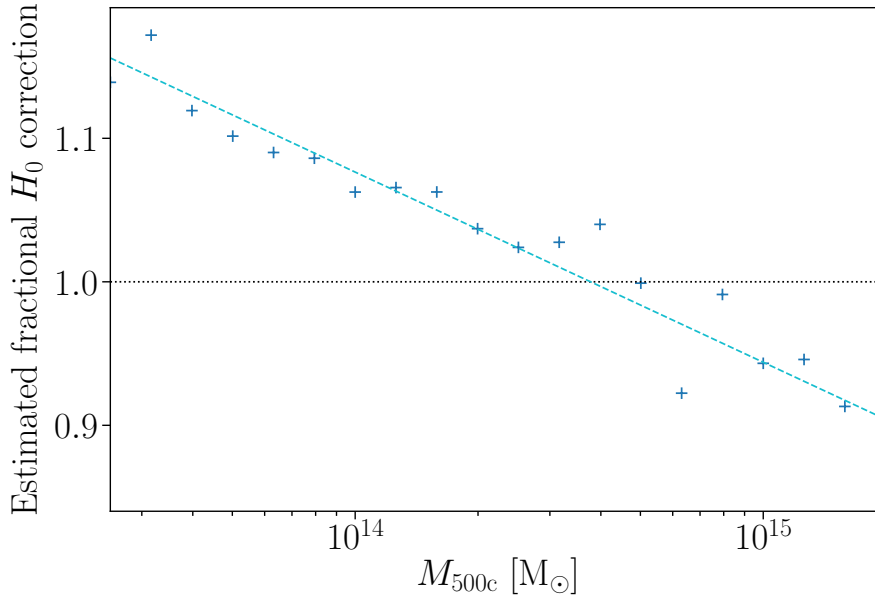


**FIGURE 2.13:** An indicative plot of the potential fractional corrections to  $H_0$ . The dashed line is merely to guide the eye. It should be noted that this is not a full or complete accounting of the corrections, merely a indication of the necessity of carrying out these two opposing corrections. These corrections are measured as  $H_{0,\text{corr}}/H_{0,0}$ . Note: No errors are quoted as a true representation of the errors would require an in-depth study of the various interlocking factors.

In this specific case, the two corrections match well and cancel each other, but generally that will not hold.

Figure 2.13 shows an indicative correction over mass. While this is not a full or complete accounting of the rSZ corrections, this exercise indicates that these corrections have the potential to swing by  $\approx 10\%$  in either direction, tending to higher values of  $H_0$  for lower masses and smaller values for higher masses. In, for instance, [Kozmany et al. \(2019\)](#) the median of the observed sample of clusters lies at  $M_{500c} = 7.3 \times 10^{14} M_\odot$ , which would indicate a potential overestimation of  $\approx 4\%$  (i.e., naively shifting the derived value of  $H_0$  to  $\approx 64 \pm 3$ ). This indicates a potentially sizeable correction in the deduced values of  $H_0$ ; however, it is not clear which way this correction will ultimately fall, and a more careful analysis of the effect should be undertaken, in particular focusing on the assessment of the error budget.

At lower masses, the profiles of the spectroscopic-like temperature will dominate this effect – which, below masses of  $\approx 2.8 \times 10^{14} M_\odot$  is no longer a good probe of the observed X-ray signal. Furthermore, these calculations are all at  $z = 0$ , while at higher redshifts  $E(z)^{-2/3} T_y$  will remain almost constant with mass and the higher-order corrections may increase; however, the behaviours of the profiles are harder to predict. The exact details of this correction should be studied more carefully, including an in-depth comparison of the different radial profiles from  $T_m$  and  $T_{sl}$ .

## 2.6 Conclusions

The importance of rSZ corrections is increasing with growing sensitivity of future CMB experiments. To incorporate the expected effects on SZ observables reliable temperature-mass scaling relations and temperature profiles are required. This chapter covers a large extension to the works of [Pointecouteau et al. \(1998\)](#); [Hansen \(2004\)](#); [Kay et al. \(2008\)](#) to classify, in detail, the three temperature measure  $T_{\text{sl}}$ ,  $T_{\text{m}}$  and  $T_{\text{y}}$  across the mass ranges allowed through the combined BAHAMAS and MACSIS simulations. Differences of  $\simeq 10 - 40\%$  are found between the three temperature measures, with a general trend that  $T_{\text{sl}} < T_{\text{m}} < T_{\text{y}}$ . The differences increase to both higher redshifts, and when the temperature measures are determined over  $R_{200\text{c}}$ , as opposed to the more commonly (and less applicable for SZ measurements) used radius,  $R_{500\text{c}}$  (i.e., Figures 2.4 and 2.3).  $T_{\text{y}}$  scales almost self-similarly, i.e.,  $\propto E(z)^{2/3}$ , out to  $z = 1$ , while  $T_{\text{sl}}$  and  $T_{\text{m}}$  both undergo significant evolution relative to this ‘expected’ scaling. Hence, for higher mass clusters, and clusters at higher redshifts (e.g., those detected in *Planck*),  $T_{\text{sl}}$  is an increasingly poor proxy for  $T_{\text{y}}$ , or equivalently, the rSZ signal will be larger than X-ray measurements would imply. The analysis also suggests that the  $y$ -weighted temperature is a better proxy for cluster mass, a possibility that could be used for self-calibration of cluster masses using rSZ measurements.

A strong correlation was found between  $T_{\text{y}}$  and  $T_{\text{m}}$ , with  $T_{\text{y}} \gtrsim 1.1 T_{\text{m}}$  at  $z = 0$ . While this correction is more complex for  $T_{\text{sl}}$ , we nonetheless find that  $T_{\text{y}} \gtrsim 1.09 T_{\text{sl}}$  at  $z = 0$ , with similarity around  $M_{500\text{c}} \sim 2.3 \times 10^{14} M_{\odot}$  ( $T_{\text{sl}} \simeq 3.0$  keV) and these values diverging increasingly to both higher and lower masses, or equivalently temperatures (see Figure 2.4). Moreover, these corrections are found to depend very little of the nature of the cluster, i.e., whether they are relaxed or not. This strong correlation leads to tight scaling relations between  $Y$ , the volume averaged Compton- $y$  parameter, and  $T_{\text{y}}$  (see Eq. (2.4)). This relationship can be used to calibrate the relativistic corrections to the SZ signal, from the signal itself. This allows for an estimate of the rSZ signal in, for instance, the *Planck* SZ whole sky maps and in computations of the SZ power spectra, e.g., using CLASS-SZ ([Bolliet et al., 2018](#)).

On average the findings suggest that X-ray-derived temperatures underestimate the level of the rSZ by  $\simeq 10 - 40\%$ . For instance, one can estimate a correction for the averaged temperature of clusters in the *Planck* maps calculated in [Hurier \(2016\)](#); [Remazeilles et al. \(2019\)](#). These papers determined them to be  $T_{\text{X}} = 6.8$  keV or  $T_{\text{X}} \gtrsim 5$  keV respectively, which would naively lead to  $T_{\text{y}} = 8.4$  keV or  $T_{\text{y}} \gtrsim 5.7$  keV, a correction  $\gtrsim 15\%$  in both cases. These differences will also affect the expected value for the sky-averaged SZ contribution, as calculated in, e.g., [Hill et al. \(2015\)](#). There a X-ray temperature-mass scaling relation was used to determine the size of the relativistic corrections, finding a value of  $kT_{\text{e}} \simeq 1.3$  keV.



This value could increase if a  $T_y - M$  relation is used. Given that in particular low-mass haloes ( $M \lesssim 10^{13} M_\odot$ ) contribute to the average SZ signal, the differences in this prediction are further amplified by redshift-evolution, likely leading to another increase of the expected value, although they may be mediated by the true spectroscopic-temperature in such regimes being poorly modelled by the spectroscopic-like temperature. Measurements of the sky-averaged rSZ effect with future CMB spectrometers (Kogut et al., 2019; Chluba et al., 2021) could lead to interesting constraints to feedback models and thus deserves more attention.

The profiles of these three radial temperature measures show similar trends (see Figure 2.8). These differences will be very important when interpreting and combining future X-ray and high-resolution SZ profile measurements (e.g., Ameglio et al., 2009; Morandi et al., 2013). From these projected profiles, it will also be possible (see Remazeilles et al., 2019) to calculate a corrected power spectrum for the tSZ effect, which could play a role in reducing the tension between  $\sigma_8$  found with *Planck* and the SZ measurements. An understanding of the differences between the three profiles could also be useful for quantifying conversions between the observed X-ray and SZ signals – in particular an understanding of the different behaviour of  $T_{\text{sl}}(r)$  and  $T_{\text{m}}(r)$ , which are commonly taken to be identical. These differences can lead to various miscalculations where these are used interchangeably, for instance in the SZ-derived  $H_0$  as discussed in Section 2.5.2.

The intracluster temperature dispersion is found to be almost mass independent (at around  $\sigma(T_y) \simeq 0.4 T_y$ , see Figure 2.7), but increases slightly toward higher redshifts as a result of cluster evolution. However, this adds little modification  $\lesssim 0.5\%$  to the SZ signal. Larger effects due to temperature dispersion could arise from intercluster temperature variation, which directly relate to the shape of the halo mass function; however, an estimation of this correction is beyond the scope of this thesis.

While a classification of all three temperature measures and the  $y$ -weighted temperature dispersion has been presented, further work must be done to establish the independence of these results from the simulations (i.e., BAHAMAS and MACSIS) used. Through comparisons to other simulations it will be possible to assess the robustness of these results with respect to feedback models and other aspects of the gas physics used to generate these clusters. In particular, it would be interesting to understand how variations of the microphysics between simulations may lead to differences in the calculated intracluster temperature dispersion,  $\sigma(T_y)$  and  $T_y - Y$  or  $T_y - M$  relations. All these could potentially be used to learn about the dynamical state of the cluster. This will be the focus of Chapter 3.

Extracting the rSZ signals with future CMB experiments still presents a challenge (Basu et al., 2019; Chluba et al., 2021). However, there is work to be done

to establish the utility of rSZ quantities across a variety of cluster models and simulations. Further, the significant temperature differences from using the more appropriate temperature measures ( $T_y$  rather than the X-ray temperature), compounded with corrections from the temperature dispersion effects (and higher-order terms to be considered in future works), will lead to improvements in the ability to interpret the rSZ signal.

## Chapter 3

# A multi-simulation study of relativistic SZ temperature scalings in galaxy clusters and groups

This chapter is based on the published work, [Lee et al. \(2022b\)](#). The code used for BAHAMAS and MACSIS was modified from code written by David J. Barnes. The data from MAGNETICUM PATHFINDER was generated by Priyanka Singh, and Dhayaa Anbajagane generated the data from ILLUSTRISTNG and THE THREE HUNDRED PROJECT. The analysis was largely done by EL, with input and interpretation from the coauthors. The BAHAMAS and MACSIS simulations were again used under the kind permission of Ian McCarthy.

### 3.1 Introduction

Modern hydrodynamical cosmological simulations have become an indispensable tool for understanding the ICM structures and evolution and their impact on SZ observables (e.g., [Nagai, 2006](#); [Nagai et al., 2007b](#); [Battaglia et al., 2012a](#); [Kay et al., 2012](#); [Pike et al., 2014](#); [Yu et al., 2015](#); [Planelles et al., 2017](#); [Le Brun et al., 2017](#); [Henden et al., 2018, 2019](#); [Pop et al., 2022a,b](#)). However, these simulations are also known to exhibit significant variations among different hydrodynamic codes ([Rasia et al., 2014](#); [Sembolini et al., 2016](#)), which gives rise to differences in a variety of cluster observables, such as the hydrostatic mass derived from X-ray mocks ([Rasia et al., 2006](#); [Nagai et al., 2007a](#)). It is therefore important to develop complementary approaches for measuring the ICM temperature based on SZ-effect observations. The rSZ effect with upcoming SZ observations promises to provide insights into the thermodynamic structure and evolution ([Lee et al., 2020](#)).

As discussed in Section 1.5 and Chapter 2, the temperature used in cluster analysis depends on the context in which they are applied. While simulations

encompass many variations, it is exciting to explore what can be learnt from common behaviour between simulations. In particular, we find the SZ temperatures demonstrate a consistency between simulations, allowing for predictions of the rSZ corrections that can be detected observationally, in addition to determining what observations may tell us about the underlying physics.

In this chapter, I study four samples of clusters and groups extracted from different hydrodynamical cosmological simulations – BAHAMAS (McCarthy et al., 2017, 2018); MACSIS (Barnes et al., 2017a); THE THREE HUNDRED PROJECT (Cui et al., 2018); MAGNETICUM PATHFINDER (Hirschmann et al., 2014; Bocquet et al., 2016); and ILLUSTRISTNG (Springel et al., 2018; Pillepich et al., 2018b; Nelson et al., 2018; Marinacci et al., 2018; Naiman et al., 2018). These simulations provide large samples of groups and clusters over five redshifts between  $z = 0$  to  $z = 1.5$ . In each simulation, the three different temperature measures are studied, corresponding to those in the previous chapter: the spectroscopic-like temperature (Mazzotta et al., 2004); the mass-weighted temperature, which is closely related to the Compton- $y$  parameter; and finally the  $y$ -weighted temperature, which is a close approximation for the averaged rSZ temperature, needed to account for the rSZ corrections (Hansen, 2004; Remazeilles & Chluba, 2020).

This chapter is an extension to a growing body of literature that uses ensembles of the latest hydrodynamical simulations to estimate theoretical uncertainties in cluster scaling relations. These uncertainties arise from our lack of knowledge of the true astrophysical mechanisms at play in our Universe. Either some, or all, of the simulations we use in this work have been used previously to marginalize over astrophysics models and estimate scaling relation uncertainties for different cluster properties, such as the thermal gas pressure (Lim et al., 2021), the central and satellite galaxy stellar properties (Anbajagane et al., 2020), and the dark matter and satellite galaxy velocity dispersions (Anbajagane et al., 2022a). Here, we extend the discussion to the modeling of the rSZ effect.

## 3.2 Simulations

This chapter uses four samples of haloes from the following simulations: (i) a subset of BAHAMAS and MACSIS, (ii) THE THREE HUNDRED PROJECT, (iii) MAGNETICUM PATHFINDER, and (iv) ILLUSTRISTNG. A summary of the cosmological properties of each simulation can be found in Table 3.3 and the simulation parameters in Table 3.1.

We take haloes within each simulation with  $M_{500c} > 10^{13} M_{\odot}$ <sup>1</sup> and consider the redshifts  $z \approx \{0.0, 0.25, 0.5, 1.0, 1.5\}$ . The population counts at each redshift can be found in Table 3.2. In each simulation, our properties are again calculated using a temperature cut – that is, only considering particles with temperatures,

<sup>1</sup>Note that here this is in  $M_{\odot}$ , while in the previous chapter I used  $M_{\odot}/h$ , as such this chapter's analysis goes to lower halo masses.

Simulation	$L$ [Mpc]	$N$	$\epsilon_{\text{DM}}^{z=0}$ [kpc]	$m_{\text{DM}}$ [ $M_{\odot}$ ]	$m_{\text{gas}}$ [ $M_{\odot}$ ]	Calibration
BAHAMAS	596	$2 \times 10^{24.3}$	5.96	$6.7 \times 10^9$	$1.2 \times 10^9$	GSMF, CL $f_{\text{gas}}$
MACSIS	—	—	5.90	$6.5 \times 10^9$	$1.2 \times 10^9$	GSMF, CL $f_{\text{gas}}$
THE300	—	—	9.6	$1.9 \times 10^9$	$3.5 \times 10^8$	See Cui et al. (2018)
MAGNETICUM	500	$2 \times 1584^3$	5.33	$9.8 \times 10^8$	$2.0 \times 10^8$	SMBH, Metals, CL $f_{\text{gas}}$
TNG	303	$2 \times 2500^3$	1.48	$5.9 \times 10^7$	$1.1 \times 10^7$	See Pillepich et al. (2018a)

**TABLE 3.1:** Simulation characteristics for each sample. Table adapted from Anbajagane et al. (2022a, Table 1). From left to right, we show: (i) simulation, (ii) comoving box size, (iii) the total particle count, (iv) force softening scale, (v) mass of DM particles, (vi) mass of gas particles and (vii) empirical sources used for tuning sub-grid parameters of each simulation, which consist of the Galaxy Stellar Mass Function (GSMF), Supermassive Black Hole scaling (SMBH), Metallicity scaling (Metals), and cluster hot-gas mass fraction  $< R_{500c}$  (CL  $f_{\text{gas}}$ ). We do not quote the box sizes or particle numbers for MACSIS and THE300 as they are zoom-in simulations.

Nominal redshift	$z = 0.00$		$z = 0.25$		$z = 0.50$		$z = 1.00$		$z = 1.50$	
	$z_{\text{sim}}$	$N_{\text{haloes}}$	$z_{\text{sim}}$	$N_{\text{haloes}}$	$z_{\text{sim}}$	$N_{\text{haloes}}$	$z_{\text{sim}}$	$N_{\text{haloes}}$	$z_{\text{sim}}$	$N_{\text{haloes}}$
BAHAMAS+MACSIS	0.00	21361	0.25/0.24	19610	0.50/0.46	17016	1.00	10928	1.50/1.56	5750
THE300	0.00	8465	0.25	8433	0.49	8300	0.99	7349	1.48	5627
MAGNETICUM	0.066	10429	0.25	9812	0.52	8265	0.96	5659	1.47	3080
TNG	0.00	2548	0.24	2333	0.50	2015	1.00	1290	1.50	700

**TABLE 3.2:** The number of haloes with  $M_{500c} > 10^{13} M_{\odot}$  within each simulation, at each considered redshift. The nominal redshift is how we will refer to each sample, while  $z_{\text{sim}}$  indicates the ‘true’ simulation redshift used. For the BAHAMAS+MACSIS sample, where the redshifts are recorded as ‘x/y’, the first number refers to  $z_{\text{sim}}$  in the BAHAMAS simulation, while the second is that in the MACSIS simulation.

**TABLE 3.3:** Cosmological parameters used in each of the simulations.

Simulation	$\Omega_\Lambda$	$\Omega_m$	$\Omega_b$	$\sigma_8$	$n_s$	$h^\dagger$
BAHAMAS	0.6825	0.3175	0.0490	0.8340	0.9624	0.6711
MACSIS	0.6930	0.3070	0.0482	0.8288	0.9611	0.6777
THE300	0.6930	0.3070	0.0480	0.8230	0.9600	0.6780
MAGNETICUM	0.7280	0.2720	0.0457	0.8090	0.9630	0.7040
TNG	0.6911	0.3089	0.0486	0.8159	0.9667	0.6774

$^\dagger$  where  $h \equiv H_0/(100 \text{ km s}^{-1} \text{ Mpc}^{-1})$

$T \geq 10^{5.2} \text{ K}$  ( $\approx 0.014 \text{ keV}$ ). Moreover, when calculating the *spectroscopic-like* temperature, a core-excision procedure is again used, as it has been shown to make X-rays a better proxy for mass (e.g., [Pratt et al., 2009](#)), and as such exclude all particles with  $r < 0.15 R_{500c}$ . In Section 3.4.4, we will show that using a relaxed subsample does not seem to meaningfully change our results at  $z = 0$ , so is only minimally examined here as it was examined in more detail for the case of BAHAMAS and MACSIS in the previous chapter.

### 3.2.1 Bahamas and Macsis

As in Chapter 2, we use a supersample of BAHAMAS ([McCarthy et al., 2017, 2018](#)) and its zoom-in counterpart MACSIS ([Barnes et al., 2017a](#)), which we will here refer to as BAHAMAS+MACSIS, or in figures simply BAHAMAS+. BAHAMAS is a calibrated version of the model used in the cosmo-OWLS simulations ([Le Brun et al., 2014](#)). Both BAHAMAS and MACSIS were run using a version of the smoothed particle hydrodynamics (SPH) code GADGET-3 last publicly discussed in [Springel \(2005\)](#), but modified as part of the OWLS Project ([Schaye et al., 2010](#)). The MACSIS simulation was developed to extend the BAHAMAS sample to higher-mass haloes. It is a sample of 390 clusters, generated through a zoomed simulation from a large Dark Matter only (DMO) simulation – a periodic cube with a side length of 3.2 Gpc. Individual separate volumes including high Friends-of-Friends (FoF) mass (clusters with  $M_{\text{FoF}} > 10^{15} M_\odot$ ) were then re-simulated with a full hydrodynamical prescription aligned with the BAHAMAS simulation. Haloes within the two simulations are then identified by a FoF algorithm, and subhaloes with the SUBFIND algorithm ([Springel et al., 2001](#); [Dolag et al., 2009](#)).

To form this supersample, all the haloes with the relevant masses from both simulations are used. The differences between cosmologies are deemed to have minimal effects in general, however, when considering the redshift variation,  $E(z)$  is calculated with the relevant cosmology for MACSIS and BAHAMAS separately. It is also worth noting, that unlike THE THREE HUNDRED PROJECT, MACSIS only provides 390 massive clusters, and no additional lower-mass clusters.

### 3.2.2 The Three Hundred Project

THE THREE HUNDRED PROJECT, here THE300, (Cui et al., 2018) comprises of massive haloes formed within 324 spherical regions each of 22 Mpc radius and each centred on the most massive clusters at redshift zero as identified in the MULTIDARK PLANCK 2 N-body, DMO simulation (Klypin et al., 2016), which has a cube of side length 1.476 Gpc with  $3840^3$  dark matter particles and used the L-GADGET-2 solver. The haloes in MULTIDARK PLANCK 2 were identified using the ROCKSTAR halo finder (Behroozi et al., 2013). These 324 spherical regions of radius 22 (comoving) Mpc were then resimulated using a full hydrodynamics prescription (Rasia et al., 2015) with the GADGET-X SPH solver (Beck et al., 2016). Haloes and subhaloes were identified with Amiga’s Halo Finder (Knollmann & Knebe, 2009), which has a binding energy criterion similar to SUBFIND, but uses an adaptive mesh refinement grid to represent the density field/contours.

While THE300 is only mass-complete above  $M_{200c} \gtrsim 10^{15} M_{\odot}$  at  $z = 0$ , it resolves many haloes below this mass. Since the scaling relations derived from these lower mass clusters are in agreement with our other simulations, we note that the selection effects do not, in general, appear to have an impact on the temperature scaling results, with one exception. That is, within large radii (i.e.,  $R_{\text{vir}}$  and  $R_{200m}$ ) the scatter of temperatures is amplified, however, the population mean behaviors remain unaffected.

In Section 3.4.3, two different simulations from THE300 are also used, which we will refer to as MUSIC and GIZMO. MUSIC uses the solver GADGET-MUSIC (Sembolini et al., 2013) in place of GADGET-X. A summary of the differences between these simulations can be found in Cui et al. (2018), but in brief, the GADGET-MUSIC and GADGET-X solvers use similar but subtly different gas treatments and stellar formation and stellar feedback mechanisms. Most notably, however, GADGET-MUSIC does not include any Black Hole or AGN feedback, while GADGET-X does.

GIZMO (Cui et al., 2022), on the other hand, uses GIZMO-SIMBA (Davé et al., 2019) in its Meshless Finite Mass solver mode instead of GADGET-X which uses SPH. A detailed discussion of the differences can be found in Cui et al. (2022, their Table 2). In general, GIZMO uses a different feedback model, with, among other things, significantly stronger kinetic feedback calibrated for high-mass haloes which causes large differences in the observed gas fractions between the GIZMO-SIMBA and GADGET-X runs.

### 3.2.3 Magneticum Pathfinder

The MAGNETICUM PATHFINDER (Hirschmann et al., 2014) simulations are a suite of magneto-hydrodynamics simulations using a version of the SPH solver GADGET-3 developed independently to that used in the BAHAMAS+MACSIS versions. This chapter uses the Box2 hr run, and will henceforth refer to it as the MAGNETICUM sample. Haloes are once again identified using a FoF algorithm, and subhaloes



using SUBFIND. Since the MAGNETICUM simulations are based on WMAP7 cosmology (Komatsu et al., 2011) they have the most distinct cosmology to the other simulations which all use Planck cosmologies (Planck Collaboration et al., 2014c, 2016a). Finally, it is important to note that while the other simulations show little variation between the core-excised and non-core-excised values for  $T_m$  and  $T_y$  (as discussed for BAHAMAS+MACSIS in the previous chapter), this is not true in MAGNETICUM. As such, we use the core-excised values for all three temperature measures obtained from MAGNETICUM. This is explored in more detail in Section 3.4.5.

### 3.2.4 IllustrisTNG

The ILLUSTRISTNG project, here TNG, (Springel et al., 2018; Pillepich et al., 2018b; Nelson et al., 2018; Marinacci et al., 2018; Naiman et al., 2018) is a follow up to the ILLUSTRIS project (Vogelsberger et al., 2014). It uses the moving-mesh code AREPO (Springel, 2010) and uses a full magneto-hydrodynamics treatment with galaxy formation models as detailed in Pillepich et al. (2018a); Weinberger et al. (2017). This chapter uses TNG300-1, the highest-resolution run from the suite, but will reference the two lower-resolution runs in Section 3.4.1. Haloes are identified using a FoF algorithm and subhaloes with SUBFIND, as for the MAGNETICUM sample.

All TNG properties are estimated using the FoF particle set. The FoF linking length of  $b = 0.2$  was chosen so that the FoF group on average contains all particles within  $R_{200c}$  of the halo center. Consequently, properties computed within significantly larger apertures (primarily  $R_{200m}$ ) will miss the contribution from particles in the far outskirts (as these are not included in the FoF, whose particle set is incomplete at such distances) and will thus incur a minor bias. However, the main analysis and results in this chapter focus on  $R_{200c}$  and  $R_{500c}$  and are thus unaffected by this bias.

## 3.3 Temperature Scaling Relations

In general, there is a good agreement between the the four samples for each temperature measure as can be seen in Figure 3.1. As a similar plotting convention is used throughout this chapter, I will briefly explain the process here. The data was sorted into logarithmically spaced mass bins, and within each bin I have then plotted the median, and 16 and 84 percentile regions for each sample. That is, the solid lines indicate the median of the data distribution, while the shaded regions show the  $1\sigma$  intrinsic scatter within each data set. Where there are fewer than 10 clusters within a mass bin, we have only plotted the median and not calculated the percentiles. Within each sample, this region accounts



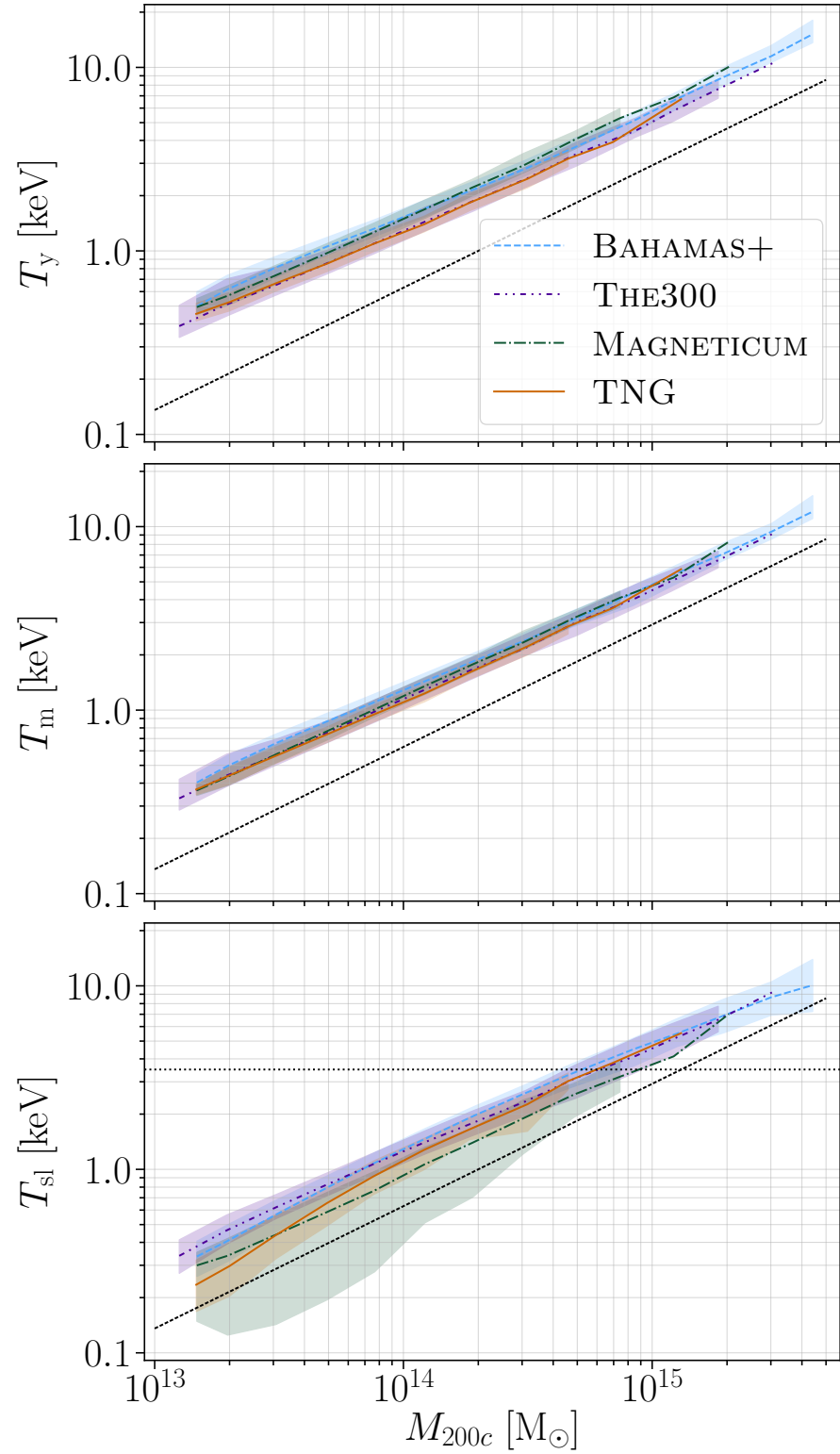


**FIGURE 3.1:** The three temperature measures in each simulation at  $z = 0$ . Here, the data is binned into logarithmically spaced mass bins. The shaded regions show the 16 and 84 percentile regions within these bins, while the lines show the medians. The dotted black line indicates the self-similar scaling  $T \propto M^{2/3}$ , with an amplitude arbitrarily set for visual clarity. The horizontal line in the lower panel indicates the temperature above which  $T_{sl}$  is considered a good proxy for the X-ray temperature.

for an intrinsic variation of around  $\pm 5.5\%$  for  $T_m$  and  $T_y$  (with this in general being marginally larger in  $T_y$  than  $T_m$ ), and  $\pm 9\%$  for  $T_{sl}$ .

For the mass-weighted temperature,  $T_m$ , all four simulations show a close agreement at  $z = 0$ , while  $T_y$  shows slightly more variation, but is, nonetheless, consistent overall. The spectroscopic-like temperature shows the most variation between the four samples, particularly at lower masses/temperatures. However, it is worth noting, that for  $T_{sl} \gtrsim 3.5$  keV, where  $T_{sl}$  is considered a good proxy for the X-ray temperature, the samples agree well. In general, however, there is far more intrinsic scatter among the  $T_{sl}$  measures (within  $R_{200c}$ ) than for the other temperature measures. We can see in particular that MAGNETICUM has a large scatter in  $T_{sl}$ , especially at lower masses. This is driven by the warm gas ( $T < 10^6$  K) in the low-mass haloes, and is discussed in more detail in Section 3.4.6. Due to the limited  $T_{sl}$  data where it is an appropriate proxy for the X-ray temperature, particularly at higher redshifts,  $T_{sl}$  will be considered in less detail in the rest of this Chapter.

In Figure 3.1, an arbitrary indicative line is also plotted to show self-similar scaling, i.e.,  $T \propto M^{2/3}$ . This allows us to see that in simulations all three temperature measures appear to scale at slightly less than  $2/3$ , with  $T_{sl}$  lying closest to this. However, at higher masses and temperatures,  $T_y$  and  $T_m$  appear to tend to this self similarity, while at lower masses and temperatures, the scaling relation seems shallower. Conversely, this also indicates there is some mild curvature within the  $T_y$  and  $T_m$  scaling relations. The two- and three-parameter fits for each of these simulations can be found tabulated in Table B.3 for a more detailed comparison, and will be discussed further in Section 3.5. The agreement at high masses may come from the decreased relative effects of feedback in this regime. That is, at lower masses the gas is hotter than expected from solely gravitational heating due to feedback processes, pushing the equilibrium away from self-similarity, while at higher masses the potential well ensures more gas is retained in haloes; this is supported by the results of Farahi et al. (2018), who use kernel-localized linear regression (Farahi et al., 2022) to show that the gas mass in BAHAMAS+MACSIS clusters approach a self-similar scaling at higher halo masses. That the lower masses lie higher than expected from self similarity for  $T_y$  and  $T_m$ , would indicate that generally the feedback is leading to hotter gas in the halo.

### 3.3.1 Redshift evolution

As discussed in Section 1.5, from self similarity we expect the cluster temperatures to scale as  $T(z) \propto E(z)^{2/3}$  at fixed mass. In Figure 3.2, it is evident that this is not quite the case within these samples. We examine the temperature measures at five different redshifts,  $z = 0.0, 0.25, 0.5, 1.0$  and  $1.5$ . In general, the

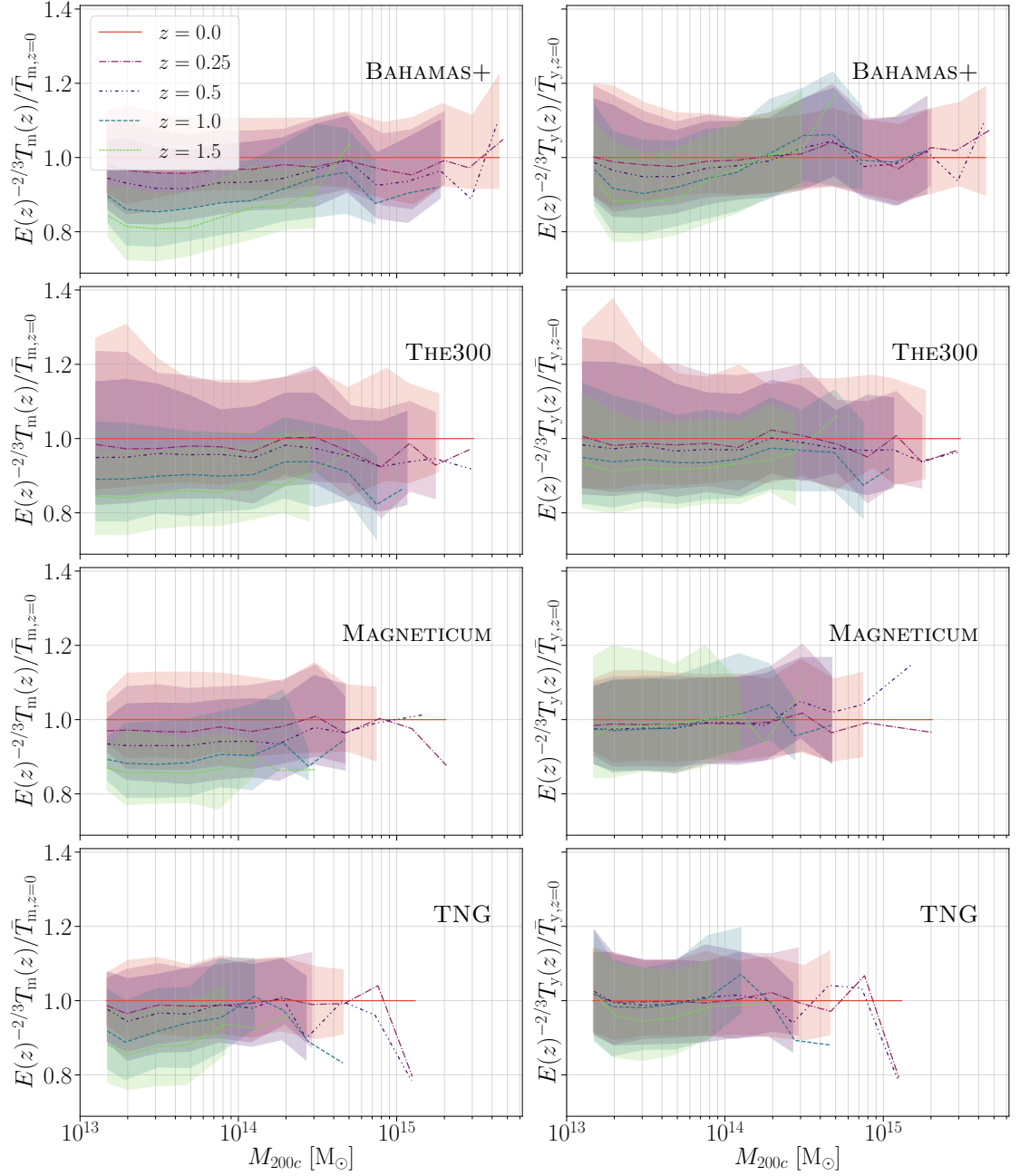


**FIGURE 3.2:** Redshift evolution of the temperature measures within each simulation. As in Fig. 3.1, the data is sorted into mass bins, with the shaded regions showing the 16 to 84 percentile region and the lines the medians. Here, each redshift for each sample is divided by the bin median at  $z = 0$ . We see there is less evolution in  $T_y$  (the right panels) than in  $T_m$  (those on the left).

**TABLE 3.4:** The median value for  $E(z)^{-2/3}T(z)/\bar{T}_{z=0}$  as shown in Fig. 3.2, for  $z = 0.5$  and 1.0. These can be understood as a broad mass-independent redshift correction. We have also tabulated the median correction to the 2-parameter fit for each simulation (described in Section 3.6.2 and tabulated in Table B.3 in Appendix B).

$z = 0.5$	$E(z)^{-2/3}T_y$	$E(z)^{-2/3}T_m$	$E(z)^{-2/3}T_{sl}$
BAHAMAS+MACSIS	$0.981^{+0.002}_{-0.002}$	$0.951^{+0.001}_{-0.001}$	$0.929^{+0.005}_{-0.011}$
THE300	$0.968^{+0.006}_{-0.004}$	$0.953^{+0.003}_{-0.002}$	$0.933^{+0.007}_{-0.005}$
MAGNETICUM	$0.969^{+0.002}_{-0.005}$	$0.932^{+0.003}_{-0.003}$	$0.728^{+0.023}_{-0.014}$
TNG	$0.984^{+0.007}_{-0.005}$	$0.972^{+0.004}_{-0.005}$	$0.746^{+0.018}_{-0.038}$
$z = 1.0$	$E(z)^{-2/3}T_y$	$E(z)^{-2/3}T_m$	$E(z)^{-2/3}T_{sl}$
BAHAMAS+MACSIS	$0.955^{+0.003}_{-0.002}$	$0.896^{+0.002}_{-0.002}$	$0.815^{+0.006}_{-0.011}$
THE300	$0.938^{+0.004}_{-0.004}$	$0.903^{+0.002}_{-0.002}$	$0.856^{+0.004}_{-0.005}$
MAGNETICUM	$0.966^{+0.004}_{-0.003}$	$0.889^{+0.003}_{-0.005}$	$0.590^{+0.020}_{-0.013}$
TNG	$0.997^{+0.007}_{-0.007}$	$0.941^{+0.006}_{-0.005}$	$0.501^{+0.018}_{-0.012}$

temperature measures increase (with increasing redshift) *slower* than self similarity would suggest. That is, in Figure 3.2, were self similar evolution to occur, we would expect all five redshifts to align – as is nearly true for  $T_y$ . We note that here we have used the cosmological parameters and true redshift for each individual simulation to calculate  $E(z)$  for each sample. Due to the larger differences in cosmology for the MAGNETICUM simulation, this allows for more consistent results between simulations.

We found that  $T_{sl}$ , while not plotted here, evolves with the least accordance to self similarity, while  $T_y$  diverges the least from it. That is, graphically, the spread in the five redshift means is *smaller* for  $T_y$  than for  $T_m$ . At  $z = 1$ ,  $T_m$  has a median lowered to around the  $1\sigma$  intrinsic scatter at  $z = 0$ .  $T_y$  however shows almost no redshift dependence in MAGNETICUM and TNG and only mild evolution in BAHAMAS+MACSIS and THE300. Physically, we can motivate this aspect, as at higher redshifts, clusters on average had shorter cooling times, leading to more cool dense gas, which down-weights  $T_{sl}$ . On the other hand,  $T_y$  is determined by the gas pressure, which, assuming hydrostatic equilibrium, would be fixed to match the size of the potential well itself, leading to a more self-similar temperature measure.

It is also interesting to note that the samples do not show overt mass dependence in the redshift evolution for the two SZ temperatures, i.e., graphically, the mean lines are roughly horizontal for all of the samples. Here, it is worth noting that we are considering the masses at the redshift the cluster temperature is measured. In Table 3.4, we quantify these offsets for all three temperature measures in each sample at  $z = 0.5$  and 1.0. Here, we can more quantitatively see that there is increasing divergence from self-similarity (value of unity), comparing  $T_y$  to  $T_m$  to  $T_{sl}$  in all cases and we can see more generally the variety in

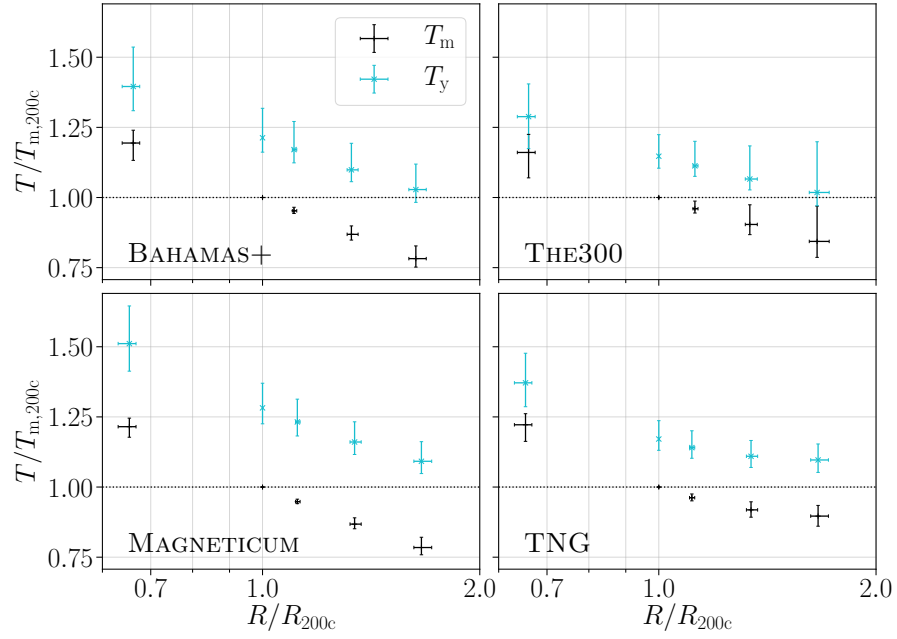


**FIGURE 3.3:** A depiction of the radial dependence of each simulation. Every cluster's temperature and radius is divided by the *same cluster's*  $T_m$  within  $R_{200c}$  and  $R_{200c}$ , for the five radii considered. These are, from left to right  $R_{500c}$ ,  $R_{200c}$ ,  $R_{500m}$ ,  $R_{vir}$  and  $R_{200m}$ . Hence, the error bars show the intrinsic scatter within each simulation for the clusters temperature profiles, fixed at  $R_{200c}$  and  $T_{m,200c}$ .

redshift behaviour for each sample. We also note that the larger errors in the  $T_{sl}$  offsets arise from there being more mass dependence to the redshift evolution (particularly for MAGNETICUM and TNG) than in  $T_y$  and  $T_m$ . The full details of the  $T_{sl}$  are not considered in much detail as the haloes included at these higher redshifts in MAGNETICUM and TNG are rarely at temperatures high enough for  $T_{sl}$  to be an accurate prediction of the observed X-ray temperature.

### 3.3.2 Radial dependence

Next, we study the dependence of the temperature measures on the radius of the sphere that we average over. Figure 3.3 shows how the averaged temperatures vary over the five radii we consider at  $z = 0$ . Here, on a cluster-by-cluster basis, we divide each radius and temperature of the cluster, by the  $R_{200c}$  and  $T_{m,200c}$  values for that cluster, and then we show the bulk averages of these values. These values can be found for each sample for convenient reference in Table B.5 in Appendix B.

The profiles are very similar within the four samples, and are consistent out to  $R_{500m}$ . The variations beyond this are likely driven by the particulars of the simulations rather than reflecting any inconsistency. We discussed in Section 3.2 that when calculating our TNG values, only particles which are linked to the FoF group are included, which may bias the large-radius temperatures high. THE300 shows a consistent profile with the other simulations, but a larger scatter due

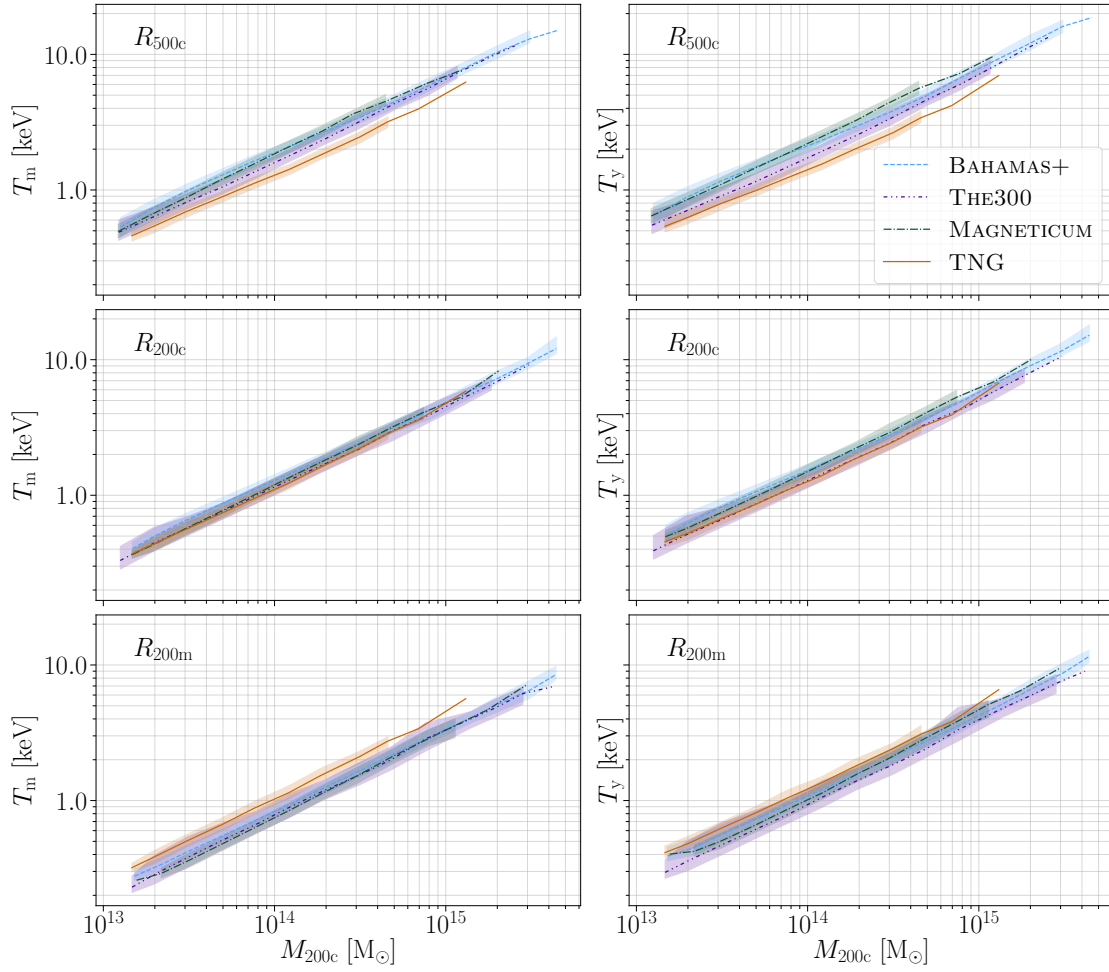


**FIGURE 3.4:** The variation in temperature scalings when averaged over three different radii, at  $z = 0$ . This figure is arranged as in Fig. 3.1, with  $T_m$  on the left and  $T_y$  on the right.

to the sample selection for the low-mass haloes. [Anbajagane et al. \(2022a\)](#) found similar scatter amplification in the velocity dispersion of low-mass clusters in THE300, and explicitly showed this was generated by the selection effect (see their Figure B1). We can also see that the offset between  $T_y$  and  $T_m$  is larger in BAHAMAS+MACSIS and MAGNETICUM than the other two simulations – this will be explored more in Section 3.3.4. This offset also seems to increase marginally at larger radii.

The difference in profile steepness can be appreciated in Figure 3.4. Here the temperature-mass relations are shown, at  $R_{500c}$ ,  $R_{200c}$  and  $R_{200m}$ , so we can see how the variation in profiles depend on the masses of the clusters. For example, we find that the differences in the ‘profiles’ between THE300 and BAHAMAS+MACSIS are largely driven by lower-mass haloes, and agree well at all radii for higher masses.

It also becomes evident that, for both  $T_m$  and  $T_y$ , the four models agree best within the  $R_{200c}$ . At lower radii, the shallow profile of TNG corresponds to temperatures below those in the other simulations, and at larger radii to temperatures above. Similarly, the steeper profile of MAGNETICUM leads to its temperatures sinking with respect to the other samples, as the radius increases.  $T_{sl}$ , while not shown here, has a larger variation at each radius – and it is harder to determine the agreement between simulations due to the difference in intrinsic scatter in each sample. Within  $R_{500c}$ ,  $T_{sl}$  in MAGNETICUM agrees far better with the other simulations – however,  $T_{sl}$  in all the other simulations agree slightly worse with each other than at  $R_{200c}$ .

### 3.3.3 Temperature–Y scalings

While temperature-mass scaling relations are important and relevant for comparison with X-ray observations, a consideration of the Compton- $y$  parameter in relation to temperature could lead to a way to self-calibrate SZ observables ([Lee et al., 2020](#)). In Figure 3.5, we show how the SZ temperatures scale within our samples with  $Y_{200c}$ . It is immediately clear that there is slightly poorer agreement within these quantities than when using  $M_{200c}$ , however, these do still predominantly agree between the different samples. In particular, as  $Y_{200c}$  increases, the agreement between  $T_m$  in each sample improves, and as we will see later in Section 3.4.2, most of this variation correlates with the variation of  $f_{gas}$  in each simulation.

We note that the  $Y_{200c} - M_{200c}$  relationship agrees very well between simulations for all masses  $\gtrsim 10^{14} M_\odot$ , which corresponds to  $Y_{200c} \gtrsim 10^{-6} \text{ Mpc}^2$ . It is also worth considering that since our haloes are selected with a mass cut-off, for the lowest values of  $Y$  ( $\lesssim 10^{-7} \text{ Mpc}^2$ ) the data we have are not necessarily complete for each value of  $Y$ , so may be biased slightly high. Self-similarity would suggest a scaling relation of  $T \propto Y^{2/5}$ , but we see shallower scaling relations  $\simeq 0.33$  in

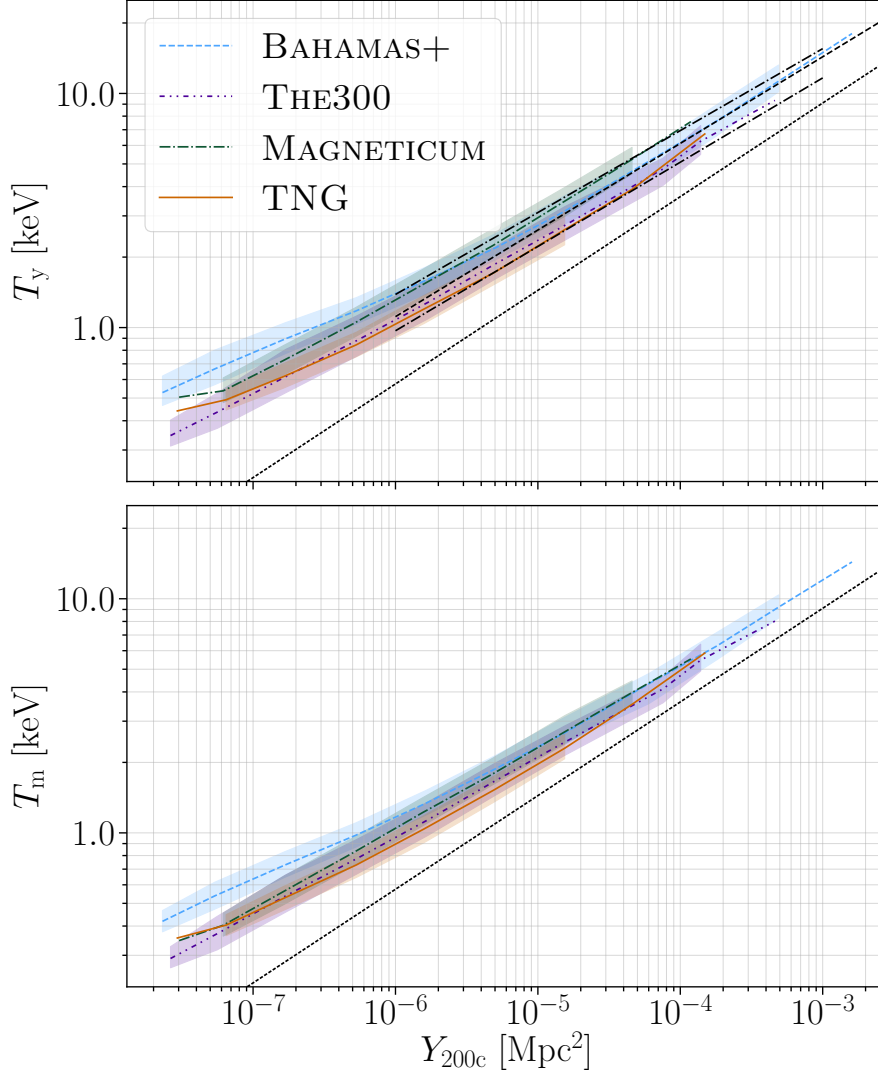


**FIGURE 3.5:** The variation of each temperature measure with respect to the volume averaged Compton- $y$  within  $R_{200c}$ . These are the measures at  $z = 0$  and the figure is arranged as in Fig. 3.1, grouped into logarithmically spaced  $Y$  bins, rather than mass bins. The dotted black line is an indicative line with scaling  $T \propto Y^{2/5}$ , i.e., a self-similar scaling.



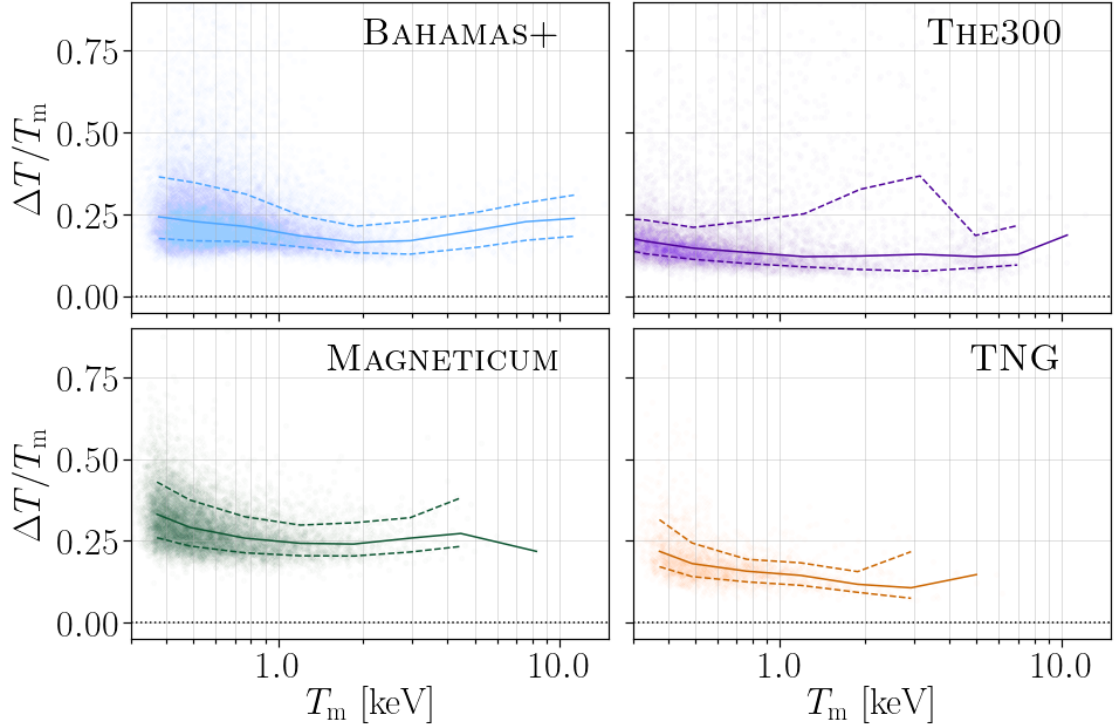


**FIGURE 3.6:** The relative variation in temperature measures,  $\Delta T = T_y - T_m$  with respect to the mass-weighted temperature,  $T_m$ . Here, each point represents a single halo within the simulation, the solid line represents the medians within logarithmically spaced  $T_m$  bins, while the dashed lines show the 16 and 84 percentiles for the same bins. The discrepancy in the scatter for THE300 around  $T \approx 3$  keV is discussed below in Section 3.3.4.

all our samples. In particular, BAHAMAS+MACSIS has a shallower scaling relation ( $\approx 0.31$ ), for both  $T_y$  and  $T_m$  than the other three samples.

### 3.3.4 $\Delta T$ -Temperature scalings

As already mentioned, we find an offset between the temperature measures, which we now explore in more detail. For this, in Figure 3.6, we plot the fractional temperature difference,  $\Delta T/T_m = (T_y - T_m)/T_m$  against  $T_m$  itself. We already identified that the mass-weighted temperature is a good proxy for the mass itself, so it is worth noting that this temperature difference has a similar, if subtly different, relationship than when plotted against mass.

The systematic offset is different in each of the four samples. However, it is interesting to note that this offset is subject to a significant skew – which is to say, at the simplest level the offset holds on a cluster by cluster basis, and  $T_y$  is *always* greater than  $T_m$  within clusters. This can be seen visually, as here we have plotted every halo within our samples in Figure 3.6, and it is evident that within each cluster, there is a minimum difference, greater than zero, between all the clusters. Taking the 1st percentile for each cluster sample we can estimate this

minimum offset as being highest in MAGNETICUM with  $\Delta T \geq 0.178 T_m$ , and smallest in THE300 where  $\Delta T \geq 0.066 T_m$ .

Here, it is worth briefly discussing why the THE300 sample has such a non-uniform intrinsic scatter compared to the other samples. This divergence is worst at  $T_m \approx 3$  keV, reaching convergence again at high temperatures ( $T_m \gtrsim 4$  keV). This is an artifact of the selection process for low-mass clusters within the THE300 sample. That is, since all ‘low-mass’ ( $M_{200c} \lesssim 0.9 \times 10^{15} M_\odot$ ) clusters exist in the region of larger haloes, this biases the temperatures of the clusters. As such, this region is less relevant for a mass-complete understanding of the temperature differences here.

### 3.4 Resilience of results

All the simulations use different physical models and numerical methods to generate the halo populations studied here. Moreover, they are all calibrated to different measurements, as such it is remarkable that we see the agreement we have found across the four different samples. However, this section will focus more specifically on the effects these differences have caused on our observed results and the variation caused by other simulation-specific parameters.

#### 3.4.1 Resolution

Firstly, it is worth briefly considering the effect of resolution in simulations. Resolution studies are generally complicated as many simulations do not have different runs at different resolutions. However, we can consider three different runs of TNG, alongside briefly discussing the two different boxes from MAGNETICUM.

The effects of the three different resolutions in TNG can be seen in Figure 3.7. Here, the highest resolution is the one used throughout the rest of this work, while the other two have 8 and 64 times worse resolutions, respectively, while the subgrid physics were kept consistent. In TNG, the resolution has little effect on the SZ temperatures ( $T_m$  and  $T_y$ ), with differences only occurring in the lowest-resolution run at high masses, where the temperatures tend to fall a little higher.

There are more systematic differences in  $T_{sl}$ , however, where with increasing resolution, the temperatures all seem to fall, especially in the lower-mass haloes. This is likely due to the cold dense clumps in the haloes being better resolved in the higher-resolution runs and as such, leading to lower averaged values for  $T_{sl}$ .

From the MAGNETICUM simulations, it is possible to compare the MAGNETICUM Box2 `hr` run (used throughout the rest of this chapter), with the Box1a `mr`, a run with around 20-times-worse resolution. This is not plotted in this thesis, but here we found a decrease for both  $T_m$  and  $T_y$  in the lower-resolution study, of a similar scale to the intrinsic scatter. However, it is also worth noting that these two runs have *different* subgrid physics, as they are independently calibrated, which may

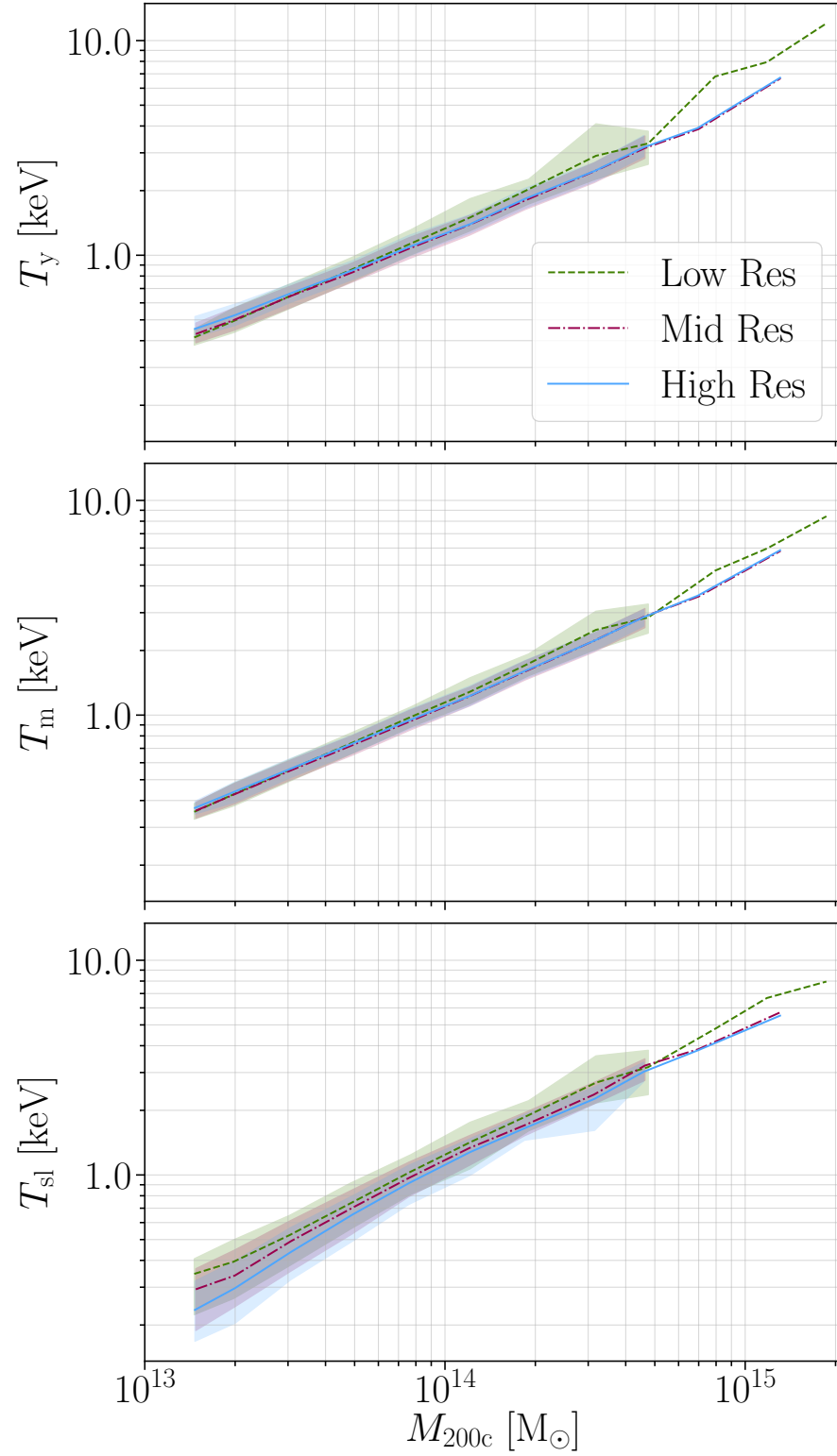


**FIGURE 3.7:** The effects of resolution in the TNG simulation. High Res here refers to the run used within the rest of this chapter. Mid Res and Low Res are runs with x8 and x64 worse resolution, respectively. This figure is arranged as in Fig. 3.1.

contribute to this difference. Due to the scatter inherent in the MAGNETICUM values for  $T_{\text{sl}}$  it is hard to gain a conclusive indication of how these vary.

The differences between these simulations can be considered in the formalism discussed in Schaye et al. (2015), as a ‘strong’ convergence test using TNG and a ‘weak’ convergence test using MAGNETICUM. As such, the small variation that is observed in MAGNETICUM is likely caused by the recalibration, more than the inherent resolution variation itself, given the lack of any resolution dependence in TNG. However, more detailed work may be necessary to determine how in general resolution effects may change the temperatures gained from simulations.

### 3.4.2 Gas fraction

Since the temperature measures are dependent on gas density, it is important to consider how the differences in gas fraction (i.e.,  $f_{\text{gas},200c} = M_{\text{gas},200c}/M_{200c}$ ) vary between the simulations. In Figure 3.8, the gas fractions within  $R_{200c}$  are shown (scaled by the cosmic baryonic fraction in the simulations) at  $z = 0$  and  $z = 1$ . In general,  $f_{\text{gas}}$  is often considered to be a probe of the level of feedback within in clusters, with lower values for  $f_{\text{gas}}$  indicating more effects from feedback. Hence generally speaking, at lower masses,  $f_{\text{gas}}$  is lower as the potential well for the haloes are shallower, allowing for more gas to be ejected from haloes through feedback.

It is evident that there are significant variations in  $f_{\text{gas}}$  among the simulations considered in this work. At the highest masses, TNG, THE300, and BAHAMAS+MACSIS start to agree, with values  $> 0.9$ , but MAGNETICUM lies greatly below this. Similarly, at the lowest masses, at  $z = 0$ , MAGNETICUM, THE300 and TNG roughly agree, while BAHAMAS+MACSIS is significantly smaller.

Furthermore, the samples exhibit a varying level of redshift evolution. The gas fraction rises, indicating that as clusters evolve, generally feedback results in gas being ejected from haloes, so younger clusters (i.e., in general, clusters at higher redshifts), will have higher values for  $f_{\text{gas}}$ . However, the slopes in each of the samples decrease by differing values – TNG most notably, with its values reducing dramatically everywhere except the lowest-mass haloes.

This diverging behaviour in  $f_{\text{gas},200c}$  is in contrast to the strong agreement found between the samples for both the  $T_{\text{m}}$ –mass relations, and the  $Y$ –mass relations, although it is indicated by the  $T - Y$  variation. Since  $Y$  is a measure of the gas pressure within clusters, we could expect it to be self-calibrating – that is, a cluster in hydrostatic equilibrium would lead to a certain gas pressure to counter the gravitational well of its own mass. As such we would expect haloes to have a strong  $Y - M$  relationship.

However, we can see a reflection of the  $f_{\text{gas}}$  variation subtly in  $T_y$ . That is, we can see that the the curvature of the  $T_y$ –mass relation as seen in, e.g., Figure 3.1,

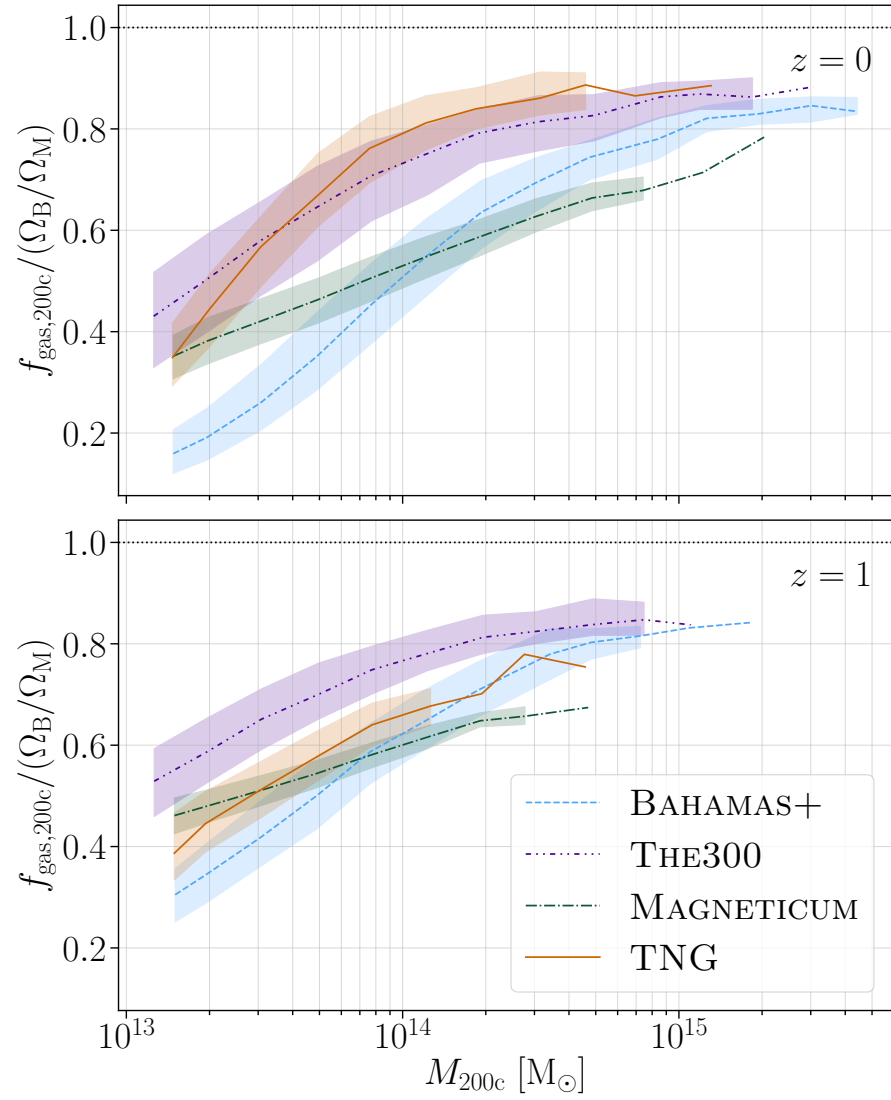


**FIGURE 3.8:** A comparison of the gas fraction between each simulation. Here, the gas fraction,  $f_{\text{gas},200c} = M_{\text{gas},200c} / M_{200c}$  has been normalised by the relevant  $\Omega_B$  and  $\Omega_M$  for each simulation. This figure is arranged as in Fig. 3.1, with  $z = 0$  in the top panel and  $z = 1$  in the lower panel.

is similar (albeit inversely) to the curvature in the  $f_{\text{gas}}$ –mass relation. In fact, we can find that this is driven by the changes in  $M_{\text{gas}}$  as  $M_{\text{gas}}T_y$  forms a tight relation with  $Y$  and a tighter relation (than  $T_y$  alone) with mass. This is perhaps unsurprising, as we already know that on a cluster-by-cluster level,  $T_y$  and  $T_m$  form a strong relationship, and since  $M_{\text{gas}}T_m \propto Y$ , we can consider  $M_{\text{gas}}T_y$  to be proportional to a relativistic ‘equivalent’ to  $Y$ . Nonetheless, this means a more detailed understanding of  $M_{\text{gas}}$  (or equivalently  $f_{\text{gas}}$ ) in clusters would lead to more assurance in the exact  $T_y$ –mass and  $T_y - Y$  relationships.

### 3.4.3 Feedback

As discussed in Section 3.2, all of the samples use very differently calibrated feedback models.<sup>2</sup> This makes it incredibly difficult to judge how the different feedback choices have changed our observed results. As such, in this section we compare the three different runs of THE300 previously described.

In Figure 3.9, the three different THE300 runs are displayed – here GADGET-X is the run used in the rest of the chapter. GIZMO is a run using a more refined feedback model that is nonetheless calibrated for high-mass clusters, leading to a lower observed  $f_{\text{gas}}$  particularly at low masses than the other runs. This is reflected in the GIZMO temperatures lying high at low masses. MUSIC, on the other hand, has no AGN feedback, and accordingly a shallower slope in  $f_{\text{gas}}$  than GADGET-X. It is worth noting that due to the calibration metrics, MUSIC thus has slightly higher values for  $f_{\text{gas}}$  at low masses and lower values, at high mass.

A quick examination of  $T_y$  immediately shows a reflection of the feedback. At high masses where THE300 is predominantly calibrated, GIZMO and GADGET-X agree, while at low masses GIZMO lies high, as previously noted. MUSIC lies a little low at the lowest masses compared to GADGET-X and high at the highest – the divergence between the three runs appears to happen almost inversely proportionally to the variation in  $f_{\text{gas}}$  between the three runs. This matches the observations for  $f_{\text{gas}}$  just discussed.

Similar, but far reduced effects can be seen by examining  $T_m$ . At high masses, all three feedback runs agree extraordinarily well. This implies that large variations in feedback – e.g., the large feedback at low masses in GIZMO – are required to disrupt the stability of  $T_m$ .

Examining  $T_{\text{sl}}$ , however, we find very different behaviour. Here, the three runs diverge significantly. GIZMO lies almost at a constant increase above GADGET-X, MUSIC, on the other hand, has a significantly shallower slope than the other two runs, with a large decrease in  $T_{\text{sl}}$  at high masses. This indicates that  $T_{\text{sl}}$  is somewhat more affected by variations in feedback models, making it somewhat less reliable as a temperature proxy.

<sup>2</sup>That is, not only are they calibrated to different properties, but also, the feedback models themselves are varied between each simulation.

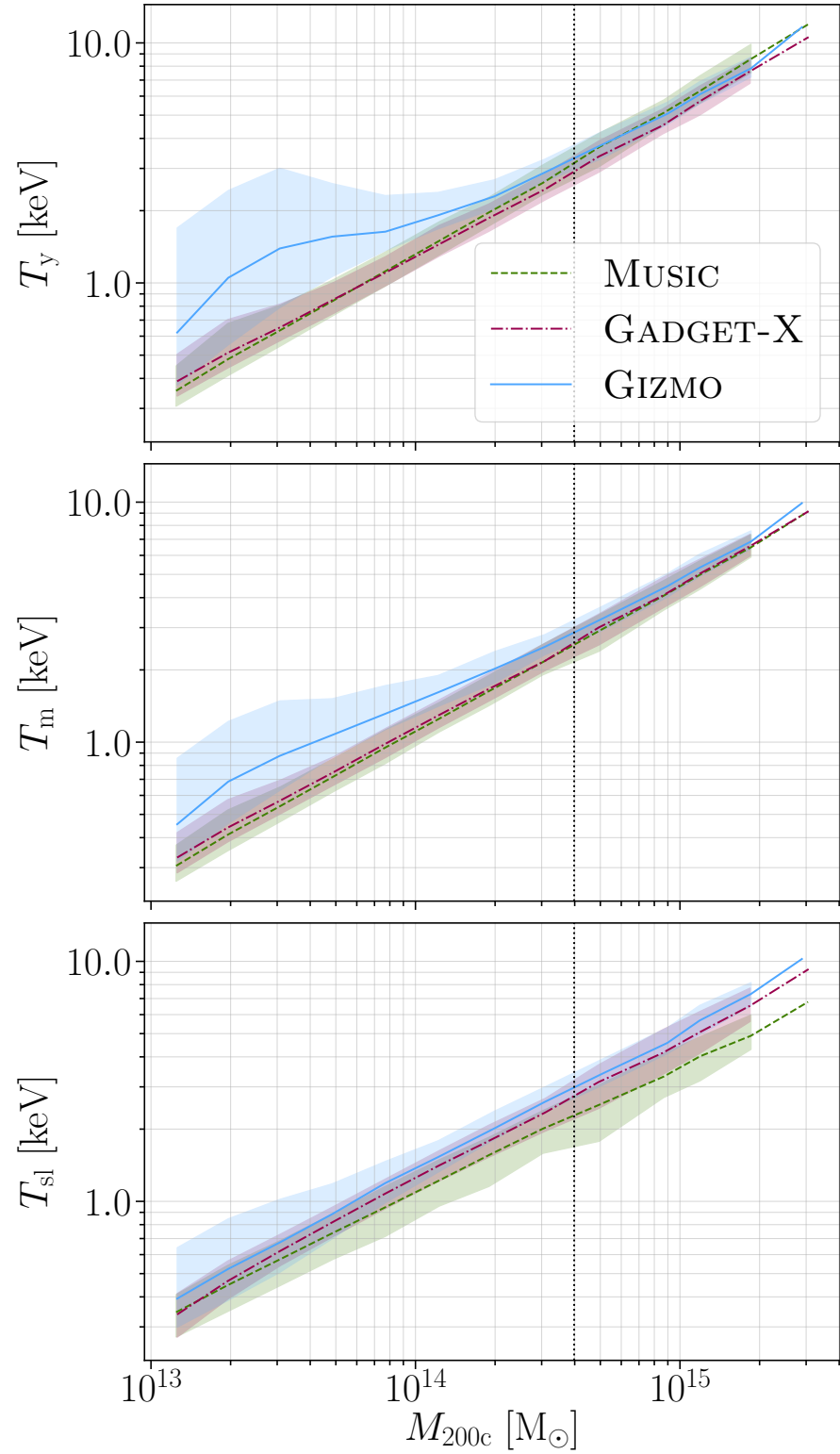


**FIGURE 3.9:** A comparison of different feedback mechanisms within THE300. Here, GADGET-X is the run used in the rest of the paper, MUSIC is a run without any AGN feedback, and GIZMO is a run using a mass-independent feedback calibrated for the highest masses. The black vertical dotted line at  $M_{200c} = 10^{14.6} M_{\odot}$  indicates an approximation for the region above which The300 was predominantly calibrated.

This figure is otherwise arranged as in Fig. 3.1.

### 3.4.4 Relaxation

It is worth very briefly considering the effects of relaxation in clusters. Here, the same relaxation criteria are used as in Chapter 2. However, for MAGNETICUM we calculated only the first constraints on  $X_{\text{off}}$  and  $f_{\text{sub}}$ . However as this restricts the population to a similar proportion of the haloes as was obtained with all three criteria in the other samples, this was considered to be a sufficient representation of the cluster relaxation for the purposes of this chapter.

In Figure 3.10, the effects of the relaxation criteria are shown for the higher mass clusters at  $z = 0$ . There is little evidence towards a bulk offset or significant change in intrinsic temperature spread between relaxed and un-relaxed clusters. However, there is a slight rise in the temperatures within THE300 at high masses. This is not present at lower masses, nor meaningfully in the other simulations. As such, we conclude, that as in Chapter 2, these relaxation constraints have little impact on the simulation-determined SZ temperatures.

### 3.4.5 Core-Excision

The MAGNETICUM simulation, in contrast to the other simulations, shows a very large intrinsic variation in the  $y$ -weighted temperature measure when averaged over the whole halo volume, especially at higher redshifts. This appears to be due to a difference in the gas behaviour of the core in the MAGNETICUM simulations compared to the other simulations (BAHAMAS+MACSIS, THE300 and TNG), and can be mitigated with core-excision.

Within the MAGNETICUM simulation there is a far larger proportion of hot ( $> 10^8$  K) gas cells in the clusters than in the other simulations, particularly located in the core of the clusters. In general, none of the simulations model the cluster cores with high fidelity, however only within the MAGNETICUM simulations do these core effects appear to significantly affect our averaged SZ temperatures. In particular, in the MAGNETICUM sample, at  $z = 1.5$  within  $R_{500c}$ , most clusters have a small fraction ( $\lesssim 0.005\%$ ) of the gas cells having these very high temperatures, with a maximal fraction of 2% in the most extreme cluster. The TNG sample, in contrast, has a tiny fraction – for most clusters  $\lesssim 0.0005\%$  of the cells (i.e., a factor of 10 fewer), with a maximal fraction of 0.5% in the most extreme cluster.

These very high-temperature gas cells, will upweight the averaged  $T_y$  more than  $T_m$  leading to the observed changes. And, due to both the instabilities within the  $T_y$  data predominantly being generated at higher redshifts and the lack of these similar effects within the other simulations, we assume that this effect is unphysical.

In Figure 3.11, the effects of different radii of core-excision can be seen within the MAGNETICUM data. In particular, we can motivate the use of the same core-excision used for our  $T_{\text{sl}}$  values, i.e.,  $0.15R_{500c}$ , as this indicates the turning point,



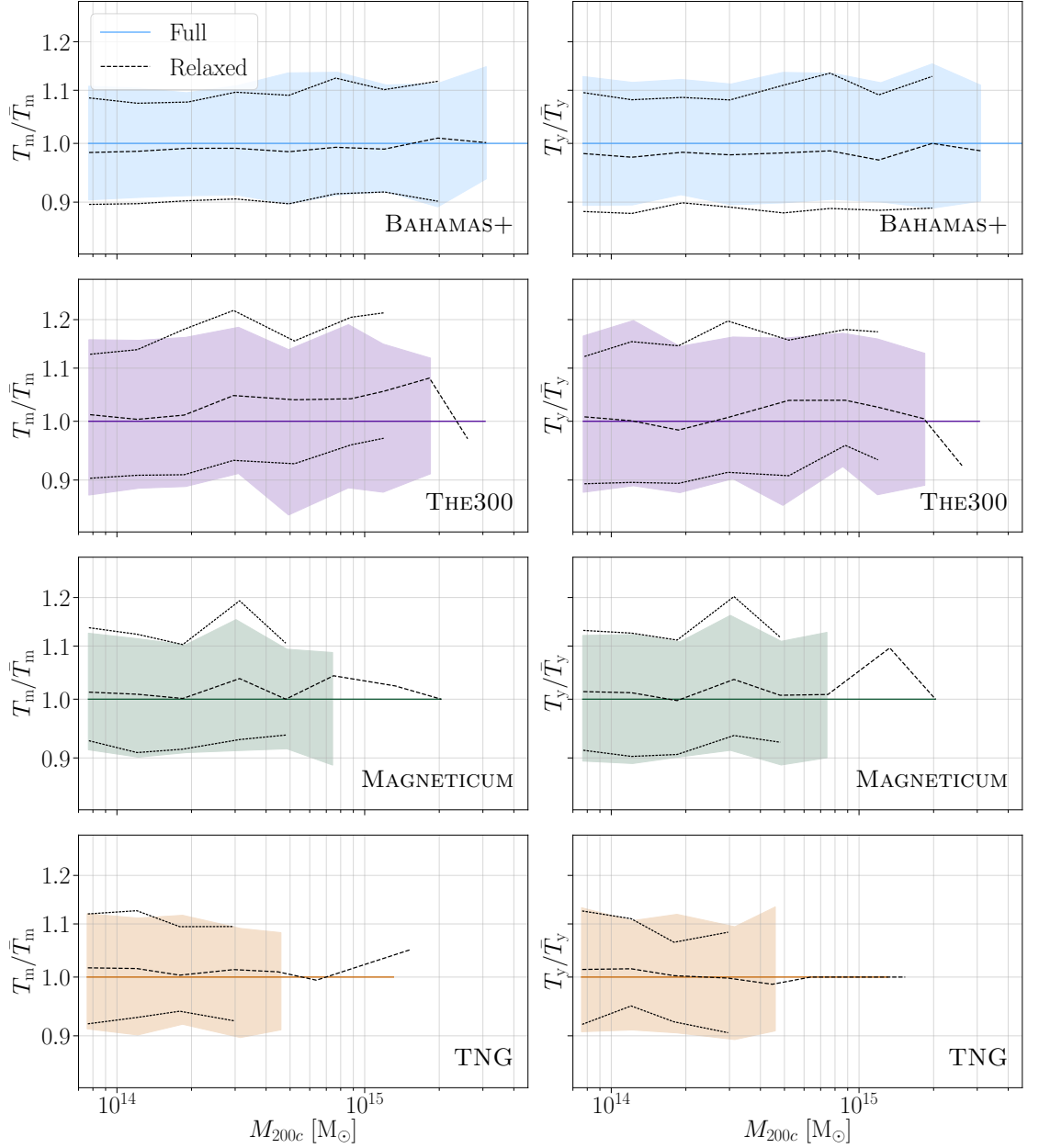


**FIGURE 3.10:** The effects of relaxation criteria on the observed temperature measures. The data is binned into logarithmically spaced mass bins, and the median of the whole sample in each bin is designated by  $\bar{T}$ . The shaded regions show the 16 and 84 percentile regions within these bins, divided by the  $\bar{T}$ . The relaxed subsample bin means (divided by  $\bar{T}$ ) are shown as dashed lines, while the relaxed 16 and 84 percentile regions are shown by the dotted lines. We can see that relaxation metrics show a limited effect on final averages of the data.

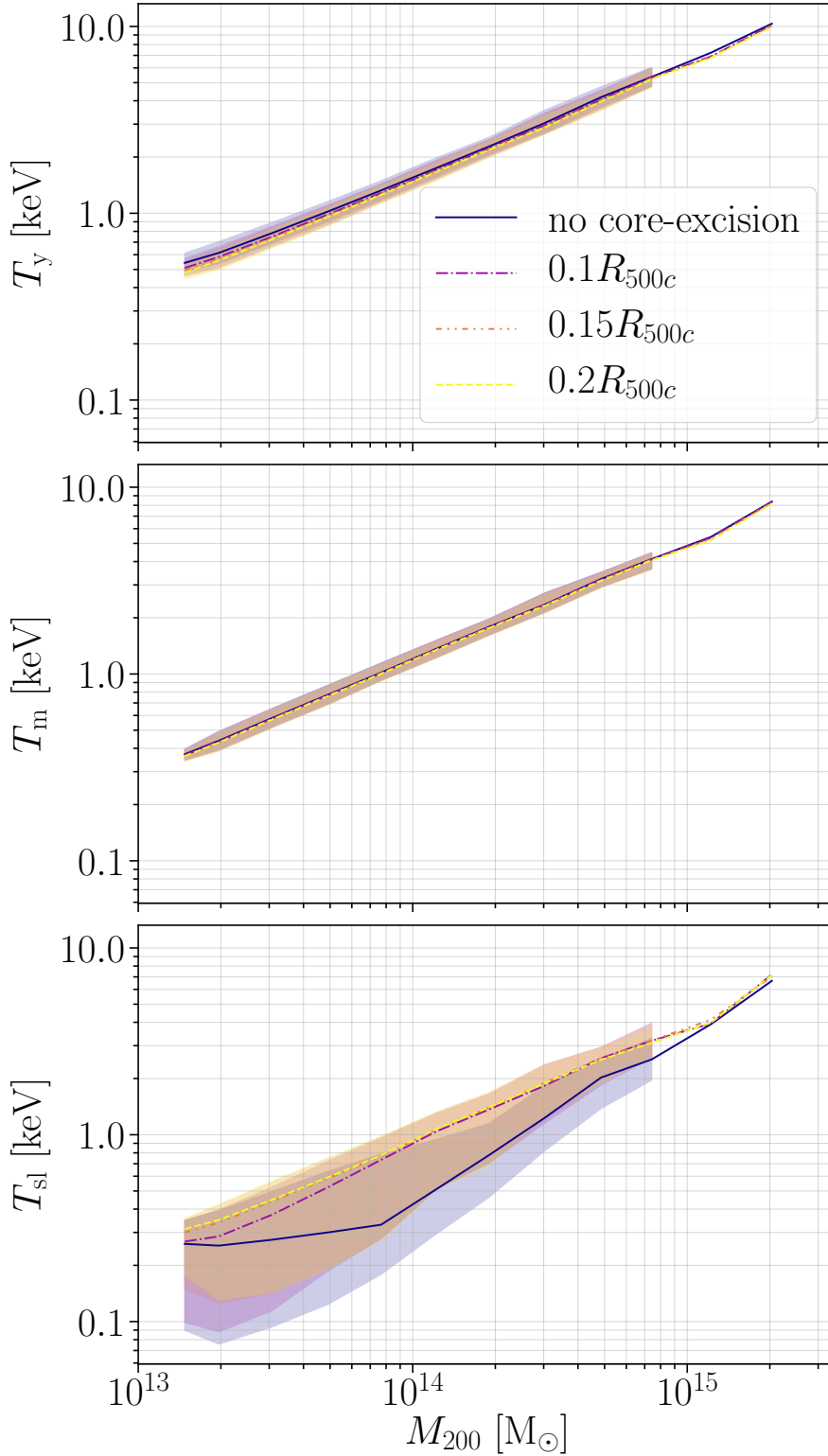


**FIGURE 3.11:** The effects of core excision on the observed temperature measures within the MAGNETICUM sample at  $z = 0$ . The line labelled ‘no core-excision’ are the volume averages with no core-excision, while the other lines are marked with the radius of the core-excision (i.e., any cells within this radius are ignored in the averaging procedure). We see little change to the value of  $T_m$  but a slight decrease within  $T_y$ . At higher redshifts, this effect is magnified within the MAGNETICUM sample. The effects for  $T_{sl}$  are discussed more below. However, we note that by core-excision of around  $0.15R_{500c}$  these effects have become stable.

after which further core-excision shows little change. This also, at higher redshifts, results in removing the unphysical variation present in the  $T_y$  data.

As such, we have used the core-excised values for all three temperature measures ( $T_y$ ,  $T_m$  and  $T_{sl}$ ) within the MAGNETICUM sample. For our other three samples, this core-excision is used *only* for  $T_{sl}$  and the whole-cluster averages are used for  $T_y$  and  $T_m$ .

### 3.4.6 Particle temperature cut

In Section 3.2, we indicated that as is common practice we use a temperature cut to exclude low-temperature particles that would not emit X-rays, and would otherwise bias  $T_{sl}$ . In particular, we use a temperature cut of  $T \geq 10^{5.2}$  K. However, in Section 3.3, we observed large scatter in the  $T_{sl}$  values found in MAGNETICUM. These seem to be driven in large part by warm particles, not excluded in this regime.

That is, in Figure 3.12, the four samples have been plotted, alongside the MAGNETICUM haloes when a stricter temperature cut  $T \geq 10^6$  K is implemented. The scatter in  $T_{sl}$  is greatly reduced, and the medians lie far closer to those obtained from the other simulations. These “warm” particles account for around 1% of the particles in most haloes, increasing at lower masses. In some of the lowest-mass haloes these “warm” particles account for around 10% of the particles. This motivates the use of the consistent temperature cut of  $T \geq 10^{5.2}$  K across all simulations, despite the increase in scatter in the MAGNETICUM sample.

It is also clear that, at least in MAGNETICUM, changing the temperature cut seems to have very minimal effects on  $T_y$  and  $T_m$ . This is to be expected, as these are far more weighted by the higher temperature gas components in haloes. In principle, the SZ effect will be caused to some extent by *all* the gas in a halo, not merely the hottest regions of gas, however this consistency across temperature cuts, shows that the contribution of the warm gas to the global SZ signal is minimal. This indicates that  $T_m$  and  $T_y$  are robust against the choice of temperature cut.

## 3.5 Cross-simulation averaged results

Due to the broad agreement of all of the samples in each temperature, we can consider the effects of averaging across simulations to obtain ‘simulation-independent’ predictions for these values from simulations. Here, these are obtained by joining all the samples to form one large population of halos, which is then sorted into mass bins as before, and sample fits are found to the mass-binned averages.<sup>3</sup> This means our averages will be weighted more by those

<sup>3</sup>This approach obtains results consistent with those obtained by, for instance, taking the mass-binned values for each sample, and joining these together.

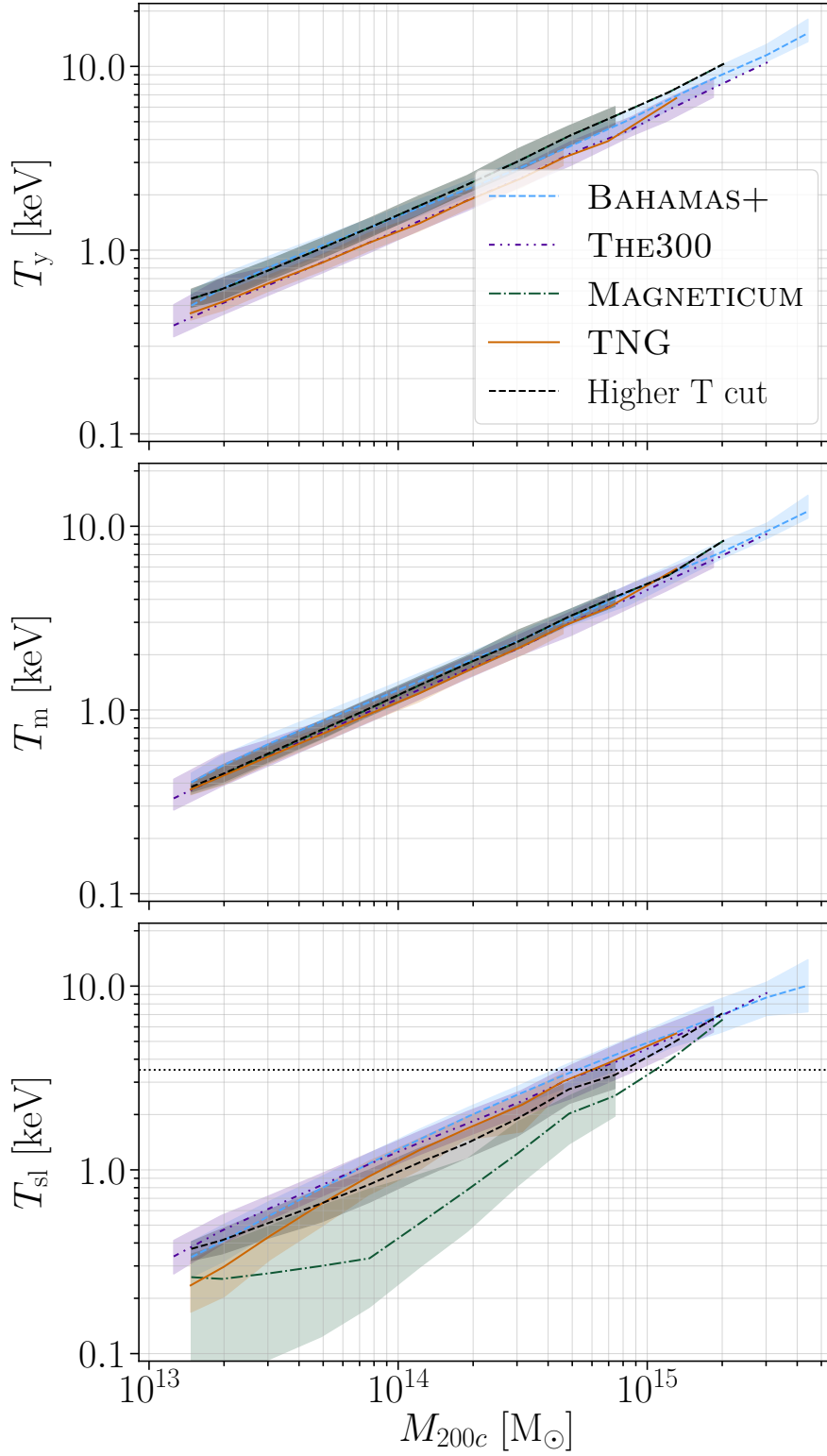


**FIGURE 3.12:** The effects of the temperature cut off on the MAGNETICUM sample at  $z = 0$ . The line labelled 'Higher T cut' are the MAGNETICUM volume averages using a temperature cut of  $T \geq 10^6$  K. Otherwise the figure is as described in Fig. 3.1.

**TABLE 3.5:** The two- and three-parameter fits (Eq. 3.1) and a measure of the intrinsic scatter (Eq. 3.2) in the fits against mass within  $R_{200c}$  at  $z = 0$  for the cross-simulation averaged sample. The errors here are the errors in the fits found through bootstrapping.

	$A$	$B$	$C$	$\sigma_{\log_{10} T}$
$T_y$	$1.465^{+0.002}_{-0.002}$	$0.586^{+0.003}_{-0.002}$	0	$0.1025^{+0.0003}_{-0.0002}$
$T_y$	$1.426^{+0.006}_{-0.007}$	$0.566^{+0.001}_{-0.001}$	$0.024^{+0.005}_{-0.004}$	$0.1011^{+0.0001}_{-0.0001}$
$T_m$	$1.210^{+0.001}_{-0.001}$	$0.591^{+0.003}_{-0.003}$	0	$0.0805^{+0.0002}_{-0.0001}$
$T_m$	$1.207^{+0.005}_{-0.005}$	$0.589^{+0.001}_{-0.001}$	$0.003^{+0.004}_{-0.005}$	$0.0804^{+0.0001}_{-0.0001}$
$T_{sl}$	$1.135^{+0.003}_{-0.003}$	$0.601^{+0.006}_{-0.011}$	0	$0.2067^{+0.0016}_{-0.0008}$
$T_{sl}$	$1.196^{+0.020}_{-0.009}$	$0.641^{+0.003}_{-0.003}$	$-0.048^{+0.007}_{-0.018}$	$0.2028^{+0.0002}_{-0.0001}$

simulations with larger populations of halos. Fits are provided to individual simulations in Table B.3, and the variations in simulation predictions can be easily used to estimate the theoretical, astrophysics-driven uncertainty in the mean temperature-mass relations, for example via the method described in [Anbajagane et al. \(2022a\)](#), see Section 4.3).

When fitting this data to obtain temperature-mass relations, we then consider both a two- and three-parameter fit of the form

$$T = E(z)^{2/3} A \left( \frac{M}{10^{14} \text{ M}_{\odot}} \right)^{B+C \log_{10}(M/10^{14} \text{ M}_{\odot})} \text{ keV}, \quad (3.1)$$

where for the two-parameter fit we set  $C = 0$ .<sup>4</sup> The cross-simulation averaged results at  $z = 0$  for all three temperatures can be found in Table 3.5 – the fits for each individual sample at  $z = 0$  can be found in Table B.3. The errors are obtained through bootstrap techniques and show the error within the mean. Here, we have, as in the previous chapter, also calculated a measure of the scatter through the root-mean-squared dispersion around these mean values,

$$\sigma_{\log_{10} T} = \sqrt{\frac{1}{N} \sum_i \left[ \log_{10} \left( \frac{T_i}{T_{\text{fit}}(M_i)} \right) \right]^2}, \quad (3.2)$$

with  $i$  indexing over all the halos at a given redshift. This measure is weighted more by the lower-mass clusters and groups, due to the larger number of them in each sample than higher-mass haloes. This runs opposite to the fits where we have minimised this bias by fitting to the averages gained from a selection of mass bins.

The first aspect to note is the exceptional lack of curvature in the  $T_m$ – Mass relationship where, even when we allow for curvature,  $C$ , is fully consistent with zero, albeit with a slight tendency towards positive curvature. This is true even if

<sup>4</sup>It is worth noting that this is a different pivot mass to that used in Chapter 2, where  $M_{\text{fid}} = 3 \times 10^{14} \text{ M}_{\odot}$  in comparison to the  $M_{\text{fid}} = 10^{14} \text{ M}_{\odot}$  used in this chapter.

**TABLE 3.6:** The median correction to the amplitude,  $A$ , of the two-parameter fit at each redshift for the temperature measures in the cross-simulation averaged sample. That is, we are tabulating the averaged value  $A^*$ , so that  $E(z)^{-2/3}T_z = A^*T_{z=0}$ . The full two-parameter fits for each redshift can be found in Table B.4.

	$E(z)^{-2/3}T_y$	$E(z)^{-2/3}T_m$	$E(z)^{-2/3}T_{sl}$
$z = 0.00$	1.000	1.000	1.000
$z = 0.25$	$0.982^{+0.002}_{-0.002}$	$0.979^{+0.002}_{-0.001}$	$0.960^{+0.017}_{-0.011}$
$z = 0.50$	$0.976^{+0.002}_{-0.002}$	$0.952^{+0.001}_{-0.001}$	$0.929^{+0.004}_{-0.007}$
$z = 1.00$	$0.944^{+0.002}_{-0.002}$	$0.897^{+0.002}_{-0.002}$	$0.837^{+0.007}_{-0.011}$
$z = 1.50$	$0.919^{+0.002}_{-0.003}$	$0.851^{+0.002}_{-0.002}$	$0.749^{+0.004}_{-0.004}$

the pivot mass of the fit is varied.  $T_y$  has clear positive curvature, as follows from our earlier discussion. On the other hand,  $T_{sl}$  shows some significant negative curvature, but this may be an artifact of the lower-mass haloes' scatter, and may not be representative of the behaviour of observed X-ray temperatures.

It is also important to note that the intrinsic variance is slightly larger in the combined sample than it is in each simulation, due to small bulk offsets between each sample. It should be reiterated, however, that the errors tabulated in Table 3.5 show the errors in the fit parameters, obtained through bootstrapping – as such these do not reflect the 16 and 84 percentile lines plotted in our figures. They also are not only caused by the variation in the mean due to the bulk offsets between simulations. At  $z = 0$ , the intrinsic variance is around  $\pm 6.0\%$  in  $T_m$ ,  $\pm 7\%$  for  $T_y$  and around  $\pm 10\%$  in  $T_{sl}$ . However, a more detailed understanding of the intrinsic variance can be found by looking at the cross-simulation fits to the 16 and 84 percentile lines which are presented in Tables B.1 and B.2.

In general, it is also important to note that there is still a fixed offset between  $T_y$  and  $T_m$  to be found in the combined sample – we find a median offset of around 22% (see Table 3.7). However, as with the discussion in Section 3.3.4, we can consider the minimal offset to be determined by the 1% percentile line – in this case giving a minimum offset of 8.4%. This large variance in  $T_y/T_m$  is, of course, largely driven by the slight disagreement between clusters, which could potentially be broken with future measurements of  $f_{\text{gas}}$ .

This cross-simulation sample can also be used to calculate the redshift evolution of these quantities, and the radial dependence of these results. The first order redshift and radial evolution can be seen in Tables 3.6 and 3.7 akin to those discussed in Section 3.3. The mean two-parameter fits can be found in Table B.4, alongside the full set of two- and three-parameter fits in Tables B.6 and B.7 for the three temperatures within  $R_{500c}$  at  $z = 0$ .

We can see in Table 3.6 that the sample-averaged redshifts show the same variation as expected from considering each sample independently. That is, all of the temperatures diverge from self similarity, with  $T_{sl}$  showing the greatest departure, and  $T_y$  the smallest. However, when looking at high-redshift haloes,

**TABLE 3.7:** The shifts and errors in the radius, mass,  $T_m$  and  $T_y$  over the combined sample against those values within  $R_{200c}$ . These values are calculated on a cluster-by-cluster basis, and then the averages are found within these (e.g., the top left box indicates  $\langle R_{500c}/R_{200c} \rangle = 0.66^{+0.01}_{-0.02}$ ). The central value here is the median with the errors given by the 16 and 84 percentiles.

	$R/R_{200c}$	$M/M_{200c}$	$T_m/T_{m,200c}$	$T_y/T_{y,200c}$
$R_{500c}$	$0.66^{+0.01}_{-0.02}$	$0.71^{+0.05}_{-0.07}$	$1.20^{+0.04}_{-0.07}$	$1.40^{+0.16}_{-0.12}$
$R_{200c}$	1.00	1.00	1.00	$1.22^{+0.11}_{-0.07}$
$R_{500m}$	$1.11^{+0.01}_{-0.01}$	$1.08^{+0.03}_{-0.02}$	$0.95^{+0.01}_{-0.01}$	$1.18^{+0.10}_{-0.06}$
$R_{vir}$	$1.33^{+0.03}_{-0.02}$	$1.22^{+0.08}_{-0.05}$	$0.87^{+0.04}_{-0.02}$	$1.11^{+0.09}_{-0.06}$
$R_{200m}$	$1.64^{+0.06}_{-0.04}$	$1.39^{+0.15}_{-0.10}$	$0.79^{+0.07}_{-0.04}$	$1.05^{+0.09}_{-0.06}$

some departure is nonetheless to be expected. Again, we reiterate that the errors here are the errors in the fit, and as such do not encapsulate any variation in the intrinsic scatter from combining samples. It is also interesting to note that, although not shown here, the  $\sigma_{\log_{10} T}$  values for both these one-parameter corrections and the two-parameter fits that are tabulated in Table B.4 are broadly the same. Although, as previously noted, these will be largely weighted by the lower-mass haloes, this does indicate that most of the evolution is in the amplitude of the scaling relations, and not in their power law.

This redshift evolution is also not linear with respect to redshift, changing faster at lower redshifts. However, we can find a parameterisation of this redshift evolution in the form of

$$\log_{10}(A^*) = p \log_{10}(1+z) + q \log_{10}^2(1+z), \quad (3.3)$$

where  $A^*$  is the redshift correction factor, so  $T_z = A^* E(z)^{2/3} T_{z=0}$ . We find for  $T_y$ ,  $T_m$  and  $T_{sl}$  that the values for  $[p, q]$  are  $[-0.05, -0.11]$ ,  $[-0.08, -0.24]$  and  $[-0.09, -0.57]$ , respectively. However, it is worth noting that at higher redshifts,  $T_{sl}$  becomes an increasingly poor proxy for  $T_x$  as the number of haloes in the samples at temperatures above 3.5 keV diminishes.

The radial corrections tabulated in Table 3.7 do show the effects of combining the samples, where the errors represent the intrinsic variance. The combined sample can be seen to only slightly increase this intrinsic radial variance. While the effects of changing the radius are more complex than a single number can fully encapsulate, this is still useful for an indicative understanding of the effects on viewing clusters through different apertures. However, it is interesting to note that the value of  $T_y/T_m$  at each radius, increases at higher radii. That is, as the radius of interest increases,  $T_m$  decreases faster than  $T_y$  or equivalently,  $T_y$  has a shallower profile. The equivalent values for each sample to those in Table 3.7, can be found in Table B.5.

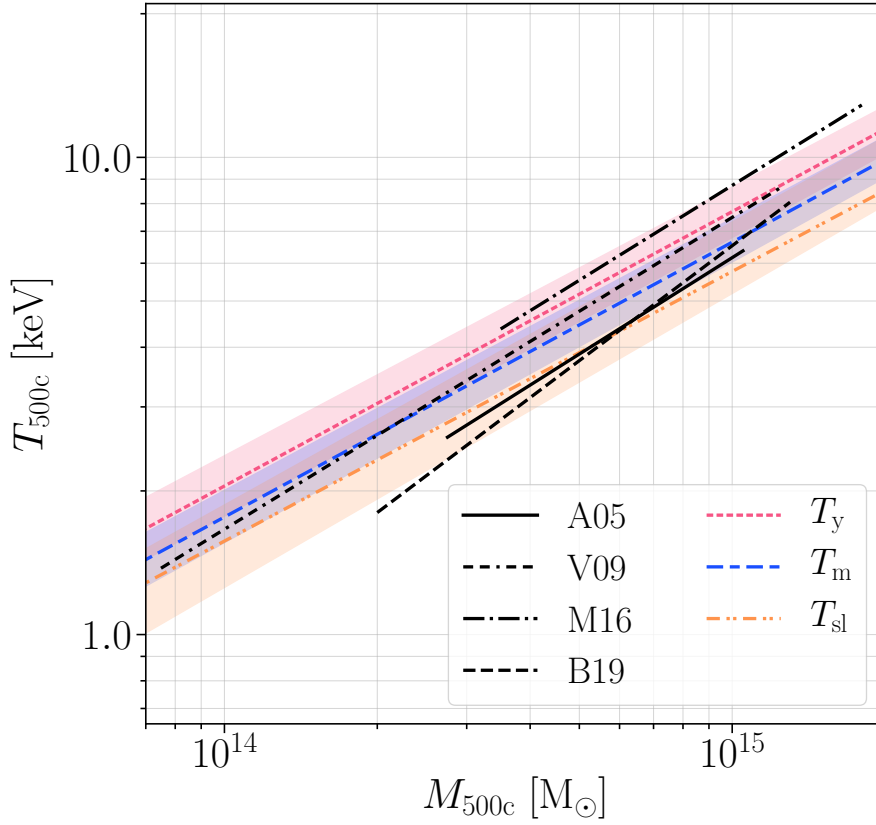


**FIGURE 3.13:** A comparison of the cross-simulation averaged temperature scaling relations, with observational results. Note these quantities are all measured within  $R_{500c}$ . The observational lines are plotted only within the mass range of each study. Here A05, V09, M16 and B19 refer to the fits from [Arnaud et al. \(2005\)](#); [Vikhlinin et al. \(2009a\)](#); [Mantz et al. \(2016\)](#) and [Bulbul et al. \(2019\)](#), respectively. A05 and V09 both depend on the hydrostatic mass bias, for which we here assumed  $1 - b = 0.8$ . Note that these observations should generally be compared to  $T_{sl}$ .



### 3.5.1 Comparison to X-ray observations

There have been many observational studies aiming to constrain the X-ray temperature,  $T_X$ , mass relationship. Here, we consider four such studies to compare to our cross-simulation averaged results. In particular, we have considered [Arnaud et al. \(2005, A05\)](#), [Vikhlinin et al. \(2009a, V09\)](#), [Mantz et al. \(2016, M16\)](#) and [Bulbul et al. \(2019, B19\)](#), all of which provide two-parameter fits for  $T_X$ - $M_{500c}$  relation.

A05, as in the previous chapter, uses 10 low-redshift ( $z < 0.15$ ) clusters from *XMM-Newton*, and obtains masses by fitting an NFW-type profile assuming hydrostatic equilibrium. Here, we use their fits for the subsample of six hot ( $> 3.5$  keV) clusters. V09 uses *Chandra* measurements of 85 clusters (over redshifts of  $z \lesssim 0.9$ ), obtaining through fits of  $\beta$ -profiles, again assuming hydrostatic equilibrium. As such, both A05 and V09's masses are offset from the 'true' mass according to the hydrostatic mass bias. This has been measured many times, both in simulations and using observational techniques, and in this chapter we will use  $(1 - b) = 0.8$ . M16 uses 40 hot ( $> 5$  keV), relaxed clusters observed by *Chandra* (with redshifts  $z \lesssim 1$ ). This work calibrates its masses using weak lensing measurements, so can be taken to be measures of the true mass. Finally, B19 uses 59 clusters from *XMM-Newton*, over redshifts  $0.2 < z < 1.5$ . The masses are obtained through SZ measurements by the South Pole Telescope. This work also provides two different fits for  $T_X$  and here we use their core-excised fits, to compare best with our other measures.

In Figure 3.13, these four fits are shown against the whole-sample fits, here all within  $R_{500c}$ . The length of each line matches the mass range of the data sets used within each observation. It is first worth noticing, that there is no strong consensus between X-ray observations about the details of the  $T_X$ - $M$  relationship. This may be exacerbated by the different techniques used in each study. For B19 and M16 an intrinsic scatter of around 13% is given, while V09 obtains a slightly higher 15 – 20%. These are calculated as  $\sigma_{\ln T}$  and lie a little smaller than those values predicted from our combined simulations.

Here A05 and B19 both use data sets from *XMM-Newton* and agree with each other best, as well as being comparable to the whole-sample  $T_{sl}$  measurement. However, B19 has a far steeper gradient (at  $B = 0.80^{+0.11}_{-0.08}$ ) than any of the other studies, which is at a huge contrast to all of our simulation fits which indicate gradients always less than self-similarity (that is  $B < 2/3$ ). The other three studies also all have gradients steeper than that obtained through our simulations, all of which are consistent with self-similarity. It is interesting to note that the full sample for A05 (rather than the hot sample displayed here) does also show a shallower gradient more compatible with our simulation results.

M16 shows the most extreme result, tending towards far higher temperatures than seen in the other scalings, and higher even than the  $T_y$  values we have

found within simulations. This may be a side effect of the sample selection towards hot clusters, pushing the average up, or may indicate the intrinsic spread within the  $T_X$  relationship. V09, the other measurement using *Chandra* observations, also lies higher than the *XMM-Newton* values, indicating an X-ray temperature more consistent with our simulation  $T_m$  values, than  $T_{sl}$ .

It is still unclear whether the variation observed here between the observational methods and simulations, indicates that simulations are not capturing some facet of real galaxy clusters, or are miscalibrated, or if this comes from the difficulties in obtaining ‘true’ masses from observations. A factor which could be exacerbated by the suggested intrinsic spread in the  $T_X$  relationship and the comparatively (when compared to the data sets from simulations) small data sets and mass ranges used within observational studies. Either way, the  $T_y$  temperature is not directly accessible by any of these X-ray studies and we thus instead recommend using the scalings derived here in future modeling of SZ observables.

## 3.6 Discussion

### 3.6.1 $T_y$ - $Y$ self-calibration

The  $T_y$ - $Y$  relation can be used in the SZ signal modeling once the  $Y$ -parameter is determined. This allows one to refine the SZ model (with the relativistic SZ corrections) even if the data for individual systems cannot provide a direct constraint on  $T_y$ . The observed  $Y$  can also differ from the true  $Y$  due to angular resolution (caused by the instrument beam) but when the resolution is  $\lesssim 1$  arcmin, these smoothing effects in  $Y$  are negligible (Yang et al., 2022), and so the true  $Y$  -  $T_y$  relation presented here can be used directly on observed data without needing any further processing. Similarly, the  $Y$  -  $T_y$  relation can easily be used in simulations of the SZ sky, where from the simulation the cluster temperature is not directly available, e.g., in the WebSky (Stein et al., 2020).

Here, I will briefly discuss the scaling relationship we have determined, alongside the effects we may be able to determine with these results. As noted, we find some complexity in this relationship, with varying levels of curvature, especially at small values of  $Y$ . As such, we have tabulated the two- and three-parameter fits for the  $T_m$  -  $Y$  and  $T_y$  -  $Y$  relationships in Table B.8. The equivalents for the medians for each sample can also be found in Table B.9.

However, we can create more stable two-parameter fits if we exclude the smallest halos with  $Y < 10^{-6} \text{ Mpc}^2$ , which are unlikely to meaningfully contribute to SZ observations, and which, even when they can be observed, will have the smallest rSZ corrections. With this restriction and

$$T = E(z)^{2/5} A \left( \frac{Y}{10^{-5} \text{ Mpc}^2} \right)^B \text{ keV}, \quad (3.4)$$

**TABLE 3.8:** The two parameter  $T_y$ - $Y$  fits (Eq. 3.4) for haloes with  $Y_{200c} > 10^{-6} \text{ Mpc}^2$ , and a measure of the intrinsic scatter (Eq. 3.2) in the fits across redshifts for the median of the cross-simulation averaged sample within  $R_{200c}$ .

	$A$	$B$	$\sigma_{\log_{10} T}$
$z = 0.00$	$2.614^{+0.006}_{-0.006}$	$0.368^{+0.003}_{-0.010}$	$0.1874^{+0.0039}_{-0.0152}$
$z = 0.25$	$2.593^{+0.007}_{-0.007}$	$0.372^{+0.002}_{-0.005}$	$0.1685^{+0.0036}_{-0.0074}$
$z = 0.50$	$2.593^{+0.008}_{-0.008}$	$0.381^{+0.003}_{-0.002}$	$0.1625^{+0.0034}_{-0.0033}$
$z = 1.00$	$2.585^{+0.013}_{-0.012}$	$0.382^{+0.004}_{-0.004}$	$0.1388^{+0.0044}_{-0.0045}$
$z = 1.50$	$2.597^{+0.052}_{-0.031}$	$0.373^{+0.020}_{-0.011}$	$0.1263^{+0.0185}_{-0.0091}$

fits for the combined sample at each redshift can be found and are given in Table 3.8 (a full form including the 16 and 84 percentiles can be found in Table B.10). It is immediately clear that there is little redshift dependence beyond the expected self-similar evolution.

While there is more intrinsic variation in this relationship than within the  $T_y - M$  relationships, it can still be used as a reliable proxy to estimate the relativistic effects to haloes. Moreover, as our understanding of  $f_{\text{gas}}$  in clusters improves, this uncertainty between clusters may be able to be reduced, as this would allow a greater understanding of the true  $M_{\text{gas}}$  values we should expect for haloes, and thus a more precise idea of exactly how the  $T_y - Y$  relationship can be expected to behave.

With those comments in mind, a sense of the expected corrections can be gained for a given cluster. For instance, from the simulations we can estimate that a cluster with a true  $Y_{200c} = 10^{-4} \text{ Mpc}^2$  at  $z = 0$ , would have a temperature of  $6.1^{+0.8}_{-1.1} \text{ keV}$ , where the errors here are driven almost entirely by the disagreement between the simulations. This would lead to a fractional change in the amplitude at 353 GHz of  $0.907^{+0.016}_{-0.011}$  – that is, a 10% underestimation of  $Y$  by using the non-relativistic approximation.

It is also important to remember that the relativistic corrections to the kinetic SZ (kSZ) effect, will be driven by  $T_m$  and not  $T_y$ . The kSZ effect has not been discussed in much detail in this chapter, but nonetheless detailed studies of kSZ signals should also consider the impact that this signal may have. These relativistic kSZ effects, are, however, broadly speaking an order of magnitude smaller than the relativistic tSZ correction (e.g., Sazonov & Sunyaev, 1998; Nozawa et al., 2006; Chluba et al., 2012b). Still, the relations given here can be used to model the effects.

### 3.6.2 Applications to current and future SZ analyses

Finally, it is worth briefly discussing where the obtained scaling relations may have applications in current and future studies of the SZ effect. First and foremost, due to sensitivity or spectral coverage, current SZ measurements are still

not directly sensitive to the rSZ effect. However, the rSZ effect already affects the inference of cosmological parameters, when it is neglected in modelling. An important example comes in the SZ power spectrum analysis, where rSZ can lead to an underestimation of the  $y$ -power spectrum, and cause a systematic shift in the inferred value of  $\sigma_8$  (Remazeilles & Chluba, 2020). It will also similarly impact cross-correlations of the SZ field with large-scale structure fields such as cosmic shear or galaxy positions. These measurements have recently been used to infer physics like the redshift-dependent mean thermal pressure of the Universe as well as the energetics of feedback in groups and clusters (e.g., Osato et al., 2018, 2020; Pandey et al., 2019, 2022; Gatti et al., 2022).

The ease of determining the rSZ bias observationally will also depend on the experimental configuration. For instance, many planned CMB experiments have all their channels at  $\nu \lesssim 220$  GHz. In these cases, the degeneracy between  $T_y$  and  $y$  cannot be easily broken through observations. However, updated scaling relations, such as those provided here will allow for the rSZ corrections to be included in the theoretical modelling of the data.

As with the SZ power-spectrum analyses, the SZ cluster number count analyses will almost certainly be affected by the rSZ effect. Here there are two important aspects. Firstly, at a certain mass, the SZ flux will be diminished due to rSZ, so that clusters will be assigned to lower signal-to-noise bins. Additionally, the multi-match-filtering (MMF) method (Melin et al., 2006) used to extract the clusters will not be optimally tuned for the correct spectral shapes, leading to a misestimation of the noise. Scaling relations can be directly used to inform the MMF and reduce the impact of the rSZ effect. The  $T_y - Y$  relation in particular will be relevant as it would allow for the construction of an iterative MMF approach (e.g., Zubeldia et al., 2022), to incorporate rSZ effects based solely on SZ observables. This would allow for a more robust comparison of theory and observation, and to improve the constraining power of the obtained SZ catalogs.

The rSZ effect also impacts studies on the thermodynamics of cluster outskirts ( $R \gtrsim R_{200m}$ ) – especially non-thermal features like cosmological accretion shocks (Aung et al., 2021; Baxter et al., 2021) – which contain astrophysical and cosmological information (see Walker et al., 2019, for a review) and have only recently been observationally explored. Anbajagane et al. (2022b) performed the first large population-level analysis of tSZ profile outskirts and found signs of cosmological shocks, which manifest as decrements in the profile. Others have seen similar signs using samples of up to ten clusters (e.g., Hurier et al., 2019; Pratt et al., 2021). However, the rSZ effect *also* causes a tSZ signal reduction. As such, a better understanding of the rSZ corrections – and the magnitude of the tSZ decrement – will be necessary to robustly infer the non-thermal pressure contributions (Shi et al., 2016a; Aung et al., 2021) and plasma physics in these outskirts (Rudd & Nagai, 2009; Avestruz et al., 2015).

As already discussed for Figure 3.2,  $T_y$  has a mass scaling relation which is

very close to self-similarity with redshift. However, it is important to emphasise that there is nonetheless significant redshift evolution *due to* self-similarity alongside the minor corrections observed. This effect can have important consequences for cosmological inferences relying on the redshift-independence of the SZ effect. One such example is attempts to use SZ effects to measure the CMB temperature-redshift relation (Rephaeli, 1980; Luzzi et al., 2009), or to calculate SZ-derived values of the Hubble constant (e.g., Birkinshaw et al., 1991; Mauskopf et al., 2000; Wan et al., 2021, described in more detail in the previous chapter). Similarly, applications using SZ measurements to constrain possible time-variations of the fine-structure constant (Bora & Desai, 2021) may be affected by the redshift dependence of the rSZ effect. Using  $T_y - Y$  relations like those provided here allow the rSZ effects on these inferences to be marginalised over.

A final application of these rSZ measurements relates to predictions of the all-sky averaged SZ and rSZ effects (Hill et al., 2015). This signal is a target of future CMB measurements (Chluba et al., 2021) and could inform us about feedback processes in cluster physics (e.g., Thiele et al., 2022). The temperature relations like those provided here allow for these predictions to be refined, to give a simulation-averaged view on the expected signal. Similarly, these relations could be used to refine the calculations of the radio (Holder & Chluba, 2021; Lee et al., 2022a, described in more detail in Chapter 4) and CIB SZ (Sabyr et al., 2022; Acharya & Chluba, 2022) effects. These signals could become important targets for future radio and sub-mm observations, allowing us to probe the evolution and origin of the cosmic radio and infra-red backgrounds.

### 3.7 Conclusions

This chapter presents detailed comparisons of three cluster temperature measures: (a) the average rSZ temperature; (b) the mass-weighted temperature relevant for the thermal SZ (tSZ) effect; and (c) X-ray spectroscopic temperature using the BAHAMAS & MACSIS, ILLUSTRIS-TNG, MAGNETICUM, and THE THREE HUNDRED PROJECT simulations. We analyzed gas temperature scaling relations of galaxy groups and clusters with  $M_{500c} > 10^{13} M_{\odot}$ , over five redshifts between  $z = 0$  to  $z = 1.5$ . We provided fits to multiple scaling relations for individual simulations and for a combined cross-simulation sample, with the former ensemble of results also providing an estimate of the theoretical, astrophysics-driven uncertainty in the relations. The main results are summarized as follows:

- There is an exceptionally strong agreement for  $T_m$  between all four simulations with  $M_{200c}$ .  $T_y$  is consistently larger than  $T_m$  (by an average of  $\simeq 22\%$ ), which is generally a little above  $T_{sl}$  at  $z = 0$ .  $T_y$  has a good agreement

between the simulations, however, there is variation in the exact magnitude of the offset between  $T_y$  and  $T_m$  between simulations.  $T_{sl}$  also shows agreement, although it is also subject to a great deal more intrinsic scatter than the other two temperatures. All three temperature measures exhibit different mass scalings and vary differently with redshift and radius.

- All three temperature measures exhibit deviation from the self-similar evolution. At higher redshifts, they all fall below the expected  $E(z)^{-2/3}$  scaling indicating all haloes will have lower temperatures at higher redshifts than the self-similar model prediction. However,  $T_y$  evolves very closely to self-similarity, while the other temperature measures depart further from self-similarity, so that at higher redshifts, all three temperature measures increasingly diverge.  $T_y$  has an increasing correction relative to  $T_m$  and an even larger correction to  $T_{sl}$ .
- The temperature measures all agree best within  $R_{200c}$  between simulations. Each simulation and temperature measure has a different radial profile leading to varied results. While the temperature measures still agree well within  $R_{500c}$ , the improvement at  $R_{200c}$  indicates this may indeed be an optimal radius to study SZ science.
- The gas fraction, feedback methods and resolution all vary significantly between the simulations. In light of this, the level of agreement we see is startling, and indicates that much of the SZ gas physics is sufficiently calibrated by the microphysical constraints (i.e., stellar properties). However, when examined in more detail, the gas fraction is found to correlate with the variation in  $T_y$  between simulations. As such, if this can be determined with more accuracy in future observations, the strength of these predictions may increase. In general, when we study resolution and feedback within equivalently calibrated simulations, we find little variation to our observed SZ temperature measures, while  $T_{sl}$  is affected slightly more.
- We created a cross-simulation sample and found the fitted values for the temperatures. In general,  $T_m$  shows a limited tendency towards curvature (i.e., a mass-dependent slope), while  $T_y$  has positive curvature, and  $T_{sl}$  negative curvature. We provide a simple regime for calculating the redshift corrections to temperatures within our redshift range, and clarified the broad effects of varying the radial aperture which we use to define haloes. When compared to observational results, we find that the temperatures broadly agree. However, there is more variation within X-ray results than our predictions, making it difficult to draw out strong conclusions. Nonetheless, observations all suggest steeper scaling relations than we have found in the simulations.

- In general, while these temperatures will be difficult to directly measure, they give rise to the possibility of self-calibrating SZ observations, to allow for relativistic corrections to be used within the determination of SZ measurements themselves. The simulations suggest that for a halo with a true  $Y_{200c} \simeq 10^{-4} \text{ Mpc}^2$ , we would measure a 10% underestimation of  $Y$  by neglecting relativistic effects. We provide  $T_y - Y$  relations to allow for further detailed modelling.

Future and ongoing experiments such as CCAT-Prime (Stacey et al., 2018), NIKA2 (Adam et al., 2018), TolTEC (Austermann et al., 2018), and The Simons Observatory (Ade et al., 2019) offer an exciting potential for measuring the ICM temperature using the rSZ effect. This will enable comprehensive analyses of the ICM structure and evolution, especially for high-redshift clusters where X-ray temperatures are difficult to obtain. These will also provide an observational test for the validity of the simulation results presented here. Where rSZ temperatures cannot be directly measured, we have provided temperature scaling relations that can be used widely to estimate the impact and potential constraining power of the relativistic SZ effects in future measurements.

## Chapter 4

# Refined modelling of the radio SZ signal: kinematic terms, relativistic temperature corrections and anisotropies in the radio background

This chapter is based on the published work, [Lee et al. \(2022a\)](#). The figures were generated using modifications to the code SZpack. The novel analytics and analysis was done by EL with input and interpretation from my coauthors.

### 4.1 Introduction

As briefly discussed in Section 1.4, galaxy clusters (or other giant bodies of hot, free electrons) can be considered as *operators* on any background source of photons (e.g., [Syunyaev, 1971](#); [Kamionkowski & Loeb, 1997](#); [Cooray, 2006](#); [Kholupenko et al., 2015](#); [Grebenev & Sunyaev, 2020](#)). Any such source, assuming the photons have energies that are much lower than those of the scattering electrons, will gain a similar kind of distortion from passing through the cluster (see Chapter 6 or [Sarkar et al., 2019](#), for a more detailed review of the Compton process). The distortion from each photon source can be considered separately and then combined to understand the total distortion to the background photon distribution.

The radio background has been considered several times over recent years ([Fixsen et al., 2011](#); [Seiffert et al., 2011](#); [Singal et al., 2018](#); [Dowell & Taylor, 2018](#)); however, its origin is still not well understood (e.g., [Feng & Holder, 2018](#); [Mittal & Kulkarni, 2022](#)). With all this in mind, [Holder & Chluba \(2021\)](#) showed that a basic analysis of the low-frequency radio background would reveal a distortion



which, when combined with the standard CMB SZ signal, would exhibit a null at around  $\nu \simeq 735$  MHz if the background truly is cosmological. As such, using the radio SZ effect, the origin of the radio background could be studied using methods similar to those employed for the standard SZ effect but at significantly lower frequencies.

In this chapter, I consider the kinematic and relativistic corrections to this combined radio and CMB SZ signal and how they will appear at low frequencies. Effects from the scattering of radio-background anisotropies will also be discussed. Much of the physical intuition is completely analogous to the standard SZ effect; however, due to the steepness of the radio background spectrum, several interesting differences arise as will be highlighted here.

## 4.2 The radio SZ signal

To derive the detailed expressions for the radio SZ signal, the analysis is based on the asymptotic expansion of the Compton collision term. For the standard SZ effect, these expansions have been written in many forms (Sazonov & Sunyaev, 1998; Challinor & Lasenby, 1998; Itoh et al., 1998), but here I will follow the formulation of Chluba et al. (2012b), henceforth CNSN.

### 4.2.1 A summary of the SZ formalism

We can recall from Chapter 1, that the phase space density can be written as (cf. Eq. 1.5)

$$\frac{\partial n}{\partial t} \simeq c \int \frac{d\sigma}{d\Omega'} [f'n' - fn] d^2\hat{\gamma}' d^3p. \quad (4.1)$$

Assuming that the electrons are fully thermalised, their phase space density can then be modelled as a relativistic Maxwell-Boltzmann distribution, which has the form

$$f(\mathbf{p}) = \frac{N_e e^{-\gamma/\theta_e}}{4\pi(m_e c)^3 K_2(1/\theta_e)\theta_e} \quad (4.2)$$

for total electron number density,  $N_e = \int d^3p f(\mathbf{p})$ . Here,  $K_2$  is the modified Bessel function of the second kind. Then, by expressing  $n(x', \hat{\gamma}')$  in terms of spherical harmonic functions  $Y_{\ell m}(\hat{\gamma}')$  with coefficients  $n_{\ell m}(x')$ , the Boltzmann equation can be rewritten, by expanding in terms of the frequency shift<sup>1</sup>  $\Delta_\nu = \frac{(\nu' - \nu)}{\nu} \ll 1$ , as

$$\begin{aligned} \frac{\partial n(x, \hat{\gamma})}{\partial \tau} &\simeq -n(x, \hat{\gamma}) + \sum_{k=0}^{\infty} \sum_{\ell, m} I_{\ell m}^k x^k \partial_x^k n_{\ell m}, \\ I_{\ell m}^k &= \frac{1}{N_e \sigma_T k!} \int \frac{d\sigma}{d\Omega'} f(\mathbf{p}) \Delta_\nu^k Y_{\ell m}(\hat{\gamma}') d^2\hat{\gamma}' d^3p. \end{aligned} \quad (4.3)$$

<sup>1</sup>Recall that  $x$  is a dimensionless frequency, defined  $x = h\nu/k_B T_{\text{CMB}}$ .

The kernel moments  $I_{\ell m}^k$  are only functions of the electron temperature (for  $h\nu \ll k_B T_e$ ) and independent of the energy-dependence of the photon distribution, which is encoded by the terms  $x^k \partial_x^k n_{\ell m}$ .

### 4.2.2 The asymptotic expansion

The moments  $I_{\ell m}^k$  can be considered in terms of a temperature expansion about  $\theta_e \ll 1$ . Up to a fixed temperature, this truncates the expression in Eq. (4.3). At high-frequencies ( $x \gtrsim 5$ ), this approach does not converge for the standard SZ effect (see CNSN for in-depth discussion); however, at low frequencies (as required for the radio SZ effect), this expansion remains accurate to extremely high cluster temperatures (i.e.,  $T_e \simeq 40$  keV or  $\theta_e \simeq 0.07$ ), as will be illustrated later in this chapter.

Assuming there is negligible *CMB frame* anisotropy in the unscattered photon distribution, i.e.,  $n(x, \hat{\gamma}) \approx n(x)$ , and ignoring effects of polarisation (since they will be small), all anisotropy in the system will accordingly come from the motion of the cluster relative to the CMB rest frame. For a cluster moving at dimensionless speed  $\beta_c = v_c/c$  and in a direction  $\tilde{\mu}_c = \cos \theta_c$  relative to the line of sight as measured in the *cluster frame*, the change in the photon occupation number due to Compton scattering is given by (compare Eq. (12) of CNSN)

$$\begin{aligned} \Delta \tilde{n} \simeq & \tau \theta_e \sum_{k=0}^{\infty} \theta_e^k \tilde{\mathcal{Y}}_k + \tau \beta_c^2 \theta_e \sum_{k=0}^{\infty} \theta_e^k \tilde{\mathcal{M}}_k \\ & + \tau \tilde{\mu}_c \beta_c \left( -\tilde{x} \partial_{\tilde{x}} \tilde{n} + \theta_e \sum_{k=0}^{\infty} \theta_e^k \tilde{\mathcal{D}}_k \right) \\ & + \tau P_2(\tilde{\mu}_c) \beta_c^2 \left( -\frac{3}{10} \tilde{x}^2 \partial_{\tilde{x}}^2 \tilde{n} + \theta_e \sum_{k=0}^{\infty} \theta_e^k \tilde{\mathcal{Q}}_k \right). \end{aligned} \quad (4.4)$$

Here, the Compton- $y$  parameter is the line-of-sight integrated,  $y = \int \theta_e N_e \sigma_T c dt = \tau \theta_e$ , and we use the Legendre polynomial  $P_2(\mu) = 3(\mu^2 - 1)/2$ . In Eq. (4.4), tildes (e.g.,  $\tilde{\mu}_c$ ,  $\tilde{n} = n(\tilde{x})$ ) indicate that these quantities are being calculated in the cluster frame. This distinction has been dropped for the electron temperature and number density that enter the scattering  $y$ -parameter, but it should be emphasized that these are cluster-frame quantities (see CNSN for a detailed discussion).

In practice, the sums in Eq. (4.4) converge quickly at  $\tilde{x} \ll 1$ , and summing up to  $k = 10$  gives a very high-precision result. The functions  $\tilde{\mathcal{Y}}_k$ ,  $\tilde{\mathcal{M}}_k$ ,  $\tilde{\mathcal{D}}_k$  and  $\tilde{\mathcal{Q}}_k$  can

be written as (see CNSN):

$$\begin{aligned}
 \tilde{\mathcal{Y}}_k &= \sum_{j=1}^{2k+2} a_j^k \hat{\mathcal{O}}_{\tilde{x}}^j \tilde{n}, \\
 \tilde{\mathcal{M}}_k &= \sum_{j=1}^{2k+2} \frac{a_j^k}{6} \left[ j(j+2) \hat{\mathcal{O}}_{\tilde{x}}^j + (2j+3) \hat{\mathcal{O}}_{\tilde{x}}^{j+1} + \hat{\mathcal{O}}_{\tilde{x}}^{j+2} \right] \tilde{n}, \\
 \tilde{\mathcal{D}}_k &= \sum_{j=0}^{2k+2} d_j^k \left[ j \hat{\mathcal{O}}_{\tilde{x}}^j + \hat{\mathcal{O}}_{\tilde{x}}^{j+1} \right] \tilde{n}, \\
 \tilde{\mathcal{Q}}_k &= \sum_{j=0}^{2k+2} \frac{q_j^k}{3} \left[ j(j-1) \hat{\mathcal{O}}_{\tilde{x}}^j + 2j \hat{\mathcal{O}}_{\tilde{x}}^{j+1} + \hat{\mathcal{O}}_{\tilde{x}}^{j+2} \right] \tilde{n}.
 \end{aligned} \tag{4.5}$$

For convenience, the differential operator has been defined,  $\hat{\mathcal{O}}_{\tilde{x}}^k = \tilde{x}^k \partial_{\tilde{x}}^k$ . The coefficients  $a_j^k$ ,  $d_j^k$  and  $q_j^k$  can be found tabulated in CNSN and are directly related to the moments,  $I_{\ell m}^k$ . They are part of SZpack and available up to 10<sup>th</sup> order in  $\theta_e$ . Multiple-scattering effects have been neglected (Chluba et al., 2014; Chluba & Dai, 2014)

In Eq. (4.4),  $\tilde{\mathcal{Y}}_k$  describes the thermal SZ effect combined with its rSZ corrections;  $\tilde{\mathcal{D}}_k$  and  $\tilde{\mathcal{Q}}_k$  are the first- and second-order (dipole and quadrupole) kinematic corrections, with their higher-order temperature terms;  $\tilde{\mathcal{M}}_k$  contains the kinematic correction to the monopole signal, and its higher-order temperature corrections. No temperature-independent terms arise as Thomson scattering ( $\propto \tau \beta_c^2$ ) of the radiation monopole does not modify the field. The combination of dipole, quadrupole and monopole corrections, together give the kSZ effect to second order in  $\beta_c$ . Their temperature corrections are, in general, also referred to as rSZ effects. These functions are all examined in more detail in CNSN.

### Final signal in the CMB rest frame

The details of converting between frames are explored in detail in CNSN. However, here I will summarise and expand on these results. To transform the distortion into the CMB rest frame, one must perform a Lorentz transformation on the variables. In particular, as the relative speed  $\beta_c$  has already been defined, we find

$$\begin{aligned}
 \tilde{x} &= \gamma_c x (1 - \beta_c \mu_c), \\
 \tilde{\mu}_c &= \frac{\mu_c - \beta_c}{1 - \beta_c \mu_c}.
 \end{aligned} \tag{4.6}$$

Due to the invariance of the photon occupation number, one can then simply use these expressions in Eq. (4.4) when evaluating the distortion. Here,  $\tilde{x}$  and  $\tilde{\mu}_c$  are defined in the cluster frame as before, and  $x$  and  $\mu_c$  are defined in the CMB frame;  $\beta_c$  (and accordingly  $\gamma_c = 1/\sqrt{1 - \beta_c^2}$ ) is identical in both frames. In

principle, the modifications of  $\theta_e$ ,  $\tau$  and  $y$  could also be considered between the two frames; however, in this chapter, these quantities are always defined in the *cluster frame*, since this is the frame in which these values have a clear physical meaning. Further justifications of this can be found in CNSN.

Alternatively, instead of transforming the variables before calculating the results, it is possible to substitute the relations, Eq. (4.6), into Eqs. (4.4) and (4.5), and then expand up to second order in  $\beta_c \ll 1$ . After some simplification one can then write (compare Eq. (25) of CNSN)

$$\begin{aligned} \Delta n \simeq & \tau \theta_e \sum_{k=0}^{\infty} \theta_e^k \mathcal{Y}_k + \tau \beta_c^2 \left( \left[ x \partial_x + \frac{1}{3} x^2 \partial_x^2 \right] n + \theta_e \sum_{k=0}^{\infty} \theta_e^k \mathcal{M}_k \right) \\ & + \tau \mu_c \beta_c \left( -x \partial_x n + \theta_e \sum_{k=0}^{\infty} \theta_e^k \mathcal{D}_k \right) \\ & + \tau P_2(\mu_c) \beta_c^2 \left( \frac{11}{30} x^2 \partial_x^2 n + \theta_e \sum_{k=0}^{\infty} \theta_e^k \mathcal{Q}_k \right). \end{aligned} \quad (4.7)$$

Here, the functions  $\mathcal{M}_k$ ,  $\mathcal{D}_k$  and  $\mathcal{Q}_k$  are modified, (while  $\mathcal{Y}_k = \tilde{\mathcal{Y}}_k$ ) and furthermore leading-order terms to the monopole correction and quadrupole terms are also changed, due to boosting and aberration effects. The transformed distortion functions become<sup>2</sup>

$$\begin{aligned} \mathcal{Y}_k &= \tilde{\mathcal{Y}}_k, \\ \mathcal{M}_k &= \sum_{j=1}^{2k+2} \frac{a_j^k - d_j^k}{3} \left[ j(j+2) \hat{\mathcal{O}}_x^j + (2j+3) \hat{\mathcal{O}}_x^{j+1} + \hat{\mathcal{O}}_x^{j+2} \right] n, \\ \mathcal{D}_k &= \sum_{j=0}^{2k+2} (d_j^k - a_j^k) \left[ j \hat{\mathcal{O}}_x^j + \hat{\mathcal{O}}_x^{j+1} \right] n, \\ \mathcal{Q}_k &= \sum_{j=0}^{2k+2} \frac{q_j^k - 2d_j^k + a_j^k}{3} \left[ j(j-1) \hat{\mathcal{O}}_x^j + 2j \hat{\mathcal{O}}_x^{j+1} + \hat{\mathcal{O}}_x^{j+2} \right] n. \end{aligned} \quad (4.8)$$

Note that  $a_0^k = 0$ , since this is not explicitly mentioned in CNSN. It is also worth noting that when doing these conversions directly, many of the corrections come from expressing  $n(\tilde{x})$  in terms of an expansion in  $\beta_c$  around  $n(x)$ . With these expressions, we can proceed to obtain the radio SZ signal in the cluster and CMB rest frames. It should also be highlighted that at second order in  $\beta_c$ , the expressions in the CMB rest frame *do not agree* with previous works, as was clarified in CNSN. Luckily, corrections at the level of  $\beta_c^2$  usually remain subdominant. However, recent works on using terms  $\propto \beta_c \theta_e$  to learn about large-scale structure (e.g., Coulton et al., 2020) may also be affected, as subtle differences in these terms arise (see CNSN).

<sup>2</sup>These functions are also used explicitly in SZpack but the expressions were not given in this form in CNSN.

### 4.2.3 The radio SZ signal

For the normal SZ effect as caused by the CMB, the blackbody occupation of  $n_{\text{CMB}} = 1/(e^x - 1)$  is used. The radio background has been estimated in [Fixsen et al. \(2011\)](#). These results were used in [Holder & Chluba \(2021\)](#), where the radio photon density was expressed as

$$n_{\text{R}} = \frac{A_{\text{R}} f(z)}{x_0} \left( \frac{x}{x_0} \right)^{-\alpha}. \quad (4.9)$$

Here,  $\alpha = 3.59 \pm 0.04$  is the radio spectral index,  $A_{\text{R}} = 8.84 \pm 0.77$  is the normalization at  $z = 0$ ,  $x_0 = 5.46 \times 10^{-3}$  and  $f(z)$  is the fraction of the radio excess that is present at a given redshift to account for any change in the radio background over time. If the radio background is fully cosmological and formed at much higher redshifts than the clusters, we would expect  $f(z) = f(z = 0) = 1$ . This formulation also assumes that there is no redshift variation in  $\alpha$ . Since  $x$  is redshift independent, as with the typical SZ signal, there will be no redshift evolution of the signal beyond that caused by the redshift evolution of the background i.e.,  $f(z)$  itself.

The derivatives of the CMB density are complicated, but can be written in closed form (see Appendix A2 of CNSN) as

$$x^k \partial_x^k n_{\text{CMB}} = \left( \frac{-x}{1 - e^{-x}} \right)^k \sum_{m=0}^{k-1} \left\langle \begin{matrix} k \\ m \end{matrix} \right\rangle e^{-mx} n_{\text{CMB}}, \quad (4.10)$$

where the coefficients  $\langle \dots \rangle$  denote the Eulerian Numbers. The latter determine the number of permutations of the numbers 1 to  $m$  in which exactly  $k$  elements are greater than the previous element. The derivatives of the Planck function exhibit very strong frequency dependence in the Wien-tail ( $x \gg 1$ ). This implies that relativistic corrections can in principle be used to measure the cluster temperature and velocity.

In contrast, for a radio-like background with  $n_{\text{R}} = Ax^{-\alpha}$ , we find

$$x^k \partial_x^k n_{\text{R}} = (-1)^k \frac{\Gamma(\alpha + k - 1)}{\Gamma(\alpha - 1)} n_{\text{R}}, \quad (4.11)$$

with  $\Gamma(\dots)$  the Gamma function. This expression implies that the relativistic corrections to the radio SZ signal do not alter the spectral shape of the radio signal, and they in total combine merely to change the amplitude of the signal. This means the cluster temperature and velocity cannot be independently determined using only the radio contribution.

It is worth noticing that, since at low frequencies the CMB background can be approximated as a power-law with  $\alpha = 1$  (i.e.,  $n_{\text{CMB}} \approx 1/x$ ), the rSZ effects are equally well behaved at  $x \ll 1$  and also do not show any new spectral shape.

Indeed from Eq. (4.10) it follows that

$$x^k \partial_x^k n_{\text{CMB}} \approx (-1)^k \sum_{m=0}^{k-1} \left\langle \begin{matrix} k \\ m \end{matrix} \right\rangle n_{\text{CMB}} = (-1)^k k! n_{\text{CMB}}, \quad (4.12)$$

where the identity  $\sum_{m=0}^{k-1} \langle \dots \rangle = k!$  has been used, which directly follows from the combinatorial definition of the Eulerian numbers. This result agrees with the one obtained from Eq. (4.11) for  $\alpha = 1$ .

### Expression inside cluster frame

Using the expressions from above, Eq. (4.5) can be simplified to

$$\begin{aligned} \tilde{\mathcal{Y}}_k^{\text{R}} &= \tilde{n}_{\text{R}} \sum_{j=1}^{2k+2} (-1)^j \frac{(\alpha + j - 1)!}{(\alpha - 1)!} a_j^k, \\ \tilde{\mathcal{M}}_k^{\text{R}} &= \tilde{n}_{\text{R}} \sum_{j=1}^{2k+2} \frac{(-1)^j}{6} \frac{(\alpha + j - 1)!}{(\alpha - 1)!} a_j^k \alpha(\alpha - 2), \\ \tilde{\mathcal{D}}_k^{\text{R}} &= \tilde{n}_{\text{R}} \sum_{j=0}^{2k+2} (-1)^j \frac{(\alpha + j - 1)!}{(\alpha - 1)!} d_j^k (-\alpha), \\ \tilde{\mathcal{Q}}_k^{\text{R}} &= \tilde{n}_{\text{R}} \sum_{j=0}^{2k+2} \frac{(-1)^j}{3} \frac{(\alpha + j - 1)!}{(\alpha - 1)!} q_j^k \alpha(\alpha + 1). \end{aligned} \quad (4.13)$$

These are the expressions for the radio background with general  $\alpha$  that can be used in Eq. (4.4). For  $\alpha = 1$ , they equally apply to the standard SZ effect at low frequencies. The first few terms of these can then be written as

$$\begin{aligned} \tilde{\mathcal{Y}}_0^{\text{R}} &= \tilde{n}_{\text{R}} \alpha(\alpha - 3), \\ \tilde{\mathcal{Y}}_1^{\text{R}} &= \frac{\tilde{n}_{\text{R}}}{10} \alpha(\alpha - 3)(7\alpha^2 - 21\alpha - 3), \\ \tilde{\mathcal{Y}}_2^{\text{R}} &= \frac{\tilde{n}_{\text{R}}}{120} \alpha(\alpha - 3)(44\alpha^4 - 264\alpha^3 + 284\alpha^2 + 336\alpha - 31), \\ \tilde{\mathcal{M}}_0^{\text{R}} &= \frac{\tilde{n}_{\text{R}}}{6} \alpha^2(\alpha - 3)(\alpha - 2), \\ \tilde{\mathcal{D}}_0^{\text{R}} &= \frac{\tilde{n}_{\text{R}}}{5} 2\alpha(\alpha^2 - 3\alpha + 1), \\ \tilde{\mathcal{D}}_1^{\text{R}} &= \frac{\tilde{n}_{\text{R}}}{5} \alpha(2\alpha^4 - 12\alpha^3 + 16\alpha^2 + 6\alpha + 1), \\ \tilde{\mathcal{Q}}_0^{\text{R}} &= \frac{\tilde{n}_{\text{R}}}{30} \alpha(\alpha + 1)(\alpha^2 - 3\alpha - 6). \end{aligned} \quad (4.14)$$

For the monopole and quadrupole terms, we only give the leading-order corrections  $\propto \tau \beta_c^2 \theta_e$ . Note also that  $\tilde{\mathcal{Y}}_0^{\text{R}}$  is the main term of the radio SZ effect (Holder & Chluba, 2021). Inserting  $\alpha = 3.59$  and  $\alpha = 1$ , to second order in temperature

and cluster velocity,

$$\begin{aligned} \frac{\Delta \tilde{n}_R}{\tilde{n}_R} &\approx 2.12y \left[ 1 + 1.18\theta_e - 0.59\theta_e^2 \right] + 2.01\beta_c^2 y \\ &\quad + 3.59\tilde{\mu}_c\beta_c \left[ \tau + y(1.25 + 1.15\theta_e) \right] - 4.94P_2(\tilde{\mu}_c)\beta_c^2 \left[ \tau + 0.43y \right], \end{aligned} \quad (4.15a)$$

$$\begin{aligned} \frac{\Delta \tilde{n}_{\text{CMB}}}{\tilde{n}_{\text{CMB}}} &\approx -2y \left[ 1 - 1.7\theta_e + 3.08\theta_e^2 \right] + 0.34\beta_c^2 y \\ &\quad + \tilde{\mu}_c\beta_c \left[ \tau + y(-0.4 + 2.6\theta_e) \right] - 0.6P_2(\tilde{\mu}_c)\beta_c^2 \left[ \tau + 0.89y \right], \end{aligned} \quad (4.15b)$$

respectively. These expressions are quite accurate as will be shown later in this chapter, but higher-order terms can be easily added in SZpack. It should be emphasized that for the individual contributions no new spectral shape is created by relativistic corrections. However, since the radio and CMB SZ effects have a *different* dependence on the temperature and cluster velocity, the spectrum of the total signal is modified.

### Expression inside CMB frame

Much like for the cluster frame, in the CMB frame using  $n_R$  the terms of Eq. (4.8) can be simplified for use with Eq (4.7) to

$$\begin{aligned} \mathcal{M}_k^R &= n_R \sum_{j=1}^{2k+2} \frac{(-1)^j}{3} \frac{(\alpha + j - 1)!}{(\alpha - 1)!} \left( a_j^k - d_j^k \right) \alpha(\alpha - 2), \\ \mathcal{D}_k^R &= n_R \sum_{j=0}^{2k+2} (-1)^j \frac{(\alpha + j - 1)!}{(\alpha - 1)!} \left( d_j^k - a_j^k \right) (-\alpha), \\ \mathcal{Q}_k^R &= n_R \sum_{j=0}^{2k+2} \frac{(-1)^j}{3} \frac{(\alpha + j - 1)!}{(\alpha - 1)!} \left( q_j^k - 2d_j^k + a_j^k \right) \alpha(\alpha + 1). \end{aligned} \quad (4.16)$$

$\mathcal{Y}_k^R$  have not been repeated as they are identical to  $\tilde{\mathcal{Y}}_k^R$  in Eq. (4.14). The first few terms in the CMB frame can now be written as

$$\begin{aligned} \mathcal{M}_0^R &= \frac{n_R}{5} 7\alpha^2(\alpha - 3)(\alpha - 2), \\ \mathcal{D}_0^R &= \frac{n_R}{5} \alpha(7\alpha^2 - 21\alpha + 2), \\ \mathcal{D}_1^R &= \frac{n_R}{10} \alpha(11\alpha^4 - 66\alpha^3 + 92\alpha^2 + 21\alpha + 2), \\ \mathcal{Q}_0^R &= \frac{n_R}{10} \alpha(\alpha + 1)(19\alpha^2 - 57\alpha + 2). \end{aligned} \quad (4.17)$$

These expressions can reproduce the kinematic and relativistic temperature corrections to the radio SZ (and standard SZ) effect to high precision.

Again inserting  $\alpha = 3.59$  and  $\alpha = 1$ , one finds

$$\frac{\Delta n_R}{n_R} \approx 2.12y[1 + 1.18\theta_e - 0.59\theta_e^2] + 9.08\beta_c^2[\tau + 0.62y] \quad (4.18a)$$

$$+ 3.59\mu_c\beta_c[\tau + y(3.37 + 3.65\theta_e)] + 6.04P_2(\mu_c)\beta_c^2[\tau + 3.84y],$$

$$\frac{\Delta n_{\text{CMB}}}{n_{\text{CMB}}} \approx -2y[1 - 1.7\theta_e + 3.08\theta_e^2] + 1.67\beta_c^2[\tau + 0.56y] \quad (4.18b)$$

$$+ \mu_c\beta_c[\tau + y(-2.4 + 6\theta_e)] + 0.73P_2(\mu_c)\beta_c^2[\tau - 3.27y].$$

The expression for the temperature corrections to the standard thermal SZ effect agrees exactly with Eq. (37) in [Nozawa et al. \(1998\)](#), even if here only two orders in  $\theta_e$  are given, which is already highly accurate. While the leading-order kinematic term  $\approx \mu_c\beta_c\tau$  also agree; all other terms depart as explained in CNSN.

It is important to stress that the temperature terms appearing in the form  $y\theta_e^k$  should be interpreted as  $y$ -weighted temperature moments, which for non-isothermal clusters can differ from mass-weighted or X-ray measured temperatures ([Chluba et al., 2013](#); [Lee et al., 2020](#), and also discussed in Chapter 2). Similarly, all other terms are caused by various temperature and velocity moments that should be treated carefully. However, for the current discussion, this complication is neglected.

The temperature corrections to the radio SZ signal are smaller than those for the CMB signal in this low-frequency regime. To first order, since the CMB signal is negative in the region, the two signals combine destructively when they are added. This leads to a source-shadow appearance of the cluster in the scattered light ([Holder & Chluba, 2021](#)). However, the temperature corrections themselves to both the CMB and radio SZ signal are in the same direction, and as a result magnify the relativistic corrections measured in either signal individually (as will be clarified in Section 4.3). Conversely, the kinematic corrections are larger for the radio SZ signal than for the CMB signal.

#### 4.2.4 Anisotropies in the radio background

In the absence of kinematic effects, the scattering effect for arbitrary photon anisotropies can be computed as in [Chluba et al. \(2012a\)](#). Neglecting stimulated scattering terms, the distortion to first order in temperature can be written

$$\begin{aligned} \Delta n &\approx \tau \left( n_0 + \frac{n_2}{10} - n \right) + y \left[ 4x\partial_x + x^2\partial_x^2 \right] \bar{n} \\ &\quad + y \left( -\frac{2}{5}n_1 - \frac{3}{5}n_2 + \frac{6}{35}n_3 \right), \\ \bar{n} &= n_0 - \frac{2}{5}n_1 + \frac{1}{10}n_2 - \frac{3}{70}n_3. \end{aligned} \quad (4.19)$$

Here,  $n_\ell \equiv \sum_m n_{\ell m} Y_{\ell m}(\hat{\gamma} \cdot \hat{\mathbf{z}})$ , where  $\hat{\mathbf{z}}$  defines the coordinate system for the multipole expansion. Thus,  $n_0$ ,  $n_1$ ,  $n_2$  and  $n_3$  refer to the monopole, dipole, quadrupole



and octupole components, and  $n$  refers to the combined signal. These can be combined explicitly by expanding and taking  $\alpha_\ell$  as the spectral index for each  $n_\ell$  to find

$$\begin{aligned} \Delta n \approx & n_0 \left[ y \alpha_0 (\alpha_0 - 3) \right] - \frac{1}{5} n_1 \left[ 5\tau + 2y(\alpha_1^2 - 3\alpha_1 + 1) \right] \\ & - \frac{1}{10} n_2 \left[ 9\tau - y(\alpha_2^2 - 3\alpha_2 - 6) \right] \\ & - \frac{1}{70} n_3 \left[ 70\tau + 3y(\alpha_3^2 - 3\alpha_3 - 4) \right]. \end{aligned} \quad (4.20)$$

These are equivalent to the expression found in Eq. (4.4) to first order in temperature, if one defines the multipoles as those derived from a kinetic boost from an isotropic CMB frame photon into the cluster frame (cf. Eq. (11) in CNSN). That is, one can observe the similarities between the terms in Eq. (4.20) and those for  $\tilde{Y}_0^R$ ,  $\tilde{D}_0^R$  and  $\tilde{Q}_0^R$  found in Eq. (4.14). In principle, it would therefore be possible to extend the expressions for the monopole, dipole and quadrupole scattering to higher order in temperature, as we have for the general SZ effect. In this case, no extra terms to the monopole scattering would appear (e.g.,  $\tilde{M} = 0$ ). Also, terms describing octupole scattering (equivalent to  $\mathcal{O}(\beta_c^3)$  in Eq. (4.4) which have been dropped) would still need to be derived. However, in this chapter we focus on a low-temperature expansion to more easily understand the effects of various anisotropies. It should also be stressed that to first order in temperature *only* the first three anisotropies could ever contribute to the SZ signal.

For a simplistic model, where the radio background has, for instance, a dipole with the same spectral shape as the background itself, say  $n_1 = f_1 n_R$ , with  $f_1 < 1$ , then the effect on the *radio* signal would be the same as the first order (in  $\beta_c$ ) kinematic corrections with  $\beta_c \tilde{\mu}_c \alpha \leftrightarrow f_1$ . However, a kinematic effect would also create a correction to the incoming CMB photons, which an intrinsic dipole anisotropy in the radio background would evidently not – accordingly these two signals would in principle be distinguishable. Furthermore, if any radio background anisotropies have a different spectral shape to the radio background itself, we would see more complex contributions to the final signal. Later in this chapter, I consider instructive examples to illustrate the effects.

#### 4.2.5 Effect of the observer motion

In Section 4.2.2, the effects of switching between the cluster frame and CMB frame has been discussed and the effects on the measured SZ signal. In actuality, of course, observations are made in neither. It is well known that there is a significant observed dipole component within the CMB due to the earth's motion relative to the CMB frame. This can be well parameterised by  $\beta_o = 1.241 \times 10^{-3} (1 \pm 0.2\%)$  (Fixsen et al., 1996; Fixsen & Mather, 2002). Then we define

$\mu_o$  as the cosine of the angle between this dipole direction, and the observed cluster (measured in the *observer frame*).

In a similar way to moving to the CMB frame from the cluster frame, this dipole motion will generate both a dipole correction and higher-order terms to the observed SZ signal. This has already been well documented (Chluba et al., 2005) for its effect on the conventional SZ signal, and the effects on radio SZ signal are similar, but worth repeating here.

From a mathematical perspective, this is all most easily expressed by simply transforming the variables such that (see CNSN)

$$\begin{aligned} x &= \gamma_o x_o (1 + \beta_o \mu_o), \\ \tilde{x} &= \gamma_c x (1 - \beta_c \mu_c) = \gamma_c \gamma_o x_o (1 - \beta_c \mu_c) (1 + \beta_o \mu_o), \\ \mu &= \frac{\mu_o + \beta_o}{1 + \beta_o \mu_o}, \end{aligned} \tag{4.21}$$

where  $x_o$  is the dimensionless frequency as measured in the observer frame and  $\gamma_o = \sqrt{1 - \beta_o^2}$  is the associated Lorentz factor;  $\mu$  is the angle between the observer dipole and the observed cluster as measured in the *CMB frame*, included here only for completeness.

It is clear that for both the radio SZ and normal SZ signals, the effect of this frame conversion is a modulation of the observed frequency. If this was to be fully expanded, as in Section 4.2.2 for the CMB frame, it would introduce dipole and quadrupole terms in  $\beta_o$  alongside cross terms in  $\beta_c \beta_o$ . However, it is easier to simply replace variables in the CMB frame expression using the above relation to obtain the transformed result. Since we know the amplitude and direction of the dipole, this effect can easily be taken into account. We thus assume this has been taken care of in any analysis.

#### 4.2.6 Additional small effects

In this discussion, I have omitted multiple-scattering effects. These can lead to additional small corrections to the SZ signals (Chluba et al., 2014; Chluba & Dai, 2014). In addition, the scattering of the intra-cluster radio light, e.g., from radio sources within the cluster, requires a more detailed modelling. Internal motions of the cluster, e.g., due to cluster rotation (Chluba & Mannheim, 2002; Cooray & Chen, 2002; Diego et al., 2003), could affect the radio SZ signal in a similar manner as for the normal SZ effect. Similarly, moving-lens effects (Birkinshaw & Gull, 1983; Molnar & Birkinshaw, 2003) will appear. Finally, as with the usual kinematic SZ effect (Sunyaev & Zeldovich, 1980) and scattering of the CMB quadrupole (Kamionkowski & Loeb, 1997; Sazonov & Sunyaev, 1999), the scattered radio light will be linearly polarized. However, modelling all these smaller effects is beyond the scope of this chapter.

## 4.3 Results

In this section, I consider how the radio and CMB signal combine to give the observable radio SZ signal; the kinematic and relativistic contributions modify the signal and affect the location of the radio SZ null. In Section 4.3.4, how the variations in the radio background change the results is explored and, in Section 4.3.5, the contributions of anisotropies in the radio background are shown. I will always give the results in the *CMB frame*.

### 4.3.1 Main dependence of total signal and degeneracies

From Eq. (4.18a) (or in general the combination of Eqs (4.11), (4.4) and (4.5)), it is evident that the radio background causes a scattering signal that is always proportional to the radio background itself. i.e.,

$$\begin{aligned}\Delta n_R &= \tau n_R(\nu, z, \alpha) F_R(\theta_e, \beta_c, \mu_c, \alpha) \\ &= \tau A_R f(z) F_R(\theta_e, \beta_c, \mu_c, \alpha) g(\nu, \alpha),\end{aligned}\tag{4.22}$$

where  $F_R$  now contains all of the kinematic and relativistic terms and can in general be thought of as a scattering amplitude. Here, I have also defined  $g(\nu, \alpha) = (x/x_0)^{-\alpha} x_0^{-1}$ .

In this formulation, the radio SZ is always positive and thus does not form an inherent null from scattering. In contrast, the normal CMB SZ signal has an inherent null at around 217 GHz – the cross-over frequency from photons being scattered out from lower frequencies into higher frequencies. However, the combination of scattering of the radio background and CMB leads to a new null at around 735.5 MHz, as discussed in Holder & Chluba (2021). That is, we can write

$$\begin{aligned}\Delta n_R + \Delta n_{\text{CMB}} &\approx \tau \left[ A_R f(z) F_R(\theta_e, \beta_c, \mu_c, \alpha) g(\nu, \alpha) \right. \\ &\quad \left. + F_{\text{CMB}}(\theta_e, \beta_c, \mu_c) n_{\text{CMB}}(\nu) \right],\end{aligned}\tag{4.23}$$

where  $F_{\text{CMB}}(\theta_e, \beta_c, \mu_c) \approx F_R(\theta_e, \beta_c, \mu_c, 1)$ , and  $F_{\text{CMB}}$  is negative in this regime. This can all be seen in Figure 4.1, where the scattering from both the radio background and the CMB are shown individually, alongside the combined signal.

Changes to the observed signal can now be quantified in a heuristic manner. The kinematic and relativistic effects cause changes to  $F_R$  and  $F_{\text{CMB}}$ , which, to first order, enhance the observed change to the signal. For example, in Figure 4.1, the relativistic corrections to each signal are shown for a cluster temperature of 10 keV. The relativistic effect on both the CMB and radio scattering increase the signal. This can be understood physically as the relativistic corrections imply there is more up-scattering for the radio SZ signal, while for the CMB distortion this results in fewer photons being up-scattered out of this region. The relativistic corrections will be quantified more precisely later in this chapter, but

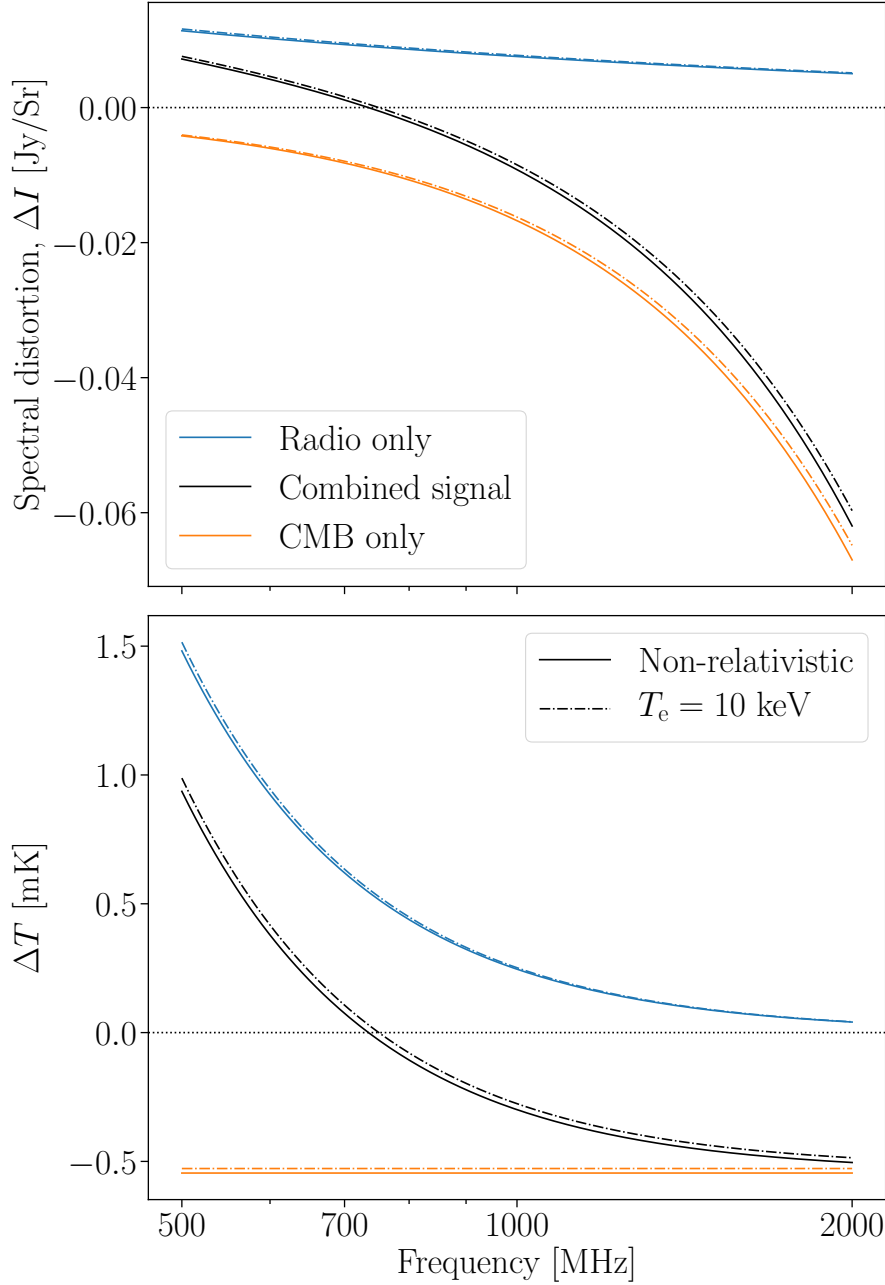


**FIGURE 4.1:** Contributions of the non-relativistic CMB SZ signal, radio SZ signal and combination of the two at low frequencies, alongside their relativistic corrections at  $T_e = 10$  keV. In the top panel we see the change in intensity relative to the background signals, the bottom panel shows the effective change in temperature measured at each frequency. We have set  $y = 10^{-4}$  and used  $n_R$  with  $f(z) = 1$ . Note this is a logarithmic plot in frequency.

at low frequencies, the effects are typically a few percent. These are comparable, if a little smaller, to the standard relativistic SZ effect.

The kinematic corrections combine in a similar way – a cluster heading towards the observer (i.e.,  $\mu_c > 0$ ) leads to more up-scattering, shifting the null to higher frequencies, while a cluster heading away shows the opposite effect. Changes to the amplitude of the radio background – either due to the uncertainty in measurements of  $A_R$ , from  $f(z)$  or from some inherent angular dependence to the signal, i.e., some  $f(\hat{\gamma}, z)$  – also leads to a re-weighting of the radio component relative to the CMB component.

Here, a degeneracy can immediately be spotted within the signal. For a given  $\alpha$ , measurements of the total radio SZ signal can only ever give the relative amplitudes of the CMB and radio components – i.e., from the shape of the combined signal. However, the more details of the clusters or the radio background are known, the more information can be obtained from the signal. For instance, if  $\tau$  (or  $y$ ) is known, the amplitude of the signal itself becomes a second independent measurement from the radio SZ signal. It should also be noted that variations in  $\alpha$ , either within the measurement of the radio background itself, or due to anisotropies, would in principle be distinguishable from the other variations within the signal. Furthermore, since  $F_R$  and  $F_{\text{CMB}}$  are not independent quantities and together give a complex dependence on  $T_e$ ,  $\beta_c$  and  $\mu_c$ , more information may be gained from them than initially supposed. However, this requires detailed forecasts and high-precision measurements.

#### 4.3.2 Relativistic and kinematic corrections

In Figure 4.2, the non-relativistic combined signal (as described in Holder & Chluba, 2021) is displayed alongside the signal including relativistic and kinematic corrections. Here, we have shown a cluster with large kinematic corrections (with  $\beta_c = 0.005$  and  $\mu_c = \pm 1.0$ ). The relativistic corrections come from a cluster temperature,  $T_e = 10$  keV, a temperature typical of the most massive clusters in the Universe (Arnaud et al., 2005; Lee et al., 2020). We have calculated all of these distortions with a recent update to SZpack. Here, the radio background is assumed to be comoving with the CMB – or, alternatively, it is isotropic in the CMB rest frame. That is, it is meaningful to use the same value of  $\beta_c$  for both the CMB induced signal and the radio SZ signal.

The first aspect to note is that, while these corrections roughly maintain the shape of the distortion in these regions, they lead to shifts in frequency. A second point is that the shapes are nonetheless distorted, as can be seen in the third panel of Figure 4.2. The kinematic effects are generally larger than the relativistic effects, as in the normal SZ effect. However, the kinematic radio SZ effect is  $\approx 3.6$  times larger than the standard kSZ effect due to the steepness of the radio background.

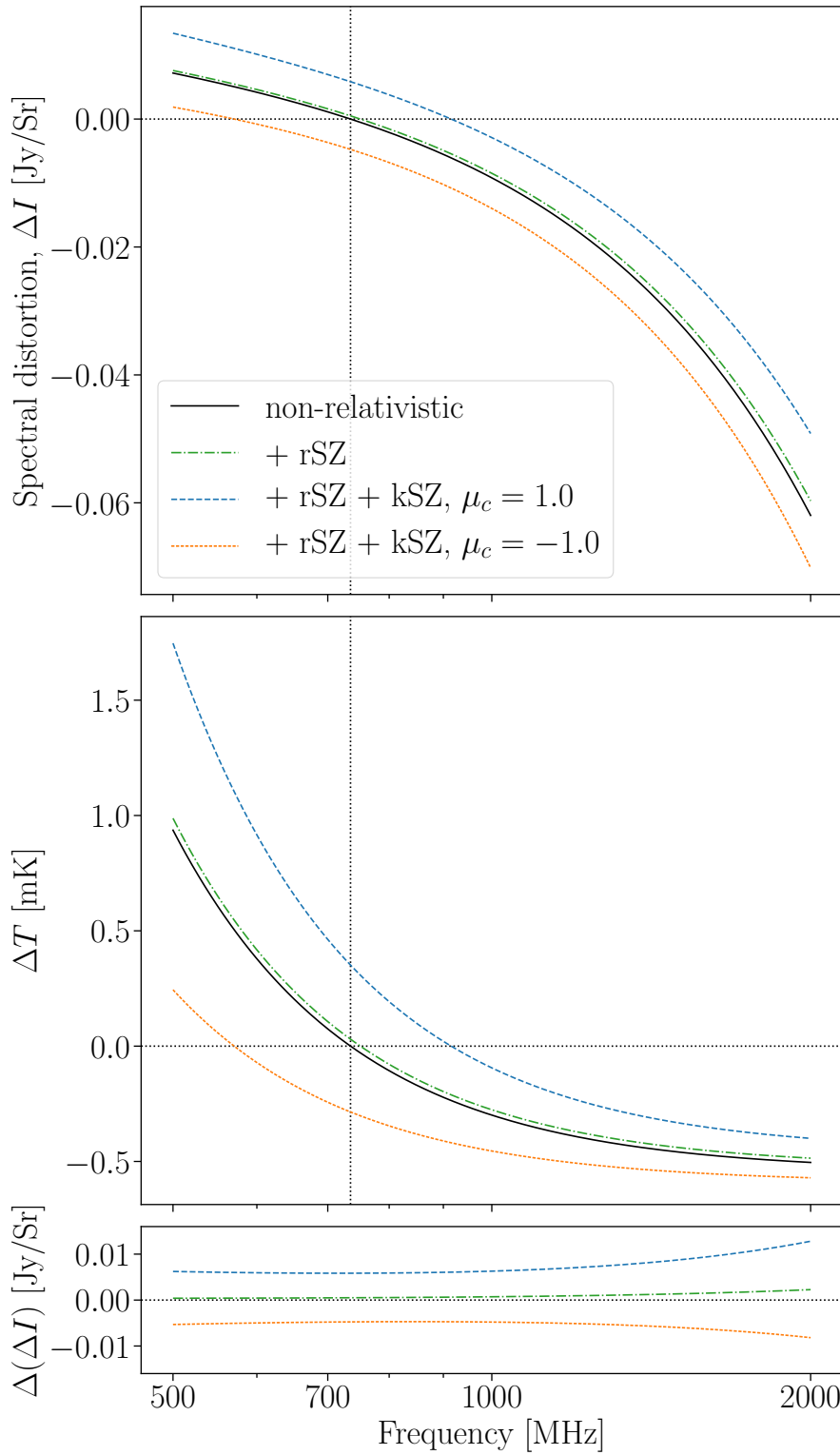


**FIGURE 4.2:** Illustration of the corrections to the combined CMB and radio SZ signals due to relativistic (rSZ) and kinematic (kSZ) effects. The rSZ corrections come from  $T_e = 10$  keV and the kSZ effects are for  $\beta_c = 0.005$ , with  $\mu_c = \pm 1.0$ . In the top panel we see the change in intensity relative to the background signals, the middle panel shows the effective change in temperature measured at each frequency. The bottom panel shows the difference between the stationary non-relativistic signal and the signals incorporating rSZ and kSZ effects. We have set  $y = 10^{-4}$  and used  $n_R$  with  $f(z) = 1$ . Note this is a logarithmic plot in frequency.

**TABLE 4.1:** The null of the radio+cmb SZ signal for various temperatures. Kinematic terms are excluded. We note that since the relativistic null is nearly linear with temperature (see Fig. 4.3), the null can be well modelled as an interpolation between these points.

$T_e$ [keV]	0	5	10	20	30	40
$\nu_N$ [MHz]	735.5	743.5	751.4	767.0	782.4	797.5
$\Delta\nu_N/\nu_N$	--	1.08%	2.16%	4.28%	6.37%	8.43%

The kinematic effects are also not reversible with respect to  $\mu_c$ . That is, for example, the  $\mu_c = 1.0$  signal contributes to more up-scattering of the photons, than the  $\mu_c = -1.0$  signal contributes to down-scattering when compared to the non-kinematic signal. This is a small effect in the figure shown, but proportional to  $\beta_c^2$ . This can be seen numerically from Eq. (4.4), where the signal has components proportional to  $\beta_c^2$  and  $\beta_c^2 P_2(\mu_c)$ . For a similar reason, the changes to the signal are non-linear under changes to  $\mu_c$ . Also, the  $\beta_c^2 \tau$  terms in the radio SZ effect are amplified by a factor of  $\simeq 7$ , which causes a larger asymmetry when flipping the direction of  $\beta_c$  in comparison to the standard kSZ effect. However, direct observations of these small terms will be difficult in the near future, but modelling of these effects will lead to improved accuracy in any measurements.

### 4.3.3 Corrections to the null

The corrections can be illustrated by considering the adjustments to the null in the signal. We define the null frequency,  $\nu_N$  to be the frequency at which there is no distortion to the original signal (i.e.,  $\Delta I(\nu_N) = 0$  Jy/Sr and  $\Delta T(\nu_N) = 0$   $\mu$ K). For the normal SZ effect, this is often referred to as the crossover frequency.

In Figure 4.3, the variation of the radio null is shown under changes in  $T_e$ . Kinematic terms are omitted. Firstly, it is worth noting the changes are small, and secondly the variations are almost linear with cluster temperature. The figure also illustrates the convergence of the asymptotic expansion, by showing the calculation of the null from considering increasing numbers of terms. In Table 4.1, I specifically calculate the null for a selection of temperatures. By interpolating these points, one can obtain accurate predictions for the null. However, at  $T_e \lesssim 15$  keV, the expressions in Eq. (4.18a) and (4.18b) should suffice. Higher-precision results can be obtained with SZpack.

The null frequency,  $\nu_N$ , increases with temperature, reflecting the general shift upwards in both the CMB and radio contributions. However the effect of increasing the temperature, decreases with temperature, e.g., the shift in null from 0 to 10 keV is slightly greater than that between 30 and 40 keV. The response of the null to changes in temperature is, however, well behaved and relatively small compared to the frequencies considered.

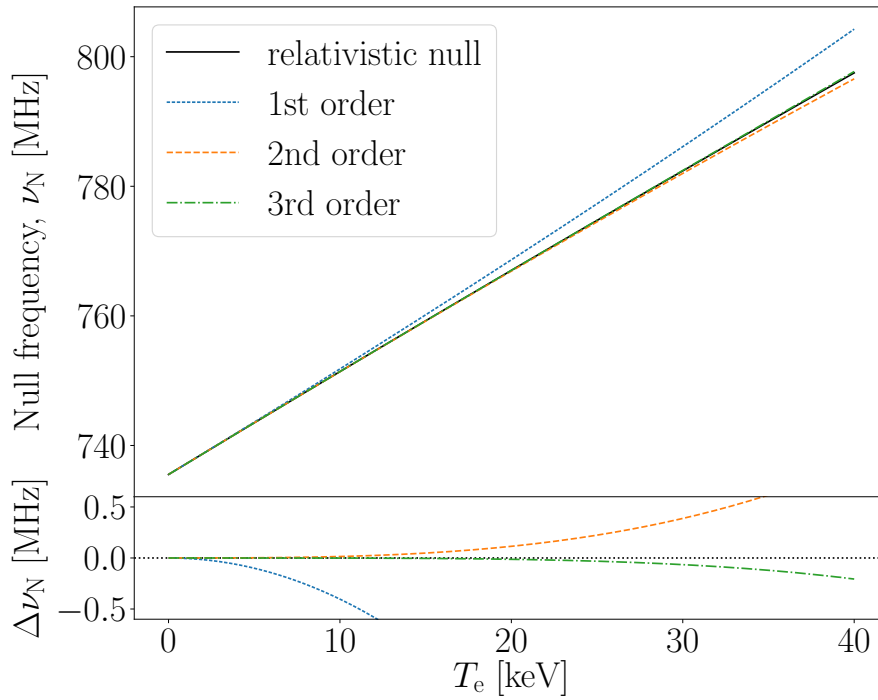


**FIGURE 4.3:** A plot showing the relativistic corrections to radio null. In black we can see this value accurately calculated, while the other lines show the result of the asymptotic expansion to 1st, 2nd and 3rd order. The lower panel shows the difference between these approximations and the true value. We can see here that a low-order expansion remains very accurate even to very high electron temperatures.



In the standard SZ scenario, the crossover frequency can be parameterised under changes in temperature as (Itoh et al., 1998),

$$\nu_{\text{N,CMB}} = 217.5 \left[ 1 + 1.1674\theta_e - 0.8533\theta_e^2 \right] \text{ GHz.} \quad (4.24)$$

The equivalent general function for the radio SZ effect is more complicated – but, allowing for changes in  $\alpha$ ,  $A_R$  and  $f(z)$ , one can find

$$\begin{aligned} \nu_{\text{N}} \approx \nu_0 \left( \frac{2}{A_R f(z) \alpha (\alpha - 3)} \right)^{\frac{1}{1-\alpha}} & \left[ 1 + \frac{7}{10} (\alpha - 2) \theta_e \right. \\ & \left. + \frac{1}{600} (73\alpha^3 - 218\alpha^2 - 730\alpha + 1748) \theta_e^2 + O(\theta_e^3) \right], \end{aligned} \quad (4.25)$$

where  $\nu_0 = 310$  MHz is the real frequency associated with the dimensionless frequency  $x_0$ . For general  $\alpha$  this is complicated to assess, but, for  $\alpha = 3.59$ , this can be simplified to

$$\nu_{\text{N}} \approx 735.5 \left( \frac{A_R f(z)}{8.84} \right)^{0.386} \left[ 1 + 1.113\theta_e - 0.5079\theta_e^2 \right] \text{ MHz.} \quad (4.26)$$

Comparing to Eq. (4.24) shows that the relative effect of temperature corrections on the radio null is similar to that for the normal tSZ effect, which enter at the few percent level.

A similar full consideration for the kinematic effect is more complex – however, for  $\mu_c \beta_c \ll \theta_e$  the lowest order kinematic correction can be expressed as

$$\nu_{\text{N}} \approx \nu_0 \left( \frac{2}{A_R f(z) \alpha (\alpha - 3)} \right)^{\frac{1}{1-\alpha}} \left[ 1 + \frac{1}{2(\alpha - 3)} \frac{\mu_c \beta_c}{\theta_e} \right]. \quad (4.27)$$

Again inserting numbers we can find

$$\nu_{\text{N}} \approx 735.5 \left( \frac{A_R f(z)}{8.84} \right)^{0.386} \left[ 1 + 0.847 \frac{\mu_c \beta_c}{\theta_e} \right] \text{ MHz.} \quad (4.28)$$

This expression immediately shows that kinetic terms can have a relatively large effect on the radio null.

An indicative plot for the kinematic corrections is shown in Figure 4.4, which shows the response of the null to  $\beta_c$  and  $\mu_c$  at  $T_e = 10$  keV. As expected, even relatively small peculiar motion can induce significant shifts in the radio null. One can observe a slight asymmetry in  $\mu_c$  that is more easily seen at higher values of  $\beta_c$ . The kinematic corrections also vary to first order about the relativistically corrected null – i.e., when  $\mu_c = 0$ , the null lies at  $\approx 751.4$  MHz as expected from Table 4.1 – although at high  $\beta_c$  the monopole corrections will have more of an effect in shifting this to higher frequencies.

As with the CMB SZ null, there is an anticorrelation between the cluster temperature and the shift in the null. That is, at lower temperatures the kinematic

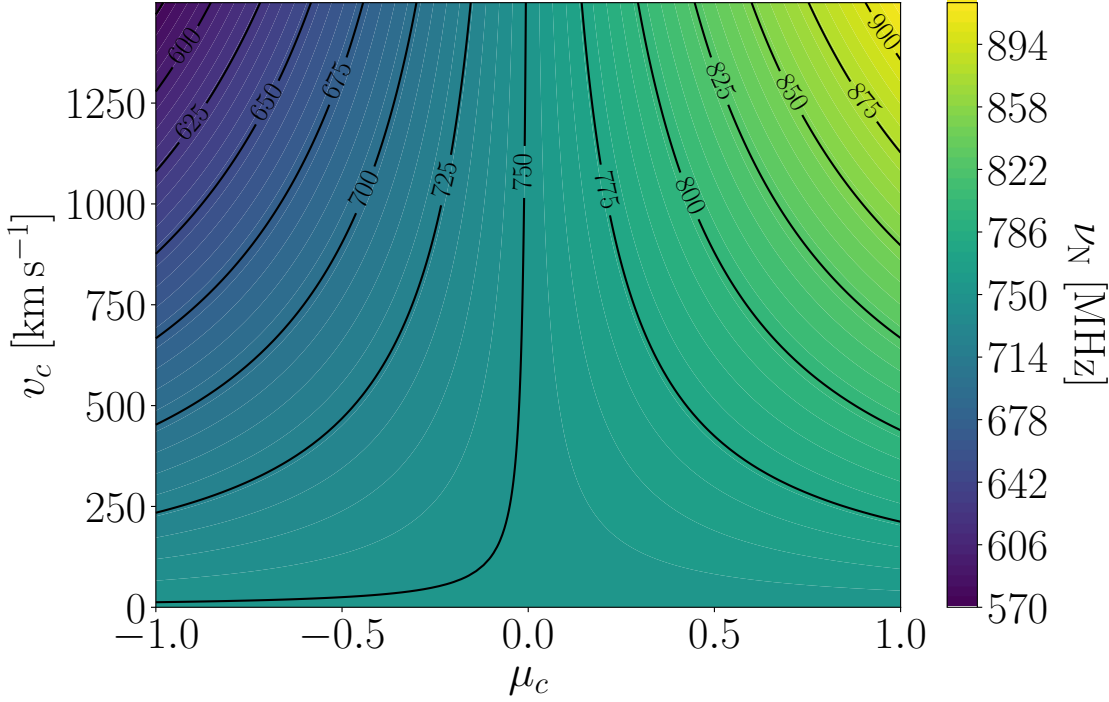


**FIGURE 4.4:** A plot showing the kinematic corrections to the radio null. We are calculating everything with relativistic corrections of  $T = 10$  keV. We can see the response of the null frequency,  $\nu_N$ , to changes in viewing angle,  $\mu_c$ , and cluster velocity,  $v_c = c\beta_c$ . A slight asymmetry around  $\mu_c = 0$  is visible, which is due to terms  $\tau\beta_c^2$ .

effects become more important than at higher temperatures for a fixed  $\beta_c$ . This can be understood in a number of ways – numerically, we can directly see that since  $y \simeq \tau\theta_e$ , even the non-relativistic tSZ signal has a dependence proportional to  $\theta_e$ , while the non-relativistic kSZ signal has none. Hence, decreasing the cluster temperature, reduces the impact of the tSZ signal, thus effectively increasing the impact of the kSZ signal. Alternatively, we can understand this energetically, in that, for a fixed velocity cluster (i.e., fixed  $\beta_c$ ), reducing the temperature of the cluster will lead to a higher proportion of the electron energy being contained in the kinematic component. Accordingly, the kinematic effect will increase proportionally with lower temperatures.

#### 4.3.4 Radio background variations

The radio background is still comparatively poorly understood, despite the measurements that have been taken (Fixsen et al., 2011; Seiffert et al., 2011; Singal et al., 2018; Dowell & Taylor, 2018). As such, the uncertainty in the background is far larger than that of the CMB. Not only is it currently unknown how the radio background varies with redshift, there may also be large-scale spatial fluctuations within it. The radio SZ signal could theoretically then be used as a measure

to determine details of the radio background itself alongside potentially bounding its inherent variations.

Figure 4.5 illustrates the effects of the  $1\sigma$  errors given for the radio background as expressed in Eq. (4.9) in both the normalization and spectral index. These changes are of a similar scale to the relativistic corrections, but small compared to any major changes from  $f(z)$ , which are illustrated in the two cases,  $f(z) = 0.5$  and  $f(z) = 1.5$ . A value  $f(z) < 1$  is consistent with the simple picture that the radio background is isotropic but slowly builds up with redshift, while  $f(z) > 1$  suggests that a local overdensity around the cluster might be present.

The displayed examples all change the shape of the signal (as would be expected). This means that these variations are theoretically separable from the relativistic corrections caused by the cluster temperature. However, the normalization  $A_R$  of  $n_R$ ,  $f(z)$  and the effective relativistic corrections are all degenerate, and only their product can be constrained. Existing priors, either from standard SZ observations or from theory using scaling relations, could thus provide additional important leverage when aiming to use radio SZ measurements to learn about  $f(z)$  and  $A_R$ . The spectral index  $\alpha$  on the other hand can in principle be separated from the other effects by measuring the precise spectral shape of the radio SZ signal.

The shift in the null from varying the spectral index,  $\alpha$ , is around  $\approx \pm 14$  MHz, while the measured uncertainty in  $A_R$  leads to a slightly larger effect of around  $\approx \pm 25$  MHz variation to the null. The scattered radio SZ signal need not have the same spectral index as the ‘off-cluster’ radio flux. This is because the scattered signal probes the local radio background at the clusters location, while the ‘off-cluster’ sky flux constrains the superposition of all radio emission along the line of sight. The value of  $\alpha$  should therefore be directly measured using the scattered signal.

Overall, assuming that the temperature and peculiar velocity of a cluster can be precisely measured, a high-precision measurement of the radio SZ signal can allow a determination of  $\alpha$  from the signal shape, and the product  $A_R f(z)$  from the location of the signal null. The exact details of the current observational feasibility of this are beyond this thesis, but it is worth noting that any large changes over redshift could be more easily detectable. Large changes in  $f(z)$  may indicate the age of the radio background or give more insight into its creation. It is also worth noting the possibility of the variation of  $\alpha$  with redshift,  $\alpha \rightarrow \alpha(z)$ , which again could theoretically be measured with a large enough sample size and high enough measurement precision.

Other variations could come if  $\alpha$  had any  $x$  dependence – for example, if the radio background exhibited significant curvature beyond the power law. A superposition of different power laws (i.e., a mix of different values for  $\alpha$ ) would lead to some curvature inherently (Chluba et al., 2017); however, there is no evidence for this within the ARCADE measurements. This indicates that there is

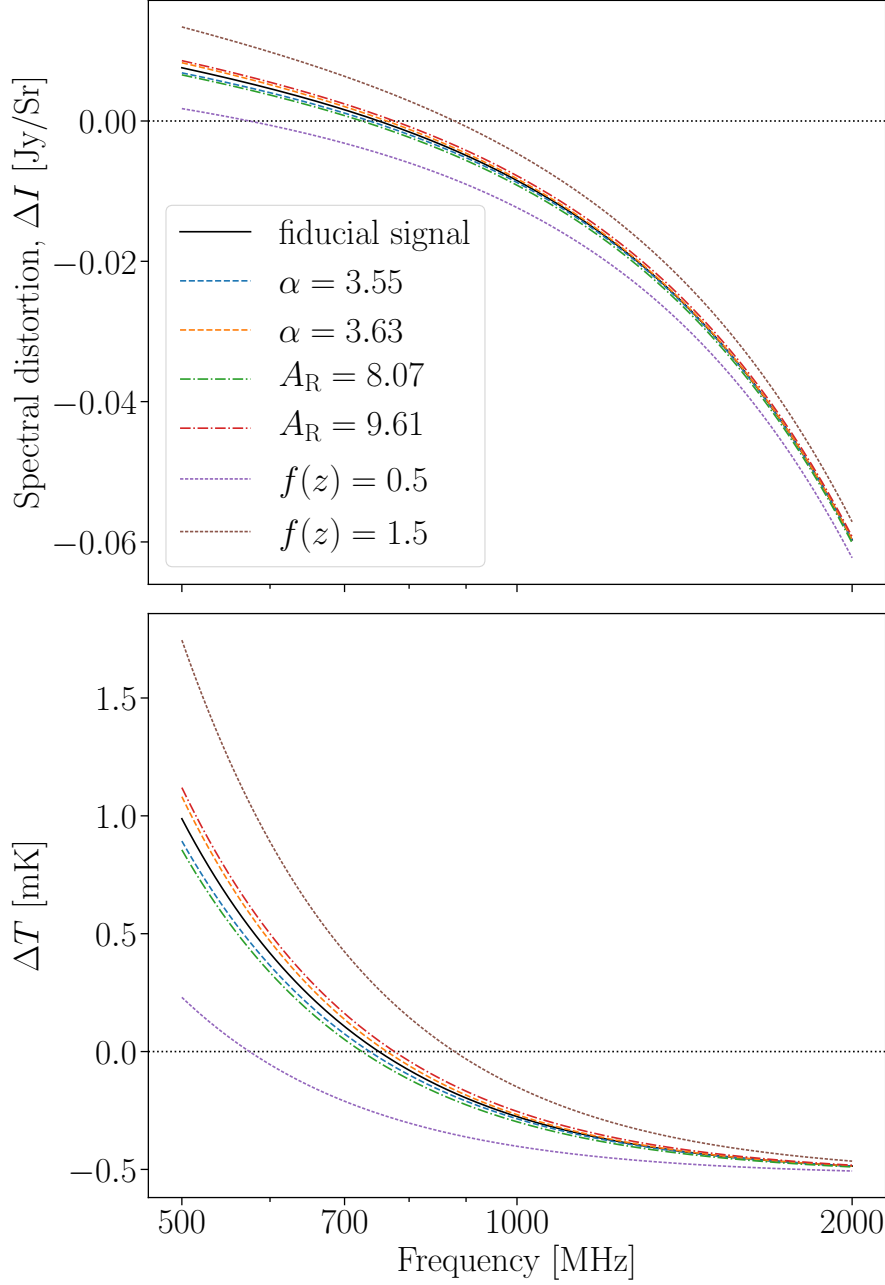


**FIGURE 4.5:** Variations in the radio SZ signal (with  $\beta_c = 0$  and  $T_e = 10$  keV) under modifications to the radio background distribution. The dashed lines show variations due to the error on  $\alpha$ , the dashed-dotted lines show the variations of the measured error in the amplitude as written in Eq. (4.9), and the dotted lines show variations according to a significant variation in  $f(z)$ . We have set  $y = 10^{-4}$ .

little variation of  $\alpha$  with redshift. A detailed analysis of curvature within the power law background is, again, beyond the scope of this thesis.

#### 4.3.5 Anisotropy in the radio background

We can also consider the effects of anisotropy in the radio background on the observed signal. Overall, this can be thought of as  $A_R f(z) \rightarrow A_R f(\hat{\gamma}, z)$ . In Section 4.2.4, the mathematical formalism was explored and it was noted that if the anisotropic components have the same spectral index, the only effect will be to change the amplitude of the radio component of the SZ signal. That is, as discussed before, this would shift the null. Hence, if it were possible to bound the average  $f(z) = \int f(\hat{\gamma}, z) d\hat{\gamma}$ ,  $T_e$  and the amplitude of the radio background, a precise measurement of the null would give some bounds on the level of anisotropy in the radio background itself. If however, the higher-multipole components have a different spectral index, there would be changes to the spectral shape, as there would be more components adding to the distortion (as opposed to just the monopole radio  $n_R$  and CMB components). This would increase the number of parameters and pose high demands on the observations.

Figure 4.6 shows the effects of a dipole in the radio background and its differences to the kinematic effect. Here, a substantially cooler cluster of 1 keV is used, both to increase the accuracy of the first-order temperature expansion used in Eq. (4.19) and to maximise the size of the distortions, so they can be more clearly observed. The radio background dipole is set to be 0.1% of the radio background as a whole (i.e.,  $n_1 = \pm 0.001 n_R$ ) and the kinematic effects are also plotted with the ‘equivalent’ magnitude, i.e.,  $\beta_c \mu_c = 0.001/\alpha$ . We note that the dipole in the CMB (induced by the relative motion of the observer frame and the CMB frame) is around  $1.24 \times 10^{-3}$  (i.e.,  $\beta_o$ ). So here this assumes a dipole of comparative size.

These two effects have very different effects on the shape of the observed signal. At low frequencies, the kinematic corrections to the CMB component are small, so the radio dipole and kinematic effect cause similar distortions. However, at higher frequencies, the CMB part of the kinematic effect is a larger component and the radio dipole and kinematic corrections diverge. These two effects are therefore observationally distinct. However, more work may be necessary to determine the possible radio anisotropies and to fully determine the radio background itself, before it would be possible to ascertain the full details of the radio background anisotropies. A similar discussion can follow for the radio quadrupole and octupole. Since these are not expected to be connected to the CMB equivalents, the spectral effects should be distinguishable and possibly larger than for the scattering of the CMB temperature anisotropies.

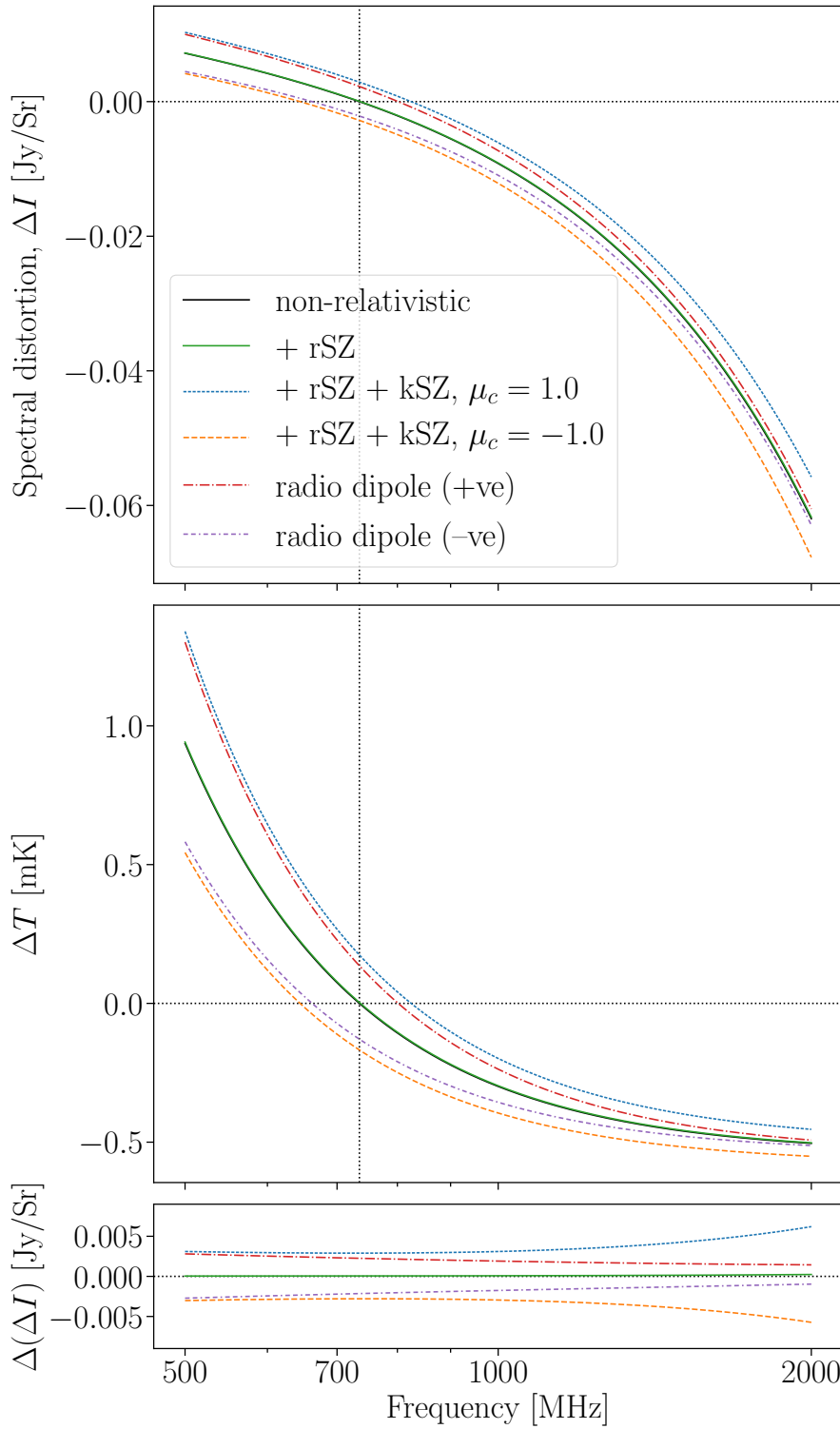


**FIGURE 4.6:** The differences between a dipole in the radio background and the kinematic corrections. With the exception of the non-relativistic line, all these signals take relativistic corrections according to  $T_e = 1$  keV. Note, this is a significantly smaller  $T_e$  than our previous figures. The radio dipole comes from a signal  $n_1 = \pm 0.001 n_R$ , while the kSZ effects use  $\beta_c = 2.79 \times 10^{-4} = 0.001/\alpha$ , with  $\mu_c = \pm 1.0$ . The top panel shows the change in intensity relative to the background signals, the middle panel shows the effective change in temperature measured at each frequency. The bottom panel here shows the difference between the stationary, non-relativistic signal and the other signals. We have set  $y = 10^{-4}$  and used  $n_R$  with  $f(z) = 1$ .

## 4.4 Discussion

It is worth taking a moment to consider the potential of different observational strategies in determining any of the discussed features in the radio SZ signal. A detailed forecast is far outside the scope of this thesis, but here I will discuss the differences between stacking approaches and individual cluster observations when it comes to the specifics of the radio SZ signal itself. Many of the ideas can be directly adapted from normal SZ observations.

If we have a catalogue of clusters, each will sit in a unique region of space – they will have a distribution of temperatures, redshifts and peculiar velocities (both  $\beta_c$  and  $\mu_c$ ), leading to variations in  $F_R(\theta_c, \beta_c, \mu_c, \alpha)$ . There is also the possibility that the background radio signal itself depends on the redshift and position of the cluster (i.e., variations in  $f(\hat{\gamma}, z)$ ). If there is any spatial or redshift dependence in  $\alpha$ , these will also modify the observed signal between clusters.

It is clear that the more we know about each cluster in our sample, (1) the better we can model the expected radio SZ signal and (2) the more certainty we can have on the cause of any measured variations in the radio background. For nearby clusters, for example, we may already know  $n$ ,  $y$ ,  $\beta_c$ ,  $\mu_c$  and  $T_e$  through the standard SZ signal measurements, or through a combination of analogous measurements, e.g., X-ray observations. In such a situation, variations in the observed signal must all come from variations in  $A_R f(z)$ , in  $\alpha$  (which would both change the shape of the radio contribution  $g(\nu, \alpha)$  and the scaling through  $F_R$ ) or through some more complicated anisotropies within the radio background. Conversely, of course, if our measurements of the radio background are significantly more constrained than those for the cluster's measurements, then we may be able to determine the parameters of clusters through the radio SZ measurement itself – as is conventional within the typical SZ experiments.

If information on individual clusters is less precise, one can resort to stacking analyses made over large samples of clusters. For the normal SZ effect, this has been attempted using *Planck* data to constrain the rSZ effect (Hurier & Tchernin, 2017; Erler et al., 2018). In Erler et al. (2018), they used 772 clusters to find an averaged  $\langle y \rangle = (1.24 \pm 0.04) \times 10^{-4}$  with an averaged SZ temperature of  $k_B T_{SZ} = 4.4^{+2.1}_{-2.0}$  keV. Since the radio SZ signal also depends on  $y$  and  $k_B T_{SZ}$ , we could expect to find a signal of a similar magnitude under the stacking procedure.

Applying this method to radio SZ measurements would allow the calculation of averages of many of the parameters. For the simplest stacking procedure, this would be averaging over temperature, peculiar velocity and redshift of the catalogue. Since the peculiar velocities can be assumed to be uncorrelated, almost all kinematic corrections would be averaged out, that is we would perform  $\langle F_R(\theta_c, \beta_c, \mu_c, \alpha) \rangle_{\mu_c}$ . This would leave kinematic terms only in the monopole corrections at  $O(\beta_c^2)$ , which are generally very small. As such, any measured stacked relativistic corrections would indicate the sample-averaged



cluster temperatures, as well as the spatially- and redshift-averaged radio background. Again, prior knowledge on the temperature distribution of the clusters can be used to refine our understanding of the deduced radio background parameters.

If stacking procedures were then performed on subsets of the catalogue, it would be possible to bound variations in  $f(\hat{\gamma}, z)$  within the radio background itself – i.e., (1) by spatially selecting clusters, it would theoretically be possible to directly constrain anisotropies in the radio background, or (2) by using priors on the redshift location of clusters, to determine the redshift evolution (e.g., redshift binning). This is very similar in spirit to using clusters as distributed observers of for the remote CMB quadrupole (and dipole) anisotropy (Deutsch et al., 2018). As for the normal SZ signal, by using priors on the orientation of the clusters' peculiar velocities (Hand et al., 2012; Cayuso et al., 2021), it may be possible to learn about the averaged cluster  $\langle\beta_c\rangle$ . In contrast to the standard SZ effect, the radio SZ effect anisotropies are not necessarily limited to being very small. This could greatly increase the observability of the radio SZ effects. For example, if there are small-scale fluctuations in the radio background then the 'on-cluster' and 'off-cluster' background may be distinct, e.g., if the cluster itself were a significant source of the radio background.

However, it is also worth noting that a full-sky signal would likely prove very difficult to detect for the radio SZ signal. In Hill et al. (2015), they predict that for the typical SZ signal, a whole-sky average would result in  $\langle y \rangle \simeq 1.7 \times 10^{-6}$ , and a  $y$ -weighted temperature of  $\langle k_B T_{\text{SZ}} \rangle \simeq 1.3$  keV.<sup>3</sup> While for the typical SZ signal this may be measured with future high-precision spectroscopy instruments such as PIXIE (Kogut et al., 2011), or Voyage 2050 (Chluba et al., 2021), no such instruments are planned which may reach this level of precision in the radio SZ regime over the full sky.

## 4.5 Conclusion

In this chapter, I derived the corrections to the radio SZ signal arising from kinematic terms, relativistic corrections and possible anisotropies in the radio background. The main goal was to give all the expressions that are required to describe these effects and to illustrate the main similarities and differences to the equivalent effects in the standard SZ effect. The discussion is meant to stimulate ideas about next steps related to the observability of these effects and how one could potentially pursue these ideas. A detailed forecast is beyond the scope of this thesis.

In general, similarly to the standard SZ signal, the kinematic effects cause the largest changes to the radio SZ signal, with these effects being  $\gtrsim 2.5$  times larger

<sup>3</sup>The conversion to  $y$ -weighted temperature was used in Abitbol et al. (2017).



in the radio SZ than for the standard CMB SZ signal. These effects must always be accounted for in single-cluster measurements, and can be easily modelled. For stacking calculations, however, the kinematic effects will be greatly reduced, as the orientations of the clusters' peculiar velocities will 'cancel' most of their contributions in large stacking considerations.

The relativistic temperature corrections are marginally smaller in the radio SZ signal than in the standard SZ signal (around a few percent over reasonable cluster temperatures). These corrections are also around the same size as those from the current errors in the measurement of the radio background from [Fixsen et al. \(2011\)](#), indicating that obtaining competitive bounds on the radio background itself, would require a similar precision of detection. However, as such it is also possible to use the radio SZ signal in concert with the normal SZ signal to obtain higher-confidence prior measures of cluster properties themselves. SZ clusters are now routinely observed with e.g., Planck ([Planck Collaboration et al., 2016b](#)), ACT ([Choi et al., 2020](#)) and SPT ([Bleem et al., 2015](#)), and with future SZ samples obtained with SPT-3G ([Benson et al., 2014](#)), the Simons Observatory ([Ade et al., 2019](#)), CMB-S4 ([Abazajian et al., 2016](#)) and CCAT-prime ([Parshley et al., 2018](#)), many of the required observables could become available.

This analysis shows that, if there are anisotropies in the radio background, or if the background has redshift evolution, these may well be far larger effects (see Figure 4.6). Any radio background anisotropies lead to contributions which scale similarly to kinematic effects. Both of these could be observationally explored with a stacking analysis on a large enough cluster sample (see Section 4.4). The radio SZ signal thus provides a unique tool to probe the nature of the radio background in determining whether it is truly 'cosmological' (in which case we would expect little to no redshift evolution).

While a forecast of the details of measuring this signal are beyond this thesis, this work provides a detailed description of the contributing factors to the radio SZ signal itself, in the hope that future forecasts might be made easier. Furthermore, with the advent of more large-scale, high-precision experiments such as the SKA ([Dewdney et al., 2009](#); [Square Kilometre Array Cosmology Science Working Group et al., 2020](#)) and MeerKAT ([Jonas & MeerKAT Team, 2016](#)), there is the potential that these measurements may not be quite as futuristic as they might seem. Another obvious way forward is through cross-correlation studies, which are also frequently used in normal SZ observations ([Hand et al., 2012](#)).

While here the discussion focused on the scattering of the radio background, this merely provides a mathematically simple example of examining the effects of scattering on background photon sources beyond only the CMB. Thus, much of the work presented here can be extended to other backgrounds, e.g., the CIB, the 21cm line, X-rays emitted by clusters themselves (e.g., [Cooray, 2006](#); [Grebenev & Sunyaev, 2020](#)). All the expressions should be directly applicable

to CIB scattering at frequencies below the CIB maximum, which essentially behaves like a power-law with  $\alpha_{\text{CIB}} \simeq 0.14$ , where we quoted the average CIB spectrum as used by the *Planck* collaboration (Planck Collaboration et al., 2014b, 2016e). This case has also been explored (as briefly mentioned in Chapter 1) in Sabyr et al. (2022); Acharya & Chluba (2022), and it is worth noting that in particular scattering of the CIB could have an important effect on current SZ analysis targeting the relativistic SZ (e.g., Erler et al., 2018).

## Chapter 5

# The SZ effect from high-energy non-thermal and anisotropic distributions

This chapter is comprised of entirely novel, unpublished work. This work was done in conjunction with a major code refurbishment of and extensions to `SZpack`. The work here is planned to be completed and released as a paper in the future.

### 5.1 Introduction

This thesis has so far focused on improvements to SZ modelling through improving our understanding of the precise temperatures in clusters (Chapters 2 and 3) allowing for improved determinations of the rSZ corrections. It has also considered the effects of modifying the photon background (Chapter 4) and how additional cosmological photon distributions will lead to further SZ-like distortions. This chapter focuses on additional effects from modifications to the CMB photon background and the electron distributions themselves. In particular, this chapter comes in two parts, the first discusses anisotropy in the photon and electron distributions, while the second explores how high-energy non-thermal components of the electron population may cause distinct SZ signals.

Anisotropy in the photon or electron distributions will lead to modified SZ signals, where generally only the first two multipoles are considered: the dipole, in terms of bulk motions of the electrons and photons (i.e., the kSZ signal); and the quadrupole, for the purposes of calculating the induced pSZ signals. Here, I will discuss a framework to consider arbitrary multipole components to SZ scattering. It has been well established that the photon anisotropies generally lead to small signals (e.g., [Sazonov & Sunyaev, 1999](#)), however, as the future of CMB observations leads to more high-resolution and high-precision measurements, these effects may come into observational reach. The electron anisotropy, conversely,

has been studied far less as it relies on a firm understanding of the magnetic fields within the ICM and other sources of microphysical anisotropies. However, recent studies by [Khabibullin et al. \(2018\)](#) indicate that these will lead to pSZ effects of a comparable size to the other commonly discussed pSZ effects. It is also worth noting that regions of electron anisotropy may also be those with high-energy, which are not well-thermalised and may magnify any effects that are generated. In this chapter we largely focus on the intensity distortions caused by these anisotropies, rather than a detailed consideration of the pSZ effect.

The second topic of this chapter, that of high-energy electron distributions, has been studied in less detail, and has been summarised in Section 1.4.2. In this chapter, I examine a selection of toy-models that encapsulate potential high energy non-thermal behaviour in clusters ([Enßlin & Kaiser, 2000](#); [Colafrancesco et al., 2003](#); [Kaastra et al., 2009](#)). These, by no means, encapsulate the full details of high-energy non-thermal electron populations – however, thus far, little work has been invested into studying analytic models for these populations. Future work could involve comparing these models with predictions from simulations, to determine a more grounded approach to understanding these effects in clusters. This chapter instead attempts to determine the scale of any corrections incurred from accounting for high-energy non-thermal components, and what effects they may have on future SZ observations.

## 5.2 The analytic anisotropic SZ scattering kernel

In Chapter 1, the formality of the scattering process was discussed in great detail. However this work was all done assuming isotropic photon and electron populations. To define anisotropic scattering kernels, it is first necessary to define exactly what this means. While in principle it would be possible to consider both an anisotropic electron and photon field, in this chapter we will only consider each separately. It should be noted that this chapter is focused on the SZ scattering and thus assumes everything is in the Doppler-dominated regime where  $\omega_0 \ll p_0$  (i.e., the dimensionless photon frequency is small compared to the dimensionless electron momentum).

While in principle an anisotropic distribution can be expressed in any frame, there is, in fact, a preferred frame for the spherical harmonic decomposition of the anisotropy. Figure 5.1 repeats a schematic of the Compton scattering problem for reference. In this preferred frame (an expansion about the axis of the outgoing photon, i.e., the  $z$ -axis as depicted in Figure 5.1), an anisotropic photon distribution can be expressed as<sup>1</sup>  $n(x, \mathbf{k}_0) = \sum_{\ell m} n_{\ell m}(x) Y_{\ell}^m(\mu_{\text{sc}}, \phi_{\text{sc}})$ . However, as will be justified in Eq. (5.5), in this frame as long as either the photon or electron distribution is isotropic, only the  $m = 0$  component will contribute to the

<sup>1</sup>Recalling that  $\phi_{\text{sc}}$  refers to the associated azimuthal angle to  $\mu_{\text{sc}}$ .

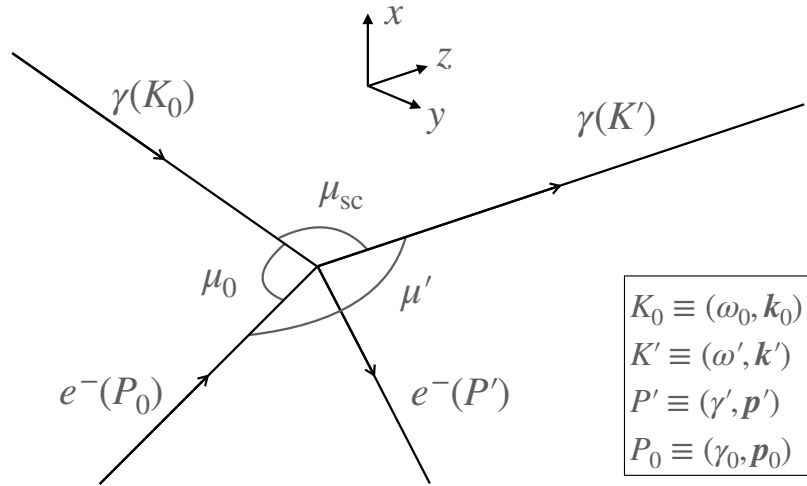


**FIGURE 5.1:** A repeated schematic of the Compton scattering problem, similar to Figure 1.3.  $K_0$  and  $K'$  are the four-vectors for the incoming and outgoing photons, with dimensionless frequencies  $\omega_0$  and  $\omega'$  and dimensionless momenta  $\mathbf{k}_0$  and  $\mathbf{k}'$ .  $P_0$  and  $P'$  are the 4-vectors for the incoming and outgoing electrons, with dimensionless energies  $\gamma_0$  and  $\gamma'$  and momenta  $\mathbf{p}_0$  and  $\mathbf{p}'$ .  $\mu_0$ ,  $\mu'$  and  $\mu_{sc}$  are the cosines of the marked angles. The axes are to emphasise the dimensionality of the scattering, with  $z$  [here](#) aligned with the line-of-sight, i.e., the outgoing photon.

distortion. This means the scattering of [any](#) anisotropic photon distribution by an isotropic electron distribution can be obtained from  $n(x, \mathbf{k}_0) = \sum_{\ell=0}^{\infty} n_{\ell}(x) P_{\ell}(\mu_{sc})$ , where  $P_{\ell}$  denote the Legendre polynomials. In a similar way, an isotropic electron distribution would become  $f'(\mathbf{p}') = \sum_{\ell'=0}^{\infty} f_{\ell'}(p') P_{\ell'}(\mu')$ .<sup>2</sup>

As such, Eq. (1.5) can be rewritten in terms of the outgoing photon and in a fully general way as

$$\begin{aligned} \frac{dn(\omega')}{d\tau} &= \int p_0^2 dp_0 \frac{d\mu_{sc} d\phi_{sc} d\mu' d\phi'}{4\pi} \frac{d\sigma}{d\Omega} [f'n'(1+n_0) - f_0 n_0 (1+n')] \\ &\simeq \int p_0^2 dp_0 \frac{d\mu_{sc} d\phi_{sc} d\mu' d\phi'}{4\pi} \frac{d\sigma}{d\Omega} [f'n' - f_0 n_0] \\ &= -n_0 + \sum_{\ell=0}^{\infty} \sum_{\ell'=0}^{\infty} \sum_{m=-\ell}^{\ell} \sum_{m'=-\ell'}^{\ell'} \int_{-\infty}^{+\infty} dt \mathcal{P}_{\ell\ell'}^{mm'}(t) n_{\ell m}(x'). \end{aligned} \quad (5.1)$$

Here, the first approximation ignores stimulated scattering effects (as is standard in SZ calculations) and the second equality uses  $t \equiv \omega'/\omega_0$ . The scattering kernel  $\mathcal{P}_{\ell\ell'}^{mm'}(t)$  is defined as

$$\begin{aligned} \mathcal{P}_{\ell\ell'}^{mm'}(t) &= \int_{p_{\min}(t)}^{\infty} p_0^2 dp_0 f'_{\ell'm'} K_{\ell\ell'}^{mm'}(t, p_0); \\ K_{\ell\ell'}^{mm'}(t, p_0) &\equiv \frac{d\phi'}{dt} \int \frac{d\mu_{sc} d\mu' d\phi_{sc}}{4\pi} \frac{d\sigma}{d\Omega} Y_{\ell}^m(\mu_{sc}) Y_{\ell'}^{m'}(\mu'), \end{aligned} \quad (5.2)$$

<sup>2</sup> $n_{\ell}$  and  $f_{\ell'}$  now implicitly contain factors of  $\sqrt{(2\ell+1)/4\pi}$ .

and  $K_{\ell\ell'}(t, p_0)$  is the general multipole kernel. However, we can define the individual photon,  $K_\ell^\gamma$ , and electron,  $K_\ell^e$ , multipole kernels<sup>3</sup> as

$$\begin{aligned} K_\ell^\gamma(t, p_0) &\equiv \frac{d\phi'}{dt} \int \frac{d\mu_{sc} d\mu' d\phi_{sc}}{4\pi} \frac{d\sigma}{d\Omega} P_\ell(\mu_{sc}) \\ K_\ell^e(t, p_0) &\equiv \frac{d\phi'}{dt} \int \frac{d\mu_{sc} d\mu' d\phi_{sc}}{4\pi} \frac{d\sigma}{d\Omega} P_\ell(\mu'). \end{aligned} \quad (5.3)$$

In [Enßlin & Kaiser \(2000\)](#), the monopole of the general kernel  $K_{0,0}(t, p_0)$  is computed and can be expressed as

$$\begin{aligned} K_{0,0}(t, \eta) &= \frac{3}{32p_0^6 t} \left[ 2t(1+t)(3+2p_0^2) \left( |\log(t)| - 2\sinh^{-1}(p_0) \right) \right. \\ &\quad \left. - |1-t| \left( 1 + (10+8p_0^2+4p_0^4)t + t^2 \right) + 4t(1+t) \frac{p_0(3+3p_0^2+p_0^4)}{\sqrt{1+p_0^2}} \right]. \end{aligned} \quad (5.4)$$

This is however, generally speaking complicated to calculate – and in such circumstances where anisotropy in both populations exist (beyond those of, for instance, a Doppler shift between frames that can be accounted for with a correction to the measured angles and frequencies directly), it may be simplest to calculate the entire integral numerically.

### 5.2.1 Anisotropy in the photon population

By considering anisotropy in each population individually, one can learn about the effects of each on the observed spectra. Here, I will first focus on the effects of an anisotropic photons, with the effects of anisotropic electrons discussed in Section 5.2.2.

Even merely considering  $K_\ell^\gamma$ , some consideration is required to calculate the kernel integral. Firstly, while in general the necessary integrations occur over the four angles ( $\mu_{sc}$ ,  $\mu'$ ,  $\phi_{sc}$  and  $\phi'$ ) and the incoming electron momentum  $p_0$ , the kernel itself has dependence on the angles  $\mu'$ ,  $\mu_{sc}$ , and  $\mu_0$ . As such, all of the implicit  $\phi_{sc}$  and  $\phi'$  behaviour is contained in  $\mu_0 = \mu'\mu_{sc} + \cos[\phi' - \phi_{sc}]\sqrt{(1-\mu_{sc}^2)(1-\mu'^2)}$  and, generally speaking,  $Y_\ell^m(\mu_{sc}, \phi_{sc}) \propto P_\ell^m(\mu_{sc})e^{im\phi_{sc}}$ . These indicate immediately a transformation to integrating instead over  $\phi_0 = \phi' - \phi_{sc}$  and  $\phi_{sc}$ . Now it is immediately clear that the  $\phi_{sc}$  integral is simply

$$\int_0^{2\pi} d\phi_{sc} e^{im\phi_{sc}} = \begin{cases} 2\pi & \text{for } m = 0 \\ 0 & \text{otherwise.} \end{cases} \quad (5.5)$$

<sup>3</sup>That is,  $K_{\ell,0}^{0,0}$  and  $K_{0,\ell}^{0,0}$  respectively – i.e., taking isotropic electrons and anisotropic photons and vice versa. We will show in the next section that the non-zero  $m, m'$  components do not contribute in either regime, so are omitted.

Hence, our previous claim that only the  $m = 0$  case contributes to the distortion is confirmed. In the case of *both* electron and photon anisotropy, the transformation to  $\phi_0$ , firstly, leads to the  $\phi_{sc}$  dependence  $e^{i(m+m')\phi_{sc}}$ , so the  $m = -m'$  terms still contribute, and further leads to significant complications to the rest of the integration process.

The  $\phi_0$  component is more complex. However, by recalling that<sup>4</sup>  $t \simeq (1 - \beta_0\mu_0)/(1 - \beta_0\mu')$ , one can rearrange to find

$$\begin{aligned}\phi_0 &= \cos^{-1} \left( \frac{1 - t + \beta_0\mu'(t - \mu_{sc})}{\beta_0\sqrt{(1 - \mu_{sc}^2)(1 - \mu'^2)}} \right); \\ \frac{d\phi_0}{dt} &= \frac{1 - \beta_0\mu'}{\beta_0^2(1 - \mu_{sc}^2)(1 - \mu'^2) - (1 - t + \beta_0\mu'(t - \mu_{sc}))^2}.\end{aligned}\quad (5.6)$$

The latter allows for the conversion of a  $\phi$  integral into a  $t$  integral as required by the formulation of the kernel. The former equation immediately indicates that the 'direct'  $\phi_0$  dependence in  $\mu_0$  is all eliminated.

Substituting all this in, and simplifying, it can be seen that the  $\mu$  integrals are now restricted and cannot be carried out over the naive range of  $-1$  to  $1$ . In fact, carrying out the  $\mu'$  integral first gives the integration limits

$$\begin{aligned}\mu'_{\text{lim}\pm} &= \frac{t^2 + t + \mu_{sc}(1 - t) \pm \sqrt{(\mu_{sc}^2 - 1)((1 - t)^2 - \beta_0^2(t^2 - 2t\mu_{sc} + 1))}}{\beta_0(t^2 - 2t\mu_{sc} + 1)}, \\ \mu_{sc,\text{lim}+} &= \frac{(\beta_0^2 - 1)t^2 + 2t + \beta_0^2 - 1}{2\beta_0^2 t}, \\ \mu_{sc,\text{lim}-} &= -1.\end{aligned}\quad (5.7)$$

The kernel can then be calculated to arbitrary  $\ell$  with, for example,

$$\begin{aligned}K_1^\gamma(t, p_0) &= \frac{3}{32p_0^8 t} \left( |1 - t| [4p_0^6(1 + t + t^2) - 2p_0^4(1 - 14t + t^2) \right. \\ &\quad \left. + p_0^2(31 + 166t + 31t^2) + 5(11 + 38t + 11t^2)] \right. \\ &\quad \left. + \frac{2p_0(1 + t)}{\sqrt{1 + p_0^2}} [2p_0^6(1 - t + t^2) + 30p_0^4t + p_0^2(11 + 142t + 11t^2) + 15(1 + 8t + t^2)] \right. \\ &\quad \left. + 3(1 + t) [4p_0^4t + 2p_0^2(1 + 17t + t^2) + 5(1 + 8t + t^2)] \left( |\log(t)| - 2\sinh^{-1}(p_0) \right) \right),\end{aligned}\quad (5.8)$$

---

<sup>4</sup>Remembering that as before  $\beta_0 = p_0/\gamma_0$  and  $\gamma_0 = \sqrt{p_0^2 + 1}$ .

$$\begin{aligned}
K_2^\gamma(t, p_0) = & \frac{3}{1280p_0^{10}t^2} \left( -|1-t| [32p_0^8(1+t+t^2+t^3+t^4) - 16p_0^6(1+t-24t^2+t^3+t^4) \right. \\
& + 4p_0^4(3+278t+1478t^2+278t^3+3t^4) \\
& + 30p_0^2(1+206t+666t^2+206t^3+t^4) \\
& \left. + 35(3+178t+478t^2+178t^3+3t^4)] \right. \\
& + \frac{8p_0(1+t)}{\sqrt{1+p_0^2}} [4p_0^8(1-t+t^2-t^3+t^4) + 120p_0^6t^2 + 20p_0^4t(7+80t+7t^2) \\
& + 25p_0^2t(25+161t+25t^2) + 525t(1+5t+t^2)] \\
& + 20t(1+t) [8p_0^6t + 12p_0^4(1+15t+t^2) + 90p_0^2(1+7t+t^2) + 105(1+5t+t^2)] \\
& \left. \left( |\log(t)| - 2\sinh^{-1}(p_0) \right) \right). \tag{5.9}
\end{aligned}$$

It is evident that these increase in complexity quickly, while still maintaining a fairly consistent structure. In particular, there always arise polynomial coefficients for three parts of the equation – a part proportional to  $|\log(t)| - 2\sinh^{-1}(p_0)$ ; a part proportional to  $|1-t|$ ; and a purely polynomial part with a leading factor of  $\frac{p_0(1+t)}{\sqrt{1+p_0^2}}$ .

This continues to be true throughout all these kernels for photon anisotropy (and indeed for electron anisotropy). By expanding the Legendre polynomials as  $P_\ell(\mu_{sc}) = \sum_{k=0}^{\ell} \binom{\ell}{k} \binom{\ell+k}{k} \left(\frac{\mu_{sc}-1}{2}\right)^k$  a general form can be found, comprising of two main components,

$$\begin{aligned}
K_\ell^\gamma(t, p_0) = & \sum_{k=0}^{\ell} \binom{\ell}{k} \binom{\ell+k}{k} \left[ \frac{3}{32p_0^6t} (G_k + H_k) \right]; \\
G_k = & \frac{p_0^5}{\gamma_0(4t)^{k-1}} \sum_{n=0}^k \frac{(-1)^n}{2n+1} \binom{k}{n} (t-1)^{2(k-n)} \left( (t+1)^{(2n+1)} - \left[ \frac{\gamma_0|t-1|}{p_0} \right]^{2n+1} \right), \tag{5.10} \\
H_k = & \frac{(1+t)}{p_0^{2k}} \left( 5(t+1)^2(p_0^2+1)h_0^{(k)} - [(t^2+1)(2p_0^2+5) + t(16p_0^2+22)]h_2^{(k)} \right. \\
& \left. + 4t(2p_0^2+3)h_4^{(k)} \right).
\end{aligned}$$

It is immediately clear that  $G_k$  is a purely polynomial function and  $H_k$  depends on the generator functions  $h_m^{(k)}$  which have been defined to be the integrals

$$h_m^{(k)} = \int \frac{\sqrt{y^2-1}(y^2-1)^k y^m}{y^6} dy \tag{5.11}$$

with  $y = \sqrt{1 + \frac{1}{2}p_0^2(1-\mu_{sc})}$  and the integration limits obtained through the transformation of  $\mu_{sc, \lim \pm}$ . These can be expressed analytically defining the first few



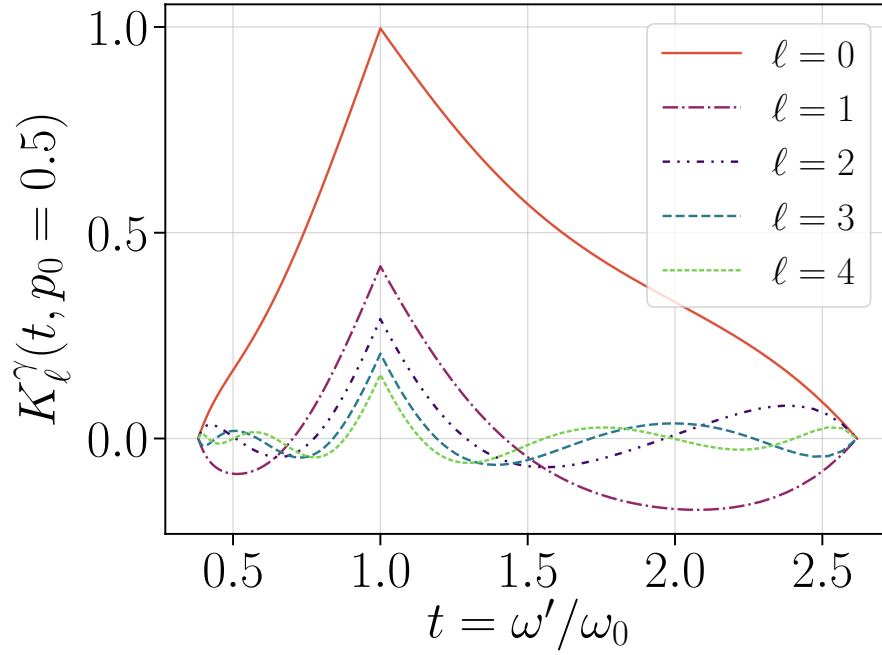


**FIGURE 5.2:** The first five multipoles,  $\ell \leq 4$ , of the anisotropic photon multipole scattering kernel,  $K_\ell^\gamma$ . Here we have arbitrarily set  $p_0 = 0.5$ . Note that all the higher multipoles have negative components, indicating scattering between multipoles.

terms specifically, using

$$\begin{aligned}
 j^{(n)} &= \frac{p_0^{2n+1}}{\gamma_0^5} - \frac{|t-1|^{2n+1}}{(4t)^{n-2}(1+t)^5}; \\
 h_0^{(0)} &= -\frac{1}{15}[2j^{(2)} + 5j^{(1)}], \quad h_0^{(1)} = \frac{1}{5}[j^{(2)}], \quad h_2^{(0)} = -\frac{1}{3}[j^{(2)} + j^{(1)}], \\
 h_0^{(2)} &= \frac{1}{2} \left( |\log(t)| - 2 \sinh^{-1}(p_0) \right) + \frac{1}{15} [23j^{(2)} + 35j^{(1)} + 15j^{(0)}].
 \end{aligned} \tag{5.12}$$

Then the higher  $k$  terms can be expressed as

$$\begin{aligned}
 h_0^{(k)} &= \frac{(2k+1)!!}{2^{k-2}(k-2)!} \left( \frac{h_0^{(2)}}{15} - \sum_{n=3}^k \frac{2^{n-3}(n-3)!}{(2n+1)!!} (-1)^n j^{(n)} \right) \quad \text{for } k \geq 3; \\
 h_2^{(k)} &= \frac{-1}{2k+3} \left( 5h_0^{(k+1)} + (-1)^k j^{(k+1)} \right) \quad \text{for } k \geq 1; \\
 h_4^{(k)} &= \frac{-1}{2k+3} \left( 3h_2^{(k+1)} + (-1)^k [j^{(k+2)} + j^{(k+1)}] \right).
 \end{aligned} \tag{5.13}$$

In general, we can see the same components as before with the ‘log’ part coming from the  $h_0^{(2)}$  term which carries into all the higher-order terms as well.  $j^{(n)}$  clearly contains both a  $|t-1|$  term and a polynomial part, which, with a consideration of  $H_k$ , will always have a leading term of  $(1+t)$  as expected.  $G_k$  directly contains both the  $|t-1|$  and  $(1+t)$  polynomial parts.

The first five multipoles can be seen in Figure 5.2. Here we see, as has been long established (e.g., [Sunyaev & Zeldovich, 1980](#); [Sazonov & Sunyaev, 2000](#)),

that the monopole scattering kernel has a cusp at  $t = 1$ , driven mathematically by the absolute values of  $|\log(t)|$  and  $|t - 1|$ . From a physical standpoint, this is indicating that a photon is most likely (modally) to maintain its same energy and merely be deflected under a scattering. However, the tail to higher energies indicate, as is long established, the propensity of SZ scatterings to move photons from lower energies to high energies – that is, to upscatter.

These multipoles are consistent with those displayed in, for instance, [Chluba & Dai \(2014\)](#), and have been verified numerically. The higher multipoles all maintain this cusp at  $t = 1$  (as can be predicted from the mathematical forms continuing to contain these absolute values). However, they all also contain negative sections, which are harder to interpret – it must be remembered that each multipole follows the scattering caused by the population of photons in a certain multipole – and as such, the negative sections indicate the scattering of photons out of the given multipole. That is, the SZ scattering causes an isotropisation of the photon distribution.

It is also interesting to note that each multipole has a kernel that crosses zero,  $\ell$  times on either side of  $t = 1$ . That is, we can consider for each multipole the kernel is composed of  $2\ell + 1$  regions where the kernel is alternately positive or negative. The large negative region in  $\ell = 1$  at higher values of  $t$  leads to an effect opposing that of the monopole, that is, the dipole is scattered preferentially to lower frequencies. This in fact is also true for the  $\ell = 3$  and  $\ell = 4$  cases, while the  $\ell = 2$  scattering leads to net upscattering like the monopole.

It should, however, be noted, that the amplitude of these scatterings falls rapidly with increasing  $\ell$  – even supposing the amplitude of the anisotropic components of the photon distribution were the equal to the monopole, for a thermal electron distribution (that is, relativistic Maxwell-Boltzmann) and CMB photons, the amplitude is suppressed with increasing  $\ell$ . This can be determined analytically, by integrating over frequency (or  $t$ ) and taking an expansion about  $p_0 = 0$ . The monopole kernel obeys (at all  $p_0$ )  $\int dt K_0(t, p_0) \equiv 1$ . In a similar way, we can find, for  $\ell \leq 4$ ,

$$\begin{aligned} \int dt K_1^\gamma(t, p_0) &\simeq -\frac{2}{15}p_0^2 + \mathcal{O}(p_0^4); & \int dt K_2^\gamma(t, p_0) &\simeq \frac{1}{10} - \frac{1}{5}p_0^2 + \mathcal{O}(p_0^4); \\ \int dt K_3^\gamma(t, p_0) &\simeq \frac{2}{35}p_0^2 + \mathcal{O}(p_0^4); & \int dt K_4^\gamma(t, p_0) &\simeq \mathcal{O}(p_0^4). \end{aligned} \quad (5.14)$$

These return the expected result obtained in the Thomson limit that only the  $\ell = 0$  and 2 components contribute at zeroth order – with the  $\ell = 2$  component at  $1/10$  the amplitude of the monopole.

### 5.2.2 Anisotropy in the electron population

In a similar way a general anisotropic electron multipole kernel can be derived and written as

$$\begin{aligned}
 K_\ell^e(t, p_0) &= \sum_{k=0}^{\ell} \binom{\ell}{k} \binom{\ell+k}{k} \left[ \frac{3}{32p_0^5 t} \left( 3 \frac{X_4^{(k)}}{\gamma_0} - 6(t+1)X_3^{(k)} \right. \right. \\
 &\quad \left. \left. + [3(t^2 + 4t + 1) + 2p_0^2(t^2 + 6t + 1)] \frac{X_2^{(k)}}{\gamma_0} \right. \right. \\
 &\quad \left. \left. - 2(3 + 2p_0^2)t(1+t)X_1^{(k)} + (3 + 4p_0 + 4p_0^2)t^2 \frac{X_0^{(k)}}{\gamma_0} \right) \right]; \\
 X_c^{(k)} &= \frac{(\gamma_0 - p_0)^{k-c+1}}{2^k p_0^{k+1}} \left[ (-1)^{c-1} \binom{k}{c-1} (2 \sinh^{-1}(p_0) - |\log(t)|) \right. \\
 &\quad \left. + \sum_{n=0; n \neq c-1}^k (-1)^n \binom{k}{n} \frac{g^{(n-c+1)}}{n-c+1} \right]; \\
 g^{(n)} &= \frac{1}{2(1-\beta_0)^n t^n} \left( (t^n + 1) [(1+\beta_0)^n - (1-\beta_0)^n] \right. \\
 &\quad \left. - \text{sign}(t-1)(t^n - 1) [(1+\beta_0)^n + (1-\beta_0)^n] \right).
 \end{aligned} \tag{5.15}$$

Here, the  $|t-1|$  term has instead been split into a  $\text{sign}(t-1)(t^n - 1)$  part, to keep the expression simpler. It is worth reiterating that little work has been done to motivate high-order anisotropies in the electron field. A ‘dipole’ would reflect the motion of a cell of electrons, as in the kinematic SZ correction and quadrupoles may occur due to the behaviour of magnetic fields in clusters. However, higher multipoles of electron anisotropy remain broadly unexamined in SZ physics and are expected to be small due to rapid Coulomb scattering.

Nonetheless, the first five multipoles are displayed now in Figure 5.3. It is immediately clear that these are significantly harder to interpret than the photon anisotropies. Firstly, it is evident that although there is a discontinuity in gradient at  $t = 1$ , there is no longer the clear cusp displayed in the photon anisotropies. Secondly, as has been long established, the dipole term leads to pure upscattering (as in the kinematic SZ effect). The higher multipoles lead to significantly more complicated behaviour. Once again, when  $t > 1$  each multipole crosses zero  $\ell$  times. However, the distinct asymmetry in the kernels means that for the odd multipoles for  $t < 1$  there are only  $\ell - 1$  crossings, while the even scattering kernels have a more ‘cuspy’ behaviour and cross  $\ell$  times.

Here also, the higher multipoles are not suppressed in the same way as for the photon anisotropy. Analytically this can be explored by expanding as  $p_0 \rightarrow 0$ , so

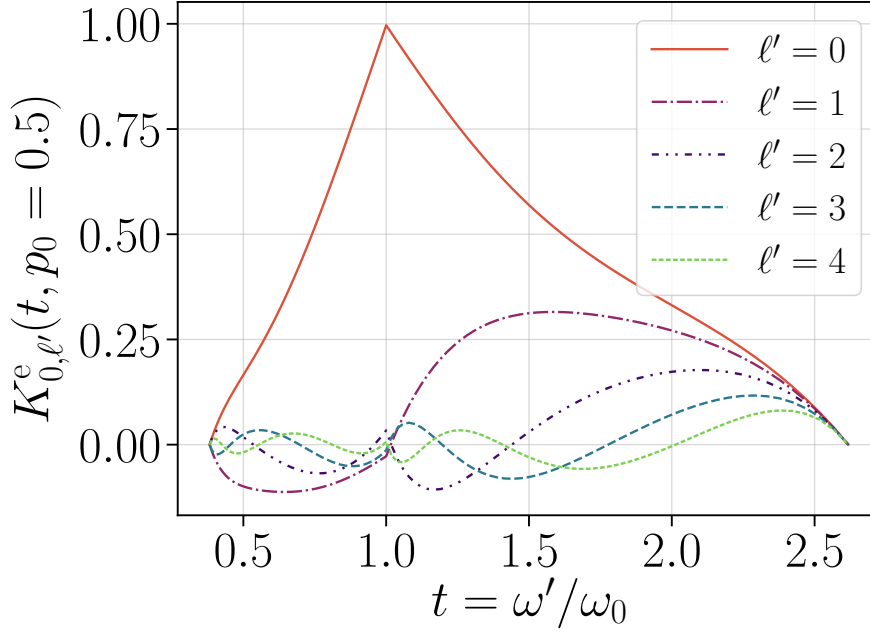


**FIGURE 5.3:** The first five multipoles,  $\ell \leq 4$ , of the anisotropic electron multipole scattering kernel,  $K_{\ell}^e$ . Here we have arbitrarily set  $p_0 = 0.5$ . Note that all the higher multipoles have negative components, indicating scattering between multipoles.

that

$$\begin{aligned} \int dt K_1^e(t, p_0) &\simeq -\frac{2}{3}p_0 - \frac{19}{75}p_0^3 + O(p_0^4); & \int dt K_2^e(t, p_0) &\simeq \frac{12}{25}p_0^2 + O(p_0^4); \\ \int dt K_3^e(t, p_0) &\simeq \frac{64}{175}p_0^3 + O(p_0^4); & \int dt K_4^e(t, p_0) &\simeq O(p_0^4). \end{aligned} \quad (5.16)$$

These appear on the surface to be well behaved, with each successive multipole having a higher leading order with  $p_0$ . However, the overwhelming asymmetry in the scattering kernel can lead to large distortions (particularly for the dipole moment  $\ell = 1$ ). For instance, when considering kSZ effects when clusters have low temperatures, the kinematic effect can dominate over thermal SZ signal as the energies held in the bulk motion become comparable to or greater than the thermal energy.

### 5.2.3 Discussion

The SZ signals from anisotropic scattering are in general expected to be small. The polarised effects generated by the CMB quadrupole and intrinsic CMB fluctuations are predicted to be around  $10^{-8}$  of the CMB temperature (i.e., [Sazonov & Sunyaev, 1999](#)). This would generate a similar scale of signal to that expected from the pSZ signals from multiple scatterings within clusters or the higher order kSZ induced pSZ signals. [Khabibullin et al. \(2018\)](#) predicts that magnetic induced electron anisotropy in shocks could generate a polarised signal of a similar magnitude (around 10 nK).

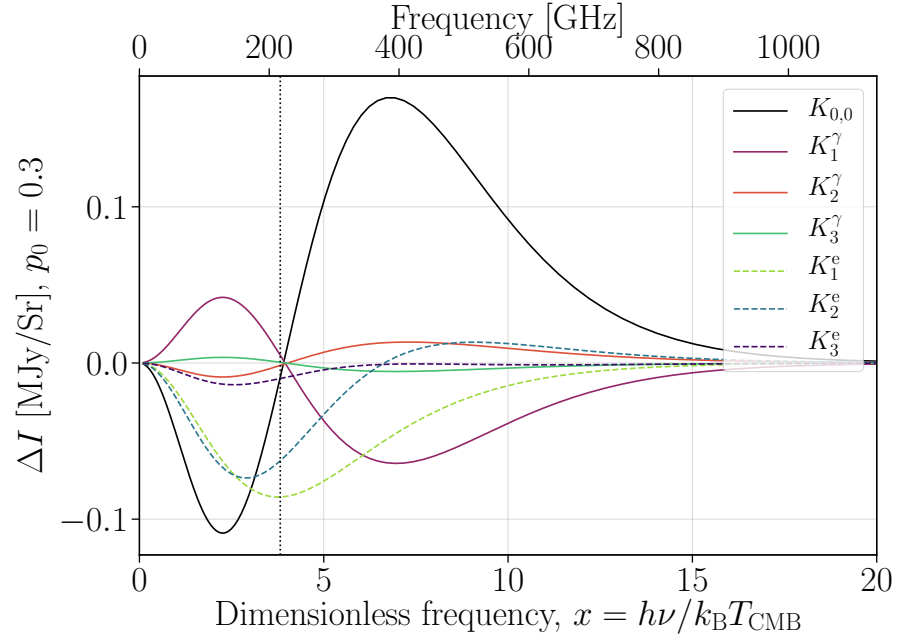


**FIGURE 5.4:** The SZ signals induced by anisotropic photon and electron distributions. Here, the  $K_\ell$  indicate which kernel is used. The integrations use a fixed electron momentum of  $p_0 = 0.3$  and a CMB blackbody photon distribution. All of these signals use the same amplitudes of both signals, and  $y = 10^{-4}$ ,  $\tau = y/(\beta_0^2/3)$ , except  $K_1^e$ , the electron dipole, which is suppressed with a factor of 0.2. The solid lines reflect the photon anisotropies while the dashed lines show the electron anisotropy. The vertical dotted line is at 217 GHz, the null of the thermal SZ effect.

Inherently, these signals are all only considering the polarised components rather than the general intensity, we have focussed on here, but the amplitude of the signals will be highly related. These predictions have all been carried out using simplistic models to generate the spectral dependence, for instance starting from the Kompaneets equation, rather than the full cross-section, and as such have simplistic models of the eventual scattering shape. However, using a similar approach to that discussed here, it would be possible to write explicit forms for the  $Q$  and  $U$  scattering shapes generated by anisotropies in the incoming photons or electrons.

An understanding of the shapes of the distortions caused by anisotropic photons and electrons can be garnered from Figure 5.4. Here, the signals are generated for a fixed momentum electron distribution  $p_0 = 0.3$  (roughly comparable to a temperature of 14 keV) and the CMB blackbody to allow for an appreciation of the shapes they take. It should be noted that CMB anisotropies will generally correspond to derivatives of the blackbody, not the blackbody itself. However, this figure exists for illustrative purposes only, and a detailed examination of these anisotropies will follow in future work. Nonetheless, the anisotropic photon distributions give rise to SZ-like distortions – that is, they have peaks, troughs, and nulls at a similar position to the isotropic signal. While there are differences between the shapes of these signals (alongside the amplitudes) these are comparable

variations to the shape changes induced by relativistic corrections, albeit sizeable relativistic corrections. Further work must be done analysing the scale of these variations. The anisotropic electron distributions however cause extremely distinct signals. It is also worth emphasising, that the electron dipole displayed in Figure 5.4 has been suppressed with a factor of 0.2.

It is important to understand what it means to select a photon or electron distribution for the anisotropic component. That is, the simplest anisotropy, for our purposes, would be an anisotropic amplitude variation within the photon or electron population, then the only differences between each  $n_\ell$  or  $f_{\ell'}$  would be a single factor. However, anisotropies could also arise in temperature, or even with an entirely different distribution for the anisotropic populations to the isotropic monopole.

For the kinematic effects, the multipoles reflect a directional boost of the thermal electrons to higher momenta. That is, as discussed in, e.g., [Nozawa et al. \(1998\)](#),  $\gamma_0^c = \gamma_c(\gamma_0 - \beta_c \mu_\gamma)$  with  $\beta_c$  the bulk motion velocity as in previous chapters, and here  $\mu_\gamma$  is the cosine of the angle between the axis of bulk motion and the incoming electron.  $\gamma_0^c$  then represents the electron energy in the cluster frame, while  $\gamma_0$  is in the CMB frame. Then, the boosted distribution function can be expressed as  $f_{\text{boost}} = f_{\text{th}}(\gamma_c \gamma_0) \times e^{-\mu_\gamma \gamma_c \beta_c / \theta}$ . The exponential can then be expanded in Legendre polynomials as

$$e^{-A\mu_c} = \sqrt{\frac{\pi}{2A}} \sum_{\ell=0}^{\infty} (-1)^\ell (2\ell+1) I_{\ell+\frac{1}{2}}(A) P_\ell(\mu_\gamma), \quad (5.17)$$

with  $I_\ell(x)$  the modified Bessel function of the first kind – which is a modification of the expression found in [Hu & White \(1997\)](#). This spherical harmonic expansion would then have to be projected into the frame, which (by reference to Wigner-D matrices) we can find that  $P_\ell(\mu_\gamma) \rightarrow P_\ell(\mu_{\text{sc}})P_\ell(\mu_c)$ , with  $\mu_c$  the cosine of the angle between the bulk cluster motion and the  $z$ -axis.

In general, each source of anisotropy in the electron or photon background will have a different angular dependence, as they will have a different angular distribution (i.e., different components under the spherical harmonic decomposition). However, the expressions derived here allow for the rapid computation of these anisotropic components. Electron anisotropies (beyond the kinematic bulk motion corrections) remain largely unstudied and should be the focus of further study which might indicate improved estimates of the scale of their contribution. These will rely on continued modelling of the magnetic effects in clusters and determining their influence on the anisotropy of the electrons in the ICM. Furthermore, high-resolution studies may increase the detectability of these effects allowing for closer study of the regions of strong anisotropy, and contribute to our understanding of the behaviour of magnetic fields in clusters.

While the higher multipole behaviour (that is  $\ell > 2$ ) may not have as large an impact on observations, these equations nonetheless allow for the size of

these effects to be fully computed and analysed. They furthermore allow for the combination of all these anisotropic effects with rSZ and kSZ corrections, to determine how each compare and/or combine. A full and closer analysis of these anisotropic (and pSZ) effects is the subject of future work.

### 5.3 Thermal and Non-thermal models of electron distributions

As has already been discussed, when talking about non-thermal electron distributions it is important to understand the source of the non-thermality. In particular, whether the deviation from a thermal distribution is an *averaging* phenomena, due to the superposition of thermal distributions within clusters, or if it is an *intrinsic* particle level contribution. While, to first order, both of these can be calculated using the same formula, there are distinct astrophysical interpretations. In the case of a non-thermal population arising from some averaging procedure – that is, for example, modelling the electron momenta over a whole cluster with the same distribution – any derived SZ signal will have some higher-order moment corrections (similar to that discussed in Chapter 2, where a single temperature was used over the entire cluster). While it may be numerically favourable to treat a cluster as a uniform distribution of electrons, an accurate model could be obtained in such circumstances by superposing the SZ signals caused by each individual thermal component, with further corrections coming from considerations of the multiple scattering effects. Any approach that attempts to measure a halo with an averaged distribution should also, for a full understanding of the problem, also consider to what extent the averaging procedure reproduces the signal that would be obtained from the full superposition consideration.

On the other hand, intrinsic, local sources of non-thermal electrons will *always* lead to an SZ-like distortion with a different shape to that generated by a thermal distribution. These non-thermal populations are assumed to arise from shocks, e.g., from mergers; AGN jets and gas accretion. These inject significant quantities of high-energy electrons, which will lead to distortions and are, generally speaking, what is intended in discussions of the non-thermal SZ effect.

Work has already been done to determine the extent of these non-thermal components, e.g., in Enßlin & Kaiser (2000) and Colafrancesco et al. (2003), where they considered the effects of simple power-law distributions for electron momenta or modified power law tails to thermal distributions, which have the advantage of being simple models which are easily constrained. Further work has been done recently trying to determine more precise models for the non-thermalities in the ICM. Some of these also are determined through an analytic approach (e.g., Petrosian et al., 2008; Kaastra et al., 2009; Shi & Komatsu, 2014),

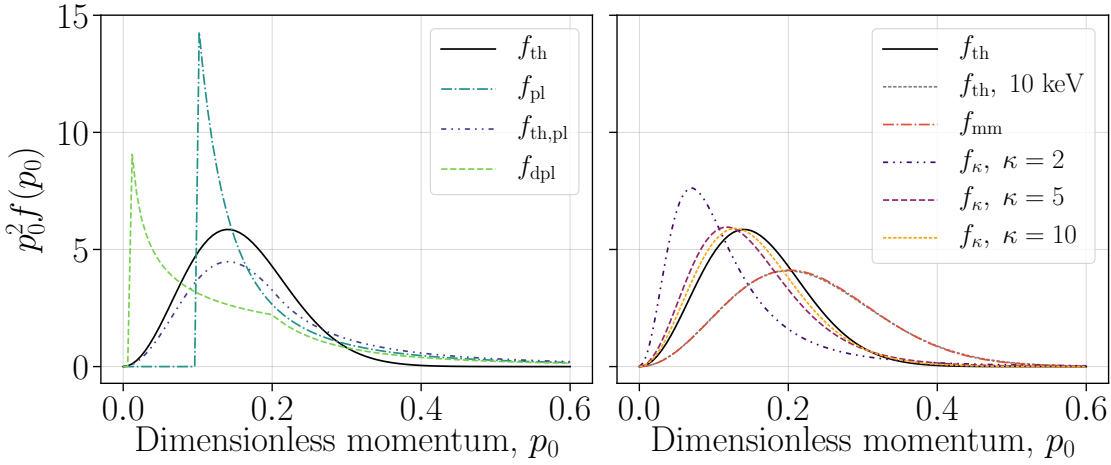


**FIGURE 5.5:** A selection of toy models for the high-energy electron momentum distributions found in clusters. In black, in both figures is the thermal, relativistic Maxwell Boltzmann distribution at 5 keV. This temperature is used for all the other temperature-dependent models (except where marked). *Left:* The power law distributions, here in particular,  $f_{\text{pl}}(p_0; 2.5, 0.1, 10)$  (Eq. 5.18),  $f_{\text{th,pl}}(p_0; 5, 2.5, 0.2, 10)$  (Eq. 5.19) and  $f_{\text{dpl}}(p_0; 0.5, 2.5, 0.01, 0.2, 10)$  (Eq. 5.20). *Right:* The Maxwellian-like distributions;  $f_{\text{mm}}$  (Eq. 5.22) using the values found in [Kaastra et al. \(2009\)](#);  $f_{\text{th}}(p_0; 10)$  (Eq. 4.2), to show the similarity between these two distributions;  $f_{\kappa}(p_0; 5, 2)$ ,  $f_{\kappa}(p_0; 5, 5)$  and finally  $f_{\kappa}(p_0; 5, 10)$  (Eq. 5.21).

which variously try to model the effects of bulk motions, cosmic rays, shocks and more. These kind of studies are generally conducted to determine the effects on either the observed X-ray emission, or to determine how neglecting non-thermal emission may cause a hydrostatic mass bias when trying to determine the meta properties of clusters. These methods lead to variously complicated models for the electron distributions which, although not designed for these purposes, we use here to consider the non-thermal SZ effect.

### 5.3.1 Toy models

In particular, in this chapter we look at five non-thermal models for the electrons in clusters. This is alongside the standard relativistic Maxwell-Jüttner distribution,  $f_{\text{th}}(p, \theta)$  defined in, e.g., Eq. (4.2). The first and simplest is a power law, as used in [Enßlin & Kaiser \(2000\)](#),

$$p^2 f_{\text{pl}}(p; \alpha, p_1, p_2) = \frac{(\alpha - 1)p^{-\alpha}}{p_1^{1-\alpha} - p_2^{1-\alpha}} \quad \text{for } p_1 < p < p_2. \quad (5.18)$$

In this work they also introduced a hybrid distribution that uses the thermal distribution at low frequencies and a power law at higher frequencies,

$$p^2 f_{\text{th,pl}}(p; \theta, \alpha, p_1, p_2) = C(\theta, \alpha, p_1, p_2) \times \begin{cases} f_{\text{th}}(p, \theta), & \text{if } p \leq p_1 \\ f_{\text{th}}(p_1, \theta) (p/p_1)^{-\alpha} & \text{if } p_1 < p < p_2, \end{cases} \quad (5.19)$$



where  $C(\theta, \alpha, p_1, p_2)$  is defined to normalise  $f_{\text{th,pl}}$  to 1 when integrated over  $p$ .

In [Colafrancesco et al. \(2003\)](#), this power law consideration was extended to a double-power-law model, to reduce the contribution at the lower energies, where a single power law became distinctly unphysical. That is,

$$p^2 f_{\text{dpl}}(p; \alpha_1, \alpha_2, p_1, p_2, p_{\text{cr}}) = K(\alpha_1, \alpha_2, p_1, p_2, p_{\text{cr}}) \times \begin{cases} p^{-\alpha_1}, & \text{if } p_1 < p \leq p_{\text{cr}} \\ p_{\text{cr}}^{-\alpha_1+\alpha_2} p^{-\alpha_2} & \text{if } p_{\text{cr}} < p < p_2, \end{cases} \quad (5.20)$$

where again  $K(\alpha_1, \alpha_2, p_1, p_2, p_{\text{cr}})$  is defined to normalise the distribution.

Moving away from power laws, [Kaastra et al. \(2009\)](#) uses two generalisations of the Maxwellian model. The first is the  $\kappa$ -distribution, which tends to a Maxwellian as  $\kappa \rightarrow \infty$ ,

$$p^2 f_{\kappa}(p; \theta, \kappa) = \frac{\frac{\sqrt{2} p^2}{\sqrt{\pi} \theta^{3/2}} \frac{\Gamma(\kappa+1)}{(\kappa-1.5)^{3/2} \Gamma(\kappa-0.5)}}{\left(1 + \frac{p^2}{2\theta(\kappa-1.5)}\right)^{\kappa+1}}, \quad (5.21)$$

with  $\kappa$  an integer and  $\Gamma$  the gamma function. Finally, they define the multi-Maxwellian distribution as an approximation to the cluster electron distribution

$$p^2 f_{\text{mm}}(p; \theta, c_i, a_i) = \frac{p^2}{(2\theta)^{3/2}} \left( c_0 e^{-a_0 z^2} + \sum_{k=1}^4 \frac{c_k}{(a_k + z^2)^{2+k/2}} \right), \quad (5.22)$$

where  $z = p/\sqrt{2\theta}$ . In [Kaastra et al. \(2009\)](#), they determine a good fit for an electron population following an MHD shock to be, for instance,  $c_i = \{0.755, 0.0609, 2.54, 13.3, 17.58\}$  and  $a_i = \{0.483, 152, 6843, 57.4, 12.4\}$ .

These models can all be seen graphically in Figure 5.5. Here, we use the suggested values for the multi-Maxwellian, and a variety of small values of  $\kappa$  for the  $\kappa$ -distribution. We have only plotted illustrative values of the power-law-related distributions.

### 5.3.2 Illustrations

To understand the effects of high-energy contributions to the SZ effect, it is first instructive to consider the effects of fixed momenta regions. This is generally unphysical, but allows for insights into the effects of non-thermal components. In particular, in Figure 5.6, we have plotted the distortion effect of a variety of electron momenta. At the lowest momenta, the effect of a single fixed momentum, is akin to that of a thermal distribution with the effective temperature of  $\theta_e = \beta_0^2/3$ . However, at higher momenta the distributions become distinctly non-thermal, with extended and increased tails to higher frequencies. These momenta correspond to relativistic speeds that boosted electrons may reach in clusters, with  $p_0 = 1$  equating to electrons travelling at  $1/\sqrt{2}$  the speed of light.

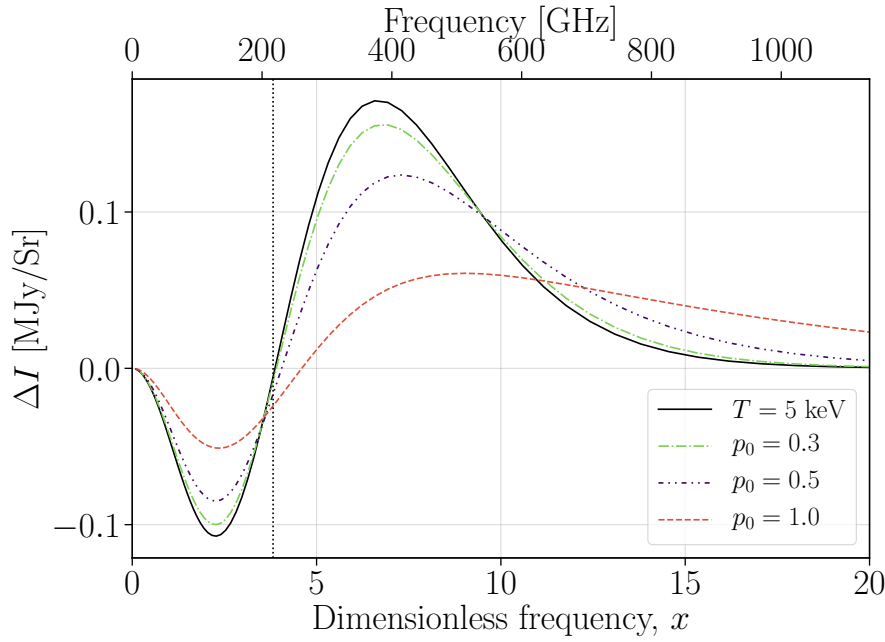


**FIGURE 5.6:** The distortion shapes for a selection of fixed momentum values. Here  $y = 10^{-4}$ , the thermal distribution in black is at 5 keV, and for the fixed momenta, the optical depth is calculated as  $\tau = y/(\beta_0^2/3)$ .

Now, we can consider how the toy-model distributions lead to variations in the observed signal. These are all displayed in Figure 5.7. It is first worth noticing that the effects of the [Kaastra et al. \(2009\)](#) models, i.e., those in the lower panel, largely have the effect of modelling the relativistic corrections to the SZ effect – that is, since these models start from the non-relativistic Maxwell-Boltzmann distributions, the effects of these toy-models are broadly comparable to those derived from the relativistic Maxwell-Jüttner distribution. This can especially be seen in the fitted multi-Maxwellian distribution, where the distortion is almost identical to that derived from a relativistic thermal distribution at 10 keV (as could be predicted from observing the initial distribution).

The power-law models, however, result in far more distinct signals. In particular, these again give rise to substantially increased tails to the ntSZ distortion. It should be noted that at the lower frequencies, these very small effects, keeping the negative parts (i.e.,  $< 217$  GHz) almost unchanged. They result in a shift to the null, comparable to high rSZ corrections, and then large changes in the tail, where the amplitude has been greatly increased.

### 5.3.3 Discussions

While these effects are all only modelled through toy-model predictions for non-thermal behaviour in clusters, some conclusions can still be drawn. Firstly, when calculating these non-thermal effects, higher resolution and precision in measurement of clusters must be obtained than is typically available. However,

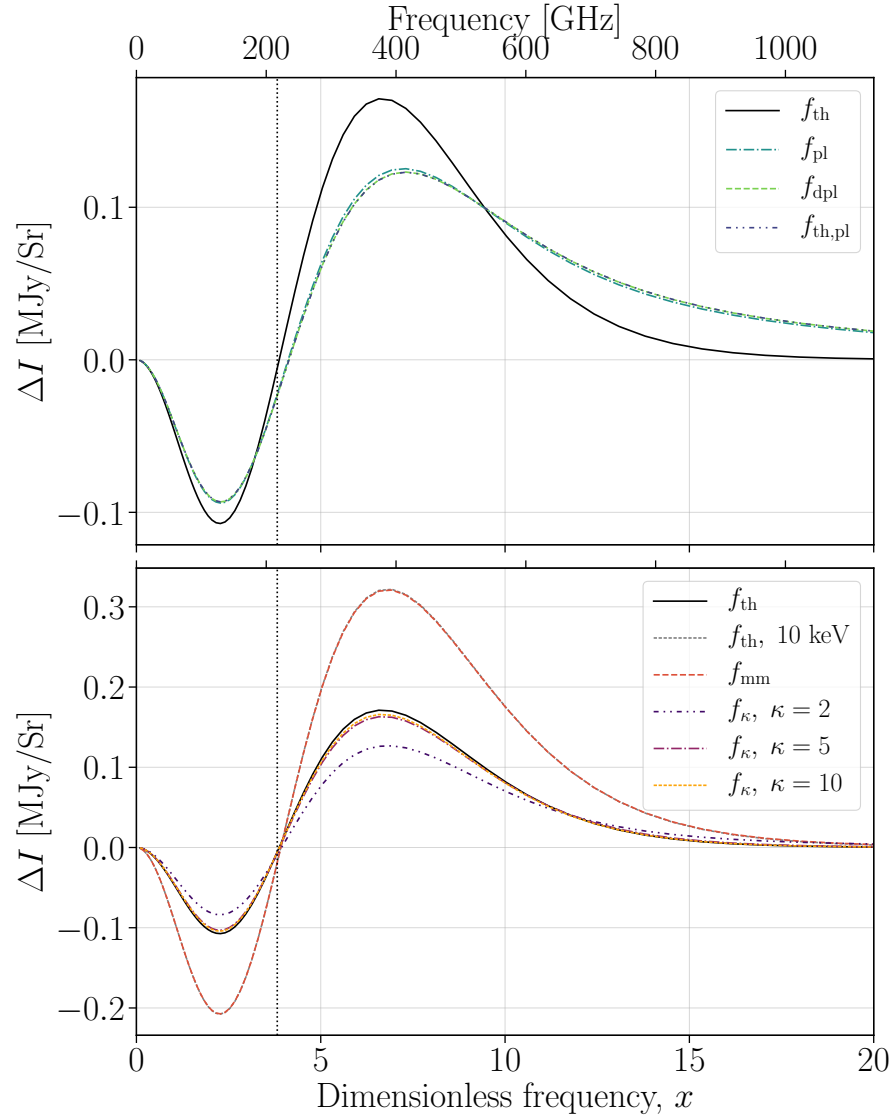


**FIGURE 5.7:** The distortion shapes for the distributions displayed in Figure 5.5. Everywhere, where a temperature is required in the distribution, 5 keV is used and a  $y = 10^{-4}$  is also assumed (with the exception of  $f_{th}(10 \text{ keV})$  where the temperature and  $y$  are both doubled). The functions including power laws (in the upper panel) all have  $\tau = y/(\overline{\beta^2}/3)$ , where  $\overline{\beta^2}$  is the averaged dimensionless velocity squared within the distribution.

these distortions are generally comparable to the rSZ corrections, either in significance of the effect, or in that they are dominant at the higher frequencies that are difficult to probe, likely requiring space-based observation.

That said, more study must be done into the proportion of electrons residing at these high energies, and the electron distributions they are residing in. For instance, if the high-energy non-thermal electrons account for 1% of the ICM, these signals would result in distortions around 1% of the scale of the rSZ corrections. However if these electrons contribute significantly more, or have extremely relativistic distributions, this may result in a larger distortion which may be sufficient to be observed.

Furthermore, for higher-resolution studies, where regions of high-energy electrons can be distinguished more clearly (i.e., jets, shocks, etc.) then the ICM in these regions will likely have a larger non-thermal component, and thus an increased distortion impact.

## 5.4 Conclusions

While the observational outlook for both sets of distortions, anisotropic and high-energy non-thermal contributions, rely on futuristic missions (i.e, CMB-S4, Voyage 2050, etc. [Chluba et al., 2021](#)), they remain an interesting avenue for further study. Determining the precise details of electrons in the ICM and their impact on observed SZ signals is a critical step in particular for calculating the precise importance of anisotropic electrons to the pSZ effect, and high-energy non-thermal electron populations to the high-frequency SZ signal.

Anisotropic photon and electron distributions have, heretofore, largely been considered using simplistic arguments, and here I have presented equations to allow for the rapid and precise computation of these anisotropic effects.<sup>5</sup> Furthermore, these equations can provide the basis for a deeper more analytic consideration of the pSZ effects, as well as the calculation of these effects under variations to the electron distribution or CMB distortions. The work presented in this chapter is only the basis for future, more-detailed study of these effects.

In much the same way, non-thermal high-energy electron distributions have been generally neglected when considering SZ effects. While they likely result in a small distortion it may well be of comparable scale to the pSZ signals, albeit largely located at higher frequencies, which can be probed with space-based observations. Further work must be carried out to determine the likely distributions caused by the non-thermal mechanisms in clusters – i.e., jets and shocks – and to calculate the prevalence of these non-thermal components in clusters. This will allow for a more detailed understanding of these non-thermal effects in the future.

---

<sup>5</sup>These have been added as a module to SZpack, which will be released shortly.

## Chapter 6

# Dissecting the Compton scattering kernel

The first half of this chapter is based on the published work, [Sarkar et al. \(2019\)](#). EL was third author on this paper, and mainly aided in the later stages with interpretation and additional analytics. The second half of this chapter – where anisotropy is discussed – is novel unpublished work, which has been predominantly carried out by EL, with some assistance in figures and code development from Abir Sarkar. All the figures in this chapter are either new, or have been remade for this thesis.

### 6.1 Introduction

In a similar way to using the SZ kernel, the general Compton-scattering kernel can be explored to understand the Compton scattering process more thoroughly. Astrophysical applications of Compton scattering have been studied extensively historically (e.g., [Zeldovich & Sunyaev, 1969](#); [Sunyaev & Zeldovich, 1970](#); [Hu & Silk, 1993](#); [Chluba & Sunyaev, 2012](#); [Mroczkowski et al., 2019](#)) using a variety of levels of simplifications and assumptions. While works exist that consider general versions of the scattering kernel (e.g., [Jones, 1968](#); [Belmont, 2009](#)), they generally end up with expressions that are either cumbersome to implement or numerically unstable. [Sarkar et al. \(2019\)](#) hereafter referred to as SCL19, and the first half of this chapter, focuses on providing a compact and numerically stable form of this general Compton-scattering kernel.

All of these works, however, are focused on Compton scattering taking place in isotropic media. In real astrophysical situations, this is not always the case – as has been discussed in the previous chapter. For instance, when CMB photons interact with high-energy electron jets from AGN or the circumstellar disk of compact X-ray binaries. In such cases, computations of the energy redistribution functions and spectra have been performed in several works (e.g., [Aharonian & Atoyan, 1981](#); [Haardt, 1993](#); [Fargion et al., 1997](#); [Moskalenko & Strong, 2000](#);

Dubus et al., 2008; Khangulyan et al., 2014). Alternately, as has already been discussed, CMB anisotropies can be scattered by largely isotropic electrons. In general an understanding of the anisotropic behaviour in Compton scattering should be obtained for accurate calculations of any kind of spectral distortions in the CMB.

However, in all these cases where previous calculations have been carried out, the energy of the electron is much larger than the photon, and, as such, the results are not general. A previous calculation of a general anisotropic Compton scattering kernel has been performed in Poutanen & Vurm (2010). There, they considered an anisotropic incident electron distribution, up to second order. In the second half of this chapter we will focus instead on the general Compton scattering kernels for anisotropic photon distributions up to 3rd order – with some discussion of the anisotropic electron distributions, although compact forms are not provided in this chapter.

## 6.2 Isotropic Compton Scattering Kernel

SCL19 reformulated the expressions of Belmont (2009). In particular, by determining that there are in general three different zones to the full Compton-scattering kernel (instead of the implied 16 from the formulation of Belmont, 2009), a more intuitive understanding of the kernel can be found.

In particular, the kernel is defined as follows, in a similar fashion to Eq. (5.1), the kinetic equation can be written as,

$$\begin{aligned} \frac{dn(\omega')}{d\tau} &= \int d\omega_0 \left[ P(\omega' \rightarrow \omega_0) n' (1 + n_0) - \frac{\omega_0^2}{\omega'^2} P(\omega_0 \rightarrow \omega') n_0 (1 + n') \right], \\ P(\omega_0 \rightarrow \omega') &= \int_{p_{0,\min}}^{\infty} dp_0 p_0^2 f(p_0) P(\omega_0 \rightarrow \omega', p_0), \\ P(\omega' \rightarrow \omega_0) &= \int_{p'_{\min}}^{\infty} dp' p'^2 f(p') P(\omega' \rightarrow \omega_0, p') \\ &= \frac{\omega_0^2}{\omega'^2} \int_{p_{0,\min}}^{\infty} dp_0 p_0^2 f(p') P(\omega_0 \rightarrow \omega', p_0). \end{aligned} \tag{6.1}$$

Now,  $P(\omega_0 \rightarrow \omega', p_0)$  is the scattering kernel and the factors of  $(\omega_0/\omega')^2$  arise from considerations of conservation of photon number count.

It should be noted then that, much as for the SZ kernel, when the electron background is a thermal (relativistic) Maxwell-Jüttner distribution, then the averaged scattering kernels, obey the detailed balance relation:

$$P^{\text{th}}(\omega' \rightarrow \omega_0) = \frac{\omega_0^2}{\omega'^2} e^{\frac{\omega' - \omega_0}{\theta_e}} P^{\text{th}}(\omega_0 \rightarrow \omega'). \tag{6.2}$$

It should be noticed that this is not in general true for an arbitrary electron background. In SCL19, the higher frequency moments of the scattering kernel are discussed in detail, but that will largely be omitted here.

### 6.2.1 Anatomy of the Compton Kernel

First, it is important to recall that there are differences between the Compton-scattering kernel and the SZ kernel, and the Compton Scattering problem is defined fully in Section 1.2. In particular, we can recall the frequency ratio is written as (e.g., Eq. 1.7)

$$\frac{\omega'}{\omega_0} = \frac{1 - \beta_0 \mu_0}{1 - \beta_0 \mu' + \frac{\omega_0}{\gamma_0} (1 - \mu_{sc})}. \quad (6.3)$$

Now, it is instructive to consider what limits are imposed upon  $\omega'$ . In particular, it is minimized when  $\mu_0 = 1$  and  $\mu' = \mu_{sc} = -1$ , i.e., an incoming photon and electron heading in the same direction with a back scattered outgoing photon, so that,

$$\omega'_{\min} = \frac{(\gamma_0 - p_0)\omega_0}{\gamma_0 + p_0 + 2\omega_0}. \quad (6.4)$$

As such, it is impossible for an incoming photon to transfer all its energy into the outgoing electron. It is more complex to find the upper limit. The maximal theoretical limit comes from conservation of energy where  $\omega' \leq \gamma_0 + \omega_0 - 1$ . However, angular dependences mean this is not always possible to obtain, and as such

$$\omega'_{\max} = \begin{cases} \omega_0 + \gamma_0 - 1 & \text{for } \omega_0 > \frac{1}{2}(1 + p_0 - \gamma_0) \\ \omega_c & \text{for } \omega_0 \leq \frac{1}{2}(1 + p_0 - \gamma_0) \end{cases} \quad (6.5)$$

$$\omega_c = \frac{(\gamma_0 + p_0)\omega_0}{\gamma_0 - p_0 + 2\omega_0}.$$

Here, the critical frequency,  $\omega_c$ , is introduced, which occurs when the incoming photon and electron have a head-on collision with full back scattering (i.e.,  $\mu_0 = \mu_{sc} = -1$  and  $\mu' = 1$ ).

This allows us to describe the scattering kernel in terms of four frequencies,  $\omega'_{\min}$ ,  $\omega_0$ ,  $\omega_c$  and  $\omega'_{\max}$ . It should be noted that for  $\omega_0 < \frac{1}{2}(1 + p_0 - \gamma_0)$ ,  $\omega_c = \omega'_{\max}$  which can only occur for  $\omega_0 < 0.5$ . Furthermore, if  $p_0 = \omega_0$ ,  $\omega_c = \omega_0$ . In general however this generates three zones in the scattering kernel,

$$\begin{aligned} \text{Zone I :} & \quad \omega'_{\min} \leq \omega' < \omega'_I \\ \text{Zone II :} & \quad \omega'_I \leq \omega' < \omega'_{II} \\ \text{Zone III :} & \quad \omega'_{II} \leq \omega' \leq \omega_{\max}. \end{aligned}$$

Here,  $\omega'_I$  and  $\omega'_{II}$  are  $\omega_0$  and  $\omega_c$ , but will switch depending on which is larger. In the special case where two of these frequencies are equal, the kernel instead

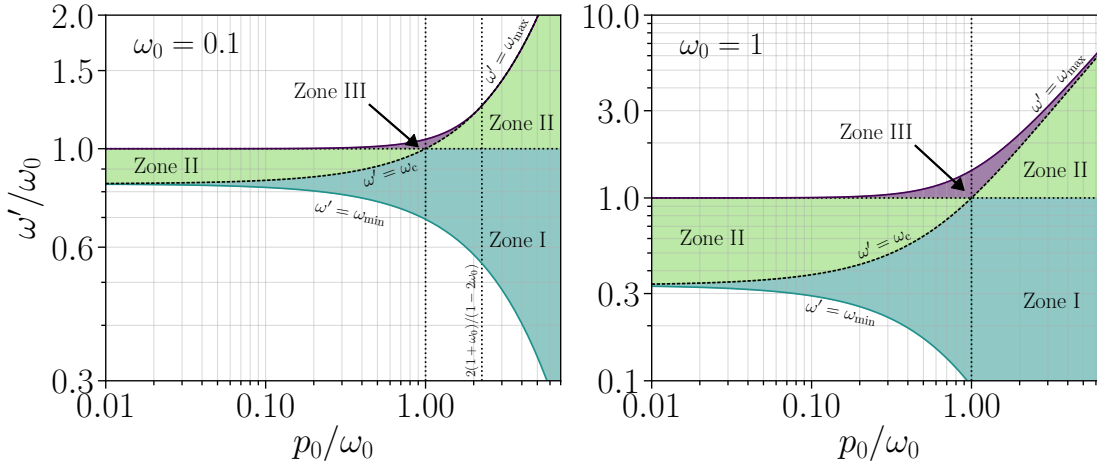


**FIGURE 6.1:** Zones of the Compton-scattering kernel for  $\omega_0 = 0.1$  and 1 over varying  $p_0$ . At  $p_0 = \omega_0$  it is clear that Zone II disappears. For  $\omega_0 < 0.5$ , above a certain momentum,  $\omega'_{\max} = \omega_c$  and Zone III disappears.

has two zones. Figure 6.1 displays these zones at  $\omega_0 = 0.1$  and 1.

### 6.2.2 Simplified exact Kernel

The kernel itself (following simplifications from Belmont, 2009) can be written in terms of an auxiliary function,

$$\mathcal{G}(\omega_0^*, \omega^*, \kappa) = \kappa \left\{ 2 + (\omega^* - \omega_0^*)^2 \frac{(1 + \omega' \omega_0)}{\omega'^2 \omega_0^2} + 2 \left[ \frac{1}{\omega^*} \mathcal{S} \left( \frac{\kappa^2 \lambda_+}{\omega^{*2}} \right) - \frac{1}{\omega_0^*} \mathcal{S} \left( \frac{\kappa^2 \lambda_-}{\omega_0^{*2}} \right) \right] \right. \\ \left. + (1 + \omega' \omega_0) \left[ \frac{1}{\omega^* \lambda_+} \mathcal{F} \left( \frac{\kappa^2 \lambda_+}{\omega^{*2}} \right) - \frac{1}{\omega_0^* \lambda_-} \mathcal{F} \left( \frac{\kappa^2 \lambda_-}{\omega_0^{*2}} \right) \right] \right\}. \quad (6.6)$$

This itself relies on the simple definitions

$$\lambda_+ = p_0^2 + 2\gamma_0 \omega_0 + \omega_0^2; \quad \lambda_- = p_0^2 - 2\gamma_0 \omega' + \omega'^2; \\ \mathcal{S}(x) = \frac{\sinh^{-1}(\sqrt{x})}{\sqrt{x}} \equiv \frac{\sin^{-1}(\sqrt{-x})}{\sqrt{-x}}; \quad \mathcal{F}(x) = \mathcal{S}(x) - \sqrt{1+x}; \quad (6.7) \\ p = \sqrt{p_0^2 + 2\gamma_0(\omega_0 - \omega') + (\omega_0 - \omega')^2}$$

with  $p$  the scattered electron momentum, in a form to minimise cancellations. For small  $x$ , it makes numerical improvements to use a Taylor expansion for  $\mathcal{S}(x)$  and  $\mathcal{F}(x)$  which, in SCL19 is taken to third order in  $x$  about  $x = 0$ . It should also be noted that  $\lambda_+ > 0$  at all energies, while  $\lambda_- = 0$  when  $\omega' = \gamma_0 \pm 1$  – however this causes no pole (Belmont, 2009). It is finally important to define the function,  $\Lambda$ ,



and the 'mean' photon energies

$$\begin{aligned}\Lambda(\omega_0, \omega', p_0, p') &= \frac{p_0 - p' + \omega_0 + \omega'}{2}; \\ \overline{\omega'} &= \sqrt{\frac{\omega_0 \omega' (\gamma' + p')}{\gamma_0 + p_0}}; \quad \overline{\omega_0} = \sqrt{\frac{\omega_0 \omega' (\gamma_0 + p_0)}{\gamma' + p'}},\end{aligned}\tag{6.8}$$

which satisfies that  $\overline{\omega_0} \overline{\omega'} = \omega_0 \omega'$ .

Now the kernel can be understood in two general cases. When  $\omega_c \leq \omega_0$  (or  $p_0 \leq \omega_0$ ), in each zone the kernel becomes

$$\begin{aligned}P_I(\omega_0 \rightarrow \omega', p_0) &= \frac{3}{8\gamma_0 p_0 \omega_0^2} \mathcal{G}(\overline{\omega_0}, \overline{\omega'}, \kappa_1) \\ P_{II}(\omega_0 \rightarrow \omega', p_0) &= \frac{3}{8\gamma_0 p_0 \omega_0^2} \mathcal{G}(\omega', \omega_0, p_0) \\ P_{III}(\omega_0 \rightarrow \omega', p_0) &= \frac{3}{8\gamma_0 p_0 \omega_0^2} \mathcal{G}(\omega_0, \omega', p'),\end{aligned}\tag{6.9}$$

with  $\kappa_1 = \Lambda(\omega_0, \omega', p_0, p')$ . On the other hand, when  $\omega_c \geq \omega_0$  (or  $p_0 \geq \omega_0$ ), the kernel is instead expressed as

$$\begin{aligned}P_I(\omega_0 \rightarrow \omega', p_0) &= \frac{3}{8\gamma_0 p_0 \omega_0^2} \mathcal{G}(\overline{\omega_0}, \overline{\omega'}, \kappa_1) \\ P_{II}(\omega_0 \rightarrow \omega', p_0) &= \frac{3}{8\gamma_0 p_0 \omega_0^2} \mathcal{G}(\overline{\omega'}, \overline{\omega_0}, \kappa_2) \\ P_{III}(\omega_0 \rightarrow \omega', p_0) &= \frac{3}{8\gamma_0 p_0 \omega_0^2} \mathcal{G}(\omega_0, \omega', p').\end{aligned}\tag{6.10}$$

Now,  $\kappa_2 = \Lambda(\omega', \omega_0, p', p_0)$  – or  $\kappa_1$  and  $\kappa_2$  can be both expressed as  $\tilde{\Lambda} = \frac{1}{2}(\omega_0 + \omega' - |p_0 - p'|)$ . It is also worth noting that only Zone II changes between the two cases.

### 6.2.3 A brief exploration of the isotropic kernel

In non-extreme cases, the kernel can be understood as displayed in Figure 6.2. First, we can identify some shared key characteristics. In particular, the predicted zones identified in, e.g., Figure 6.1, occur as expected in the kernels, with cusps on the boundaries between each zone. Accordingly, there is a universal cusp at  $\omega_0$ , and a second cusp in the down-scattering region when  $\omega_0 > p_0$  (i.e.,  $\omega_c < \omega_0$ ) and into the up-scattering region when  $\omega_0 < p_0$ . When  $\omega_0 = \omega_c$  these two cusps are co-located and only two zones arise. When  $\omega_c$  is in the upscattering region, this cusp is often referred to as the Doppler peak.

Furthermore, as either particle energy increases the kernel broadens as the photon can be scattered to a larger range of energies. Increasing the incoming photon energy (i.e.,  $\omega_0$ ) results in stronger downscattering – that is, more energy being transferred from the photon to the electron – while increasing  $p_0$

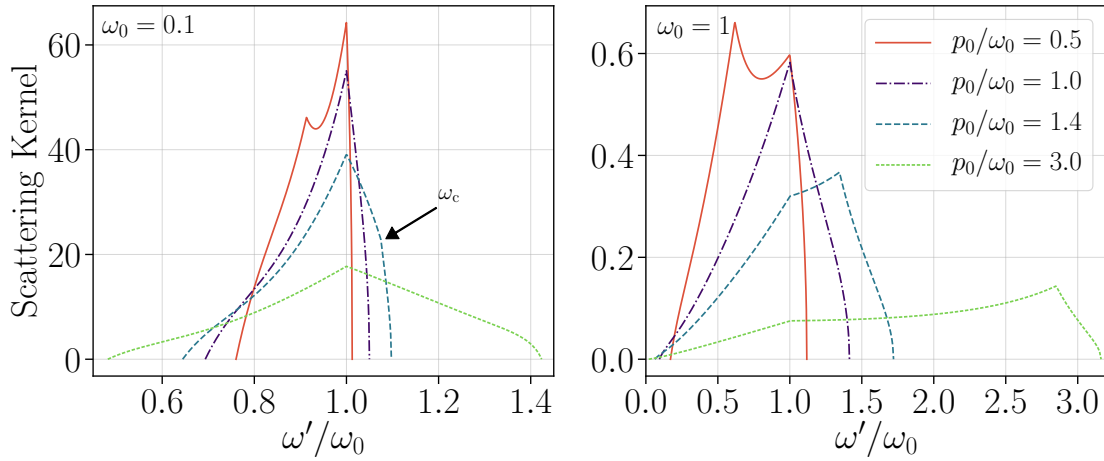


**FIGURE 6.2:** The Compton-scattering kernel,  $P(\omega_0 \rightarrow \omega', p_0)$ , for some illustrative non-extreme values of  $\omega_0$  and  $p_0$ . Note that the cusp at  $\omega_c$  moves to higher  $\omega'$  with increasing  $p_0$ , coinciding with  $\omega_0$  when  $p_0 = \omega_0$ . Furthermore, when  $\omega_0 = 0.1$  the cusp disappears for the  $p_0/\omega_0 = 3$  case, as  $\omega'_{\max} = \omega_c$  (the cusp for  $p_0/\omega_0 = 1.4$  is indicated with an arrow).

(i.e., electron momentum) leads to more upscattering. This is a natural consequence of Compton scattering (e.g., [Blumenthal & Gould, 1970](#); [Pomraning, 1972](#); [Nagirner & Poutanen, 1994](#); [Sazonov & Sunyaev, 2000](#)).

In more detail, when  $p_0/\omega_0 = 0.5$ , there is very little upscattering (Zone III) in either case, but a higher  $\omega_0$  leads to greatly broader downscattering. However, when  $p_0 \gg \omega_0$  – that is there are very energetic electrons – there is strong upscattering, and the tail is broadened beyond the doppler peak especially when  $\omega_0 = 1$ . However, for  $\omega_0 < 0.5$ , by  $p_0/\omega_0 = 3$ ,  $\omega_c = \omega'_{\max}$  and Zone III has vanished. For  $\omega_0 > 0.5$  this is impossible, and instead the Doppler peak becomes increasingly distinct for higher  $p_0$ , as Zone III may become increasingly slim.

### Extreme cases

It is worth briefly exploring extreme cases in Compton scattering which are often taken as approximations for calculating the kernel behaviour. In particular, *recoil-dominated* scattering, *Doppler-dominated* scattering and scattering from *ultra-relativistic electrons*.

Recoil-dominated scattering arises when both  $p_0 \ll \omega_0$  and  $p_0 \ll 1$ . In this scenario the kernel is predominately Zone II. That is,  $\omega_c$  asymptotically tends to  $\omega'_{\min}$  while  $\omega'_{\max}$  approaches  $\omega_0$ . As such, almost all of the photons are downscattered as can be seen in the left panel of Figure 6.3. As  $\omega_0$  increases, the likelihood of a photon retaining its energy decreases – that is, as photons get more energetic they are increasingly likely to transfer energy to the incident electrons. This amplitude can be shown to in fact scale with  $1/\omega_0^2$ . As this scenario becomes increasingly extreme, the kernel is increasingly well approximated by the simple model described in [Sarkar et al. \(2019\)](#).

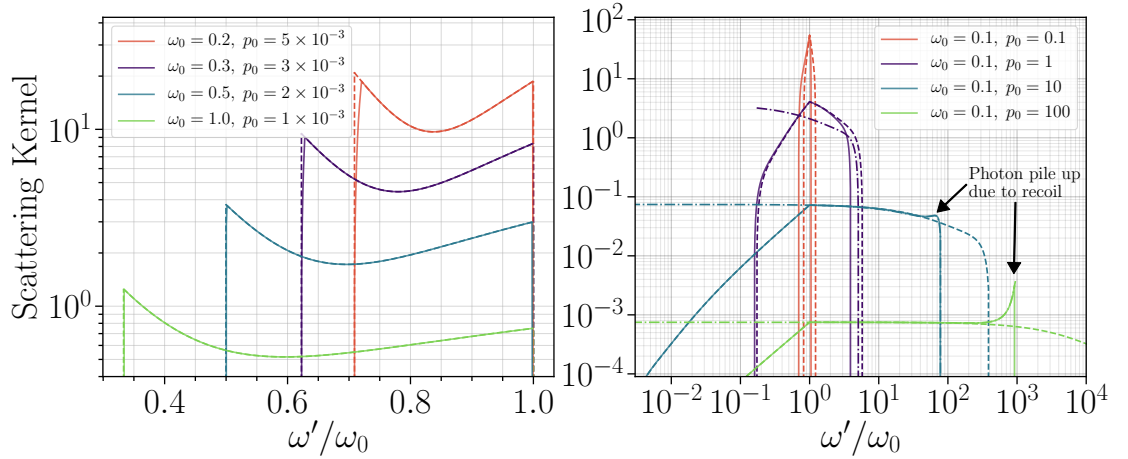


**FIGURE 6.3:** The Compton scattering kernel,  $P(\omega_0 \rightarrow \omega', p_0)$ , for some extreme values of  $\omega_0$  and  $p_0$ . *Left:* Recoil-dominated scattering, the dashed lines are the standard model summarised in [Sarkar et al. \(2019\)](#). *Right:* Doppler-dominated scattering, the dashed lines are the SZ kernel, while the dot dashed line shows the ultra-relativistic approximation (e.g., [Jones, 1968](#); [Blumenthal & Gould, 1970](#)).

Doppler-dominated scattering however occurs when  $\omega_0 \ll p_0$  and  $\omega_0 < 0.5$  and Zone III vanishes. In this case the scattering can be approximated by the SZ kernel, as described previously in this thesis. These are displayed in the right panel of Figure 6.3, here however, it should be noted that the value of  $\omega_0 = 0.1$  is not very extreme. Nonetheless, as  $p_0$  increases Doppler broadening increases, and photons are increasingly upscattered. In the downscattering region, here the SZ kernel converges to the exact shape of the Compton scattering kernel, while at high frequencies it diverges. This is due to the extreme cases of very high  $p_0$  where the electrons are becoming strongly relativistic. These lead to a pile up of photons caused by recoil (i.e., the ‘cusp’ at  $\omega_c$  reemerges) – however, it is smooth in behaviour, instead of causing a sharp cusp. This leads to the understanding that the SZ approximation relies not only on low photon energies, but also, broadly speaking, non-relativistic electrons.

When  $p_0 \gg 1/(4\omega_0)$ , it is in fact more accurate to use approximations for scatterings caused by ultra-relativistic electrons. This scattering kernel approximation was presented in [Jones \(1968\)](#); [Blumenthal & Gould \(1970\)](#) and summarised in [Sarkar et al. \(2019\)](#) and is only valid in the regime when  $\omega_0 < 0.5$ . It also is always incorrect for  $\omega' < \omega_0$  where this approximation tends to a constant. This is also displayed in the right panel of Figure 6.3. The ultra-relativistic approximation models the photon pile up well when  $\omega_0$  is low, but becomes increasingly inaccurate with increasing  $\omega_0$ .

This highlights an important difference between these regimes: in the recoil-dominated regime, for any  $p_0 \ll 1$ , it is always possible to find an  $\omega_0$  above which the approximation will hold to a certain degree of accuracy. However, for Doppler-dominated scattering this is no longer true, as increasing  $p_0$  will always cause recoil effects, regardless of the value for  $\omega_0$ . It should, however, be noted,

that the SZ approximation remains appropriate in most cases where it is used.

Sarkar et al. (2019) also contains a detailed discussion of the effects of thermal averaging in the general isotropic Compton scattering case which is not summarised here, alongside detailed discussion of the moments of the Compton scattering kernel and its approximations.

### 6.3 Anisotropic Compton Scattering Kernels

The anisotropic Compton scattering kernel can be defined in an analogous way to that described in Chapter 5, that is,  $n(\omega_0, \mu_{sc}) = \sum_{\ell} n_{\ell}(\omega_0) P_{\ell}(\mu_{sc})$  or  $f(p_0, \mu') = \sum_{\ell'} f_{\ell'}(p_0) P_{\ell'}(\mu')$ . As such the anisotropic photon kernel can be expressed as

$$P^{\ell}(\omega_0 \rightarrow \omega', p_0) = \frac{3}{8\gamma_0 p_0 \omega_0} \int d\mu_{sc} d\mu' \bar{X} P_{\ell}(\mu_{sc}) \frac{d\phi_0}{dt}. \quad (6.11)$$

This allows for the kinetic equation to be written (cf. Eq 6.1) as

$$\frac{dn(\omega')}{d\tau} = \int d\omega_0 \left[ \sum_{\ell=0}^{\infty} P^{\ell}(\omega' \rightarrow \omega_0) n' (1 + n_{\ell}) - \frac{\omega_0^2}{\omega'^2} P^{\ell}(\omega_0 \rightarrow \omega') n_{\ell} (1 + n') \right], \quad (6.12)$$

with  $P^{\ell}(\omega' \rightarrow \omega_0)$  defined analogously to  $P(\omega' \rightarrow \omega_0)$ . The anisotropic electron kernel can be defined in much the same way, with the appropriate switching of angles.

It should be reiterated that these two kernels – for both anisotropic electrons and photons – cannot easily be derived from one another through some simple transformation of variables. This is understandable in a few ways: analytically this is motivated by the distinct lack of symmetry between  $\mu_{sc}$  and  $\mu'$  within  $\bar{X}$  (i.e., Eq. 1.2). The complexity of behaviour between these two angles leads to vastly different behaviour between the kernels. This can also be understood from a physical perspective as expressing an anisotropy in the electron distribution as instead being a function of the photon distribution (or vice versa) requires finding a frame in which the electron distribution is isotropic and transforming the photon field into this frame, which is a non-trivial transformation. In this chapter, I only calculate an analytic form for the anisotropic photon Compton scattering kernels, although reference is made to the anisotropic electron scattering kernels in Section 6.3.2.

#### 6.3.1 Analytics

The anisotropic kernels follow the same zone configuration of the isotropic Compton scattering case – as they still rely on the same energetic and angular frequency restrictions. Alternatively, this can be identified as the Zone constraints have no direct angular dependence on  $\mu'$  or  $\mu_{sc}$ .

As such the anisotropic kernels can be expressed in much the same way, i.e., when  $\omega_c \leq \omega_0$ , (or  $p_0 \leq \omega_0$ ) the kernel becomes in each zone

$$\begin{aligned} P_I^\ell(\omega_0 \rightarrow \omega', p_0) &= \frac{3}{8\gamma_0 p_0 \omega_0^2} \mathcal{G}^\ell(\overline{\omega_0}, \overline{\omega'}, \kappa_1) \\ P_{II}^\ell(\omega_0 \rightarrow \omega', p_0) &= \frac{3}{8\gamma_0 p_0 \omega_0^2} \mathcal{G}^\ell(\omega', \omega_0, p_0) \\ P_{III}^\ell(\omega_0 \rightarrow \omega', p_0) &= \frac{3}{8\gamma_0 p_0 \omega_0^2} \mathcal{G}^\ell(\omega_0, \omega', p'), \end{aligned} \quad (6.13)$$

and when  $\omega_c \geq \omega_0$  (or  $p_0 \geq \omega_0$ ), the kernel is instead expressed as,

$$\begin{aligned} P_I^\ell(\omega_0 \rightarrow \omega', p_0) &= \frac{3}{8\gamma_0 p_0 \omega_0^2} \mathcal{G}^\ell(\overline{\omega_0}, \overline{\omega'}, \kappa_1) \\ P_{II}^\ell(\omega_0 \rightarrow \omega', p_0) &= \frac{3}{8\gamma_0 p_0 \omega_0^2} \mathcal{G}^\ell(\overline{\omega'}, \overline{\omega_0}, \kappa_2) \\ P_{III}^\ell(\omega_0 \rightarrow \omega', p_0) &= \frac{3}{8\gamma_0 p_0 \omega_0^2} \mathcal{G}^\ell(\omega_0, \omega', p'). \end{aligned} \quad (6.14)$$

Here  $\kappa_1, \kappa_2, \overline{\omega_0}$  and  $\overline{\omega'}$  are all defined as before.

A solution for these  $\mathcal{G}^\ell$  for a general  $\ell$  is complicated and far beyond the scope of this work. However, here I provide forms for  $\ell = [0, 1, 2, 3]$ , noting that  $\ell = 0$  is the form already provided earlier in this chapter. The function  $\mathcal{G}^\ell(\omega_0^*, \omega^*, \kappa)$  can be written as a summation of three functions as follows,

$$\mathcal{G}^\ell(\omega_0^*, \omega^*, \kappa) = \mathcal{I}_0^\ell(\omega_0^*, \omega^*, \kappa) + \mathcal{I}_{1+}^\ell(\omega_0^*, \omega^*, \kappa) + \mathcal{I}_{1-}^\ell(\omega_0^*, \omega^*, \kappa). \quad (6.15)$$

The  $\mathcal{I}$  functions are listed below for  $\ell = \{0, 1, 2, 3\}$  and it is easy to note that the  $\mathcal{G}^0$  does in fact reflect a regrouping of the same expression found in Eq. (6.6). Beyond this, these equations are somewhat complex to interact with directly, which is amplified by modifications to maintain numerical stability.

$\ell = 0$

$$\mathcal{I}_0^0(\omega_0^*, \omega^*, \kappa) = \kappa \frac{(\omega^* - \omega_0^*)^2}{\omega'^2 \omega_0^2} (1 + \omega' \omega_0) + 2\kappa \mathcal{H}_0, \quad (6.16a)$$

$$\mathcal{I}_{1\pm}^0(\omega_0^*, \omega^*, \kappa) = \bar{\kappa}_\pm \left[ \frac{1 + \omega' \omega_0}{\lambda_\pm} \mathcal{F}_1(\bar{\kappa}_\pm^2 \lambda_\pm) + 2\mathcal{S}(\bar{\kappa}_\pm^2 \lambda_\pm) \right]. \quad (6.16b)$$

$\ell = 1$ 

$$\mathcal{I}_0^1(\omega_0^*, \omega^*, \kappa) = \kappa \frac{(\omega^* - \omega_0^*)^2}{\omega'^2 \omega_0^2} + \frac{2}{3} \left[ \kappa \mathcal{H}_1 + (-2X_* \kappa + (\bar{X} - X_*) |p - p_0|) \right], \quad (6.17a)$$

$$\begin{aligned} \mathcal{I}_{1\pm}^1(\omega_0^*, \omega^*, \kappa) = & \bar{\kappa}_{\pm} \left[ \frac{3}{2\lambda_{\pm}^2} (2 + \omega' \omega_0) \mathcal{F}_2(\bar{\kappa}_{\pm}^2 \lambda_{\pm}) + \frac{g_{1\pm}}{\lambda_{\pm}} + \frac{5 + \omega' \omega_0}{\lambda_{\pm}} \mathcal{F}_1(\bar{\kappa}_{\pm}^2 \lambda_{\pm}) \right. \\ & \left. + 2 \frac{-1 + \omega' \omega_0}{\omega' \omega_0} \mathcal{S}(\bar{\kappa}_{\pm}^2 \lambda_{\pm}) + \delta_* \left( \omega' \omega_0 (\delta_* \mathcal{R}(\bar{\kappa}_{\pm}^2 \lambda_{\pm}) + 2\bar{\kappa}_{\pm}^2 - 1) - 2 \right) \right]. \end{aligned} \quad (6.17b)$$

 $\ell = 2$ 

$$\begin{aligned} \mathcal{I}_0^2(\omega_0^*, \omega^*, \kappa) = & \kappa \frac{(\omega^* - \omega_0^*)^2}{\omega'^2 \omega_0^2} + \frac{2}{5} \left[ \kappa \mathcal{H}_2 + (-2X_* \kappa + (\bar{X} - X_*) |p - p_0|) \mathcal{J}_2 \right. \\ & \left. + 3(-2X_*^2 \kappa + (\bar{X}^2 - X_*^2) |p - p_0|) \right], \end{aligned} \quad (6.18a)$$

$$\begin{aligned} \mathcal{I}_{1\pm}^2(\omega_0^*, \omega^*, \kappa) = & \bar{\kappa}_{\pm} \left[ \frac{15}{4\lambda_{\pm}^3} (3 + \omega' \omega_0) \mathcal{F}_3(\bar{\kappa}_{\pm}^2 \lambda_{\pm}) - \frac{3g_{2\pm}}{\lambda_{\pm}^2} + \frac{9}{2\lambda_{\pm}^2} (5 + \omega' \omega_0) \mathcal{F}_2(\bar{\kappa}_{\pm}^2 \lambda_{\pm}) \right. \\ & + \frac{3g_{1\pm}}{\lambda_{\pm}} + \frac{1}{\lambda_{\pm}} \frac{-3 + 13\omega' \omega_0 + \omega'^2 \omega_0^2}{\omega' \omega_0} \mathcal{F}_1(\bar{\kappa}_{\pm}^2 \lambda_{\pm}) + 2 \frac{-3 + \omega' \omega_0}{\omega' \omega_0} \mathcal{S}(\bar{\kappa}_{\pm}^2 \lambda_{\pm}) \\ & + \delta_* \left( 6(1 + \omega' \omega_0 \bar{\kappa}_{\pm}^2)(1 - \bar{\kappa}_{\pm}^2) - \frac{3}{\omega' \omega_0} + \omega' \omega_0 + \delta_*^2 \omega' \omega_0 \left( \frac{3}{2} + 2\bar{\kappa}_{\pm}^2 \lambda_{\pm} \right) \right) \\ & \left. + 3\delta_*^2 \mathcal{R}(\bar{\kappa}_{\pm}^2 \lambda_{\pm}) \left( (1 + \omega' \omega_0) - 2\omega' \omega_0 \bar{\kappa}_{\pm}^2 \right) \right]. \end{aligned} \quad (6.18b)$$

 $\ell = 3$ 

$$\begin{aligned} \mathcal{I}_0^3(\omega_0^*, \omega^*, \kappa) = & \kappa \frac{(\omega^* - \omega_0^*)^2}{\omega'^2 \omega_0^2} + \frac{2}{7} \left[ \kappa \mathcal{H}_3 + (-2X_* \kappa + (\bar{X} - X_*) |p - p_0|) \mathcal{J}_3 \right. \\ & \left. + 3(-2X_*^2 \kappa + (\bar{X}^2 - X_*^2) |p - p_0|) \mathcal{K}_3 + 10(-2X_*^3 \kappa + (\bar{X}^3 - X_*^3) |p - p_0|) \right], \end{aligned} \quad (6.19a)$$

$$\begin{aligned} \mathcal{I}_{1\pm}^3(\omega_0^*, \omega^*, \kappa) = & \bar{\kappa}_{\pm} \left[ \frac{175}{16\lambda_{\pm}^4} (4 + \omega' \omega_0) \mathcal{F}_4(\bar{\kappa}_{\pm}^2 \lambda_{\pm}) + \frac{10g_{3\pm}}{\lambda_{\pm}^3} + \frac{25}{4\lambda_{\pm}^3} (17 + 3\omega' \omega_0) \mathcal{F}_3(\bar{\kappa}_{\pm}^2 \lambda_{\pm}) \right. \\ & - \frac{15g_{2\pm}}{\lambda_{\pm}^2} + \frac{3}{2\lambda_{\pm}^2} \frac{-5 + 57\omega' \omega_0 + 6\omega'^2 \omega_0^2}{\omega' \omega_0} \mathcal{F}_2(\bar{\kappa}_{\pm}^2 \lambda_{\pm}) + \frac{6g_{1\pm}}{\lambda_{\pm}} \\ & + \frac{1}{\lambda_{\pm}} \frac{-15 + 25\omega' \omega_0 + \omega'^2 \omega_0^2}{\omega' \omega_0} \mathcal{F}_1(\bar{\kappa}_{\pm}^2 \lambda_{\pm}) + 2 \frac{-6 + \omega' \omega_0}{\omega' \omega_0} \mathcal{S}(\bar{\kappa}_{\pm}^2 \lambda_{\pm}) \\ & + \delta_* \left\{ 10\bar{\kappa}_{\pm}^4 \omega' \omega_0 \left( 2\bar{\kappa}_{\pm}^2 + 3\delta_* \mathcal{R}(\bar{\kappa}_{\pm}^2 \lambda_{\pm}) \right) - 10\bar{\kappa}_{\pm}^2 (2 + 3\omega' \omega_0) \left( \bar{\kappa}_{\pm}^2 + \delta_* \mathcal{R}(\bar{\kappa}_{\pm}^2 \lambda_{\pm}) \right) \right. \\ & + \delta_*^2 \left( \frac{5}{2} (-2 + 3\omega' \omega_0) + \frac{10}{3} \bar{\kappa}_{\pm}^2 (-1 + 5\omega' \omega_0) + \frac{5}{2} \omega' \omega_0 (1 + 2\bar{\kappa}_{\pm}^2 \lambda_{\pm}) \delta_* \mathcal{R}(\bar{\kappa}_{\pm}^2 \lambda_{\pm}) \right) \\ & \left. + \frac{-5 + 15\omega' \omega_0 + 6\omega'^2 \omega_0^2}{\omega' \omega_0} \left( 2\bar{\kappa}_{\pm}^2 + \delta_* \mathcal{R}(\bar{\kappa}_{\pm}^2 \lambda_{\pm}) \right) - \frac{-15 + 12\omega' \omega_0 + \omega'^2 \omega_0^2}{\omega' \omega_0} \right\} \right]. \end{aligned} \quad (6.19b)$$

Here, the additional auxiliary functions are defined as

$$\begin{aligned}\bar{\kappa}_+ &= \frac{\kappa}{\omega^*}, & \bar{\kappa}_- &= \frac{\kappa}{\omega_0^*}, & \mathcal{R}(x) &= \sqrt{1+x}, \\ \mathcal{F}_1(x) &= \mathcal{S}(x) - \mathcal{R}(x), & \mathcal{F}_2(x) &= \mathcal{S}(x) - \left(1 - \frac{2}{3}x\right)\mathcal{R}(x), \\ \mathcal{F}_3(x) &= \mathcal{S}(x) - \left(1 - \frac{2}{3}x + \frac{8}{15}x^2\right)\mathcal{R}(x), & \mathcal{F}_4(x) &= \mathcal{S}(x) - \left(1 - \frac{2}{3}x + \frac{8}{15}x^2 - \frac{16}{35}x^3\right)\mathcal{R}(x). \\ X_* &= \frac{(\omega^* - \omega_0^*)^2}{(\bar{\omega}' - \bar{\omega}_0)^2}, & \bar{X} &= \frac{(\bar{\omega}' - \bar{\omega}_0)^2}{4\omega'^2\omega_0^2}.\end{aligned}$$

It should be noted that  $\mathcal{F}_1 = \mathcal{F}$ , and that furthermore the  $\mathcal{F}_i$  indicate the removal of the Taylor series of  $\mathcal{S}$  for small  $x$  to maintain numerical stability. The  $g$  functions are given by

$$\begin{aligned}\delta_* &= \frac{\omega^* - \omega_0^*}{\omega\omega_0}, & \mathcal{L}_\pm &= s_{1\pm}\sqrt{1+\lambda_\pm}\frac{\omega+\omega_0}{\omega\omega_0}, & s_{1+} &= 1, & s_{1-} &= -\text{Sign}(\gamma_0 - \omega'), \\ g_{1\pm} &= 2(1 - \bar{\kappa}_\pm^2) \pm 2\frac{\bar{\kappa}_\pm}{\kappa} - \mathcal{L}_\pm\mathcal{S}(\bar{\kappa}_\pm^2\lambda_\pm) - \delta_*, \\ g_{2\pm} &= 2[\bar{\kappa}_\pm^2\mathcal{R}(\bar{\kappa}_\pm^2\lambda_\pm) + \delta_*][1 + \lambda_\pm(1 - \bar{\kappa}_\pm^2)] + \frac{1}{2}\mathcal{L}_\pm[3\mathcal{S}(\bar{\kappa}_\pm^2\lambda_\pm) - \mathcal{R}(\bar{\kappa}_\pm^2\lambda_\pm) - \lambda_\pm\delta_*] \\ &\quad - 2\mathcal{R}(\bar{\kappa}_\pm^2\lambda_\pm) \mp 2\frac{\bar{\kappa}_\pm}{\kappa} - \frac{1}{2}\mathcal{R}(\bar{\kappa}_\pm^2\lambda_\pm)\lambda_\pm\delta_*^2, \\ g_{3\pm} &= [2\mathcal{R}(\bar{\kappa}_\pm^2\lambda_\pm)(1 - \bar{\kappa}_\pm^2) - \delta_*](1 - \bar{\kappa}_\pm^2\lambda_\pm + \bar{\kappa}_\pm^4\lambda_\pm^2) - \lambda_\pm\delta_*(1 - \bar{\kappa}_\pm^2\lambda_\pm) \pm 2\frac{\bar{\kappa}_\pm}{\kappa} \\ &\quad - \frac{1}{8}\mathcal{L}_\pm[15\mathcal{S}(\bar{\kappa}_\pm^2\lambda_\pm) + (2\bar{\kappa}_\pm^2\lambda_\pm - 7)\mathcal{R}(\bar{\kappa}_\pm^2\lambda_\pm)] - \frac{1}{4}\mathcal{L}_\pm\lambda_\pm\delta_*[\lambda_\pm\delta_*\mathcal{R}(\bar{\kappa}_\pm^2\lambda_\pm) - 2(1 - \bar{\kappa}_\pm^2\lambda_\pm)] \\ &\quad + \frac{1}{4}\lambda_\pm\delta_*^2[2(1 - 2\bar{\kappa}_\pm^2\lambda_\pm + \lambda_\pm)\mathcal{R}(\bar{\kappa}_\pm^2\lambda_\pm) - \lambda_\pm\delta_*].\end{aligned}$$

Finally the  $\mathcal{H}$ ,  $\mathcal{J}$  and  $\mathcal{K}$  functions are given by

$$\begin{aligned}\mathcal{H}_\ell &= \frac{\sum_{n=0}^{2\ell} \omega^n \omega_0^{2\ell-n}}{(\omega'\omega_0)^\ell}, \\ \mathcal{J}_1 &= 1, & \mathcal{J}_2 &= \frac{\omega'^2 + 3\omega'\omega_0 + \omega_0^2}{\omega'\omega_0}, & \mathcal{J}_3 &= \frac{\omega'^4 + 3\omega'^3\omega_0 + 6\omega'^2\omega_0^2 + 3\omega'\omega_0^3 + \omega_0^4}{\omega'^2\omega_0^2}, \\ \mathcal{K}_1 &= 0, & \mathcal{K}_2 &= 1, & \mathcal{K}_3 &= \frac{\omega'^2 + 5\omega'\omega_0 + \omega_0^2}{\omega'\omega_0}.\end{aligned}$$

These  $\mathcal{H}$ ,  $\mathcal{J}$  and  $\mathcal{K}$  account for the increasing polynomial complexity in the  $\mathcal{I}_0^\ell$  terms. The  $g$  terms reflect repeating complex functions between each multipole. Nonetheless, while these expressions reflect a fast way of accurately computing these higher-multipole terms, the equations themselves allow for little interpretation of the behaviour of these kernels. It should also be noted that these expressions have all been numerically verified to ensure accuracy.

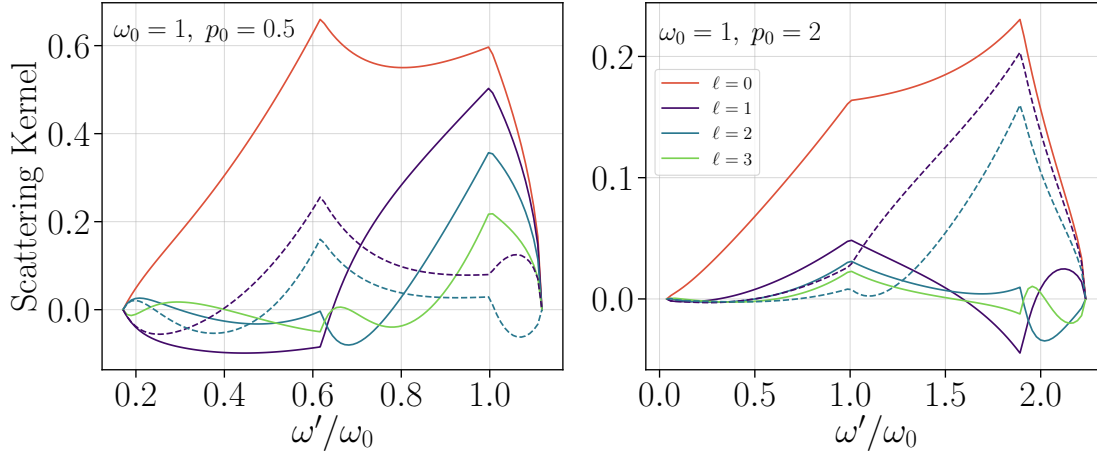


**FIGURE 6.4:** The multipole Compton scattering kernel,  $P^\ell(\omega_0 \rightarrow \omega', p_0)$ , for some illustrative non-extreme values of  $\omega_0$  and  $p_0$ . The solid lines show the kernels for anisotropic photon distributions, while the dashed lines indicate the anisotropic electron distributions for  $\ell = 1$  and  $2$ .

### 6.3.2 Exploration

To better understand these kernels, it is helpful to once again visually examine them under variations in  $\omega_0$ ,  $\omega'$  and  $p_0$ . Figure 6.4 shows the kernels generated for  $\omega_0 = 1$  with  $p_0 = 0.5$  and  $2$ . Here, the monopole kernels are plotted which allows for comparison with Figure 6.2 to consider further modifications in  $\omega_0$  and  $p_0$ . This figure shows not only the photon multipole kernels, analytically expressed here, but also the scattering kernels for an electron dipole and quadrupole.

In general, the complexity in the analytic expressions are immediately reflected in the plotted kernels. However, once again there are some shared key features immediately discernible. In particular, the kernels all share the same cusps as expected. This indicates that again increasing either the photon or electron momentum will result in broader kernels, indicating effects on an increased range of frequencies  $\omega'$ . The cusp at  $\omega_0$  is also always positive for photon anisotropies while  $\omega_0 \leq 1$ , but the electron anisotropies do not seem to share this behaviour. This can be understood as the photon anisotropies lead to energy redistribution between multipoles, but there will always be a chance the photon retains its energy. An electron dipole however, indicates that in certain directions there is a strong likelihood that all interacting photons will be upscattered, and as such, there will be fewer photons at  $\omega_0$  than in the original distribution. However, although plotted here, it can be found that when  $\omega_0 > 1$  this is no longer always the case for photon anisotropies. In these cases, particularly when  $\omega_0 \simeq p_0$ , there is a chance that the photon anisotropies will lead to photons disappearing at  $\omega_0$  for the odd  $\ell$ .

In general the negative components of the kernel, much as was described in Chapter 5, reflect that photons will be scattered *between* multipoles. Furthermore, unlike in the SZ case, there is no simple pattern for the behaviour of the



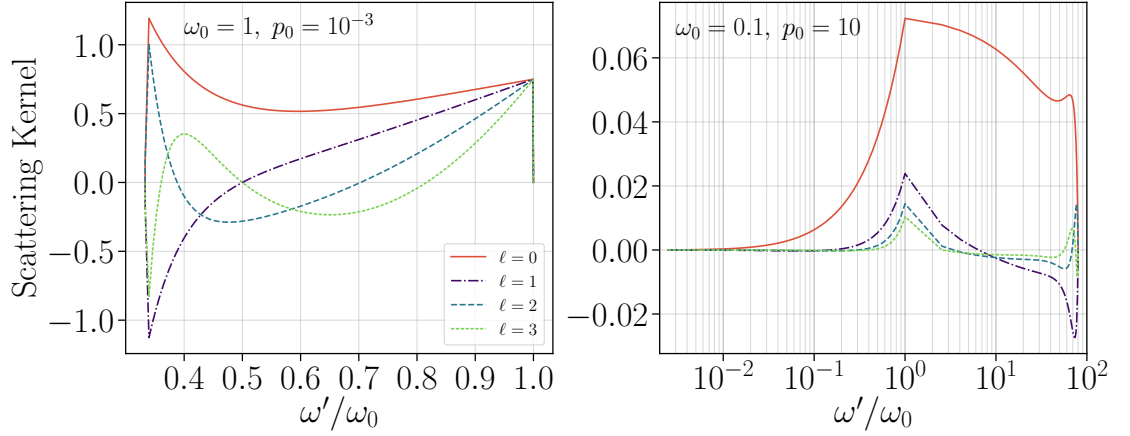


**FIGURE 6.5:** The anisotropic photon scattering kernel,  $P^\ell(\omega_0 \rightarrow \omega', p_0)$ , for some extreme values of  $\omega_0$  and  $p_0$ . The left panel shows recoil-dominated scattering and on the right is Doppler-dominated scattering.

zero crossings in each kernel – however it is clear that the magnitude of kernels and the number of zero-crossings are dependent on the degree of anisotropy ( $\ell$ ) as well as the ‘expected’ parameters of  $p_0$  and  $\omega_0$ .

### Extreme cases

It is also instructive to consider these kernels in the extreme cases discussed for the monopole Compton-scattering kernel. Figure 6.5 displays the anisotropic kernels in these regimes (cf. Figure 6.3).

Once again recoil-dominated scattering ( $p_0 \ll \omega_0$  and  $p_0 \ll 1$ ) is almost entirely determined by Zone II. This allows for greatly simplified anisotropic kernels. In particular, now the zero-crossings align exactly with  $\ell$ . And accordingly, since all the kernels are positive at  $\omega_0$ , the even multipoles (i.e.,  $\ell$  is even) are positive at  $\omega_c$ , while the odd multipoles are negative at  $\omega_c$ . At each multipole, the probability of a photon maintaining its initial energy is constant. As such, determining an analytic approximation for multipole kernels in this regime seems eminently possible, and will be explored in future work on this subject.

Doppler-dominated scattering is once again more complex. Here again at low  $\omega'$ , the kernel greatly resembles those found for the SZ multipole kernels (i.e., Figure 5.2) – as would be expected as the SZ kernel is an approximation for this regime. However, at high  $\omega'$  we again see a Doppler peak, not encapsulated by SZ approximations. This is triggered again by the recoil effects caused by the ultra-relativistic electrons used in this case. In particular, at  $\omega_0$ , the peak decreases with increasing  $\ell$ , and there are  $\ell$  zero-crossings on each side of  $\omega_0$ . A large number of these crossings are located very close to  $\omega'_{\min}$  and  $\omega'_{\max}$  respectively, leading to highly fluctuating behaviour in the frequency extremes. A more detailed understanding of the recoil-induced photon pile-up in these multipole cases may be obtained through analytic approximations of these anisotropic

kernels in the ultra-relativistic regime. However, this has not been attempted within this thesis.

## 6.4 Conclusion

This chapter presents analytic forms of the isotropic and anisotropic photon Compton-scattering kernels. For all the Compton-scattering kernels the behaviour is defined by three zones, determined by energy constraints on the form of scattering that can occur. In particular, four frequencies must be emphasised,  $\omega' = \omega'_{\min}$ ,  $\omega_c$ ,  $\omega_0$  and  $\omega' = \omega_0 + \gamma_0 - 1$ . A summary of part of the work of [Sarkar et al. \(2019\)](#) has been included – although [Sarkar et al. \(2019\)](#) considers the isotropic kernel in even more depth including explorations of the moment behaviour and thermal averaging of the general Compton-scattering kernel. Nonetheless, here we demonstrate the numerically stable and simple form of the isotropic Compton-scattering kernel.

In the recoil-dominated regime ( $p_0 \ll 1$  and  $p_0 \ll \omega_0$ ), the isotropic kernel is dominated by only one zone, and can be well modelled by a simple analytic approximation. In the Doppler-dominated regime however ( $\omega_0 \ll p_0$ ) the commonly used approximation (i.e., the SZ kernel) breaks when  $p_0 \gg (4\omega_0)^{-1}$ . In this case recoil effects lead to a photon ‘pile-up’ at high frequencies which can be modelled by an analytic approximation for ultra-relativistic photons. However, even this will break when the third scattering zone begins to contribute (e.g., for  $\omega_0 > 0.5$ ). In general, if there is any doubt over the appropriateness of the approximate kernels, the full Compton-scattering kernel should be used. To this end, `CSpack` has been created as a code base to allow for the rapid and accurate computation of the full Compton-scattering kernel and its integrated forms.

The anisotropic kernels work analogously to the isotropic kernel, albeit with a significant increase in complexity which increases substantially with increase  $\ell$ . Each kernel (for  $\ell \neq 0$ ) contains negative regions indicating the scattering occurring *between* multipoles – that is the significant angular redistribution under anisotropic Compton scattering. While analytic approximations have yet to be calculated, the recoil-dominated regime, once again is dominated by a single zone, and reveals a greatly simplified scattering behaviour. The Doppler-dominated regime, however, once again cannot be modelled by the SZ approximation (i.e., Chapter 5) alone when  $p_0$  becomes large. Again, a recoil-induced pile-up at high frequencies is observed, leading to high amplitudes in the kernel which would not be predicted from anisotropic SZ considerations. While the ultra-relativistic anisotropic approximation has again not been calculated, it is our expectation that it will fail in a similar way to the isotropic form, as  $\omega_0$  increases and Zone III becomes a substantial contributor to the kernel.

These analytic kernels allow for a rapid and accurate computation of the Compton-scattering process, relevant for radiative transfer problems in astrophysical plasmas. For instance, high-energy photons and electrons can be found in accretion flows (e.g., [Shakura & Sunyaev, 1973](#); [Abramowicz et al., 1988](#); [Narayan et al., 2003](#); [McKinney et al., 2017](#)) and electromagnetic particle cascades which occur in multiple phases of evolution in the Universe ([Zdziarski, 1988](#); [Shull & van Steenberg, 1985](#); [Slatyer et al., 2009](#); [Valdés et al., 2010](#); [Slatyer, 2016](#); [Liu et al., 2019](#)). Furthermore, jets from AGN, supernovae and gamma-ray bursts will lead to highly relativistic non-thermal electron populations (e.g., [Giannios, 2006](#); [Mimica et al., 2009](#); [Giannios, 2010](#)), also relevant to the non-thermal SZ effect ([Enßlin & Kaiser, 2000](#); [Colafrancesco et al., 2003](#)). Many common approximations can be avoided using the general expressions provided here, allowing for accurate calculation at little extra numerical cost.

## Chapter 7

# Summary and Future Work

This thesis has considered a number of modifications to the standard SZ formalism to determine what effects they may generate in the observed signal. In particular, Chapters 2 and 3 used simulations to determine temperature scaling relations for clusters which can be used to predict the magnitude of rSZ corrections that will be incurred in standard observations of the SZ effect. Chapter 2 used the BAHAMAS and MACSIS simulations to examine not only broad scaling relations, but also temperature profiles, and determine that higher-order temperature corrections to the SZ signal appear to be small. Chapter 3 extended this work to compare the broad scaling relations across four different simulation samples to determine how variations in simulations may lead to different temperature predictions.

Chapter 4 instead considered a variation to the incoming photons to the SZ effect. Here, in particular, the signal that may be formed from the ARCADE radio excess is discussed – and how variations in any observed radio SZ signal may be used to determine information on the nature of the radio excess itself, or used in conjunction with the ‘normal’ CMB-induced SZ effect to learn more about the properties of the clusters.

Chapter 5 presented analytic SZ-scattering kernels for anisotropies in the incoming electron or photon distributions, alongside a brief discussion of high-energy non-thermal electron populations and how each would affect the observed SZ signal. Chapter 6 discusses the general Compton-scattering kernel. An analytic and numerically stable form of the isotropic Compton-scattering kernel has been presented (as in the work of Sarkar et al., 2019), alongside the newly calculated anisotropic photon scattering kernels.

Many of the figures presented here have been computed using SZpack and CSpack. The latter was developed for the work of Sarkar et al. (2019), and will be extended for anisotropic calculations shortly. SZpack however, was first released in 2012 (Chluba et al., 2012b), but has undergone significant extensions since. As part of my PhD, an overhaul of the base code has been carried out including creating an integrated python wrapper for the code. An early access version of

this is available at [bitbucket.org/ElizabethLee/szpack.v2.0](https://bitbucket.org/ElizabethLee/szpack.v2.0), and further updates and extensions will be rolled out within the next year.

Other work is also planned to complete the project analysing the anisotropic SZ-scattering kernels. This would include a more detailed examination of electron anisotropies and the relationship between anisotropic scattering kernels and the pSZ effects. Further work into the general anisotropic Compton-scattering kernels must also be carried out, both to fully determine the numerical stability of the anisotropic kernels, as well as to determine and compare these kernels with approximations in the extreme scenarios. This may also contain more discussion of electron anisotropies, thermal averaging and the behaviour of frequency moments of these kernels.

Other avenues to explore include using the temperature scaling results to generate observational predictions and/or estimate the scale of the rSZ-induced  $y$  miscalibration in past SZ studies; more detailed modelling of the radio SZ signal, including the effects of scattering of radio sources within clusters and their impact on the viability of radio SZ detections; using the analytics for the SZ- and Compton-scattering kernels to determine the effects of high-energy particles in clusters (e.g., caused by jets and shocks) on the spectral shape caused by their scattering with the CMB; and analysis of the evolution of anisotropies in primordial distortions using the anisotropic Compton-scattering kernels.

# Bibliography

- Abazajian K. N., et al., 2016, arXiv e-prints, p. arXiv:1610.02743
- Abitbol M. H., Chluba J., Hill J. C., Johnson B. R., 2017, [Monthly Notices of the RAS](#), **471**, 1126
- Abramowicz M. A., Czerny B., Lasota J. P., Szuszkiewicz E., 1988, [Astrophysical Journal](#), **332**, 646
- Acharya S. K., Chluba J., 2022, arXiv e-prints, p. arXiv:2205.00857
- Acharya S. K., Majumdar S., Nath B. B., 2021, [Monthly Notices of the RAS](#), **503**, 5473
- Adam R., et al., 2016, [Astronomy and Astrophysics](#), **586**, A122
- Adam R., et al., 2017, [Astronomy and Astrophysics](#), **598**, A115
- Adam R., et al., 2018, [Astronomy and Astrophysics](#), **609**, A115
- Ade P., et al., 2019, [Journal of Cosmology and Astroparticle Physics](#), **2019**, 056
- Aharonian F. A., Atoyan A. M., 1981, [Astrophysics and Space Science](#), **79**, 321
- Allen S. W., Evrard A. E., Mantz A. B., 2011, [Annual Review of Astron and Astrophys](#), **49**, 409
- Ameglio S., Borgani S., Pierpaoli E., Dolag K., Ettori S., Morandi A., 2009, [Monthly Notices of the RAS](#), **394**, 479
- Anbajagane D., Evrard A. E., Farahi A., Barnes D. J., Dolag K., McCarthy I. G., Nelson D., Pillepich A., 2020, [Monthly Notices of the RAS](#), **495**, 686
- Anbajagane D., et al., 2022a, [Monthly Notices of the RAS](#), **510**, 2980
- Anbajagane D., et al., 2022b, [Monthly Notices of the RAS](#), **514**, 1645
- Ansarifard S., et al., 2020, [Astronomy and Astrophysics](#), **634**, A113
- Arnaud M., Pointecouteau E., Pratt G. W., 2005, [Astronomy and Astrophysics](#), **441**, 893

- Arnaud M., Pratt G. W., Piffaretti R., Böhringer H., Croston J. H., Pointecouteau E., 2010, *Astronomy and Astrophysics*, 517, A92
- Aung H., Nagai D., Lau E. T., 2021, *Monthly Notices of the RAS*, 508, 2071
- Austermann J. E., et al., 2018, *Journal of Low Temperature Physics*, 193, 120
- Avestruz C., Nagai D., Lau E. T., Nelson K., 2015, *Astrophysical Journal*, 808, 176
- Barnes D. J., Kay S. T., Henson M. A., McCarthy I. G., Schaye J., Jenkins A., 2017a, *Monthly Notices of the RAS*, 465, 213
- Barnes D. J., et al., 2017b, *Monthly Notices of the RAS*, 471, 1088
- Basu K., et al., 2019, *Bulletin of the AAS*, 51, 302
- Battaglia N., Bond J. R., Pfrommer C., Sievers J. L., Sijacki D., 2010, *Astrophysical Journal*, 725, 91
- Battaglia N., Bond J. R., Pfrommer C., Sievers J. L., 2012a, *Astrophysical Journal*, 758, 75
- Battaglia N., Bond J. R., Pfrommer C., Sievers J. L., 2012b, *Astrophysical Journal*, 758, 74
- Baxter E. J., Adhikari S., Vega-Ferrero J., Cui W., Chang C., Jain B., Knebe A., 2021, *Monthly Notices of the RAS*, 508, 1777
- Beck A. M., et al., 2016, *Monthly Notices of the RAS*, 455, 2110
- Behroozi P. S., Wechsler R. H., Wu H.-Y., 2013, *Astrophysical Journal*, 762, 109
- Belmont R., 2009, *Astronomy and Astrophysics*, 506, 589
- Bennett C. L., et al., 1996, *Astrophysical Journal, Letters*, 464, L1
- Benson B. A., et al., 2014, in Holland W. S., Zmuidzinas J., eds, *Society of Photo-Optical Instrumentation Engineers (SPIE) Conference Series Vol. 9153, Millimeter, Submillimeter, and Far-Infrared Detectors and Instrumentation for Astronomy VII*. p. 91531P ([arXiv:1407.2973](https://arxiv.org/abs/1407.2973)), [doi:10.1117/12.2057305](https://doi.org/10.1117/12.2057305)
- Biffi V., et al., 2016, *Astrophysical Journal*, 827, 112
- Birkinshaw M., 1979, *Monthly Notices of the RAS*, 187, 847
- Birkinshaw M., Gull S. F., 1983, *Nature*, 302, 315
- Birkinshaw M., Gull S. F., Hardebeck H., 1984, *Nature*, 309, 34
- Birkinshaw M., Hughes J. P., Arnaud K. A., 1991, *Astrophysical Journal*, 379, 466
- Bleem L. E., et al., 2015, *Astrophysical Journal, Supplement*, 216, 27

- Blumenthal G. R., Gould R. J., 1970, [Reviews of Modern Physics](#), **42**, 237
- Bocquet S., Saro A., Dolag K., Mohr J. J., 2016, [Monthly Notices of the RAS](#), **456**, 2361
- Bolliet B., Comis B., Komatsu E., Macías-Pérez J. F., 2018, [Monthly Notices of the RAS](#), **477**, 4957
- Bonamente M., Joy M. K., LaRoque S. J., Carlstrom J. E., Reese E. D., Dawson K. S., 2006, [Astrophysical Journal](#), **647**, 25
- Bora K., Desai S., 2021, [Journal of Cosmology and Astroparticle Physics](#), **2021**, 012
- Bourdin H., Mazzotta P., Kozmanyán A., Jones C., Vikhlinin A., 2017, [Astrophysical Journal](#), **843**, 72
- Briel U. G., Henry J. P., Boehringer H., 1992, [Astronomy and Astrophysics](#), **259**, L31
- Bryan G. L., Norman M. L., 1998, [Astrophysical Journal](#), **495**, 80
- Buchler J. R., Yueh W. R., 1976, [Astrophysical Journal](#), **210**, 440
- Bulbul E., et al., 2019, [Astrophysical Journal](#), **871**, 50
- Bullock J. S., Dekel A., Kolatt T. S., Kravtsov A. V., Klypin A. A., Porciani C., Primack J. R., 2001, [Astrophysical Journal](#), **555**, 240
- Butler V. L., et al., 2022, [Astrophysical Journal](#), **932**, 55
- Carlstrom J. E., Holder G. P., Reese E. D., 2002, [Annual Review of Astronomy and Astrophysics](#), **40**, 643
- Cavaliere A., Danese L., de Zotti G., 1979, [Astronomy and Astrophysics](#), **75**, 322
- Cayuso J., Bloch R., Hotinli S. C., Johnson M. C., McCarthy F., 2021, arXiv e-prints, [p. arXiv:2111.11526](#)
- Challinor A., Lasenby A., 1998, [Astrophysical Journal](#), **499**, 1
- Chluba J., Dai L., 2014, [Monthly Notices of the RAS](#), **438**, 1324
- Chluba J., Mannheim K., 2002, [Astronomy and Astrophysics](#), **396**, 419
- Chluba J., Sunyaev R. A., 2012, [Monthly Notices of the RAS](#), **419**, 1294
- Chluba J., Hütsi G., Sunyaev R. A., 2005, [Astronomy and Astrophysics](#), **434**, 811
- Chluba J., Khatri R., Sunyaev R. A., 2012a, [Monthly Notices of the RAS](#), **425**, 1129
- Chluba J., Nagai D., Sazonov S., Nelson K., 2012b, [Monthly Notices of the RAS](#), **426**, 510



- Chluba J., Switzer E., Nelson K., Nagai D., 2013, [Monthly Notices of the RAS](#), 430, 3054
- Chluba J., Dai L., Kamionkowski M., 2014, [Monthly Notices of the RAS](#), 437, 67
- Chluba J., Hill J. C., Abitbol M. H., 2017, [Monthly Notices of the RAS](#), 472, 1195
- Chluba J., et al., 2021, [Experimental Astronomy](#), 51, 1515
- Choi S. K., et al., 2020, [Journal of Cosmology and Astroparticle Physics](#), 2020, 045
- Colafrancesco S., Marchegiani P., Palladino E., 2003, [Astronomy and Astrophysics](#), 397, 27
- Cooray A., 2006, [Physical Review D](#), 73, 103001
- Cooray A., Chen X., 2002, [Astrophysical Journal](#), 573, 43
- Coulton W., Ota A., van Engelen A., 2020, [Physical Review Letters](#), 125, 111301
- Cui W., et al., 2018, [Monthly Notices of the RAS](#), 480, 2898
- Cui W., et al., 2022, [Monthly Notices of the RAS](#), 514, 977
- Davé R., Anglés-Alcázar D., Narayanan D., Li Q., Rafieferantsoa M. H., Appleby S., 2019, [Monthly Notices of the RAS](#), 486, 2827
- Deutsch A.-S., Dimastrogiovanni E., Johnson M. C., Münchmeyer M., Terrana A., 2018, [Physical Review D](#), 98, 123501
- Dewdney P. E., Hall P. J., Schilizzi R. T., Lazio T. J. L. W., 2009, [IEEE Proceedings](#), 97, 1482
- Diego J. M., Mazzotta P., Silk J., 2003, [Astrophysical Journal, Letters](#), 597, L1
- Dolag K., Borgani S., Murante G., Springel V., 2009, [Monthly Notices of the RAS](#), 399, 497
- Dowell J., Taylor G. B., 2018, [Astrophysical Journal, Letters](#), 858, L9
- Dubus G., Cerutti B., Henri G., 2008, [Astronomy and Astrophysics](#), 477, 691
- Duffy A. R., Schaye J., Kay S. T., Dalla Vecchia C., 2008, [Monthly Notices of the RAS](#), 390, L64
- Dutton A. A., Macciò A. V., 2014, [Monthly Notices of the RAS](#), 441, 3359
- Enßlin T. A., Kaiser C. R., 2000, [Astronomy and Astrophysics](#), 360, 417
- Erlar J., Basu K., Chluba J., Bertoldi F., 2018, [Monthly Notices of the RAS](#), 476, 3360
- Farahi A., Evrard A. E., McCarthy I., Barnes D. J., Kay S. T., 2018, [Monthly Notices of the RAS](#), 478, 2618

- Farahi A., Anbajagane D., Evrard A. E., 2022, *Astrophysical Journal*, 931, 166
- Fargion D., Konoplich R. V., Salis A., 1997, *Zeitschrift fur Physik C Particles and Fields*, 74, 571
- Feng C., Holder G., 2018, *Astrophysical Journal, Letters*, 858, L17
- Fixsen D. J., Mather J. C., 2002, *Astrophysical Journal*, 581, 817
- Fixsen D. J., Cheng E. S., Gales J. M., Mather J. C., Shafer R. A., Wright E. L., 1996, *Astrophysical Journal*, 473, 576
- Fixsen D. J., et al., 2011, *Astrophysical Journal*, 734, 5
- Gatti M., et al., 2022, *Physical Review D*, 105, 123525
- Giannios D., 2006, *Astronomy and Astrophysics*, 457, 763
- Giannios D., 2010, *Monthly Notices of the RAS*, 408, L46
- Grainge K., Jones M., Pooley G., Saunders R., Edge A., 1993, *Monthly Notices of the RAS*, 265, L57
- Grebenev S. A., Sunyaev R. A., 2020, *Astronomy Letters*, 45, 791
- Haardt F., 1993, *Astrophysical Journal*, 413, 680
- Hanany S., et al., 2019, arXiv e-prints, p. arXiv:1902.10541
- Hand N., et al., 2012, *Physical Review Letters*, 109, 041101
- Hansen S. H., 2004, *Monthly Notices of the RAS*, 351, L5
- Hansen S. H., Pastor S., Semikoz D. V., 2002, *Astrophysical Journal, Letters*, 573, L69
- Henden N. A., Puchwein E., Shen S., Sijacki D., 2018, *Monthly Notices of the RAS*, 479, 5385
- Henden N. A., Puchwein E., Sijacki D., 2019, *Monthly Notices of the RAS*, 489, 2439
- Henson M. A., Barnes D. J., Kay S. T., McCarthy I. G., Schaye J., 2017, *Monthly Notices of the RAS*, 465, 3361
- Hill J. C., Battaglia N., Chluba J., Ferraro S., Schaan E., Spergel D. N., 2015, *Physical Review Letters*, 115, 261301
- Hirschmann M., Dolag K., Saro A., Bachmann L., Borgani S., Burkert A., 2014, *Monthly Notices of the RAS*, 442, 2304
- Holder G., Chluba J., 2021, arXiv e-prints, p. arXiv:2110.08373

- Hu W., Silk J., 1993, [Physical Review D](#), 48, 485
- Hu W., White M., 1997, [Physical Review D](#), 56, 596
- Hughes J. P., Birkinshaw M., 1998, [Astrophysical Journal](#), 501, 1
- Hurier G., 2016, [Astronomy and Astrophysics](#), 596, A61
- Hurier G., Tchernin C., 2017, [Astronomy and Astrophysics](#), 604, A94
- Hurier G., Adam R., Keshet U., 2019, [Astronomy and Astrophysics](#), 622, A136
- Ichiki K., 2014, [Progress of Theoretical and Experimental Physics](#), 2014, 06B109
- Itoh N., Nozawa S., 2004, [Astronomy and Astrophysics](#), 417, 827
- Itoh N., Kohyama Y., Nozawa S., 1998, [Astrophysical Journal](#), 502, 7
- Itoh N., Kawana Y., Nozawa S., Kohyama Y., 2001, [Monthly Notices of the RAS](#), 327, 567
- Jonas J., MeerKAT Team 2016, in MeerKAT Science: On the Pathway to the SKA. p. 1
- Jones F. C., 1968, [Physical Review](#), 167, 1159
- Jones M., et al., 1993, [Nature](#), 365, 320
- Jones M. E., et al., 2005, [Monthly Notices of the RAS](#), 357, 518
- Kaastra J. S., Bykov A. M., Werner N., 2009, [Astronomy and Astrophysics](#), 503, 373
- Kamionkowski M., Loeb A., 1997, [Physical Review D](#), 56, 4511
- Katz J. I., 1987, High energy astrophysics
- Katz N., White S. D. M., 1993, [Astrophysical Journal](#), 412, 455
- Kay S. T., Powell L. C., Liddle A. R., Thomas P. A., 2008, [Monthly Notices of the RAS](#), 386, 2110
- Kay S. T., Peel M. W., Short C. J., Thomas P. A., Young O. E., Battye R. A., Liddle A. R., Pearce F. R., 2012, [Monthly Notices of the RAS](#), 422, 1999
- Khabibullin I., Komarov S., Churazov E., Schekochihin A., 2018, [Monthly Notices of the RAS](#), 474, 2389
- Khangulyan D., Aharonian F. A., Kelner S. R., 2014, [Astrophysical Journal](#), 783, 100
- Kholupenko E. E., Balashev S. A., Ivanchik A. V., Varshalovich D. A., 2015, [Monthly Notices of the RAS](#), 446, 3593
- Klypin A. A., Trujillo-Gomez S., Primack J., 2011, [Astrophysical Journal](#), 740, 102

- Klypin A., Yepes G., Gottlöber S., Prada F., Heß S., 2016, [Monthly Notices of the RAS](#), **457**, 4340
- Knollmann S. R., Knebe A., 2009, [Astrophysical Journal, Supplement](#), **182**, 608
- Kogut A., et al., 2011, [Journal of Cosmology and Astroparticle Physics](#), **2011**, 025
- Kogut A., Abitbol M. H., Chluba J., Delabrouille J., Fixsen D., Hill J. C., Patil S. P., Rotti A., 2019, in *Bulletin of the American Astronomical Society*, p. 113 ([arXiv:1907.13195](#))
- Komatsu E., et al., 2011, [Astrophysical Journal, Supplement](#), **192**, 18
- Kompaneets A., 1956, *Sov. Phys. JETP*, **31**, 876
- Kozmanyán A., Bourdin H., Mazzotta P., Rasia E., Sereno M., 2019, [Astronomy and Astrophysics](#), **621**, A34
- Kravtsov A. V., Borgani S., 2012, [Annual Review of Astron and Astrophys](#), **50**, 353
- Lau E. T., Kravtsov A. V., Nagai D., 2009, [Astrophysical Journal](#), **705**, 1129
- Lau E. T., Nagai D., Nelson K., 2013, [Astrophysical Journal](#), **777**, 151
- Le Brun A. M. C., McCarthy I. G., Schaye J., Ponman T. J., 2014, [Monthly Notices of the RAS](#), **441**, 1270
- Le Brun A. M. C., McCarthy I. G., Schaye J., Ponman T. J., 2017, [Monthly Notices of the RAS](#), **466**, 4442
- Lee E., Chluba J., Kay S. T., Barnes D. J., 2020, [Monthly Notices of the RAS](#), **493**, 3274
- Lee E., Chluba J., Holder G. P., 2022a, [Monthly Notices of the RAS](#), **512**, 5153
- Lee E., et al., 2022b, [Monthly Notices of the RAS](#), **517**, 5303
- Lim S. H., Mo H. J., Wang H., Yang X., 2020, [Astrophysical Journal](#), **889**, 48
- Lim S. H., Barnes D., Vogelsberger M., Mo H. J., Nelson D., Pillepich A., Dolag K., Marinacci F., 2021, [Monthly Notices of the RAS](#), **504**, 5131
- Liu H., Ridgway G. W., Slatyer T. R., 2019, arXiv e-prints,
- Luzzi G., Shimon M., Lamagna L., Rephaeli Y., De Petris M., Conte A., De Gregori S., Battistelli E. S., 2009, [Astrophysical Journal](#), **705**, 1122
- Malu S., Datta A., Colafrancesco S., Marchegiani P., Subrahmanyam R., Narasimha D., Wieringa M. H., 2017, [Scientific Reports](#), **7**, 16918
- Mantz A. B., Allen S. W., Morris R. G., Schmidt R. W., 2016, [Monthly Notices of the RAS](#), **456**, 4020

- Marinacci F., et al., 2018, [Monthly Notices of the RAS](#), 480, 5113
- Mather J. C., et al., 1994, [Astrophysical Journal](#), 420, 439
- Mauskopf P. D., et al., 2000, [Astrophysical Journal](#), 538, 505
- Mazzotta P., Rasia E., Moscardini L., Tormen G., 2004, [Monthly Notices of the RAS](#), 354, 10
- McCarthy I. G., Schaye J., Bird S., Le Brun A. M. C., 2017, [Monthly Notices of the RAS](#), 465, 2936
- McCarthy I. G., Bird S., Schaye J., Harnois-Deraps J., Font A. S., van Waerbeke L., 2018, [Monthly Notices of the RAS](#), 476, 2999
- McKinney J. C., Chluba J., Wielgus M., Narayan R., Sadowski A., 2017, [Monthly Notices of the RAS](#), 467, 2241
- Melin J. B., Bartlett J. G., Delabrouille J., 2006, [Astronomy and Astrophysics](#), 459, 341
- Melin J. B., et al., 2018, [Journal of Cosmology and Astroparticle Physics](#), 2018, 019
- Menanteau F., et al., 2010, [Astrophysical Journal](#), 723, 1523
- Meneghetti M., Rasia E., Merten J., Bellagamba F., Ettori S., Mazzotta P., Dolag K., Marri S., 2010, [Astronomy and Astrophysics](#), 514, A93
- Mimica P., Aloy M.-A., Agudo I., Martí J. M., Gómez J. L., Miralles J. A., 2009, [Astrophysical Journal](#), 696, 1142
- Mittal S., Kulkarni G., 2022, [Monthly Notices of the RAS](#), 510, 4992
- Moffet A. T., Birkinshaw M., 1989, [Astronomical Journal](#), 98, 1148
- Molnar S. M., Birkinshaw M., 2003, [Astrophysical Journal](#), 586, 731
- Morandi A., Nagai D., Cui W., 2013, [Monthly Notices of the RAS](#), 431, 1240
- Moskalenko I. V., Strong A. W., 2000, [Astrophysical Journal](#), 528, 357
- Mroczkowski T., et al., 2019, [Space Science Reviews](#), 215, 17
- Nagai D., 2006, [Astrophysical Journal](#), 650, 538
- Nagai D., Kravtsov A. V., Kosowsky A., 2003, [Astrophysical Journal](#), 587, 524
- Nagai D., Vikhlinin A., Kravtsov A. V., 2007a, [Astrophysical Journal](#), 655, 98
- Nagai D., Kravtsov A. V., Vikhlinin A., 2007b, [Astrophysical Journal](#), 668, 1
- Nagirner D. I., Poutanen J., 1994, Single Compton scattering

- Naiman J. P., et al., 2018, [Monthly Notices of the RAS](#), 477, 1206
- Narayan R., Igumenshchev I. V., Abramowicz M. A., 2003, [Publications of the ASJ](#), 55, L69
- Nelson K., Rudd D. H., Shaw L., Nagai D., 2012, [Astrophysical Journal](#), 751, 121
- Nelson K., Lau E. T., Nagai D., Rudd D. H., Yu L., 2014, [Astrophysical Journal](#), 782, 107
- Nelson D., et al., 2018, [Monthly Notices of the RAS](#), 475, 624
- Neto A. F., et al., 2007, [Monthly Notices of the RAS](#), 381, 1450
- Nozawa S., Kohyama Y., 2009, [Physical Review D](#), 79, 083005
- Nozawa S., Itoh N., Kohyama Y., 1998, [Astrophysical Journal](#), 508, 17
- Nozawa S., Itoh N., Kawana Y., Kohyama Y., 2000, [Astrophysical Journal](#), 536, 31
- Nozawa S., Itoh N., Kohyama Y., 2005, [Astronomy and Astrophysics](#), 440, 39
- Nozawa S., Itoh N., Suda Y., Ohhata Y., 2006, [Nuovo Cimento B Serie](#), 121, 487
- Osato K., Flender S., Nagai D., Shirasaki M., Yoshida N., 2018, [Monthly Notices of the RAS](#), 475, 532
- Osato K., Shirasaki M., Miyatake H., Nagai D., Yoshida N., Oguri M., Takahashi R., 2020, [Monthly Notices of the RAS](#), 492, 4780
- Pandey S., et al., 2019, [Physical Review D](#), 100, 063519
- Pandey S., et al., 2022, [Physical Review D](#), 105, 123526
- Parshley S. C., et al., 2018, in Marshall H. K., Spyromilio J., eds, Society of Photo-Optical Instrumentation Engineers (SPIE) Conference Series Vol. 10700, Ground-based and Airborne Telescopes VII. p. 107005X ([arXiv:1807.06675](#)), [doi:10.1117/12.2314046](#)
- Pearce F. A., Kay S. T., Barnes D. J., Bower R. G., Schaller M., 2020, [Monthly Notices of the RAS](#), 491, 1622
- Penzias A. A., Wilson R. W., 1965, [Astrophysical Journal](#), 142, 419
- Petrosian V., Bykov A., Rephaeli Y., 2008, [Space Science Reviews](#), 134, 191
- Pike S. R., Kay S. T., Newton R. D. A., Thomas P. A., Jenkins A., 2014, [Monthly Notices of the RAS](#), 445, 1774
- Pillepich A., et al., 2018a, [Monthly Notices of the RAS](#), 473, 4077
- Pillepich A., et al., 2018b, [Monthly Notices of the RAS](#), 475, 648

- Planck Collaboration et al., 2013, [Astronomy and Astrophysics](#), 550, A131
- Planck Collaboration et al., 2014a, [Astronomy and Astrophysics](#), 571, A1
- Planck Collaboration et al., 2014b, [Astronomy and Astrophysics](#), 571, A12
- Planck Collaboration et al., 2014c, [Astronomy and Astrophysics](#), 571, A16
- Planck Collaboration et al., 2016a, [Astronomy and Astrophysics](#), 594, A13
- Planck Collaboration et al., 2016b, [Astronomy and Astrophysics](#), 594, A22
- Planck Collaboration et al., 2016c, [Astronomy and Astrophysics](#), 594, A24
- Planck Collaboration et al., 2016d, [Astronomy and Astrophysics](#), 594, A27
- Planck Collaboration et al., 2016e, [Astronomy and Astrophysics](#), 596, A109
- Planck Collaboration et al., 2020a, [Astronomy and Astrophysics](#), 641, A1
- Planck Collaboration et al., 2020b, [Astronomy and Astrophysics](#), 641, A6
- Planelles S., et al., 2017, [Monthly Notices of the RAS](#), 467, 3827
- Pointecouteau E., Giard M., Barret D., 1998, [Astronomy and Astrophysics](#), 336, 44
- Pomraning G. C., 1972, [Journal of Quantitative Spectroscopy and Radiative Transfer](#), 12, 1047
- Pop A.-R., et al., 2022a, arXiv e-prints, p. [arXiv:2205.11528](#)
- Pop A.-R., et al., 2022b, arXiv e-prints, p. [arXiv:2205.11537](#)
- Postman M., et al., 2012, [Astrophysical Journal, Supplement](#), 199, 25
- Poutanen J., Vurm I., 2010, [Astrophysical Journal, Supplement](#), 189, 286
- Pratt G. W., Croston J. H., Arnaud M., Böhringer H., 2009, [Astronomy and Astrophysics](#), 498, 361
- Pratt C. T., Qu Z., Bregman J. N., 2021, [Astrophysical Journal](#), 920, 104
- Prokhorov D. A., Colafrancesco S., 2012, [Monthly Notices of the RAS](#), 424, L49
- Rasia E., et al., 2006, [Monthly Notices of the RAS](#), 369, 2013
- Rasia E., et al., 2012, [New Journal of Physics](#), 14, 055018
- Rasia E., et al., 2014, [Astrophysical Journal](#), 791, 96
- Rasia E., et al., 2015, [Astrophysical Journal, Letters](#), 813, L17
- Reese E. D., 2004, in Freedman W. L., ed., *Measuring and Modeling the Universe*. p. 138 ([arXiv:astro-ph/0306073](#))



- Reese E. D., Carlstrom J. E., Joy M., Mohr J. J., Grego L., Holzapfel W. L., 2002, [Astrophysical Journal](#), **581**, 53
- Remazeilles M., Chluba J., 2020, [Monthly Notices of the RAS](#), **494**, 5734
- Remazeilles M., Bolliet B., Rotti A., Chluba J., 2019, [Monthly Notices of the RAS](#), **483**, 3459
- Rephaeli Y., 1980, [Astrophysical Journal](#), **241**, 858
- Rephaeli Y., 1995, [Annual Review of Astron and Astrophys](#), **33**, 541
- Riess A. G., Casertano S., Yuan W., Macri L. M., Scolnic D., 2019, [Astrophysical Journal](#), **876**, 85
- Ruan J. J., Quinn T. R., Babul A., 2013, [Monthly Notices of the RAS](#), **432**, 3508
- Rudd D. H., Nagai D., 2009, [Astrophysical Journal, Letters](#), **701**, L16
- Rybicki G. B., Lightman A. P., 1979, Radiative processes in astrophysics. New York, Wiley-Interscience, 1979. 393 p.
- Sabyr A., Hill J. C., Bolliet B., 2022, [Physical Review D](#), **106**, 023529
- Sarazin C. L., 1986, [Reviews of Modern Physics](#), **58**, 1
- Sarkar A., Chluba J., Lee E., 2019, [Monthly Notices of the RAS](#), **490**, 3705
- Sayers J., et al., 2013, [Astrophysical Journal](#), **778**, 52
- Sazonov S. Y., Sunyaev R. A., 1998, [Astrophysical Journal](#), **508**, 1
- Sazonov S. Y., Sunyaev R. A., 1999, [Monthly Notices of the RAS](#), **310**, 765
- Sazonov S. Y., Sunyaev R. A., 2000, [Astrophysical Journal](#), **543**, 28
- Schaye J., et al., 2010, [Monthly Notices of the RAS](#), **402**, 1536
- Schaye J., et al., 2015, [Monthly Notices of the RAS](#), **446**, 521
- Seiffert M., et al., 2011, [Astrophysical Journal](#), **734**, 6
- Sembolini F., Yepes G., De Petris M., Gottlöber S., Lamagna L., Comis B., 2013, [Monthly Notices of the RAS](#), **429**, 323
- Sembolini F., et al., 2016, [Monthly Notices of the RAS](#), **459**, 2973
- Shakura N. I., Sunyaev R. A., 1973, *Astronomy and Astrophysics*, **24**, 337
- Shi X., Komatsu E., 2014, [Monthly Notices of the RAS](#), **442**, 521
- Shi X., Komatsu E., Nelson K., Nagai D., 2015, [Monthly Notices of the RAS](#), **448**, 1020



- Shi X., Komatsu E., Nagai D., Lau E. T., 2016a, [Monthly Notices of the RAS](#), 455, 2936
- Shi X., Komatsu E., Nagai D., Lau E. T., 2016b, [Monthly Notices of the RAS](#), 455, 2936
- Shull J. M., van Steenberg M. E., 1985, [Astrophysical Journal](#), 298, 268
- Singal J., et al., 2018, [Publications of the ASP](#), 130, 036001
- Slatyer T. R., 2016, [Physical Review D](#), 93, 023521
- Slatyer T. R., Padmanabhan N., Finkbeiner D. P., 2009, [Physical Review D](#), 80, 043526
- Smoot G. F., Tenorio L., Banday A. J., Kogut A., Wright E. L., Hinshaw G., Bennett C. L., 1994, [Astrophysical Journal](#), 437, 1
- Springel V., 2005, [Monthly Notices of the RAS](#), 364, 1105
- Springel V., 2010, [Monthly Notices of the RAS](#), 401, 791
- Springel V., White S. D. M., Tormen G., Kauffmann G., 2001, [Monthly Notices of the RAS](#), 328, 726
- Springel V., et al., 2018, [Monthly Notices of the RAS](#), 475, 676
- Square Kilometre Array Cosmology Science Working Group et al., 2020, [Publications of the Astron. Soc. of Australia](#), 37, e007
- Stacey G. J., et al., 2018, in Society of Photo-Optical Instrumentation Engineers (SPIE) Conference Series. p. 107001M, [doi:10.1117/12.2314031](#)
- Staniszewski Z., et al., 2009, [Astrophysical Journal](#), 701, 32
- Stein G., Alvarez M. A., Bond J. R., van Engelen A., Battaglia N., 2020, [Journal of Cosmology and Astroparticle Physics](#), 2020, 012
- Sunyaev R. A., Zeldovich Y. B., 1970, [Astrophysics and Space Science](#), 7, 20
- Sunyaev R. A., Zeldovich Y. B., 1972, Comments on Astrophysics and Space Physics, 4, 173
- Sunyaev R. A., Zeldovich I. B., 1980, [Monthly Notices of the RAS](#), 190, 413
- Sunyaev R. A., 1971, Soviet Astronomy, 15, 190
- Thiele L., et al., 2022, [Physical Review D](#), 105, 083505
- Tormen G., Bouchet F. R., White S. D. M., 1997, [Monthly Notices of the RAS](#), 286, 865

- Valdés M., Evoli C., Ferrara A., 2010, [Monthly Notices of the RAS](#), 404, 1569
- Vikhlinin A., 2006, [Astrophysical Journal](#), 640, 710
- Vikhlinin A., Kravtsov A., Forman W., Jones C., Markevitch M., Murray S. S., Van Speybroeck L., 2006, [Astrophysical Journal](#), 640, 691
- Vikhlinin A., et al., 2009a, [Astrophysical Journal](#), 692, 1033
- Vikhlinin A., et al., 2009b, [Astrophysical Journal](#), 692, 1060
- Vogelsberger M., et al., 2014, [Nature](#), 509, 177
- Voit G. M., 2005, [Reviews of Modern Physics](#), 77, 207
- Walker S., et al., 2019, [Space Science Reviews](#), 215, 7
- Wan J. T., Mantz A. B., Sayers J., Allen S. W., Morris R. G., Golwala S. R., 2021, [Monthly Notices of the RAS](#), 504, 1062
- Weinberg D. H., Mortonson M. J., Eisenstein D. J., Hirata C., Riess A. G., Rozo E., 2013, [Physics Reports](#), 530, 87
- Weinberger R., et al., 2017, [Monthly Notices of the RAS](#), 465, 3291
- Wright E. L., 1979, [Astrophysical Journal](#), 232, 348
- Yang T., Cai Y.-C., Cui W., Davé R., Peacock J. A., Sorini D., 2022, arXiv e-prints, [p. arXiv:2202.11430](#)
- Yu L., Nelson K., Nagai D., 2015, [Astrophysical Journal](#), 807, 12
- Zdziarski A. A., 1988, [Astrophysical Journal](#), 335, 786
- Zeldovich Y. B., Sunyaev R. A., 1969, [Astrophysics and Space Science](#), 4, 301
- Zemcov M., et al., 2012, [Astrophysical Journal](#), 749, 114
- Zitrin A., Broadhurst T., Barkana R., Rephaeli Y., Benítez N., 2011, [Monthly Notices of the RAS](#), 410, 1939
- Zitrin A., et al., 2015, [Astrophysical Journal](#), 801, 44
- Zubeldia Í., Rotti A., Chluba J., Battye R., 2022, arXiv e-prints, [p. arXiv:2204.13780](#)

## Appendix A

# Scaling fits for Bahamas+Macsis

This appendix corresponds with the data discussed in Chapter 2. The following tables display the fits for all of the relations mentioned there. For each scaling relationship, at each redshift, the fits are bootstrapped with 5000 iterations to gain fits for the binned medians of our data and the 16 and 84 percentiles in each of these bins. Hence, the errors on each value are the bootstrapped errors in these median fits, alongside the 84 and 16 percentile bounding region edges. This allows the intercluster variance to be calculated – that is, for example, at some mass,  $M_{500c}$ , the median  $y$ -weighted temperature at redshift  $z = 0$  is given by Equation (2.1), using A, B and C given by the first row of Table A.1. However, the 68% confidence region of that value, given by the intrinsic intercluster variation can be found through using Equation (2.1) using parameters given by rows 4 and 7 of Table A.1.

### A.1 Volume Averages over $R_{500c}$

Tables A.1 to A.5 show the temperature-mass and temperature-temperature volume averaged scalings for the sphere of radius  $R_{500c}$ .

### A.2 Volume Averages over $R_{200c}$

Tables A.6 to A.10 show the same as the previous section, but for the sphere of radius  $R_{200c}$ .

### A.3 Volume Averaged $Y$ Fits

The  $Y - M$  and  $Y - T^y$  relations over spheres of both radii are found in tables A.11 to A.14.

**TABLE A.1:** The fit values for the medians, 84 and 16 percentiles of each temperature measure at each redshift. The errors are determined through bootstrap methods. The fit parameters correspond to those described in Eq. (2.1).

$M = M_{500c}$	$A$	$B$	$C$
$z = 0.0$ , median			
$T_y$	$4.763^{+0.015}_{-0.015}$	$0.581^{+0.003}_{-0.002}$	$0.013^{+0.001}_{-0.001}$
$T_m$	$4.248^{+0.013}_{-0.012}$	$0.565^{+0.003}_{-0.002}$	$0.002^{+0.001}_{-0.001}$
$T_{sl}$	$4.295^{+0.023}_{-0.025}$	$0.514^{+0.012}_{-0.013}$	$-0.039^{+0.005}_{-0.005}$
84%			
$T_y$	$5.147^{+0.020}_{-0.020}$	$0.568^{+0.002}_{-0.004}$	$0.017^{+0.001}_{-0.002}$
$T_m$	$4.544^{+0.015}_{-0.015}$	$0.564^{+0.002}_{-0.008}$	$0.005^{+0.001}_{-0.003}$
$T_{sl}$	$4.660^{+0.022}_{-0.022}$	$0.527^{+0.004}_{-0.008}$	$-0.027^{+0.001}_{-0.003}$
16%			
$T_y$	$4.438^{+0.016}_{-0.017}$	$0.593^{+0.003}_{-0.003}$	$0.014^{+0.001}_{-0.001}$
$T_m$	$4.000^{+0.012}_{-0.013}$	$0.571^{+0.002}_{-0.003}$	$0.001^{+0.001}_{-0.001}$
$T_{sl}$	$3.915^{+0.026}_{-0.030}$	$0.503^{+0.009}_{-0.010}$	$-0.058^{+0.003}_{-0.003}$
$z = 0.5$ , median			
$T_y$	$4.353^{+0.019}_{-0.020}$	$0.571^{+0.006}_{-0.006}$	$0.008^{+0.002}_{-0.002}$
$T_m$	$3.702^{+0.013}_{-0.013}$	$0.546^{+0.005}_{-0.004}$	$-0.006^{+0.002}_{-0.001}$
$T_{sl}$	$3.474^{+0.027}_{-0.025}$	$0.483^{+0.023}_{-0.028}$	$-0.051^{+0.008}_{-0.010}$
84%			
$T_y$	$4.704^{+0.027}_{-0.027}$	$0.556^{+0.008}_{-0.007}$	$0.008^{+0.003}_{-0.003}$
$T_m$	$3.944^{+0.016}_{-0.016}$	$0.541^{+0.006}_{-0.006}$	$-0.004^{+0.002}_{-0.002}$
$T_{sl}$	$3.789^{+0.028}_{-0.032}$	$0.497^{+0.011}_{-0.046}$	$-0.038^{+0.004}_{-0.016}$
16%			
$T_y$	$4.083^{+0.017}_{-0.018}$	$0.588^{+0.006}_{-0.005}$	$0.009^{+0.002}_{-0.002}$
$T_m$	$3.498^{+0.015}_{-0.014}$	$0.557^{+0.004}_{-0.004}$	$-0.004^{+0.001}_{-0.001}$
$T_{sl}$	$3.131^{+0.028}_{-0.028}$	$0.478^{+0.040}_{-0.012}$	$-0.068^{+0.014}_{-0.004}$
$z = 1.0$ , median			
$T_y$	$3.997^{+0.021}_{-0.020}$	$0.593^{+0.004}_{-0.004}$	$0.009^{+0.001}_{-0.001}$
$T_m$	$3.237^{+0.015}_{-0.017}$	$0.558^{+0.004}_{-0.005}$	$-0.005^{+0.001}_{-0.001}$
$T_{sl}$	$2.754^{+0.036}_{-0.035}$	$0.478^{+0.015}_{-0.014}$	$-0.053^{+0.004}_{-0.004}$
84%			
$T_y$	$4.227^{+0.025}_{-0.022}$	$0.564^{+0.006}_{-0.007}$	$0.007^{+0.002}_{-0.003}$
$T_m$	$3.407^{+0.017}_{-0.018}$	$0.540^{+0.005}_{-0.006}$	$-0.006^{+0.002}_{-0.002}$
$T_{sl}$	$2.980^{+0.027}_{-0.033}$	$0.450^{+0.010}_{-0.018}$	$-0.050^{+0.004}_{-0.005}$
16%			
$T_y$	$3.785^{+0.027}_{-0.023}$	$0.618^{+0.007}_{-0.007}$	$0.012^{+0.002}_{-0.002}$
$T_m$	$3.084^{+0.016}_{-0.017}$	$0.576^{+0.006}_{-0.005}$	$-0.003^{+0.002}_{-0.002}$
$T_{sl}$	$2.543^{+0.030}_{-0.024}$	$0.518^{+0.017}_{-0.011}$	$-0.055^{+0.005}_{-0.004}$

**TABLE A.2:** The fit values for the medians, 84 and 16 percentiles of each temperature measure against  $T_{500c}$  at each redshift. The errors are determined through bootstrap methods. The fit parameters correspond to those described in Eq. (2.3).

$T_{\text{rel}} = T_{500c}$	$A$	$B$	$C$
$z = 0.0$ , median			
$T_y$	$4.812^{+0.014}_{-0.013}$	$0.889^{+0.003}_{-0.003}$	$0.041^{+0.002}_{-0.002}$
$T_m$	$4.289^{+0.011}_{-0.011}$	$0.873^{+0.004}_{-0.004}$	$0.021^{+0.002}_{-0.002}$
$T_{\text{sl}}$	$4.293^{+0.023}_{-0.022}$	$0.825^{+0.018}_{-0.018}$	$-0.049^{+0.010}_{-0.011}$
84%			
$T_y$	$5.174^{+0.023}_{-0.021}$	$0.865^{+0.005}_{-0.005}$	$0.047^{+0.003}_{-0.003}$
$T_m$	$4.575^{+0.013}_{-0.013}$	$0.859^{+0.004}_{-0.004}$	$0.023^{+0.002}_{-0.002}$
$T_{\text{sl}}$	$4.661^{+0.024}_{-0.025}$	$0.837^{+0.019}_{-0.009}$	$-0.028^{+0.011}_{-0.006}$
16%			
$T_y$	$4.490^{+0.016}_{-0.016}$	$0.906^{+0.005}_{-0.006}$	$0.042^{+0.003}_{-0.003}$
$T_m$	$4.020^{+0.013}_{-0.012}$	$0.880^{+0.005}_{-0.005}$	$0.019^{+0.003}_{-0.003}$
$T_{\text{sl}}$	$3.923^{+0.025}_{-0.027}$	$0.801^{+0.019}_{-0.015}$	$-0.096^{+0.010}_{-0.008}$
$z = 0.5$ , median			
$T_y$	$4.964^{+0.021}_{-0.019}$	$0.868^{+0.006}_{-0.005}$	$0.026^{+0.004}_{-0.003}$
$T_m$	$4.247^{+0.013}_{-0.013}$	$0.835^{+0.005}_{-0.004}$	$-0.006^{+0.003}_{-0.002}$
$T_{\text{sl}}$	$4.039^{+0.021}_{-0.022}$	$0.804^{+0.010}_{-0.011}$	$-0.093^{+0.005}_{-0.006}$
84%			
$T_y$	$5.395^{+0.030}_{-0.030}$	$0.843^{+0.008}_{-0.007}$	$0.026^{+0.005}_{-0.005}$
$T_m$	$4.535^{+0.017}_{-0.018}$	$0.828^{+0.006}_{-0.006}$	$-0.003^{+0.004}_{-0.004}$
$T_{\text{sl}}$	$4.390^{+0.029}_{-0.033}$	$0.795^{+0.007}_{-0.007}$	$-0.073^{+0.005}_{-0.005}$
16%			
$T_y$	$4.651^{+0.017}_{-0.018}$	$0.891^{+0.004}_{-0.004}$	$0.029^{+0.003}_{-0.003}$
$T_m$	$4.006^{+0.015}_{-0.016}$	$0.851^{+0.004}_{-0.005}$	$-0.004^{+0.003}_{-0.003}$
$T_{\text{sl}}$	$3.627^{+0.027}_{-0.027}$	$0.827^{+0.009}_{-0.008}$	$-0.117^{+0.006}_{-0.005}$
$z = 1.0$ , median			
$T_y$	$5.108^{+0.024}_{-0.024}$	$0.875^{+0.005}_{-0.005}$	$0.020^{+0.003}_{-0.003}$
$T_m$	$4.196^{+0.017}_{-0.016}$	$0.846^{+0.004}_{-0.006}$	$-0.010^{+0.003}_{-0.003}$
$T_{\text{sl}}$	$3.681^{+0.029}_{-0.029}$	$0.807^{+0.015}_{-0.015}$	$-0.118^{+0.009}_{-0.009}$
84%			
$T_y$	$5.481^{+0.034}_{-0.031}$	$0.835^{+0.006}_{-0.006}$	$0.016^{+0.005}_{-0.006}$
$T_m$	$4.457^{+0.020}_{-0.021}$	$0.822^{+0.005}_{-0.006}$	$-0.014^{+0.004}_{-0.004}$
$T_{\text{sl}}$	$4.048^{+0.034}_{-0.034}$	$0.760^{+0.009}_{-0.019}$	$-0.113^{+0.008}_{-0.011}$
16%			
$T_y$	$4.770^{+0.027}_{-0.027}$	$0.906^{+0.008}_{-0.007}$	$0.028^{+0.005}_{-0.005}$
$T_m$	$3.960^{+0.019}_{-0.020}$	$0.869^{+0.006}_{-0.006}$	$-0.006^{+0.004}_{-0.004}$
$T_{\text{sl}}$	$3.316^{+0.026}_{-0.027}$	$0.870^{+0.017}_{-0.012}$	$-0.123^{+0.010}_{-0.008}$

**TABLE A.3:** The fit values for the medians, 84 and 16 percentiles of each temperature measure against  $T_m$  at each redshift. The errors are determined through bootstrap methods. The fit parameters correspond to those described in Eq. (2.3).

$T_{\text{rel}} = T_{m,500c}$	$A$	$B$	$C$
$z = 0.0, \text{ median}$			
$T_y$	$5.650^{+0.015}_{-0.014}$	$1.028^{+0.008}_{-0.008}$	$0.029^{+0.004}_{-0.004}$
$T_{\text{sl}}$	$4.946^{+0.033}_{-0.037}$	$0.927^{+0.029}_{-0.037}$	$-0.095^{+0.014}_{-0.017}$
84%			
$T_y$	$5.946^{+0.024}_{-0.022}$	$1.013^{+0.008}_{-0.008}$	$0.031^{+0.005}_{-0.006}$
$T_{\text{sl}}$	$5.323^{+0.036}_{-0.038}$	$0.944^{+0.012}_{-0.057}$	$-0.065^{+0.009}_{-0.026}$
16%			
$T_y$	$5.356^{+0.016}_{-0.016}$	$1.037^{+0.008}_{-0.008}$	$0.030^{+0.004}_{-0.004}$
$T_{\text{sl}}$	$4.416^{+0.040}_{-0.042}$	$0.904^{+0.054}_{-0.020}$	$-0.138^{+0.026}_{-0.012}$
$z = 0.5, \text{ median}$			
$T_y$	$5.904^{+0.018}_{-0.017}$	$1.035^{+0.007}_{-0.006}$	$0.032^{+0.004}_{-0.004}$
$T_{\text{sl}}$	$4.665^{+0.025}_{-0.025}$	$0.961^{+0.009}_{-0.009}$	$-0.092^{+0.005}_{-0.005}$
84%			
$T_y$	$6.230^{+0.022}_{-0.023}$	$1.036^{+0.007}_{-0.007}$	$0.044^{+0.005}_{-0.005}$
$T_{\text{sl}}$	$4.998^{+0.027}_{-0.028}$	$0.944^{+0.009}_{-0.015}$	$-0.069^{+0.007}_{-0.009}$
16%			
$T_y$	$5.616^{+0.017}_{-0.019}$	$1.040^{+0.007}_{-0.007}$	$0.032^{+0.003}_{-0.003}$
$T_{\text{sl}}$	$4.193^{+0.040}_{-0.045}$	$0.999^{+0.022}_{-0.025}$	$-0.107^{+0.013}_{-0.017}$
$z = 1.0, \text{ median}$			
$T_y$	$6.144^{+0.039}_{-0.033}$	$1.031^{+0.022}_{-0.013}$	$0.029^{+0.011}_{-0.007}$
$T_{\text{sl}}$	$4.351^{+0.041}_{-0.040}$	$0.978^{+0.029}_{-0.025}$	$-0.092^{+0.015}_{-0.013}$
84%			
$T_y$	$6.500^{+0.032}_{-0.033}$	$1.014^{+0.012}_{-0.013}$	$0.028^{+0.006}_{-0.007}$
$T_{\text{sl}}$	$4.682^{+0.035}_{-0.036}$	$0.914^{+0.016}_{-0.022}$	$-0.097^{+0.010}_{-0.012}$
16%			
$T_y$	$5.800^{+0.031}_{-0.031}$	$1.046^{+0.013}_{-0.014}$	$0.034^{+0.007}_{-0.007}$
$T_{\text{sl}}$	$3.928^{+0.051}_{-0.053}$	$1.058^{+0.031}_{-0.031}$	$-0.080^{+0.016}_{-0.016}$

**TABLE A.4:** The fit values for the Hot and Hot, Relaxed Samples against  $M_{500c}$  at each redshift. The fit parameters correspond to those described in Eq. (2.1), with  $C = 0$ .

$M_{500c}$	Hot Sample		Hot, Relaxed Sample	
	$A$	$B$	$A$	$B$
$z = 0.0$ , median				
$T_y$	$4.693^{+0.028}_{-0.028}$	$0.633^{+0.009}_{-0.010}$	$4.635^{+0.035}_{-0.036}$	$0.626^{+0.010}_{-0.010}$
$T_m$	$4.174^{+0.023}_{-0.025}$	$0.598^{+0.019}_{-0.010}$	$4.147^{+0.033}_{-0.034}$	$0.593^{+0.019}_{-0.013}$
$T_{sl}$	$4.117^{+0.064}_{-0.053}$	$0.531^{+0.043}_{-0.055}$	$4.206^{+0.049}_{-0.051}$	$0.531^{+0.051}_{-0.014}$
84%				
$T_y$	$5.157^{+0.035}_{-0.036}$	$0.622^{+0.010}_{-0.010}$	$4.992^{+0.042}_{-0.040}$	$0.647^{+0.010}_{-0.028}$
$T_m$	$4.528^{+0.030}_{-0.027}$	$0.607^{+0.012}_{-0.018}$	$4.433^{+0.035}_{-0.030}$	$0.633^{+0.009}_{-0.034}$
$T_{sl}$	$4.620^{+0.044}_{-0.036}$	$0.559^{+0.012}_{-0.022}$	$4.632^{+0.048}_{-0.044}$	$0.581^{+0.013}_{-0.025}$
16%				
$T_y$	$4.240^{+0.032}_{-0.031}$	$0.646^{+0.011}_{-0.010}$	$4.252^{+0.030}_{-0.029}$	$0.633^{+0.010}_{-0.009}$
$T_m$	$3.802^{+0.023}_{-0.022}$	$0.602^{+0.011}_{-0.012}$	$3.835^{+0.025}_{-0.027}$	$0.600^{+0.010}_{-0.009}$
$T_{sl}$	$3.704^{+0.051}_{-0.056}$	$0.443^{+0.043}_{-0.027}$	$3.839^{+0.069}_{-0.074}$	$0.441^{+0.079}_{-0.048}$
$z = 0.5$ , median				
$T_y$	$4.335^{+0.030}_{-0.027}$	$0.597^{+0.017}_{-0.016}$	$4.329^{+0.040}_{-0.034}$	$0.598^{+0.018}_{-0.016}$
$T_m$	$3.677^{+0.018}_{-0.021}$	$0.561^{+0.011}_{-0.011}$	$3.681^{+0.021}_{-0.024}$	$0.561^{+0.011}_{-0.011}$
$T_{sl}$	$3.433^{+0.034}_{-0.033}$	$0.457^{+0.023}_{-0.099}$	$3.445^{+0.036}_{-0.037}$	$0.455^{+0.025}_{-0.098}$
84%				
$T_y$	$4.701^{+0.042}_{-0.029}$	$0.579^{+0.015}_{-0.017}$	$4.686^{+0.038}_{-0.032}$	$0.581^{+0.017}_{-0.018}$
$T_m$	$3.947^{+0.024}_{-0.023}$	$0.541^{+0.011}_{-0.011}$	$3.926^{+0.032}_{-0.027}$	$0.540^{+0.013}_{-0.012}$
$T_{sl}$	$3.827^{+0.033}_{-0.034}$	$0.446^{+0.016}_{-0.039}$	$3.809^{+0.043}_{-0.043}$	$0.447^{+0.017}_{-0.038}$
16%				
$T_y$	$4.020^{+0.029}_{-0.028}$	$0.621^{+0.015}_{-0.013}$	$4.039^{+0.029}_{-0.031}$	$0.615^{+0.015}_{-0.013}$
$T_m$	$3.417^{+0.019}_{-0.019}$	$0.576^{+0.010}_{-0.010}$	$3.442^{+0.025}_{-0.027}$	$0.570^{+0.012}_{-0.011}$
$T_{sl}$	$3.062^{+0.030}_{-0.037}$	$0.422^{+0.066}_{-0.041}$	$3.073^{+0.035}_{-0.035}$	$0.414^{+0.064}_{-0.041}$
$z = 1.0$ , median				
$T_y$	$3.984^{+0.029}_{-0.030}$	$0.611^{+0.016}_{-0.016}$	$3.974^{+0.035}_{-0.035}$	$0.610^{+0.020}_{-0.018}$
$T_m$	$3.235^{+0.019}_{-0.023}$	$0.586^{+0.008}_{-0.011}$	$3.228^{+0.023}_{-0.024}$	$0.581^{+0.012}_{-0.013}$
$T_{sl}$	$2.745^{+0.036}_{-0.049}$	$0.469^{+0.017}_{-0.037}$	$2.767^{+0.036}_{-0.043}$	$0.473^{+0.017}_{-0.027}$
84%				
$T_y$	$4.262^{+0.044}_{-0.039}$	$0.581^{+0.019}_{-0.022}$	$4.255^{+0.049}_{-0.048}$	$0.580^{+0.019}_{-0.022}$
$T_m$	$3.429^{+0.024}_{-0.025}$	$0.544^{+0.010}_{-0.010}$	$3.423^{+0.028}_{-0.029}$	$0.540^{+0.011}_{-0.011}$
$T_{sl}$	$3.026^{+0.040}_{-0.045}$	$0.416^{+0.018}_{-0.019}$	$3.024^{+0.039}_{-0.041}$	$0.405^{+0.017}_{-0.018}$
16%				
$T_y$	$3.717^{+0.031}_{-0.029}$	$0.644^{+0.022}_{-0.015}$	$3.720^{+0.033}_{-0.033}$	$0.653^{+0.022}_{-0.017}$
$T_m$	$3.027^{+0.041}_{-0.023}$	$0.618^{+0.027}_{-0.013}$	$3.044^{+0.025}_{-0.035}$	$0.628^{+0.014}_{-0.022}$
$T_{sl}$	$2.464^{+0.042}_{-0.031}$	$0.501^{+0.033}_{-0.021}$	$2.510^{+0.038}_{-0.049}$	$0.531^{+0.025}_{-0.038}$

**TABLE A.5:** The fit values for the medians, 84 and 16 percentiles of  $\sigma(T_y)$  at each redshift. The errors are determined through bootstrap methods. The fit parameters correspond to those described in Eq. (2.1), with  $C = 0$ .

$(\sigma(T_y)/T_y)(M_{500c})$	$A$	$B$
$z = 0.0$		
median	$0.386^{+0.002}_{-0.003}$	$0.026^{+0.003}_{-0.004}$
84%	$0.450^{+0.003}_{-0.003}$	$-0.013^{+0.003}_{-0.003}$
16%	$0.332^{+0.003}_{-0.003}$	$0.031^{+0.004}_{-0.004}$
$z = 0.5$		
median	$0.446^{+0.003}_{-0.003}$	$0.022^{+0.003}_{-0.003}$
84%	$0.504^{+0.004}_{-0.003}$	$-0.020^{+0.003}_{-0.003}$
16%	$0.400^{+0.003}_{-0.003}$	$0.042^{+0.004}_{-0.004}$
$z = 1.0$		
median	$0.489^{+0.003}_{-0.003}$	$0.017^{+0.002}_{-0.003}$
84%	$0.519^{+0.005}_{-0.005}$	$-0.040^{+0.005}_{-0.005}$
16%	$0.455^{+0.004}_{-0.004}$	$0.049^{+0.004}_{-0.003}$

## A.4 Profile Fits

Tables A.15 to A.18 display the fit quantities for the radial profiles of the median temperature measures,  $(T/T_{500c})$  and variance,  $\sigma(T_y)/T_{500c}$ . The same quantities for the cylindrical profiles are in tables A.19 to A.22.

These mass bins are organised so that the highest mass bin always corresponds to the MACSIS sample, hence the discrepancy in mass bin sizes.



**TABLE A.6:** The fit values for the medians, 84 and 16 percentiles of each temperature measure at each redshift. The errors are determined through bootstrap methods. The fit parameters correspond to those described in Eq. (2.1).

$M = M_{200c}$	$A$	$B$	$C$
$z = 0.0$ , median			
$T_y$	$3.488^{+0.010}_{-0.009}$	$0.595^{+0.002}_{-0.002}$	$0.016^{+0.001}_{-0.001}$
$T_m$	$2.974^{+0.010}_{-0.009}$	$0.588^{+0.003}_{-0.004}$	$0.008^{+0.001}_{-0.002}$
$T_{sl}$	$3.128^{+0.051}_{-0.023}$	$0.572^{+0.011}_{-0.023}$	$-0.022^{+0.005}_{-0.014}$
84%			
$T_y$	$3.764^{+0.016}_{-0.014}$	$0.585^{+0.003}_{-0.003}$	$0.018^{+0.002}_{-0.001}$
$T_m$	$3.200^{+0.012}_{-0.012}$	$0.587^{+0.003}_{-0.003}$	$0.008^{+0.001}_{-0.002}$
$T_{sl}$	$3.535^{+0.022}_{-0.019}$	$0.583^{+0.008}_{-0.008}$	$-0.018^{+0.004}_{-0.005}$
16%			
$T_y$	$3.247^{+0.010}_{-0.010}$	$0.599^{+0.003}_{-0.003}$	$0.015^{+0.001}_{-0.002}$
$T_m$	$2.760^{+0.011}_{-0.011}$	$0.587^{+0.004}_{-0.004}$	$0.008^{+0.002}_{-0.002}$
$T_{sl}$	$2.743^{+0.028}_{-0.031}$	$0.554^{+0.017}_{-0.012}$	$-0.039^{+0.009}_{-0.006}$
$z = 0.5$ , median			
$T_y$	$3.221^{+0.011}_{-0.010}$	$0.600^{+0.009}_{-0.010}$	$0.010^{+0.004}_{-0.004}$
$T_m$	$2.616^{+0.009}_{-0.009}$	$0.585^{+0.004}_{-0.014}$	$0.000^{+0.002}_{-0.006}$
$T_{sl}$	$2.555^{+0.015}_{-0.015}$	$0.567^{+0.009}_{-0.017}$	$-0.033^{+0.004}_{-0.007}$
84%			
$T_y$	$3.501^{+0.018}_{-0.017}$	$0.593^{+0.006}_{-0.007}$	$0.013^{+0.003}_{-0.003}$
$T_m$	$2.805^{+0.011}_{-0.012}$	$0.585^{+0.005}_{-0.006}$	$0.001^{+0.002}_{-0.002}$
$T_{sl}$	$2.895^{+0.022}_{-0.021}$	$0.565^{+0.007}_{-0.009}$	$-0.029^{+0.003}_{-0.004}$
16%			
$T_y$	$2.975^{+0.011}_{-0.012}$	$0.599^{+0.008}_{-0.006}$	$0.010^{+0.003}_{-0.003}$
$T_m$	$2.413^{+0.011}_{-0.012}$	$0.577^{+0.009}_{-0.007}$	$-0.000^{+0.004}_{-0.003}$
$T_{sl}$	$2.200^{+0.021}_{-0.019}$	$0.565^{+0.014}_{-0.011}$	$-0.039^{+0.005}_{-0.004}$
$z = 1.0$ , median			
$T_y$	$2.962^{+0.019}_{-0.018}$	$0.626^{+0.008}_{-0.009}$	$0.013^{+0.003}_{-0.003}$
$T_m$	$2.286^{+0.013}_{-0.012}$	$0.600^{+0.006}_{-0.007}$	$0.002^{+0.002}_{-0.003}$
$T_{sl}$	$2.056^{+0.020}_{-0.020}$	$0.557^{+0.010}_{-0.029}$	$-0.038^{+0.004}_{-0.011}$
84%			
$T_y$	$3.243^{+0.030}_{-0.028}$	$0.599^{+0.007}_{-0.009}$	$0.006^{+0.003}_{-0.003}$
$T_m$	$2.467^{+0.018}_{-0.017}$	$0.580^{+0.005}_{-0.005}$	$-0.006^{+0.002}_{-0.002}$
$T_{sl}$	$2.302^{+0.022}_{-0.019}$	$0.517^{+0.007}_{-0.008}$	$-0.046^{+0.003}_{-0.003}$
16%			
$T_y$	$2.725^{+0.016}_{-0.016}$	$0.647^{+0.008}_{-0.007}$	$0.020^{+0.003}_{-0.002}$
$T_m$	$2.131^{+0.012}_{-0.013}$	$0.616^{+0.005}_{-0.006}$	$0.007^{+0.002}_{-0.002}$
$T_{sl}$	$1.790^{+0.026}_{-0.028}$	$0.587^{+0.019}_{-0.018}$	$-0.034^{+0.007}_{-0.005}$

**TABLE A.7:** The fit values for the medians, 84 and 16 percentiles of each temperature measure against  $T_{200c}$  at each redshift. The errors are determined through bootstrap methods. The fit parameters correspond to those described in Eq. (2.3).

$T_{\text{rel}} = T_{200c}$	$A$	$B$	$C$
$z = 0.0, \text{ median}$			
$T_y$	$4.650^{+0.013}_{-0.014}$	$0.918^{+0.004}_{-0.006}$	$0.038^{+0.002}_{-0.003}$
$T_m$	$3.946^{+0.010}_{-0.011}$	$0.896^{+0.004}_{-0.003}$	$0.020^{+0.002}_{-0.002}$
$T_{\text{sl}}$	$4.101^{+0.029}_{-0.030}$	$0.846^{+0.010}_{-0.025}$	$-0.041^{+0.005}_{-0.012}$
84%			
$T_y$	$5.014^{+0.025}_{-0.024}$	$0.900^{+0.006}_{-0.004}$	$0.039^{+0.003}_{-0.003}$
$T_m$	$4.243^{+0.016}_{-0.016}$	$0.891^{+0.005}_{-0.006}$	$0.018^{+0.002}_{-0.003}$
$T_{\text{sl}}$	$4.647^{+0.026}_{-0.026}$	$0.850^{+0.017}_{-0.008}$	$-0.038^{+0.008}_{-0.004}$
16%			
$T_y$	$4.329^{+0.015}_{-0.015}$	$0.922^{+0.005}_{-0.007}$	$0.037^{+0.003}_{-0.003}$
$T_m$	$3.666^{+0.016}_{-0.017}$	$0.901^{+0.005}_{-0.010}$	$0.023^{+0.003}_{-0.005}$
$T_{\text{sl}}$	$3.538^{+0.031}_{-0.032}$	$0.819^{+0.014}_{-0.011}$	$-0.062^{+0.007}_{-0.005}$
$z = 0.5, \text{ median}$			
$T_y$	$4.814^{+0.021}_{-0.021}$	$0.915^{+0.016}_{-0.018}$	$0.026^{+0.008}_{-0.010}$
$T_m$	$3.893^{+0.014}_{-0.016}$	$0.886^{+0.008}_{-0.025}$	$0.004^{+0.004}_{-0.013}$
$T_{\text{sl}}$	$3.784^{+0.025}_{-0.028}$	$0.838^{+0.016}_{-0.030}$	$-0.072^{+0.008}_{-0.016}$
84%			
$T_y$	$5.234^{+0.033}_{-0.029}$	$0.907^{+0.011}_{-0.013}$	$0.032^{+0.006}_{-0.007}$
$T_m$	$4.182^{+0.020}_{-0.019}$	$0.886^{+0.008}_{-0.011}$	$0.005^{+0.004}_{-0.006}$
$T_{\text{sl}}$	$4.290^{+0.035}_{-0.034}$	$0.836^{+0.013}_{-0.015}$	$-0.065^{+0.007}_{-0.008}$
16%			
$T_y$	$4.440^{+0.019}_{-0.020}$	$0.912^{+0.015}_{-0.011}$	$0.023^{+0.008}_{-0.005}$
$T_m$	$3.584^{+0.019}_{-0.021}$	$0.873^{+0.017}_{-0.013}$	$0.001^{+0.009}_{-0.006}$
$T_{\text{sl}}$	$3.250^{+0.033}_{-0.030}$	$0.829^{+0.023}_{-0.019}$	$-0.087^{+0.012}_{-0.009}$
$z = 1.0, \text{ median}$			
$T_y$	$4.936^{+0.029}_{-0.029}$	$0.936^{+0.011}_{-0.012}$	$0.028^{+0.006}_{-0.007}$
$T_m$	$3.818^{+0.021}_{-0.019}$	$0.900^{+0.009}_{-0.010}$	$0.003^{+0.005}_{-0.006}$
$T_{\text{sl}}$	$3.449^{+0.030}_{-0.032}$	$0.848^{+0.014}_{-0.041}$	$-0.086^{+0.008}_{-0.024}$
84%			
$T_y$	$5.420^{+0.049}_{-0.047}$	$0.896^{+0.010}_{-0.012}$	$0.013^{+0.006}_{-0.007}$
$T_m$	$4.129^{+0.030}_{-0.028}$	$0.871^{+0.007}_{-0.007}$	$-0.014^{+0.004}_{-0.004}$
$T_{\text{sl}}$	$3.876^{+0.035}_{-0.031}$	$0.790^{+0.010}_{-0.012}$	$-0.105^{+0.006}_{-0.007}$
16%			
$T_y$	$4.527^{+0.027}_{-0.024}$	$0.965^{+0.011}_{-0.009}$	$0.044^{+0.006}_{-0.005}$
$T_m$	$3.550^{+0.020}_{-0.021}$	$0.923^{+0.007}_{-0.008}$	$0.017^{+0.004}_{-0.004}$
$T_{\text{sl}}$	$2.989^{+0.038}_{-0.042}$	$0.892^{+0.025}_{-0.025}$	$-0.077^{+0.016}_{-0.012}$

**TABLE A.8:** The fit values for the medians, 84 and 16 percentiles of each temperature measure against  $T_m$  at each redshift. The errors are determined through bootstrap methods. The fit parameters correspond to those described in Eq. (2.3).

$T_{\text{rel}} = T_{m,200c}$	$A$	$B$	$C$
$z = 0.0$ , median			
$T_y$	$5.936^{+0.017}_{-0.016}$	$1.030^{+0.007}_{-0.005}$	$0.023^{+0.003}_{-0.003}$
$T_{\text{sl}}$	$5.148^{+0.047}_{-0.066}$	$0.935^{+0.017}_{-0.076}$	$-0.072^{+0.008}_{-0.034}$
84%			
$T_y$	$6.275^{+0.025}_{-0.024}$	$1.021^{+0.008}_{-0.008}$	$0.024^{+0.004}_{-0.004}$
$T_{\text{sl}}$	$5.647^{+0.031}_{-0.037}$	$0.927^{+0.013}_{-0.017}$	$-0.063^{+0.006}_{-0.008}$
16%			
$T_y$	$5.632^{+0.018}_{-0.021}$	$1.038^{+0.007}_{-0.009}$	$0.025^{+0.003}_{-0.004}$
$T_{\text{sl}}$	$4.510^{+0.066}_{-0.064}$	$0.868^{+0.047}_{-0.040}$	$-0.120^{+0.022}_{-0.019}$
$z = 0.5$ , median			
$T_y$	$6.257^{+0.020}_{-0.019}$	$1.052^{+0.007}_{-0.007}$	$0.033^{+0.003}_{-0.003}$
$T_{\text{sl}}$	$4.801^{+0.038}_{-0.039}$	$0.942^{+0.016}_{-0.018}$	$-0.073^{+0.008}_{-0.009}$
84%			
$T_y$	$6.623^{+0.031}_{-0.028}$	$1.048^{+0.009}_{-0.008}$	$0.037^{+0.005}_{-0.004}$
$T_{\text{sl}}$	$5.247^{+0.035}_{-0.032}$	$0.925^{+0.013}_{-0.011}$	$-0.067^{+0.007}_{-0.007}$
16%			
$T_y$	$5.953^{+0.027}_{-0.028}$	$1.051^{+0.010}_{-0.011}$	$0.029^{+0.005}_{-0.005}$
$T_{\text{sl}}$	$4.280^{+0.052}_{-0.060}$	$0.929^{+0.026}_{-0.035}$	$-0.099^{+0.012}_{-0.015}$
$z = 1.0$ , median			
$T_y$	$6.546^{+0.029}_{-0.039}$	$1.048^{+0.007}_{-0.013}$	$0.026^{+0.004}_{-0.005}$
$T_{\text{sl}}$	$4.404^{+0.063}_{-0.062}$	$0.901^{+0.029}_{-0.031}$	$-0.100^{+0.013}_{-0.013}$
84%			
$T_y$	$6.921^{+0.043}_{-0.042}$	$1.011^{+0.012}_{-0.013}$	$0.013^{+0.006}_{-0.006}$
$T_{\text{sl}}$	$4.815^{+0.034}_{-0.089}$	$0.855^{+0.012}_{-0.056}$	$-0.109^{+0.006}_{-0.025}$
16%			
$T_y$	$6.207^{+0.038}_{-0.040}$	$1.074^{+0.012}_{-0.012}$	$0.036^{+0.005}_{-0.005}$
$T_{\text{sl}}$	$3.972^{+0.063}_{-0.052}$	$0.960^{+0.048}_{-0.021}$	$-0.087^{+0.021}_{-0.010}$

**TABLE A.9:** The fit values for the Hot and Hot, Relaxed Samples against  $M_{200c}$  at each redshift. The fit parameters correspond to those described in Eq. (2.1), with  $C = 0$ .

$M_{200c}$	Hot Sample		Hot, Relaxed Sample	
	$A$	$B$	$A$	$B$
$z = 0.0$ , median				
$T_y$	$3.406^{+0.028}_{-0.045}$	$0.633^{+0.025}_{-0.010}$	$3.422^{+0.051}_{-0.053}$	$0.633^{+0.013}_{-0.012}$
$T_m$	$2.915^{+0.042}_{-0.041}$	$0.609^{+0.020}_{-0.025}$	$2.976^{+0.037}_{-0.042}$	$0.600^{+0.016}_{-0.013}$
$T_{sl}$	$3.103^{+0.084}_{-0.116}$	$0.515^{+0.067}_{-0.041}$	$3.337^{+0.122}_{-0.104}$	$0.516^{+0.043}_{-0.050}$
84%				
$T_y$	$3.741^{+0.040}_{-0.033}$	$0.644^{+0.010}_{-0.012}$	$3.713^{+0.092}_{-0.067}$	$0.650^{+0.014}_{-0.024}$
$T_m$	$3.174^{+0.036}_{-0.031}$	$0.626^{+0.011}_{-0.015}$	$3.161^{+0.066}_{-0.052}$	$0.636^{+0.013}_{-0.032}$
$T_{sl}$	$3.573^{+0.064}_{-0.054}$	$0.559^{+0.013}_{-0.020}$	$3.593^{+0.077}_{-0.057}$	$0.576^{+0.014}_{-0.024}$
16%				
$T_y$	$3.139^{+0.027}_{-0.027}$	$0.624^{+0.011}_{-0.011}$	$3.129^{+0.042}_{-0.040}$	$0.634^{+0.012}_{-0.016}$
$T_m$	$2.692^{+0.024}_{-0.023}$	$0.587^{+0.011}_{-0.008}$	$2.733^{+0.043}_{-0.036}$	$0.599^{+0.013}_{-0.024}$
$T_{sl}$	$2.761^{+0.061}_{-0.068}$	$0.442^{+0.038}_{-0.032}$	$3.029^{+0.097}_{-0.112}$	$0.434^{+0.053}_{-0.030}$
$z = 0.5$ , median				
$T_y$	$3.182^{+0.028}_{-0.024}$	$0.627^{+0.012}_{-0.020}$	$3.195^{+0.066}_{-0.052}$	$0.624^{+0.018}_{-0.024}$
$T_m$	$2.592^{+0.025}_{-0.024}$	$0.591^{+0.015}_{-0.021}$	$2.629^{+0.038}_{-0.037}$	$0.580^{+0.017}_{-0.021}$
$T_{sl}$	$2.594^{+0.046}_{-0.048}$	$0.491^{+0.031}_{-0.027}$	$2.676^{+0.084}_{-0.065}$	$0.469^{+0.032}_{-0.033}$
84%				
$T_y$	$3.543^{+0.059}_{-0.065}$	$0.603^{+0.020}_{-0.019}$	$3.518^{+0.070}_{-0.067}$	$0.613^{+0.022}_{-0.024}$
$T_m$	$2.831^{+0.025}_{-0.028}$	$0.577^{+0.013}_{-0.012}$	$2.830^{+0.037}_{-0.035}$	$0.576^{+0.018}_{-0.017}$
$T_{sl}$	$2.993^{+0.065}_{-0.048}$	$0.495^{+0.022}_{-0.030}$	$3.112^{+0.086}_{-0.102}$	$0.452^{+0.032}_{-0.031}$
16%				
$T_y$	$2.936^{+0.036}_{-0.037}$	$0.618^{+0.028}_{-0.015}$	$2.939^{+0.051}_{-0.045}$	$0.630^{+0.023}_{-0.024}$
$T_m$	$2.396^{+0.024}_{-0.025}$	$0.578^{+0.023}_{-0.011}$	$2.419^{+0.040}_{-0.039}$	$0.581^{+0.022}_{-0.020}$
$T_{sl}$	$2.236^{+0.045}_{-0.064}$	$0.488^{+0.031}_{-0.025}$	$2.325^{+0.054}_{-0.051}$	$0.455^{+0.029}_{-0.024}$
$z = 1.0$ , median				
$T_y$	$2.964^{+0.029}_{-0.035}$	$0.626^{+0.019}_{-0.023}$	$2.944^{+0.031}_{-0.032}$	$0.636^{+0.020}_{-0.024}$
$T_m$	$2.275^{+0.019}_{-0.018}$	$0.606^{+0.014}_{-0.016}$	$2.259^{+0.023}_{-0.020}$	$0.614^{+0.015}_{-0.017}$
$T_{sl}$	$2.079^{+0.030}_{-0.038}$	$0.515^{+0.033}_{-0.039}$	$2.069^{+0.038}_{-0.048}$	$0.508^{+0.038}_{-0.040}$
84%				
$T_y$	$3.308^{+0.051}_{-0.045}$	$0.603^{+0.022}_{-0.021}$	$3.235^{+0.047}_{-0.043}$	$0.625^{+0.019}_{-0.020}$
$T_m$	$2.512^{+0.022}_{-0.022}$	$0.577^{+0.013}_{-0.014}$	$2.475^{+0.025}_{-0.026}$	$0.587^{+0.014}_{-0.015}$
$T_{sl}$	$2.368^{+0.035}_{-0.032}$	$0.468^{+0.020}_{-0.025}$	$2.366^{+0.047}_{-0.038}$	$0.465^{+0.023}_{-0.033}$
16%				
$T_y$	$2.681^{+0.029}_{-0.040}$	$0.656^{+0.026}_{-0.024}$	$2.704^{+0.031}_{-0.042}$	$0.647^{+0.028}_{-0.026}$
$T_m$	$2.079^{+0.024}_{-0.024}$	$0.633^{+0.020}_{-0.021}$	$2.101^{+0.021}_{-0.024}$	$0.627^{+0.021}_{-0.022}$
$T_{sl}$	$1.765^{+0.037}_{-0.033}$	$0.581^{+0.036}_{-0.036}$	$1.793^{+0.046}_{-0.045}$	$0.556^{+0.040}_{-0.038}$

**TABLE A.10:** The fit values for the medians, 84 and 16 percentiles of  $\sigma(T_y)$  at each redshift. The errors are determined through bootstrap methods. The fit parameters correspond to those described in Eq. (2.1), with  $C = 0$ .

$(\sigma(T_y)/T_y)(M_{200c})$	$A$	$B$
$z = 0.0$		
median	$0.437^{+0.002}_{-0.002}$	$0.008^{+0.004}_{-0.002}$
84%	$0.508^{+0.003}_{-0.003}$	$-0.023^{+0.003}_{-0.003}$
16%	$0.388^{+0.002}_{-0.003}$	$0.016^{+0.003}_{-0.004}$
$z = 0.5$		
median	$0.496^{+0.003}_{-0.003}$	$0.011^{+0.004}_{-0.003}$
84%	$0.560^{+0.004}_{-0.004}$	$-0.026^{+0.004}_{-0.004}$
16%	$0.451^{+0.002}_{-0.002}$	$0.028^{+0.003}_{-0.003}$
$z = 1.0$		
median	$0.535^{+0.003}_{-0.003}$	$0.007^{+0.003}_{-0.003}$
84%	$0.579^{+0.003}_{-0.003}$	$-0.044^{+0.003}_{-0.003}$
16%	$0.498^{+0.003}_{-0.002}$	$0.035^{+0.003}_{-0.002}$

**TABLE A.11:** The fit values for the medians, 84 and 16 percentiles of  $T^y$  to  $Y_{500c}$  at each redshift. The errors are determined through bootstrap methods. The fit parameters correspond to those described in Eq. (2.4). This is a replica of Table 2.6 found in Section 2.3.6.

$T^y - Y_{500c}$	$A$	$B$	$C$
$z = 0.0$			
median	$4.784^{+0.022}_{-0.019}$	$0.3363^{+0.0026}_{-0.0031}$	$0.0118^{+0.0005}_{-0.0006}$
84	$5.203^{+0.026}_{-0.024}$	$0.3276^{+0.0017}_{-0.0020}$	$0.0120^{+0.0005}_{-0.0005}$
16	$4.415^{+0.047}_{-0.024}$	$0.3438^{+0.0026}_{-0.0030}$	$0.0120^{+0.0007}_{-0.0015}$
$z = 0.5$			
median	$5.370^{+0.020}_{-0.020}$	$0.3358^{+0.0017}_{-0.0010}$	$0.0106^{+0.0003}_{-0.0002}$
84	$5.860^{+0.027}_{-0.028}$	$0.3218^{+0.0015}_{-0.0016}$	$0.0090^{+0.0003}_{-0.0003}$
16	$4.954^{+0.016}_{-0.016}$	$0.3508^{+0.0009}_{-0.0008}$	$0.0128^{+0.0002}_{-0.0002}$
$z = 1.0$			
median	$6.250^{+0.042}_{-0.038}$	$0.3429^{+0.0044}_{-0.0037}$	$0.0090^{+0.0009}_{-0.0007}$
84	$6.656^{+0.053}_{-0.062}$	$0.3329^{+0.0071}_{-0.0058}$	$0.0096^{+0.0015}_{-0.0011}$
16	$5.784^{+0.042}_{-0.040}$	$0.3579^{+0.0051}_{-0.0048}$	$0.0107^{+0.0009}_{-0.0008}$

**TABLE A.12:** The fit values for the medians, 84 and 16 percentiles of  $T^Y$  to  $Y_{200c}$  at each redshift. The errors are determined through bootstrap methods. The fit parameters correspond to those described in Eq. (2.4).

$T^Y - Y_{200c}$	$A$	$B$	$C$
$z = 0.0$			
median	$3.856^{+0.013}_{-0.013}$	$0.3490^{+0.0022}_{-0.0029}$	$0.0128^{+0.0005}_{-0.0006}$
84	$4.175^{+0.027}_{-0.031}$	$0.3429^{+0.0019}_{-0.0021}$	$0.0131^{+0.0010}_{-0.0008}$
16	$3.580^{+0.035}_{-0.019}$	$0.3544^{+0.0022}_{-0.0021}$	$0.0130^{+0.0007}_{-0.0013}$
$z = 0.5$			
median	$4.320^{+0.057}_{-0.045}$	$0.3605^{+0.0020}_{-0.0023}$	$0.0145^{+0.0016}_{-0.0020}$
84	$4.694^{+0.092}_{-0.027}$	$0.3481^{+0.0016}_{-0.0033}$	$0.0136^{+0.0005}_{-0.0031}$
16	$4.015^{+0.018}_{-0.078}$	$0.3701^{+0.0035}_{-0.0010}$	$0.0152^{+0.0030}_{-0.0006}$
$z = 1.0$			
median	$5.129^{+0.032}_{-0.028}$	$0.3698^{+0.0035}_{-0.0029}$	$0.0112^{+0.0008}_{-0.0007}$
84	$5.608^{+0.056}_{-0.053}$	$0.3597^{+0.0057}_{-0.0057}$	$0.0106^{+0.0015}_{-0.0014}$
16	$4.765^{+0.026}_{-0.026}$	$0.3820^{+0.0037}_{-0.0038}$	$0.0125^{+0.0009}_{-0.0009}$

**TABLE A.13:** The fit values for the medians, 84 and 16 percentiles of  $Y_{500}$  to  $M_{500c}$  at each redshift. The errors are determined through bootstrap methods. The fit parameters correspond to those described in Eq. (2.1), with  $Y$  in the place of  $E(z)^{-2/3}T$ .

$Y - M_{500c}$	$A [\times 10^{-5}]$	$B$	$C$
$z = 0.0$			
median	$2.850^{+0.017}_{-0.017}$	$1.783^{+0.005}_{-0.003}$	$-0.0860^{+0.0021}_{-0.0017}$
84	$3.281^{+0.021}_{-0.019}$	$1.757^{+0.004}_{-0.013}$	$-0.0762^{+0.0019}_{-0.0050}$
16	$2.466^{+0.017}_{-0.017}$	$1.823^{+0.005}_{-0.005}$	$-0.0920^{+0.0020}_{-0.0019}$
$z = 0.5$			
median	$2.813^{+0.021}_{-0.019}$	$1.731^{+0.003}_{-0.003}$	$-0.0688^{+0.0014}_{-0.0015}$
84	$3.227^{+0.025}_{-0.024}$	$1.681^{+0.004}_{-0.004}$	$-0.0724^{+0.0017}_{-0.0018}$
16	$2.476^{+0.017}_{-0.019}$	$1.776^{+0.003}_{-0.003}$	$-0.0693^{+0.0017}_{-0.0015}$
$z = 1.0$			
median	$2.753^{+0.035}_{-0.037}$	$1.652^{+0.019}_{-0.028}$	$-0.0792^{+0.0063}_{-0.0087}$
84	$3.135^{+0.034}_{-0.038}$	$1.597^{+0.011}_{-0.018}$	$-0.0828^{+0.0041}_{-0.0057}$
16	$2.431^{+0.027}_{-0.025}$	$1.697^{+0.019}_{-0.011}$	$-0.0796^{+0.0062}_{-0.0045}$

**TABLE A.14:** The fit values for the medians, 84 and 16 percentiles of  $Y_{200}$  to  $M_{200c}$  at each redshift. The errors are determined through bootstrap methods. The fit parameters correspond to those described in Eq. (2.1), with  $Y$  in the place of  $E(z)^{-2/3}T$ .

$Y - M_{200c}$	$A [\times 10^{-5}]$	$B$	$C$
$z = 0.0$			
median	$2.024^{+0.010}_{-0.010}$	$1.789^{+0.003}_{-0.003}$	$-0.0608^{+0.0016}_{-0.0016}$
84	$2.357^{+0.015}_{-0.015}$	$1.754^{+0.004}_{-0.003}$	$-0.0571^{+0.0021}_{-0.0020}$
16	$1.748^{+0.011}_{-0.012}$	$1.822^{+0.004}_{-0.006}$	$-0.0665^{+0.0022}_{-0.0028}$
$z = 0.5$			
median	$2.035^{+0.014}_{-0.015}$	$1.739^{+0.003}_{-0.004}$	$-0.0506^{+0.0016}_{-0.0016}$
84	$2.381^{+0.016}_{-0.015}$	$1.703^{+0.003}_{-0.003}$	$-0.0552^{+0.0014}_{-0.0014}$
16	$1.742^{+0.015}_{-0.015}$	$1.777^{+0.003}_{-0.002}$	$-0.0471^{+0.0019}_{-0.0019}$
$z = 1.0$			
median	$2.025^{+0.021}_{-0.020}$	$1.705^{+0.013}_{-0.020}$	$-0.0511^{+0.0047}_{-0.0077}$
84	$2.375^{+0.021}_{-0.023}$	$1.645^{+0.007}_{-0.010}$	$-0.0655^{+0.0037}_{-0.0041}$
16	$1.770^{+0.017}_{-0.018}$	$1.741^{+0.014}_{-0.009}$	$-0.0508^{+0.0053}_{-0.0039}$

**TABLE A. 15:** The fit values for the medians of the radial temperature profiles,  $T/T_{500}$ , at  $z = 0$ . The errors are determined through bootstrap methods – errors written as 0.00, correspond to very small values,  $< 10^{-9}$ . The fit parameters correspond to those described in Eq. (2.5).  $m_{500} = M_{500}/M_{\odot}$ .

$z = 0$	$T_0$	$r_t$	$a$	$b$	$c$	$r_{\text{cool}}$	$a_{\text{cool}}$	$T_{\text{min}}$
$\log_{10} m_{500} < 13.5$								
$T_y$	$2.44^{+0.89}_{-0.88}$	$0.26^{+0.28}_{-0.11}$	$0.27^{+0.31}_{-0.37}$	$5.00^{+0.00}_{-1.37}$	$0.33^{+0.39}_{-0.33}$	$0.193^{+0.023}_{-0.055}$	$2.52^{+0.48}_{-0.231}$	$0.49^{+0.29}_{-0.12}$
$T_y$	$1.29^{+2.20}_{-0.09}$	$0.69^{+0.08}_{-0.49}$	$0.32^{+0.12}_{-0.28}$	$5.00^{+0.00}_{-1.13}$	$0.42^{+0.32}_{-0.11}$	$0.161^{+0.112}_{-0.015}$	$2.92^{+0.08}_{-0.875}$	$0.39^{+0.29}_{-0.14}$
$T_{\text{sl}}$	$1.07^{+1.13}_{-0.19}$	$1.00^{+0.17}_{-0.23}$	$0.33^{+0.12}_{-0.31}$	$2.33^{+1.01}_{-1.15}$	$0.73^{+0.51}_{-0.16}$	$0.159^{+0.014}_{-0.015}$	$3.00^{+0.00}_{-0.239}$	$0.33^{+0.46}_{-0.11}$
$13.5 < \log_{10} m_{500} < 14.0$								
$T_y$	$1.41^{+0.17}_{-0.05}$	$0.50^{+0.04}_{-0.08}$	$0.32^{+0.05}_{-0.15}$	$5.00^{+0.00}_{-1.40}$	$0.28^{+0.15}_{-0.05}$	$0.103^{+0.008}_{-0.022}$	$2.22^{+0.35}_{-0.20}$	$0.32^{+0.11}_{-0.11}$
$T_y$	$1.11^{+0.72}_{-0.08}$	$0.76^{+0.07}_{-0.34}$	$0.56^{+0.09}_{-0.65}$	$5.00^{+0.00}_{-3.01}$	$0.24^{+0.67}_{-0.07}$	$0.152^{+0.027}_{-0.071}$	$1.69^{+1.31}_{-0.19}$	$0.05^{+0.27}_{-0.05}$
$T_{\text{sl}}$	$0.43^{+0.04}_{-0.04}$	$2.23^{+0.89}_{-0.19}$	$0.89^{+0.04}_{-0.23}$	$4.09^{+0.91}_{-3.03}$	$0.55^{+1.13}_{-0.08}$	$0.278^{+0.027}_{-0.065}$	$1.49^{+0.06}_{-0.04}$	$0.000^{+0.005}_{-0.000}$
$14.0 < \log_{10} m_{500} < 14.5$								
$T_y$	$0.77^{+3.07}_{-0.06}$	$1.23^{+0.23}_{-1.14}$	$0.45^{+0.03}_{-0.19}$	$5.00^{+0.00}_{-4.00}$	$0.11^{+1.22}_{-0.03}$	$0.115^{+0.030}_{-0.006}$	$1.73^{+1.27}_{-0.20}$	$0.11^{+2.80}_{-0.06}$
$T_y$	$0.53^{+0.04}_{-0.05}$	$2.07^{+0.47}_{-0.26}$	$0.56^{+0.04}_{-0.05}$	$3.27^{+1.04}_{-0.98}$	$0.43^{+0.17}_{-0.08}$	$0.145^{+0.013}_{-0.011}$	$1.60^{+0.14}_{-0.12}$	$0.042^{+0.026}_{-0.021}$
$T_{\text{sl}}$	$0.446^{+0.018}_{-0.021}$	$2.22^{+0.17}_{-0.14}$	$0.61^{+0.05}_{-0.06}$	$3.27^{+0.49}_{-0.53}$	$1.33^{+0.20}_{-0.18}$	$0.168^{+0.024}_{-0.014}$	$1.67^{+0.16}_{-0.12}$	$0.033^{+0.024}_{-0.015}$
$14.5 < \log_{10} m_{500} < 14.78$								
$T_y$	$0.72^{+0.02}_{-0.02}$	$1.36^{+0.11}_{-0.11}$	$0.29^{+0.03}_{-0.02}$	$5.00^{+0.00}_{-0.99}$	$0.33^{+0.04}_{-0.04}$	$0.099^{+0.008}_{-0.009}$	$2.72^{+0.28}_{-0.44}$	$0.26^{+0.05}_{-0.07}$
$T_y$	$0.61^{+0.03}_{-0.05}$	$1.56^{+0.26}_{-0.18}$	$0.35^{+0.04}_{-0.05}$	$3.58^{+1.42}_{-0.96}$	$0.70^{+0.15}_{-0.09}$	$0.110^{+0.009}_{-0.008}$	$2.55^{+0.42}_{-0.46}$	$0.18^{+0.05}_{-0.06}$
$T_{\text{sl}}$	$0.54^{+0.03}_{-0.41}$	$1.66^{+0.16}_{-1.47}$	$0.37^{+0.04}_{-0.82}$	$3.71^{+1.17}_{-0.64}$	$1.62^{+0.23}_{-0.73}$	$0.123^{+1.840}_{-0.006}$	$2.72^{+0.28}_{-0.31}$	$0.15^{+0.99}_{-0.04}$
$14.78 < \log_{10} m_{500}$								
$T_y$	$0.79^{+0.61}_{-0.03}$	$1.23^{+0.21}_{-0.51}$	$0.14^{+0.03}_{-0.11}$	$2.82^{+1.07}_{-0.99}$	$0.68^{+1.98}_{-0.16}$	$0.059^{+0.015}_{-0.008}$	$2.84^{+0.16}_{-0.91}$	$0.33^{+3.47}_{-0.20}$
$T_y$	$6.62^{+0.83}_{-5.93}$	$1.68^{+1.91}_{-0.36}$	$-1.39^{+1.51}_{-0.11}$	$1.00^{+0.34}_{-0.00}$	$3.91^{+0.40}_{-0.64}$	$0.075^{+0.011}_{-0.011}$	$1.76^{+1.24}_{-0.09}$	$124^{+71}_{-124}$
$T_{\text{sl}}$	$0.51^{+0.02}_{-0.02}$	$1.34^{+0.05}_{-0.05}$	$0.36^{+0.04}_{-0.04}$	$4.00^{+0.45}_{-0.43}$	$1.66^{+0.10}_{-0.11}$	$0.079^{+0.006}_{-0.004}$	$2.11^{+0.31}_{-0.17}$	$0.00^{+0.03}_{-0.00}$



**TABLE A. 16:** The fit values for the medians of the radial temperature profiles,  $T/T_{500}$ , at  $z = 0.5$ . The errors are determined through bootstrap methods – errors written as 0.00, correspond to very small values,  $< 10^{-9}$ . The fit parameters correspond to those described in Eq. (2.5).

$z = 0.5$	$T_0$	$r_t$	$a$	$b$	$c$	$r_{\text{cool}}$	$a_{\text{cool}}$	$T_{\text{min}}$
$\log_{10} m_{500} < 13.5$								
$T_y$	$1.53^{+0.20}_{-0.07}$	$0.51^{+0.05}_{-0.10}$	$0.23^{+0.09}_{-0.19}$	$5.00^{+0.00}_{-1.48}$	$0.38^{+0.18}_{-0.09}$	$0.115^{+0.013}_{-0.022}$	$2.80^{+0.20}_{-0.53}$	$0.49^{+0.19}_{-0.18}$
$T_y$	$1.34^{+0.49}_{-0.23}$	$0.65^{+0.19}_{-0.19}$	$0.26^{+0.33}_{-0.35}$	$3.19^{+1.81}_{-1.04}$	$0.53^{+0.37}_{-0.32}$	$0.126^{+0.050}_{-0.031}$	$2.59^{+0.41}_{-0.80}$	$0.29^{+0.50}_{-0.24}$
$T_{\text{sl}}$	$0.62^{+0.96}_{-0.12}$	$1.83^{+0.40}_{-0.78}$	$0.57^{+0.25}_{-0.47}$	$1.77^{+3.23}_{-0.77}$	$0.92^{+0.62}_{-0.52}$	$0.184^{+0.072}_{-0.064}$	$1.71^{+0.99}_{-0.16}$	$0.014^{+0.391}_{-0.014}$
$13.5 < \log_{10} m_{500} < 14.0$								
$T_y$	$1.28^{+0.08}_{-0.05}$	$0.50^{+0.04}_{-0.06}$	$0.33^{+0.05}_{-0.07}$	$5.00^{+0.00}_{-0.91}$	$0.24^{+0.07}_{-0.05}$	$0.103^{+0.006}_{-0.008}$	$2.37^{+0.37}_{-0.23}$	$0.40^{+0.13}_{-0.09}$
$T_y$	$0.86^{+0.09}_{-0.05}$	$0.99^{+0.10}_{-0.12}$	$0.61^{+0.07}_{-0.13}$	$4.84^{+0.16}_{-1.72}$	$0.22^{+0.13}_{-0.05}$	$0.155^{+0.021}_{-0.023}$	$1.70^{+0.29}_{-0.16}$	$0.07^{+0.10}_{-0.04}$
$T_{\text{sl}}$	$0.46^{+0.02}_{-0.02}$	$1.96^{+0.13}_{-0.10}$	$0.84^{+0.04}_{-0.07}$	$4.19^{+0.81}_{-0.90}$	$0.69^{+0.13}_{-0.07}$	$0.249^{+0.024}_{-0.034}$	$1.50^{+0.09}_{-0.04}$	$0.003^{+0.010}_{-0.003}$
$14.0 < \log_{10} m_{500} < 14.55$								
$T_y$	$0.70^{+0.02}_{-0.03}$	$1.51^{+0.13}_{-0.11}$	$0.40^{+0.02}_{-0.02}$	$5.00^{+0.00}_{-0.00}$	$0.18^{+0.03}_{-0.03}$	$0.106^{+0.005}_{-0.006}$	$1.84^{+0.16}_{-0.17}$	$0.14^{+0.04}_{-0.04}$
$T_y$	$0.55^{+0.03}_{-0.03}$	$1.84^{+0.19}_{-0.16}$	$0.51^{+0.03}_{-0.04}$	$4.33^{+0.67}_{-1.19}$	$0.46^{+0.12}_{-0.05}$	$0.137^{+0.010}_{-0.008}$	$1.72^{+0.16}_{-0.14}$	$0.06^{+0.03}_{-0.03}$
$T_{\text{sl}}$	$0.47^{+0.02}_{-0.04}$	$2.07^{+0.15}_{-0.19}$	$0.55^{+0.06}_{-0.14}$	$3.46^{+0.64}_{-0.66}$	$1.40^{+0.21}_{-0.24}$	$0.155^{+0.051}_{-0.013}$	$1.83^{+0.45}_{-0.19}$	$0.05^{+0.07}_{-0.02}$
$14.55 < \log_{10} m_{500}$								
$T_y$	$1.00^{+1.18}_{-0.17}$	$0.80^{+0.37}_{-0.42}$	$-0.27^{+0.42}_{-0.45}$	$1.95^{+1.20}_{-0.95}$	$0.89^{+0.49}_{-0.42}$	$0.094^{+0.113}_{-0.033}$	$3.00^{+0.00}_{-1.36}$	$1.64^{+3.16}_{-1.19}$
$T_y$	$0.64^{+0.07}_{-0.09}$	$1.61^{+0.21}_{-0.16}$	$0.24^{+0.12}_{-0.06}$	$2.30^{+0.69}_{-0.44}$	$1.22^{+0.27}_{-0.20}$	$0.079^{+0.009}_{-0.013}$	$2.44^{+0.56}_{-0.84}$	$0.23^{+0.08}_{-0.23}$
$T_{\text{sl}}$	$0.57^{+0.02}_{-0.45}$	$0.95^{+0.04}_{-0.80}$	$0.38^{+0.04}_{-1.01}$	$5.00^{+0.04}_{-0.44}$	$1.26^{+1.00}_{-0.18}$	$0.103^{+1.190}_{-0.007}$	$2.40^{+0.60}_{-0.37}$	$0.09^{+0.92}_{-0.06}$

**TABLE A. 17:** The fit values for the medians of the radial temperature profiles,  $T/T_{500}$ , at  $z = 1$ . The errors are determined through bootstrap methods – errors written as 0.00, correspond to very small values,  $< 10^{-9}$ . The fit parameters correspond to those described in Eq. (2.5).

$z = 1$	$T_0$	$r_t$	$a$	$b$	$c$	$r_{\text{cool}}$	$d_{\text{cool}}$	$T_{\text{min}}$
$\log_{10} m_{500} < 13.5$								
$T_y$	$1.36^{+0.18}_{-0.06}$	$0.53^{+0.05}_{-0.10}$	$0.36^{+0.06}_{-0.14}$	$5.00^{+0.00}_{-1.34}$	$0.24^{+0.14}_{-0.05}$	$0.112^{+0.008}_{-0.016}$	$2.30^{+0.47}_{-0.23}$	$0.33^{+0.14}_{-0.11}$
$T_y$	$1.07^{+0.62}_{-0.14}$	$0.80^{+0.16}_{-0.33}$	$0.51^{+0.16}_{-0.49}$	$3.73^{+1.27}_{-1.75}$	$0.30^{+0.51}_{-0.15}$	$0.144^{+0.040}_{-0.045}$	$1.90^{+1.10}_{-0.33}$	$0.11^{+0.69}_{-0.08}$
$T_{\text{sl}}$	$0.44^{+0.03}_{-0.04}$	$2.18^{+0.34}_{-0.16}$	$0.84^{+0.05}_{-0.11}$	$4.88^{+0.12}_{-2.25}$	$0.59^{+0.32}_{-0.07}$	$0.252^{+0.028}_{-0.046}$	$1.53^{+0.12}_{-0.05}$	$0.004^{+0.014}_{-0.004}$
$13.5 < \log_{10} m_{500} < 14.0$								
$T_y$	$0.86^{+1.31}_{-0.06}$	$0.91^{+0.13}_{-0.73}$	$0.45^{+0.03}_{-0.93}$	$5.00^{+0.00}_{-2.90}$	$0.11^{+0.83}_{-0.03}$	$0.115^{+0.140}_{-0.006}$	$1.95^{+1.05}_{-0.24}$	$0.18^{+2.80}_{-0.06}$
$T_y$	$0.59^{+0.04}_{-0.04}$	$1.59^{+0.19}_{-0.14}$	$0.57^{+0.04}_{-0.05}$	$3.34^{+1.00}_{-0.84}$	$0.41^{+0.11}_{-0.06}$	$0.138^{+0.010}_{-0.010}$	$1.73^{+0.14}_{-0.13}$	$0.06^{+0.03}_{-0.03}$
$T_{\text{sl}}$	$0.47^{+0.02}_{-0.14}$	$1.84^{+0.09}_{-1.61}$	$0.61^{+0.07}_{-0.95}$	$3.29^{+0.52}_{-0.57}$	$1.20^{+0.16}_{-0.19}$	$0.162^{+2.000}_{-0.016}$	$1.81^{+0.35}_{-0.17}$	$0.05^{+1.37}_{-0.02}$
$14.0 < \log_{10} m_{500} < 14.3$								
$T_y$	$0.62^{+0.04}_{-0.04}$	$2.26^{+0.34}_{-0.35}$	$0.33^{+0.03}_{-0.03}$	$5.00^{+0.00}_{-0.48}$	$0.36^{+0.09}_{-0.07}$	$0.104^{+0.010}_{-0.013}$	$2.14^{+0.38}_{-0.40}$	$0.18^{+0.06}_{-0.08}$
$T_y$	$0.53^{+0.04}_{-0.05}$	$2.18^{+0.46}_{-0.27}$	$0.41^{+0.05}_{-0.07}$	$4.03^{+0.97}_{-1.44}$	$0.73^{+0.29}_{-0.12}$	$0.120^{+0.012}_{-0.010}$	$2.08^{+0.39}_{-0.38}$	$0.11^{+0.06}_{-0.05}$
$T_{\text{sl}}$	$0.49^{+0.03}_{-0.30}$	$1.78^{+0.14}_{-1.57}$	$0.46^{+0.07}_{-0.88}$	$4.44^{+0.56}_{-1.04}$	$1.30^{+0.20}_{-0.40}$	$0.140^{+2.160}_{-0.013}$	$2.21^{+0.79}_{-0.36}$	$0.09^{+1.12}_{-0.04}$
$14.3 < \log_{10} m_{500}$								
$T_y$	$0.11^{+0.14}_{-0.11}$	$3.46^{+0.57}_{-0.48}$	$-0.17^{+0.10}_{-0.14}$	$5.00^{+0.00}_{-0.27}$	$0.86^{+0.41}_{-0.26}$	$0.513^{+0.245}_{-0.237}$	$1.08^{+0.23}_{-0.10}$	$2.52^{+2.28}_{-0.89}$
$T_y$	$0.52^{+0.08}_{-0.04}$	$1.43^{+0.12}_{-0.16}$	$0.64^{+0.11}_{-0.25}$	$4.55^{+0.45}_{-1.77}$	$0.78^{+0.27}_{-0.11}$	$0.167^{+0.070}_{-0.060}$	$1.32^{+0.61}_{-0.07}$	$0.00^{+0.12}_{-0.00}$
$T_{\text{sl}}$	$0.61^{+0.02}_{-0.54}$	$0.79^{+0.03}_{-0.65}$	$0.35^{+0.05}_{-1.08}$	$5.00^{+0.00}_{-0.00}$	$1.41^{+0.05}_{-0.36}$	$0.103^{+0.912}_{-0.008}$	$2.63^{+0.37}_{-0.37}$	$0.12^{+0.86}_{-0.06}$

**TABLE A.18:** The fit values for the medians of the radial profiles of  $\sigma(T_y)/T_{500}$  across all redshifts. The errors are determined through bootstrap methods – errors written as 0.00, correspond to very small values,  $< 10^{-9}$ . The fit parameters correspond to those described in Eq. (2.5).

$\sigma(T_y)$	$T_0$	$r_t$	$a$	$b$	$c$	$r_{\text{cool}}$	$a_{\text{cool}}$	$T_{\text{min}}$
$z = 0$								
$\log_{10} m_{500} < 13.5$	$0.401^{+0.016}_{-0.386}$	$0.186^{+0.018}_{-0.010}$	$-3.00^{+0.00}_{-0.00}$	$5.00^{+0.00}_{-0.00}$	$3.06^{+0.02}_{-0.94}$	$0.118^{+0.300}_{-0.010}$	$3.00^{+0.00}_{-1.33}$	$0.00^{+0.47}_{-0.00}$
$13.5 < \log_{10} m_{500} < 14.0$	$0.046^{+0.029}_{-0.012}$	$0.093^{+0.004}_{-0.003}$	$-3.00^{+0.00}_{-0.00}$	$5.00^{+0.00}_{-0.00}$	$2.58^{+0.12}_{-0.06}$	$0.30^{+0.10}_{-0.042}$	$1.27^{+0.10}_{-0.04}$	$0.418^{+0.023}_{-0.020}$
$14.0 < \log_{10} m_{500} < 14.5$	$0.286^{+0.025}_{-0.012}$	$1.04^{+0.07}_{-0.14}$	$-1.58^{+0.26}_{-0.21}$	$3.83^{+0.73}_{-0.34}$	$1.62^{+0.20}_{-0.21}$	$0.075^{+0.022}_{-0.009}$	$2.23^{+0.25}_{-0.10}$	$36.7^{+41.8}_{-24.8}$
$14.5 < \log_{10} m_{500} < 14.78$	$0.374^{+0.056}_{-0.022}$	$1.09^{+0.12}_{-0.98}$	$-0.61^{+0.13}_{-0.17}$	$4.37^{+0.63}_{-1.62}$	$0.87^{+0.18}_{-0.15}$	$0.16^{+0.60}_{-0.03}$	$2.67^{+0.33}_{-0.47}$	$1.40^{+1.12}_{-1.06}$
$14.78 < \log_{10} m_{500}$	$1.40^{+0.25}_{-0.23}$	$1.85^{+2.52}_{-0.86}$	$-0.86^{+0.57}_{-0.26}$	$1.00^{+0.17}_{-0.00}$	$2.07^{+1.02}_{-0.16}$	$0.0023^{+0.0100}_{-0.0007}$	$1.27^{+0.67}_{-0.12}$	$231^{+727}_{-226}$
$z = 0.5$								
$\log_{10} m_{500} < 13.5$	$0.021^{+0.025}_{-0.010}$	$0.116^{+0.008}_{-0.007}$	$-3.00^{+0.00}_{-0.00}$	$5.00^{+0.00}_{-0.00}$	$2.36^{+0.17}_{-0.14}$	$0.36^{+0.13}_{-0.07}$	$1.51^{+0.11}_{-0.04}$	$0.37^{+0.06}_{-0.03}$
$13.5 < \log_{10} m_{500} < 14.0$	$0.025^{+0.026}_{-0.025}$	$0.060^{+0.018}_{-0.005}$	$-3.00^{+0.00}_{-0.00}$	$3.15^{+1.02}_{-0.49}$	$2.54^{+0.29}_{-0.95}$	$0.05^{+0.19}_{-0.03}$	$0.90^{+1.54}_{-0.13}$	$0.83^{+3.97}_{-0.40}$
$14.0 < \log_{10} m_{500} < 14.55$	$0.341^{+0.240}_{-0.020}$	$1.02^{+0.08}_{-0.93}$	$-1.10^{+0.20}_{-0.17}$	$3.38^{+1.39}_{-0.53}$	$1.26^{+0.16}_{-0.17}$	$0.103^{+0.751}_{-0.018}$	$2.12^{+0.76}_{-0.09}$	$7.33^{+6.62}_{-6.98}$
$14.55 < \log_{10} m_{500}$	$0.73^{+0.19}_{-0.12}$	$22.5^{+5.3}_{-4.2}$	$-0.16^{+0.04}_{-0.05}$	$1.44^{+0.23}_{-0.18}$	$10.0^{+0.0}_{-0.0}$	$0.024^{+0.007}_{-0.004}$	$1.86^{+0.38}_{-0.24}$	$1.50^{+0.82}_{-0.47}$
$z = 1$								
$\log_{10} m_{500} < 13.5$	$0.030^{+0.706}_{-0.019}$	$0.088^{+0.004}_{-0.004}$	$-3.00^{+0.00}_{-0.00}$	$5.00^{+0.00}_{-0.11}$	$2.51^{+0.18}_{-0.20}$	$0.23^{+0.67}_{-0.08}$	$1.21^{+1.06}_{-0.05}$	$0.44^{+0.05}_{-0.03}$
$13.5 < \log_{10} m_{500} < 14.0$	$0.268^{+0.026}_{-0.009}$	$0.96^{+0.05}_{-0.12}$	$-1.36^{+0.23}_{-0.20}$	$4.35^{+0.65}_{-0.40}$	$1.38^{+0.19}_{-0.17}$	$0.087^{+0.037}_{-0.012}$	$2.13^{+0.14}_{-0.07}$	$15.9^{+15.3}_{-11.2}$
$14.0 < \log_{10} m_{500} < 14.3$	$0.60^{+0.39}_{-0.14}$	$1.08^{+0.24}_{-0.31}$	$-1.02^{+0.23}_{-0.29}$	$1.76^{+0.96}_{-0.55}$	$1.46^{+0.31}_{-0.29}$	$0.12^{+0.04}_{-0.03}$	$2.33^{+0.38}_{-0.23}$	$5.39^{+8.49}_{-3.50}$
$14.3 < \log_{10} m_{500}$	$0.57^{+0.25}_{-0.16}$	$3.10^{+1.49}_{-0.48}$	$-0.15^{+0.11}_{-0.10}$	$1.62^{+2.29}_{-0.48}$	$1.45^{+0.58}_{-0.41}$	$0.102^{+0.017}_{-0.011}$	$3.00^{+0.00}_{-0.00}$	$0.90^{+0.71}_{-0.37}$

**TABLE A.19:** The fit values for the medians of the cylindrical temperature profiles,  $T/T_{500}$ , at  $z = 0$ . The errors are determined through bootstrap methods – errors written as 0.00, correspond to very small values,  $< 10^{-9}$ . The fit parameters correspond to those described in Eq. (2.5).

$z = 0$	$T_0$	$r_t$	$a$	$b$	$c$	$r_{\text{cool}}$	$a_{\text{cool}}$	$T_{\text{min}}$
$\log_{10} m_{500} < 13.5$								
$T_y$	$0.94^{+0.02}_{-0.02}$	$2.13^{+0.36}_{-0.26}$	$0.24^{+0.02}_{-0.02}$	$1.10^{+0.25}_{-0.09}$	$0.00^{+0.00}_{-0.00}$	$0.120^{+0.006}_{-0.007}$	$2.39^{+0.26}_{-0.24}$	$0.37^{+0.04}_{-0.05}$
$T_y$	$1.04^{+0.19}_{-0.11}$	$0.38^{+0.14}_{-0.11}$	$0.10^{+0.16}_{-0.21}$	$4.23^{+5.80}_{-2.09}$	$0.24^{+0.22}_{-0.14}$	$0.092^{+0.057}_{-0.058}$	$3.00^{+0.00}_{-1.41}$	$0.64^{+0.43}_{-0.64}$
$T_{\text{sl}}$	$1.17^{+0.45}_{-0.22}$	$0.40^{+0.26}_{-0.09}$	$0.05^{+0.53}_{-0.27}$	$2.85^{+2.13}_{-1.49}$	$0.48^{+0.29}_{-0.40}$	$0.100^{+0.184}_{-0.054}$	$3.00^{+0.00}_{-1.63}$	$0.68^{+0.62}_{-0.68}$
$13.5 < \log_{10} m_{500} < 14.0$								
$T_y$	$0.87^{+0.07}_{-0.05}$	$1.03^{+0.14}_{-0.16}$	$0.45^{+0.02}_{-0.02}$	$1.02^{+0.10}_{-0.02}$	$0.00^{+0.00}_{-0.00}$	$0.119^{+0.006}_{-0.005}$	$1.61^{+0.14}_{-0.13}$	$0.18^{+0.04}_{-0.04}$
$T_y$	$1.31^{+0.77}_{-0.18}$	$0.34^{+0.05}_{-0.07}$	$-0.10^{+0.08}_{-0.15}$	$1.68^{+0.46}_{-0.68}$	$0.73^{+0.31}_{-0.14}$	$0.053^{+0.477}_{-0.034}$	$3.00^{+0.00}_{-0.36}$	$0.15^{+1.81}_{-0.15}$
$T_{\text{sl}}$	$1.10^{+0.25}_{-0.71}$	$0.63^{+0.19}_{-0.11}$	$-0.15^{+0.03}_{-0.05}$	$2.28^{+1.18}_{-0.66}$	$1.19^{+0.29}_{-0.54}$	$0.304^{+0.113}_{-0.026}$	$3.00^{+0.00}_{-1.19}$	$1.56^{+0.30}_{-0.12}$
$14.0 < \log_{10} m_{500} < 14.5$								
$T_y$	$0.77^{+0.25}_{-0.09}$	$0.98^{+0.36}_{-0.72}$	$0.38^{+0.05}_{-0.43}$	$11.9^{+775}_{-10.0}$	$0.09^{+0.30}_{-0.05}$	$0.107^{+0.035}_{-0.011}$	$1.46^{+1.54}_{-0.24}$	$0.22^{+0.98}_{-0.08}$
$T_y$	$0.64^{+0.06}_{-0.06}$	$1.09^{+0.14}_{-0.10}$	$0.69^{+0.07}_{-0.11}$	$8.85^{+6.76}_{-4.35}$	$0.20^{+0.18}_{-0.06}$	$0.240^{+0.096}_{-0.059}$	$1.12^{+0.14}_{-0.07}$	$0.023^{+0.044}_{-0.018}$
$T_{\text{sl}}$	$0.54^{+0.87}_{-0.31}$	$1.77^{+12.5}_{-0.70}$	$0.24^{+0.29}_{-0.51}$	$2.05^{+1.46}_{-0.76}$	$2.67^{+47.3}_{-1.86}$	$0.141^{+0.176}_{-0.038}$	$2.06^{+0.51}_{-0.46}$	$0.23^{+2.17}_{-0.17}$
$14.5 < \log_{10} m_{500} < 14.78$								
$T_y$	$0.71^{+0.25}_{-0.36}$	$1.07^{+1.15}_{-0.89}$	$0.18^{+0.12}_{-0.32}$	$3.98^{+20.6}_{-2.37}$	$0.38^{+1.07}_{-0.16}$	$0.106^{+1.51}_{-0.017}$	$2.42^{+0.58}_{-1.05}$	$0.52^{+1.15}_{-0.23}$
$T_y$	$0.22^{+1.39}_{-0.22}$	$0.17^{+2.01}_{-0.03}$	$-0.18^{+0.08}_{-0.15}$	$2.31^{+1.73}_{-1.30}$	$0.61^{+2.32}_{-0.25}$	$1.79^{+0.40}_{-1.56}$	$2.19^{+0.81}_{-0.49}$	$1.10^{+1.10}_{-0.11}$
$T_{\text{sl}}$	$0.54^{+0.05}_{-0.48}$	$1.47^{+1.84}_{-1.29}$	$0.30^{+0.08}_{-0.65}$	$2.89^{+1.03}_{-0.92}$	$2.56^{+6.09}_{-1.73}$	$0.104^{+1.23}_{-0.008}$	$2.60^{+0.40}_{-0.40}$	$0.21^{+0.89}_{-0.07}$
$14.78 < \log_{10} m_{500}$								
$T_y$	$0.80^{+0.02}_{-0.04}$	$0.83^{+0.17}_{-0.16}$	$0.13^{+0.01}_{-0.28}$	$4.88^{+3.21}_{-2.02}$	$0.25^{+0.30}_{-0.06}$	$0.066^{+0.109}_{-0.009}$	$3.00^{+0.00}_{-0.78}$	$0.57^{+0.52}_{-0.05}$
$T_y$	$0.69^{+0.04}_{-0.09}$	$0.78^{+0.13}_{-0.16}$	$0.17^{+0.04}_{-1.04}$	$3.54^{+2.35}_{-1.47}$	$0.39^{+0.72}_{-0.11}$	$0.059^{+0.023}_{-0.018}$	$2.34^{+0.66}_{-0.80}$	$0.41^{+1.15}_{-0.24}$
$T_{\text{sl}}$	$0.11^{+0.50}_{-0.04}$	$0.76^{+0.04}_{-0.67}$	$-1.65^{+0.60}_{-0.07}$	$4.08^{+1.14}_{-1.35}$	$1.10^{+0.75}_{-0.28}$	$0.067^{+0.951}_{-0.005}$	$2.07^{+0.93}_{-0.13}$	$64.3^{+35.7}_{-63.2}$

**TABLE A.20:** The fit values for the medians of the cylindrical temperature profiles,  $T/T_{500}$ , at  $z = 0.5$ . The errors are determined through bootstrap methods – errors written as 0.00, correspond to very small values,  $< 10^{-9}$ . The fit parameters correspond to those described in Eq. (2.5).

$z = 0.5$	$T_0$	$r_t$	$a$	$b$	$c$	$r_{\text{cool}}$	$a_{\text{cool}}$	$T_{\text{min}}$
$\log_{10} m_{500} < 13.5$								
$T_y$	$0.85^{+0.04}_{-0.02}$	$1.45^{+0.16}_{-0.20}$	$0.38^{+0.02}_{-0.03}$	$1.02^{+0.13}_{-0.02}$	$0.00^{+0.00}_{-0.00}$	$0.121^{+0.006}_{-0.006}$	$1.86^{+0.19}_{-0.17}$	$0.23^{+0.04}_{-0.04}$
$T_y$	$0.95^{+0.29}_{-0.53}$	$0.47^{+1.58}_{-0.13}$	$0.03^{+0.56}_{-0.16}$	$3.97^{+3.77}_{-1.96}$	$0.29^{+0.31}_{-0.29}$	$0.206^{+0.334}_{-0.104}$	$1.88^{+1.12}_{-0.66}$	$0.76^{+0.63}_{-0.72}$
$T_{\text{sl}}$	$0.97^{+0.26}_{-0.36}$	$0.59^{+0.25}_{-0.19}$	$0.17^{+0.51}_{-0.34}$	$3.40^{+6.38}_{-1.43}$	$0.53^{+0.39}_{-0.40}$	$0.178^{+0.218}_{-0.075}$	$2.47^{+0.53}_{-1.10}$	$0.68^{+0.86}_{-0.64}$
$13.5 < \log_{10} m_{500} < 14.0$								
$T_y$	$1.12^{+0.15}_{-0.39}$	$0.47^{+0.80}_{-0.12}$	$0.22^{+0.24}_{-0.10}$	$2.74^{+1.10}_{-1.05}$	$0.22^{+0.13}_{-0.22}$	$0.090^{+0.019}_{-0.010}$	$3.00^{+0.00}_{-1.60}$	$0.74^{+0.19}_{-0.62}$
$T_y$	$0.74^{+0.23}_{-0.26}$	$0.74^{+0.14}_{-0.44}$	$0.20^{+0.48}_{-0.34}$	$4.72^{+10.2}_{-2.86}$	$0.27^{+0.52}_{-0.18}$	$0.214^{+0.268}_{-0.103}$	$1.44^{+1.56}_{-0.27}$	$0.46^{+1.04}_{-0.42}$
$T_{\text{sl}}$	$0.61^{+0.06}_{-0.13}$	$1.00^{+0.32}_{-0.15}$	$0.63^{+0.17}_{-0.45}$	$4.14^{+1.91}_{-1.57}$	$0.65^{+0.55}_{-0.20}$	$0.162^{+0.112}_{-0.042}$	$1.59^{+0.46}_{-0.21}$	$0.07^{+0.40}_{-0.05}$
$14.0 < \log_{10} m_{500} < 14.55$								
$T_y$	$0.67^{+0.10}_{-0.28}$	$1.43^{+2.30}_{-0.62}$	$0.34^{+0.07}_{-0.19}$	$5.37^{+7.73}_{-2.83}$	$0.32^{+7.32}_{-0.16}$	$0.105^{+0.039}_{-0.013}$	$1.53^{+0.58}_{-0.34}$	$0.22^{+0.31}_{-0.11}$
$T_y$	$0.58^{+0.06}_{-0.10}$	$1.12^{+0.36}_{-0.92}$	$0.45^{+0.17}_{-0.54}$	$4.01^{+5.15}_{-2.01}$	$0.45^{+0.48}_{-0.16}$	$0.155^{+1.490}_{-0.056}$	$1.39^{+1.10}_{-0.30}$	$0.12^{+0.95}_{-0.09}$
$T_{\text{sl}}$	$0.56^{+0.03}_{-0.07}$	$1.23^{+0.28}_{-0.16}$	$0.44^{+0.10}_{-0.63}$	$3.67^{+1.02}_{-0.90}$	$1.37^{+0.73}_{-0.42}$	$0.124^{+0.136}_{-0.013}$	$1.96^{+0.47}_{-0.33}$	$0.14^{+0.95}_{-0.06}$
$14.55 < \log_{10} m_{500}$								
$T_y$	$0.92^{+0.14}_{-0.42}$	$0.74^{+0.23}_{-0.53}$	$0.02^{+0.23}_{-0.17}$	$3.47^{+9.16}_{-2.14}$	$0.32^{+0.32}_{-0.18}$	$0.114^{+1.100}_{-0.066}$	$1.85^{+1.15}_{-0.85}$	$0.86^{+0.73}_{-0.68}$
$T_y$	$0.74^{+0.19}_{-0.25}$	$0.70^{+0.30}_{-0.55}$	$0.28^{+0.16}_{-0.45}$	$3.81^{+15.2}_{-2.55}$	$0.31^{+0.55}_{-0.18}$	$0.094^{+1.100}_{-0.042}$	$1.47^{+1.53}_{-0.47}$	$0.16^{+0.92}_{-0.16}$
$T_{\text{sl}}$	$0.62^{+0.04}_{-0.19}$	$0.65^{+0.05}_{-0.52}$	$0.41^{+0.11}_{-1.01}$	$6.80^{+5.21}_{-2.85}$	$0.47^{+0.31}_{-0.12}$	$0.098^{+0.823}_{-0.017}$	$1.76^{+1.24}_{-0.26}$	$0.09^{+0.99}_{-0.09}$

**TABLE A.21:** The fit values for the medians of the cylindrical temperature profiles,  $T/T_{500}$ , at  $z = 1$ . The errors are determined through bootstrap methods – errors written as 0.00, correspond to very small values,  $< 10^{-9}$ . The fit parameters correspond to those described in Eq. (2.5).

$z = 1$	$T_0$	$r_t$	$a$	$b$	$c$	$r_{\text{cool}}$	$u_{\text{cool}}$	$T_{\text{min}}$
$\log_{10} m_{500} < 13.5$								
$T_y$	$1.35^{+0.29}_{-0.34}$	$0.34^{+0.37}_{-0.08}$	$0.24^{+0.26}_{-0.28}$	$2.54^{+75.1}_{-1.32}$	$0.22^{+0.28}_{-0.22}$	$0.088^{+0.039}_{-0.050}$	$1.91^{+1.09}_{-0.68}$	$0.20^{+0.82}_{-0.20}$
$T_y$	$1.03^{+0.83}_{-0.97}$	$0.36^{+0.40}_{-0.18}$	$-0.15^{+0.54}_{-0.12}$	$1.73^{+15.0}_{-0.72}$	$0.76^{+0.38}_{-0.66}$	$0.289^{+1.170}_{-0.224}$	$3.00^{+0.00}_{-1.85}$	$1.27^{+0.77}_{-1.24}$
$T_{\text{sl}}$	$0.73^{+0.12}_{-0.31}$	$0.88^{+0.70}_{-0.19}$	$0.42^{+0.16}_{-0.39}$	$3.38^{+1.52}_{-1.60}$	$0.73^{+1.23}_{-0.30}$	$0.119^{+0.120}_{-0.014}$	$2.04^{+0.84}_{-0.44}$	$0.27^{+0.77}_{-0.17}$
$13.5 < \log_{10} m_{500} < 14.0$								
$T_y$	$0.76^{+0.33}_{-0.34}$	$0.91^{+0.35}_{-0.66}$	$0.41^{+0.07}_{-0.54}$	$10.5^{+45.4}_{-8.68}$	$0.10^{+0.39}_{-0.06}$	$0.113^{+0.601}_{-0.018}$	$1.44^{+1.56}_{-0.31}$	$0.23^{+1.22}_{-0.14}$
$T_y$	$0.57^{+0.41}_{-0.40}$	$0.92^{+0.32}_{-0.21}$	$-0.12^{+0.08}_{-0.07}$	$3.61^{+4.89}_{-2.14}$	$0.72^{+0.80}_{-0.49}$	$0.335^{+0.072}_{-0.101}$	$1.62^{+0.95}_{-0.39}$	$1.46^{+0.45}_{-0.38}$
$T_{\text{sl}}$	$1.42^{+1.20}_{-1.31}$	$1.33^{+2.09}_{-0.52}$	$-0.30^{+0.11}_{-0.08}$	$1.47^{+1.76}_{-0.39}$	$2.93^{+3.08}_{-2.11}$	$0.249^{+0.059}_{-0.048}$	$2.31^{+0.69}_{-0.62}$	$2.44^{+1.71}_{-1.25}$
$14.0 < \log_{10} m_{500} < 14.3$								
$T_y$	$0.72^{+0.06}_{-0.24}$	$1.16^{+0.95}_{-0.39}$	$0.24^{+0.05}_{-0.27}$	$5.56^{+13.1}_{-2.83}$	$0.29^{+1.04}_{-0.10}$	$0.102^{+0.167}_{-0.012}$	$2.28^{+0.72}_{-0.69}$	$0.43^{+0.68}_{-0.15}$
$T_y$	$0.57^{+0.37}_{-0.28}$	$1.07^{+0.40}_{-0.89}$	$-0.09^{+0.50}_{-0.09}$	$3.49^{+2.74}_{-1.78}$	$0.61^{+1.15}_{-0.24}$	$0.275^{+1.45}_{-0.167}$	$2.02^{+0.98}_{-0.57}$	$1.00^{+0.65}_{-0.85}$
$T_{\text{sl}}$	$0.52^{+0.05}_{-0.12}$	$1.48^{+1.39}_{-0.31}$	$0.37^{+0.00}_{-0.64}$	$3.24^{+1.10}_{-1.06}$	$2.18^{+4.25}_{-0.77}$	$0.112^{+0.127}_{-0.009}$	$2.34^{+0.39}_{-0.37}$	$0.15^{+0.92}_{-0.06}$
$14.3 < \log_{10} m_{500}$								
$T_y$	$1.04^{+0.22}_{-0.19}$	$0.53^{+0.24}_{-0.16}$	$0.08^{+0.30}_{-0.16}$	$3.78^{+42.2}_{-2.05}$	$0.35^{+0.32}_{-0.25}$	$0.115^{+0.348}_{-0.081}$	$2.99^{+0.01}_{-1.93}$	$0.73^{+0.62}_{-0.73}$
$T_y$	$0.91^{+0.19}_{-0.11}$	$0.54^{+0.26}_{-0.08}$	$0.10^{+0.30}_{-0.13}$	$2.44^{+4.01}_{-0.95}$	$0.55^{+0.29}_{-0.34}$	$0.066^{+0.109}_{-0.036}$	$3.00^{+0.00}_{-1.84}$	$0.49^{+0.23}_{-0.49}$
$T_{\text{sl}}$	$0.70^{+0.05}_{-0.07}$	$0.60^{+0.06}_{-0.05}$	$0.25^{+0.22}_{-0.08}$	$3.81^{+1.78}_{-0.82}$	$0.88^{+0.17}_{-0.26}$	$0.083^{+0.033}_{-0.013}$	$3.00^{+0.00}_{-1.38}$	$0.28^{+0.06}_{-0.28}$

**TABLE A.22:** The fit values for the medians of the cylindrical profiles of  $\sigma(T_y)/T_{500}$  across all redshifts. The errors are determined through bootstrap methods – errors written as 0.00, correspond to very small values,  $< 10^{-9}$ . The fit parameters correspond to those described in Eq. (2.5).

$\sigma(T_y)$	$T_0$	$r_t$	$a$	$b$	$c$	$r_{\text{cool}}$	$a_{\text{cool}}$	$T_{\text{min}}$
$z = 0$								
$\log_{10} m_{500} < 13.5$	$0.44^{+0.99}_{-0.08}$	$0.27^{+0.09}_{-0.19}$	$-3.00^{+0.00}_{-0.00}$	$3.76^{+0.98}_{-1.94}$	$2.76^{+0.35}_{-0.18}$	$0.066^{+1.360}_{-0.005}$	$2.71^{+0.29}_{-0.18}$	$26.5^{+36.0}_{-25.2}$
$13.5 < \log_{10} m_{500} < 14.0$	$0.30^{+0.49}_{-0.16}$	$0.64^{+0.74}_{-0.50}$	$-1.15^{+0.12}_{-0.11}$	$3.9^{+20.0}_{-1.9}$	$0.85^{+0.81}_{-0.65}$	$0.133^{+0.044}_{-0.021}$	$1.76^{+0.44}_{-0.10}$	$5.5^{+16.5}_{-4.0}$
$14.0 < \log_{10} m_{500} < 14.5$	$0.20^{+0.53}_{-0.08}$	$0.96^{+0.14}_{-0.89}$	$-0.94^{+0.36}_{-0.33}$	$6.7^{+18.9}_{-5.1}$	$0.41^{+0.67}_{-0.14}$	$0.053^{+0.931}_{-0.020}$	$1.45^{+0.82}_{-0.13}$	$10.2^{+31.8}_{-9.6}$
$14.5 < \log_{10} m_{500} < 14.78$	$0.32^{+0.04}_{-0.17}$	$1.01^{+0.12}_{-0.11}$	$-0.29^{+0.16}_{-0.87}$	$16^{+621}_{-10}$	$0.34^{+0.27}_{-0.12}$	$0.078^{+0.070}_{-0.064}$	$1.37^{+0.97}_{-0.37}$	$1.1^{+98.9}_{-0.6}$
$14.78 < \log_{10} m_{500}$	$0.40^{+0.04}_{-0.01}$	$0.96^{+0.25}_{-0.10}$	$-0.20^{+0.02}_{-0.02}$	$8.97^{+48.2}_{-4.86}$	$0.34^{+0.40}_{-0.08}$	$0.007^{+0.001}_{-0.001}$	$1.00^{+0.00}_{-0.00}$	$1.91^{+0.37}_{-0.32}$
$z = 0.5$								
$\log_{10} m_{500} < 13.5$	$0.34^{+0.07}_{-0.18}$	$0.30^{+1.12}_{-0.10}$	$-2.98^{+1.46}_{-0.02}$	$3.5^{+91.2}_{-1.6}$	$2.78^{+0.56}_{-2.37}$	$0.101^{+0.057}_{-0.059}$	$2.42^{+0.32}_{-0.55}$	$44.5^{+51.7}_{-32.9}$
$13.5 < \log_{10} m_{500} < 14.0$	$0.29^{+0.39}_{-0.11}$	$0.31^{+0.37}_{-0.23}$	$-0.92^{+0.22}_{-0.52}$	$3.82^{+2.24}_{-2.25}$	$0.64^{+0.91}_{-0.18}$	$0.110^{+0.066}_{-0.059}$	$1.76^{+0.60}_{-0.36}$	$1.57^{+7.09}_{-1.09}$
$14.0 < \log_{10} m_{500} < 14.55$	$0.25^{+0.08}_{-0.13}$	$1.06^{+0.11}_{-0.08}$	$-0.65^{+0.34}_{-0.58}$	$12.6^{+125}_{-7.6}$	$0.34^{+0.23}_{-0.15}$	$0.045^{+0.060}_{-0.032}$	$1.24^{+0.17}_{-0.25}$	$3.5^{+96.5}_{-2.5}$
$14.55 < \log_{10} m_{500}$	$0.49^{+0.04}_{-0.02}$	$0.99^{+0.32}_{-0.16}$	$-0.20^{+0.03}_{-0.03}$	$4.65^{+1.89}_{-1.21}$	$0.57^{+0.54}_{-0.15}$	$0.012^{+0.001}_{-0.001}$	$1.00^{+0.00}_{-0.00}$	$1.93^{+0.41}_{-0.35}$
$z = 1$								
$\log_{10} m_{500} < 13.5$	$0.33^{+0.06}_{-0.13}$	$0.37^{+0.31}_{-0.13}$	$-0.86^{+0.10}_{-0.22}$	$5.42^{+3.36}_{-1.44}$	$0.67^{+0.12}_{-0.29}$	$0.134^{+0.019}_{-0.033}$	$2.17^{+0.83}_{-0.55}$	$1.56^{+4.09}_{-0.62}$
$13.5 < \log_{10} m_{500} < 14.0$	$0.19^{+0.11}_{-0.08}$	$0.92^{+0.11}_{-0.10}$	$-0.80^{+0.32}_{-0.48}$	$10.4^{+16.3}_{-5.5}$	$0.29^{+0.21}_{-0.09}$	$0.052^{+0.061}_{-0.027}$	$1.33^{+0.23}_{-0.12}$	$6.1^{+40.0}_{-4.5}$
$14.0 < \log_{10} m_{500} < 14.3$	$0.19^{+0.16}_{-0.07}$	$1.07^{+0.08}_{-0.07}$	$-1.02^{+0.68}_{-0.23}$	$34.5^{+922}_{-30.1}$	$0.38^{+0.30}_{-0.13}$	$0.019^{+0.074}_{-0.006}$	$1.34^{+0.14}_{-0.27}$	$32.0^{+68.0}_{-30.8}$
$14.3 < \log_{10} m_{500}$	$0.50^{+0.03}_{-0.01}$	$4.30^{+4.22}_{-3.45}$	$-0.015^{+0.011}_{-0.068}$	$3.23^{+1.35}_{-0.79}$	$50.0^{+0.0}_{-49.6}$	$0.054^{+0.011}_{-0.031}$	$3.00^{+0.00}_{-2.00}$	$0.60^{+0.42}_{-0.04}$

## Appendix B

# Scaling fits for multi-Simulation SZ temperature scalings

Here we tabulate a number of the data fits referenced in the text above. In general, the haloes have been processed by taking the data into logarithmically spaced mass (or  $Y$ ) bins, and calculating the median, 16 and 84 percentiles within these bins. The fits are then the fits to these data points, with respect to the median mass (or  $Y$ ) within the same bin.

In particular, the fits we have tabulated here are: Tables B.1 and B.2, the 2- and 3-parameter cross-simulation sample  $T - M$  fits at  $z = 0$ , including the 16 and 84 percentiles; Table B.3, the 2- and 3-parameter median  $T - M$  fits for each sample individually at  $z = 0$ ; Table B.4, the 2-parameter median  $T - M$  fits for the cross-simulation sample at each redshift; Table B.5, the shifts and errors in the radius, mass and temperatures over varying radial halo extent definitions for each sample and the cross-simulation sample at  $z = 0$ ; Tables B.6 and B.7, the 2- and 3-parameter cross-simulation sample, within  $R_{500c}$ ,  $T - M$  fits at  $z = 0$ , including the 16 and 84 percentiles; Tables B.8 and B.9, the 2- and 3-parameter  $T - Y$  fits for the cross-simulation sample and each individual sample respectively; and Table B.10, the 2-parameter  $T_y - Y$  fits over each redshift for the cross-simulation sample, taking only haloes with  $Y_{200c} > 10^{-6}$ , including the 16 and 84 percentiles.



**TABLE B.1:** The two parameter fits (Eq. (3.1)) and a measure of the intrinsic scatter (Eq. (3.2)) in the fits at  $z = 0$  for the median and 16 and 84 percentiles of the cross simulation averaged sample within  $R_{200c}$ .

median	$A$	$B$	$\sigma_{\log_{10} T}$
$T_y$	$1.465^{+0.002}_{-0.002}$	$0.586^{+0.003}_{-0.002}$	$0.1025^{+0.0003}_{-0.0002}$
$T_m$	$1.210^{+0.001}_{-0.001}$	$0.591^{+0.003}_{-0.003}$	$0.0805^{+0.0002}_{-0.0001}$
$T_{sl}$	$1.135^{+0.003}_{-0.003}$	$0.601^{+0.006}_{-0.011}$	$0.2067^{+0.0016}_{-0.0008}$
16%			
$T_y$	$1.259^{+0.002}_{-0.003}$	$0.590^{+0.002}_{-0.002}$	—
$T_m$	$1.063^{+0.002}_{-0.002}$	$0.597^{+0.002}_{-0.002}$	—
$T_{sl}$	$0.872^{+0.003}_{-0.003}$	$0.636^{+0.003}_{-0.003}$	—
84%			
$T_y$	$1.694^{+0.003}_{-0.003}$	$0.573^{+0.002}_{-0.002}$	—
$T_m$	$1.381^{+0.002}_{-0.002}$	$0.585^{+0.003}_{-0.002}$	—
$T_{sl}$	$1.364^{+0.003}_{-0.003}$	$0.611^{+0.002}_{-0.002}$	—

**TABLE B.2:** The three parameter fits (Eq. (3.1)) and a measure of the intrinsic scatter (Eq. (3.2)) in the fits at  $z = 0$  for the median and 16 and 84 percentiles within the cross simulation averaged sample within  $R_{200c}$ .

median	$A$	$B$	$C$	$\sigma_{\log_{10} T}$
$T_y$	$1.426^{+0.006}_{-0.007}$	$0.566^{+0.001}_{-0.001}$	$0.024^{+0.005}_{-0.004}$	$0.1011^{+0.0001}_{-0.0001}$
$T_m$	$1.207^{+0.005}_{-0.005}$	$0.589^{+0.001}_{-0.001}$	$0.003^{+0.004}_{-0.005}$	$0.0804^{+0.0001}_{-0.0001}$
$T_{sl}$	$1.196^{+0.020}_{-0.009}$	$0.641^{+0.003}_{-0.003}$	$-0.048^{+0.007}_{-0.018}$	$0.2028^{+0.0002}_{-0.0001}$
16%				
$T_y$	$1.248^{+0.005}_{-0.005}$	$0.585^{+0.001}_{-0.001}$	$0.008^{+0.004}_{-0.004}$	—
$T_m$	$1.068^{+0.004}_{-0.003}$	$0.600^{+0.001}_{-0.001}$	$-0.005^{+0.003}_{-0.003}$	—
$T_{sl}$	$0.920^{+0.006}_{-0.005}$	$0.667^{+0.003}_{-0.003}$	$-0.051^{+0.004}_{-0.005}$	—
84%				
$T_y$	$1.641^{+0.005}_{-0.004}$	$0.555^{+0.001}_{-0.001}$	$0.030^{+0.002}_{-0.003}$	—
$T_m$	$1.370^{+0.004}_{-0.005}$	$0.580^{+0.001}_{-0.001}$	$0.007^{+0.004}_{-0.002}$	—
$T_{sl}$	$1.398^{+0.005}_{-0.005}$	$0.625^{+0.002}_{-0.002}$	$-0.023^{+0.003}_{-0.003}$	—

**TABLE B.3:** The two and three parameter fits (Eq. (3.1)) and a measure of the intrinsic scatter (Eq. (3.2)) in the fits at  $z = 0$  for the median of each sample within  $R_{200c}$ .

	BAHAMAS+MACSIS			$\sigma_{\log_{10} T}$
	$A$	$B$	$C$	
$T_y$	$1.529^{+0.003}_{-0.003}$	$0.582^{+0.003}_{-0.003}$	0	$0.0829^{+0.0005}_{-0.0004}$
$T_y$	$1.494^{+0.007}_{-0.008}$	$0.564^{+0.002}_{-0.002}$	$0.022^{+0.005}_{-0.004}$	$0.0808^{+0.0001}_{-0.0001}$
$T_m$	$1.264^{+0.002}_{-0.002}$	$0.581^{+0.003}_{-0.003}$	0	$0.0445^{+0.0002}_{-0.0002}$
$T_m$	$1.261^{+0.006}_{-0.006}$	$0.580^{+0.002}_{-0.002}$	$0.002^{+0.004}_{-0.005}$	$0.0444^{+0.0001}_{-0.0001}$
$T_{sl}$	$1.186^{+0.004}_{-0.004}$	$0.596^{+0.007}_{-0.011}$	0	$0.0945^{+0.0024}_{-0.0013}$
$T_{sl}$	$1.277^{+0.022}_{-0.010}$	$0.654^{+0.004}_{-0.003}$	$-0.069^{+0.008}_{-0.019}$	$0.0849^{+0.0002}_{-0.0001}$
	THE300			$\sigma_{\log_{10} T}$
	$A$	$B$	$C$	
$T_y$	$1.295^{+0.004}_{-0.004}$	$0.596^{+0.005}_{-0.005}$	0	$0.1779^{+0.0008}_{-0.0008}$
$T_y$	$1.263^{+0.010}_{-0.011}$	$0.582^{+0.002}_{-0.002}$	$0.023^{+0.009}_{-0.009}$	$0.1754^{+0.0003}_{-0.0003}$
$T_m$	$1.137^{+0.004}_{-0.004}$	$0.599^{+0.005}_{-0.004}$	0	$0.1567^{+0.0007}_{-0.0006}$
$T_m$	$1.125^{+0.009}_{-0.009}$	$0.593^{+0.002}_{-0.002}$	$0.010^{+0.009}_{-0.008}$	$0.1558^{+0.0003}_{-0.0002}$
$T_{sl}$	$1.205^{+0.004}_{-0.006}$	$0.585^{+0.005}_{-0.012}$	0	$0.1520^{+0.0005}_{-0.0001}$
$T_{sl}$	$1.224^{+0.020}_{-0.011}$	$0.593^{+0.002}_{-0.002}$	$-0.013^{+0.007}_{-0.022}$	$0.1513^{+0.0003}_{-0.0005}$
	MAGNETICUM			$\sigma_{\log_{10} T}$
	$A$	$B$	$C$	
$T_y$	$1.511^{+0.007}_{-0.006}$	$0.612^{+0.006}_{-0.003}$	0	$0.0452^{+0.0005}_{-0.0003}$
$T_y$	$1.473^{+0.006}_{-0.005}$	$0.601^{+0.003}_{-0.003}$	$0.026^{+0.006}_{-0.004}$	$0.0438^{+0.0000}_{-0.0000}$
$T_m$	$1.182^{+0.004}_{-0.004}$	$0.622^{+0.004}_{-0.004}$	0	$0.0327^{+0.0002}_{-0.0001}$
$T_m$	$1.167^{+0.004}_{-0.004}$	$0.616^{+0.003}_{-0.003}$	$0.013^{+0.004}_{-0.004}$	$0.0326^{+0.0001}_{-0.0001}$
$T_{sl}$	$0.930^{+0.007}_{-0.006}$	$0.629^{+0.008}_{-0.006}$	0	$0.3020^{+0.0008}_{-0.0008}$
$T_{sl}$	$0.904^{+0.008}_{-0.008}$	$0.616^{+0.006}_{-0.006}$	$0.030^{+0.007}_{-0.006}$	$0.3035^{+0.0007}_{-0.0007}$
	TNG			$\sigma_{\log_{10} T}$
	$A$	$B$	$C$	
$T_y$	$1.302^{+0.008}_{-0.008}$	$0.583^{+0.007}_{-0.008}$	0	$0.0388^{+0.0010}_{-0.0010}$
$T_y$	$1.242^{+0.011}_{-0.010}$	$0.569^{+0.005}_{-0.005}$	$0.057^{+0.012}_{-0.014}$	$0.0356^{+0.0002}_{-0.0002}$
$T_m$	$1.129^{+0.006}_{-0.007}$	$0.604^{+0.005}_{-0.008}$	0	$0.0322^{+0.0007}_{-0.0008}$
$T_m$	$1.089^{+0.008}_{-0.007}$	$0.594^{+0.004}_{-0.005}$	$0.042^{+0.009}_{-0.012}$	$0.0304^{+0.0002}_{-0.0002}$
$T_{sl}$	$0.998^{+0.008}_{-0.009}$	$0.704^{+0.009}_{-0.009}$	0	$0.2030^{+0.0009}_{-0.0008}$
$T_{sl}$	$1.070^{+0.012}_{-0.013}$	$0.722^{+0.008}_{-0.008}$	$-0.084^{+0.019}_{-0.013}$	$0.2010^{+0.0006}_{-0.0005}$

**TABLE B.4:** The two parameter fits (Eq. (3.1)) and a measure of the intrinsic scatter (Eq. (3.2)) in the fits for the median across the higher redshifts of the cross simulation averaged sample within  $R_{200c}$ .

$z = 0.25$	$A$	$B$	$\sigma_{\log_{10} T}$
$T_y$	$1.448^{+0.002}_{-0.002}$	$0.600^{+0.002}_{-0.004}$	$0.0896^{+0.0003}_{-0.0005}$
$T_m$	$1.173^{+0.002}_{-0.002}$	$0.601^{+0.004}_{-0.005}$	$0.0669^{+0.0003}_{-0.0003}$
$T_{sl}$	$1.059^{+0.004}_{-0.004}$	$0.608^{+0.013}_{-0.017}$	$0.2151^{+0.0025}_{-0.0017}$
$z = 0.50$			
$T_y$	$1.423^{+0.003}_{-0.003}$	$0.591^{+0.003}_{-0.002}$	$0.0804^{+0.0002}_{-0.0002}$
$T_m$	$1.136^{+0.002}_{-0.002}$	$0.599^{+0.003}_{-0.002}$	$0.0589^{+0.0001}_{-0.0001}$
$T_{sl}$	$1.002^{+0.003}_{-0.003}$	$0.633^{+0.004}_{-0.003}$	$0.2246^{+0.0003}_{-0.0004}$
$z = 1.00$			
$T_y$	$1.376^{+0.004}_{-0.004}$	$0.594^{+0.003}_{-0.003}$	$0.0733^{+0.0001}_{-0.0001}$
$T_m$	$1.073^{+0.003}_{-0.002}$	$0.607^{+0.002}_{-0.002}$	$0.0513^{+0.0001}_{-0.0001}$
$T_{sl}$	$0.916^{+0.003}_{-0.003}$	$0.661^{+0.003}_{-0.004}$	$0.2394^{+0.0003}_{-0.0003}$
$z = 1.50$			
$T_y$	$1.343^{+0.006}_{-0.006}$	$0.594^{+0.004}_{-0.004}$	$0.0882^{+0.0001}_{-0.0001}$
$T_m$	$1.038^{+0.004}_{-0.005}$	$0.619^{+0.003}_{-0.004}$	$0.0515^{+0.0001}_{-0.0001}$
$T_{sl}$	$0.864^{+0.005}_{-0.005}$	$0.682^{+0.005}_{-0.005}$	$0.2999^{+0.0003}_{-0.0003}$

**TABLE B.5:** The shifts and errors in the radius, mass,  $T_m$  and  $T_y$  for each sample against those values within  $R_{200c}$ . We have also repeated the cross-simulation averages found in Table 3.7. These values are calculated on a cluster by cluster basis, and then the averages are found within these. The central value here is the median with the errors given by the 16 and 84 percentiles. NB. We do not here have values for  $M_{vir}$  and  $M_{200m}$  within the TNG sample.

	Cross simulation averaged sample			
	$R/R_{200c}$	$M/M_{200c}$	$T_m/T_{m,200c}$	$T_y/T_{m,200c}$
$R_{500c}$	$0.66^{+0.01}_{-0.02}$	$0.71^{+0.05}_{-0.07}$	$1.20^{+0.04}_{-0.07}$	$1.40^{+0.16}_{-0.12}$
$R_{200c}$	1.00	1.00	1.00	$1.22^{+0.11}_{-0.07}$
$R_{500m}$	$1.11^{+0.01}_{-0.01}$	$1.08^{+0.03}_{-0.02}$	$0.95^{+0.01}_{-0.01}$	$1.18^{+0.10}_{-0.06}$
$R_{vir}$	$1.33^{+0.03}_{-0.02}$	$1.22^{+0.08}_{-0.05}$	$0.87^{+0.04}_{-0.02}$	$1.11^{+0.09}_{-0.06}$
$R_{200m}$	$1.64^{+0.06}_{-0.04}$	$1.39^{+0.15}_{-0.10}$	$0.79^{+0.07}_{-0.04}$	$1.05^{+0.09}_{-0.06}$
	BAHAMAS+MACSIS			
	$R/R_{200c}$	$M/M_{200c}$	$T_m/T_{m,200c}$	$T_y/T_{m,200c}$
$R_{500c}$	$0.66^{+0.01}_{-0.02}$	$0.73^{+0.05}_{-0.07}$	$1.19^{+0.05}_{-0.06}$	$1.40^{+0.14}_{-0.09}$
$R_{200c}$	1.00	1.00	1.00	$1.21^{+0.11}_{-0.05}$
$R_{500m}$	$1.11^{+0.01}_{-0.01}$	$1.07^{+0.03}_{-0.02}$	$0.95^{+0.01}_{-0.01}$	$1.17^{+0.10}_{-0.05}$
$R_{vir}$	$1.33^{+0.03}_{-0.02}$	$1.21^{+0.08}_{-0.05}$	$0.87^{+0.03}_{-0.02}$	$1.10^{+0.09}_{-0.04}$
$R_{200m}$	$1.63^{+0.06}_{-0.04}$	$1.38^{+0.14}_{-0.09}$	$0.78^{+0.05}_{-0.03}$	$1.03^{+0.09}_{-0.05}$
	THE300			
	$R/R_{200c}$	$M/M_{200c}$	$T_m/T_{m,200c}$	$T_y/T_{m,200c}$
$R_{500c}$	$0.66^{+0.01}_{-0.03}$	$0.71^{+0.05}_{-0.08}$	$1.16^{+0.06}_{-0.09}$	$1.29^{+0.11}_{-0.11}$
$R_{200c}$	1.00	1.00	1.00	$1.15^{+0.08}_{-0.04}$
$R_{500m}$	$1.12^{+0.01}_{-0.01}$	$1.08^{+0.03}_{-0.03}$	$0.96^{+0.02}_{-0.02}$	$1.11^{+0.08}_{-0.04}$
$R_{vir}$	$1.33^{+0.03}_{-0.02}$	$1.21^{+0.09}_{-0.06}$	$0.90^{+0.06}_{-0.04}$	$1.07^{+0.11}_{-0.04}$
$R_{200m}$	$1.65^{+0.06}_{-0.04}$	$1.38^{+0.16}_{-0.11}$	$0.84^{+0.11}_{-0.06}$	$1.02^{+0.17}_{-0.05}$
	MAGNETICUM			
	$R/R_{200c}$	$M/M_{200c}$	$T_m/T_{m,200c}$	$T_y/T_{m,200c}$
$R_{500c}$	$0.65^{+0.01}_{-0.02}$	$0.70^{+0.05}_{-0.07}$	$1.22^{+0.03}_{-0.04}$	$1.51^{+0.13}_{-0.10}$
$R_{200c}$	1.00	1.00	1.00	$1.28^{+0.09}_{-0.06}$
$R_{500m}$	$1.12^{+0.01}_{-0.01}$	$1.09^{+0.03}_{-0.02}$	$0.95^{+0.01}_{-0.01}$	$1.23^{+0.08}_{-0.05}$
$R_{vir}$	$1.34^{+0.03}_{-0.02}$	$1.24^{+0.08}_{-0.05}$	$0.87^{+0.02}_{-0.02}$	$1.16^{+0.07}_{-0.04}$
$R_{200m}$	$1.66^{+0.06}_{-0.04}$	$1.43^{+0.15}_{-0.10}$	$0.78^{+0.04}_{-0.03}$	$1.09^{+0.07}_{-0.04}$
	TNG			
	$R/R_{200c}$	$M/M_{200c}$	$T_m/T_{m,200c}$	$T_y/T_{m,200c}$
$R_{500c}$	$0.65^{+0.01}_{-0.02}$	$0.70^{+0.04}_{-0.07}$	$1.22^{+0.04}_{-0.06}$	$1.37^{+0.11}_{-0.09}$
$R_{200c}$	1.00	1.00	1.00	$1.17^{+0.07}_{-0.04}$
$R_{500m}$	$1.11^{+0.01}_{-0.01}$	$1.06^{+0.03}_{-0.02}$	$0.96^{+0.01}_{-0.01}$	$1.14^{+0.06}_{-0.04}$
$R_{vir}$	$1.34^{+0.03}_{-0.02}$	—	$0.92^{+0.03}_{-0.03}$	$1.11^{+0.06}_{-0.04}$
$R_{200m}$	$1.66^{+0.06}_{-0.04}$	—	$0.90^{+0.04}_{-0.04}$	$1.10^{+0.06}_{-0.04}$

**TABLE B.6:** The two parameter fits (Eq. (3.1)) within  $R_{500c}$  and a measure of the intrinsic scatter (Eq. (3.2)) in the fits at  $z = 0$  for the median and 16 and 84 percentiles of the cross simulation averaged sample.

median	$A$	$B$	$\sigma_{\log_{10} T}$
$T_y$	$2.048^{+0.003}_{-0.003}$	$0.575^{+0.001}_{-0.002}$	$0.1020^{+0.0002}_{-0.0002}$
$T_m$	$1.763^{+0.002}_{-0.002}$	$0.576^{+0.001}_{-0.001}$	$0.0790^{+0.0000}_{-0.0000}$
$T_{sl}$	$1.570^{+0.003}_{-0.004}$	$0.565^{+0.003}_{-0.003}$	$0.2050^{+0.0007}_{-0.0007}$
16%			
$T_y$	$1.770^{+0.003}_{-0.003}$	$0.584^{+0.002}_{-0.003}$	—
$T_m$	$1.558^{+0.003}_{-0.002}$	$0.588^{+0.002}_{-0.002}$	—
$T_{sl}$	$1.255^{+0.006}_{-0.005}$	$0.616^{+0.012}_{-0.006}$	—
84%			
$T_y$	$2.370^{+0.006}_{-0.006}$	$0.563^{+0.005}_{-0.004}$	—
$T_m$	$2.005^{+0.007}_{-0.004}$	$0.570^{+0.010}_{-0.003}$	—
$T_{sl}$	$1.869^{+0.006}_{-0.008}$	$0.593^{+0.008}_{-0.011}$	—

**TABLE B.7:** The three parameter fits (Eq. (3.1)) within  $R_{500c}$  and a measure of the intrinsic scatter (Eq. (3.2)) in the fits at  $z = 0$  for the median and 16 and 84 percentiles within the cross simulation averaged sample.

median	$A$	$B$	$C$	$\sigma_{\log_{10} T}$
$T_y$	$1.996^{+0.005}_{-0.005}$	$0.557^{+0.001}_{-0.001}$	$0.023^{+0.001}_{-0.002}$	$0.1007^{+0.0000}_{-0.0000}$
$T_m$	$1.772^{+0.004}_{-0.004}$	$0.579^{+0.001}_{-0.001}$	$-0.004^{+0.001}_{-0.001}$	$0.0790^{+0.0000}_{-0.0000}$
$T_{sl}$	$1.736^{+0.006}_{-0.005}$	$0.633^{+0.002}_{-0.002}$	$-0.089^{+0.003}_{-0.003}$	$0.1886^{+0.0001}_{-0.0001}$
16%				
$T_y$	$1.706^{+0.008}_{-0.008}$	$0.564^{+0.001}_{-0.001}$	$0.034^{+0.004}_{-0.005}$	—
$T_m$	$1.552^{+0.005}_{-0.006}$	$0.586^{+0.001}_{-0.001}$	$0.003^{+0.004}_{-0.003}$	—
$T_{sl}$	$1.414^{+0.014}_{-0.023}$	$0.681^{+0.002}_{-0.002}$	$-0.111^{+0.022}_{-0.010}$	—
84%				
$T_y$	$2.292^{+0.014}_{-0.016}$	$0.545^{+0.001}_{-0.001}$	$0.031^{+0.008}_{-0.006}$	—
$T_m$	$1.988^{+0.010}_{-0.027}$	$0.566^{+0.001}_{-0.001}$	$0.007^{+0.017}_{-0.005}$	—
$T_{sl}$	$1.911^{+0.030}_{-0.020}$	$0.604^{+0.001}_{-0.001}$	$-0.020^{+0.012}_{-0.020}$	—

**TABLE B.8:** The two and three parameter  $T$ - $Y$  fits (Eq. (3.4)) and a measure of the intrinsic scatter (Eq. (3.2)) in the fits at  $z = 0$  for the median and 16 and 84 percentiles of the cross simulation averaged sample within  $R_{200c}$ .

median	$A$	$B$	$C$	$\sigma_{\log_{10} T}$
$T_y$	$2.887^{+0.009}_{-0.035}$	$0.323^{+0.001}_{-0.005}$	0	$0.1154^{+0.0003}_{-0.0013}$
$T_y$	$2.525^{+0.011}_{-0.008}$	$0.335^{+0.002}_{-0.005}$	$0.025^{+0.001}_{-0.003}$	$0.1069^{+0.0001}_{-0.0001}$
$T_m$	$2.395^{+0.015}_{-0.020}$	$0.326^{+0.002}_{-0.003}$	0	$0.0913^{+0.0005}_{-0.0007}$
$T_m$	$2.146^{+0.008}_{-0.008}$	$0.336^{+0.002}_{-0.004}$	$0.021^{+0.001}_{-0.002}$	$0.0860^{+0.0001}_{-0.0001}$
16%				
$T_y$	$2.340^{+0.010}_{-0.009}$	$0.318^{+0.001}_{-0.001}$	0	—
$T_y$	$2.123^{+0.008}_{-0.008}$	$0.341^{+0.002}_{-0.002}$	$0.024^{+0.001}_{-0.001}$	—
$T_m$	$1.993^{+0.006}_{-0.006}$	$0.324^{+0.001}_{-0.001}$	0	—
$T_m$	$1.846^{+0.005}_{-0.004}$	$0.342^{+0.002}_{-0.001}$	$0.019^{+0.001}_{-0.001}$	—
84%				
$T_y$	$3.321^{+0.011}_{-0.014}$	$0.305^{+0.001}_{-0.001}$	0	—
$T_y$	$3.013^{+0.010}_{-0.009}$	$0.328^{+0.001}_{-0.002}$	$0.024^{+0.001}_{-0.001}$	—
$T_m$	$2.729^{+0.012}_{-0.009}$	$0.312^{+0.001}_{-0.001}$	0	—
$T_m$	$2.539^{+0.006}_{-0.006}$	$0.329^{+0.002}_{-0.001}$	$0.018^{+0.001}_{-0.001}$	—

**TABLE B.9:** The two parameter  $T_y$ - $Y$  fits (Eq. (3.4)) for each sample and a measure of the intrinsic scatter (Eq. (3.2)) in the fits at  $z = 0$  for the median within  $R_{200c}$ .

median	$A$	$B$	$C$	$\sigma_{\log_{10} T}$
BAHAMAS+	$3.053^{+0.013}_{-0.036}$	$0.313^{+0.001}_{-0.004}$	0	$0.0979^{+0.0005}_{-0.0023}$
BAHAMAS+	$2.690^{+0.009}_{-0.008}$	$0.323^{+0.001}_{-0.001}$	$0.023^{+0.001}_{-0.001}$	$0.0815^{+0.0001}_{-0.0001}$
THE300	$2.411^{+0.012}_{-0.011}$	$0.338^{+0.001}_{-0.001}$	0	$0.1452^{+0.0003}_{-0.0003}$
THE300	$2.294^{+0.008}_{-0.009}$	$0.350^{+0.003}_{-0.002}$	$0.013^{+0.001}_{-0.001}$	$0.1450^{+0.0003}_{-0.0003}$
MAGNETICUM	$2.903^{+0.057}_{-0.052}$	$0.329^{+0.006}_{-0.005}$	0	$0.0462^{+0.0010}_{-0.0006}$
MAGNETICUM	$2.789^{+0.024}_{-0.027}$	$0.379^{+0.006}_{-0.008}$	$0.030^{+0.003}_{-0.003}$	$0.0461^{+0.0015}_{-0.0009}$
TNG	$2.326^{+0.028}_{-0.040}$	$0.316^{+0.004}_{-0.005}$	0	$0.0464^{+0.0011}_{-0.0013}$
TNG	$2.154^{+0.020}_{-0.022}$	$0.365^{+0.007}_{-0.008}$	$0.032^{+0.003}_{-0.003}$	$0.0353^{+0.0003}_{-0.0003}$

**TABLE B.10:** The two parameter  $T_y$ - $Y$  fits (Eq. (3.4)) for the ‘hot’ haloes (that is,  $Y_{200c} > 10^{-6}$ ) and a measure of the intrinsic scatter (Eq. (3.2)) in the fits across redshifts for the median and 16 and 84 percentiles of the cross simulation averaged sample within  $R_{200c}$ .

$z = 0.00$	$A$	$B$	$\sigma_{\log_{10} T}$
50%	$2.614^{+0.006}_{-0.006}$	$0.368^{+0.003}_{-0.010}$	$0.1873^{+0.0041}_{-0.0152}$
16%	$2.216^{+0.008}_{-0.008}$	$0.357^{+0.003}_{-0.003}$	—
84%	$3.102^{+0.009}_{-0.009}$	$0.350^{+0.002}_{-0.003}$	—
$z = 0.25$			
50%	$2.593^{+0.007}_{-0.007}$	$0.372^{+0.002}_{-0.005}$	$0.1685^{+0.0036}_{-0.0074}$
16%	$2.193^{+0.008}_{-0.007}$	$0.367^{+0.003}_{-0.003}$	—
84%	$3.093^{+0.010}_{-0.010}$	$0.355^{+0.002}_{-0.002}$	—
$z = 0.50$			
50%	$2.593^{+0.008}_{-0.008}$	$0.381^{+0.003}_{-0.002}$	$0.1625^{+0.0034}_{-0.0033}$
16%	$2.177^{+0.009}_{-0.008}$	$0.380^{+0.003}_{-0.003}$	—
84%	$3.074^{+0.010}_{-0.010}$	$0.354^{+0.003}_{-0.003}$	—
$z = 1.00$			
50%	$2.585^{+0.013}_{-0.012}$	$0.382^{+0.004}_{-0.004}$	$0.1388^{+0.0044}_{-0.0045}$
16%	$2.145^{+0.018}_{-0.020}$	$0.376^{+0.008}_{-0.014}$	—
84%	$3.091^{+0.020}_{-0.023}$	$0.361^{+0.008}_{-0.010}$	—
$z = 1.50$			
50%	$2.597^{+0.052}_{-0.031}$	$0.373^{+0.020}_{-0.011}$	$0.1263^{+0.0185}_{-0.0091}$
16%	$2.228^{+0.024}_{-0.023}$	$0.400^{+0.009}_{-0.008}$	—
84%	$3.115^{+0.032}_{-0.045}$	$0.368^{+0.008}_{-0.014}$	—